HYPERVELOCITY IMPACT CRATERING CALCULATIONS

PIFR-190

by

D. E. Maxwell and H. Moises

January 1971

Prepared for

NASA Manned Spacecraft Center
Technical Information Dissemination
Branch, Houston, Texas 77058

Under Contract NAS 9-9586

PHYSICS INTERNATIONAL COMPANY
2700 MERCED STREET • SAN LEANDRO, CALIFORNIA 94577 • PHONE 357-4610 (415) • TWX 891-9689 (415)

HYPERVELOCITY IMPACT CRATERING CALCULATIONS

PIFR-190

by

D. E. Maxwell and H. Moises

January 1971

Prepared for

NASA Manned Spacecraft Center
Technical Information Dissemination
Branch, Houston, Texas 77058

Under Contract NAS 9-9586

Prepared by

Physics International Company
2700 Merced Street
San Leandro, California 94577

UNCLASSIFIED
Security Classification

DOCUMENT CONTROL DATA - R&D

(Security classification of title, body of abstract and indexing annotation must be entered when the overall report is classified)

1. ORIGINATING ACTIVITY *(Corporate author)* Physics International Company	2a. REPORT SECURITY CLASSIFICATION Unclassified 2b. GROUP

3 REPORT TITLE

Hypervelocity Impact Cratering Calculations

4. DESCRIPTIVE NOTES *(Type of report and inclusive dates)*

Final Report

5. AUTHOR(S) *(Last name, first name, initial)*

Maxwell, D. E. and Moises, H.

6. REPORT DATE	7a. TOTAL NO. OF PAGES	7b. NO. OF REFS
January 1971	209	15

8a. CONTRACT OR GRANT NO. NAS 9-9586 b. PROJECT NO. c. d.	9a. ORIGINATOR'S REPORT NUMBER(S) PIFR-190 9b. OTHER REPORT NO(S) *(Any other numbers that may be assigned this report)*

10. AVAILABILITY/LIMITATION NOTICES

11. SUPPLEMENTARY NOTES	12. SPONSORING MILITARY ACTIVITY NASA Manned Spacecraft Center Technical Information Dissemination Branch, Houston, Texas

13. ABSTRACT

A summary is presented in this report of prediction calculations performed by Physics International Company to gain a better understanding of the mechanisms involved in hypervelocity impact cratering and response of earth media. Physics International Company's Eulerian-Lagrange (ELK) code was used for the calculations.

DD FORM 1 JAN 64 1473

Security Classification

14. KEY WORDS	LINK A		LINK B		LINK C	
	ROLE	WT	ROLE	WT	ROLE	WT
Hypervelocity Impact						
Finite Difference Calculations						
Cratering Study and Calculation						
Meteor Impact						
Sierra Madera Calculation						

INSTRUCTIONS

1. ORIGINATING ACTIVITY: Enter the name and address of the contractor, subcontractor, grantee, Department of Defense activity or other organization *(corporate author)* issuing the report.

2a. REPORT SECURITY CLASSIFICATION: Enter the overall security classification of the report. Indicate whether "Restricted Data" is included. Marking is to be in accordance with appropriate security regulations.

2b. GROUP: Automatic downgrading is specified in DoD Directive 5200.10 and Armed Forces Industrial Manual. Enter the group number. Also, when applicable, show that optional markings have been used for Group 3 and Group 4 as authorized.

3. REPORT TITLE: Enter the complete report title in all capital letters. Titles in all cases should be unclassified. If a meaningful title cannot be selected without classification, show title classification in all capitals in parenthesis immediately following the title.

4. DESCRIPTIVE NOTES: If appropriate, enter the type of report, e.g., interim, progress, summary, annual, or final. Give the inclusive dates when a specific reporting period is covered.

5. AUTHOR(S): Enter the name(s) of author(s) as shown on or in the report. Enter last name, first name, middle initial. If military, show rank and branch of service. The name of the principal author is an absolute minimum requirement.

6. REPORT DATE: Enter the date of the report as day, month, year; or month, year. If more than one date appears on the report, use date of publication.

7a. TOTAL NUMBER OF PAGES: The total page count should follow normal pagination procedures, i.e., enter the number of pages containing information.

7b. NUMBER OF REFERENCES: Enter the total number of references cited in the report.

8a. CONTRACT OR GRANT NUMBER: If appropriate, enter the applicable number of the contract or grant under which the report was written.

8b, 8c, & 8d. PROJECT NUMBER: Enter the appropriate military department identification, such as project number, subproject number, system numbers, task number, etc.

9a. ORIGINATOR'S REPORT NUMBER(S): Enter the official report number by which the document will be identified and controlled by the originating activity. This number must be unique to this report.

9b. OTHER REPORT NUMBER(S): If the report has been assigned any other report numbers *(either by the originator or by the sponsor)*, also enter this number(s).

10. AVAILABILITY/LIMITATION NOTICES: Enter any limitations on further dissemination of the report, other than those imposed by security classification, using standard statements such as:

(1) "Qualified requesters may obtain copies of this report from DDC."

(2) "Foreign announcement and dissemination of this report by DDC is not authorized."

(3) "U. S. Government agencies may obtain copies of this report directly from DDC. Other qualified DDC users shall request through _____."

(4) "U. S. military agencies may obtain copies of this report directly from DDC. Other qualified users shall request through _____."

(5) "All distribution of this report is controlled. Qualified DDC users shall request through _____."

If the report has been furnished to the Office of Technical Services, Department of Commerce, for sale to the public, indicate this fact and enter the price, if known.

11. SUPPLEMENTARY NOTES: Use for additional explanatory notes.

12. SPONSORING MILITARY ACTIVITY: Enter the name of the departmental project office or laboratory sponsoring *(paying for)* the research and development. Include address.

13. ABSTRACT: Enter an abstract giving a brief and factual summary of the document indicative of the report, even though it may also appear elsewhere in the body of the technical report. If additional space is required, a continuation sheet shall be attached.

It is highly desirable that the abstract of classified reports be unclassified. Each paragraph of the abstract shall end with an indication of the military security classification of the information in the paragraph, represented as *(TS)*, *(S)*, *(C)*, or *(U)*.

There is no limitation on the length of the abstract. However, the suggested length is from 150 to 225 words.

14. KEY WORDS: Key words are technically meaningful terms or short phrases that characterize a report and may be used as index entries for cataloging the report. Key words must be selected so that no security classification is required. Identifiers, such as equipment model designation, trade name, military project code name, geographic location, may be used as key words but will be followed by an indication of technical context. The assignment of links, roles, and weights is optional.

FOREWORD

This report, PIFR-190, is submitted by Physics International Company in partial fulfillment of Contract NAS 9-9586.

SUMMARY

In this report, a summary is presented of prediction calculations performed by Physics International Company. The object of the study was to gain a better understanding of the mechanisms involved in hypervelocity impact cratering and response of earth media. Physics International Company's Eulerian-Lagrange (ELK) code was used for the calculations. Originally, three cases were selected:

Case 1: A one-gram lithium-magnesium alloy impacting basalt normally at 6.4 km/sec.

Case 2: A large terrestrial impact corresponding to that of Sierra Madera.

Case 3: A large lunar impact on the scale of Tychos or Copernicus.

The Case 3 calculations, however, were not carried out because of questions regarding lunar material modeling. Instead, that time was used to investigate other cracking models for the LiMg-basalt impact of Case 1.

The LiMg-basalt impact calculation is discussed in Section 2 of this report; the Sierra Madera simulation in Section 3. Conclusions and recommendations are presented in Section 4. Appendix A contains details of the equation-of-state models. The vertical and horizontal responses of selected points of the Sierra Madera calculation are shown in Appendix B.

CONTENTS

ILLUSTRATIONS

ILLUSTRATIONS (Cont.)

ILLUSTRATIONS (Cont.)

ILLUSTRATIONS (cont.)

SECTION 1
INTRODUCTION

The primary objective of this study was to perform prediction calculations through which a better understanding would be gained of the mechanisms involved in the impact cratering and response of earth media. The Physics International two-dimensional ELK code was used as the basic computational tool. Originally, three impact cases were selected for study:

Case 1: A one-gram lithium-magnesium alloy sphere impacting basalt normally at 6.4 km/sec.

Case 2: The large terrestrial impact corresponding to that of Sierra Madera.

Case 3: A large lunar impact on the scale of Tychos or Copernicus.

Before Case 3 was initiated, the question arose of the very long duration of the seismic pulses recorded by the Apollo lunar seismographs. It was possible that present models for lunar material and lithology would be inadequate for the computer simulation of lunar impacts. For this reason the portion of the study originally scheduled for the lunar impact case was used to investigate other cracking models for the LiMg-basalt impact of Case 1. This was a fortunate decision because it turned out that the original basalt cracking model was entirely inadequate. This aspect of the study is discussed in Section 2. A new model, with admitted shortcomings, was discovered that did predict the basalt crater adequately and to some extent the crack pattern beneath

the crater.

The Sierra Madera computer simulation was laborious to perform because of the very long times required. It was originally anticipated that 10 seconds of cratering process would be required to establish the objective. It was determined that 30 seconds was required to predict the final upthrust displacements. The upthrust flow mechanism did not start until about 5.5 seconds, requiring a substantial effort in achieving maximum computing efficiency to complete the problem.

The results, however, were quite gratifying and indicate that the Sierra Madera structure can be entirely explained by the response following a large impact.

SECTION 2

ONE-GRAM LiMg SPHERE IMPACTING BASALT AT 6.4 km/sec

2.1 Real and Simulated Geometries

Figure 2.1 shows the geometry of the experiment. Details are reported in Reference 1. The experimental aluminum plate and concrete containment of the basalt was eliminated in the calculation for expediency. Instead, in the calculation, the basalt material effectively extended throughout the entire half-space below the surface.

2.2 Calculation Grid Space

Figure 2.2 shows the axisymmetric regions of space defined by the Euler and Lagrange grids of the ELK code. The regions were chosen so that the violent material flow in the region of impact would occur in the uncovered part of the Euler grid thus maintaining a reasonable time step for the ELK code computing cycles consistent with restricting computer costs and obtaining good resolution.

At t = 0 (impact time) the uncovered Euler region existed above the surface as shown in Figure 2.2 and below the surface inside the radius R = 1.23 cm. At this time the Lagrange grid extended over all of the half-space below the surface except for

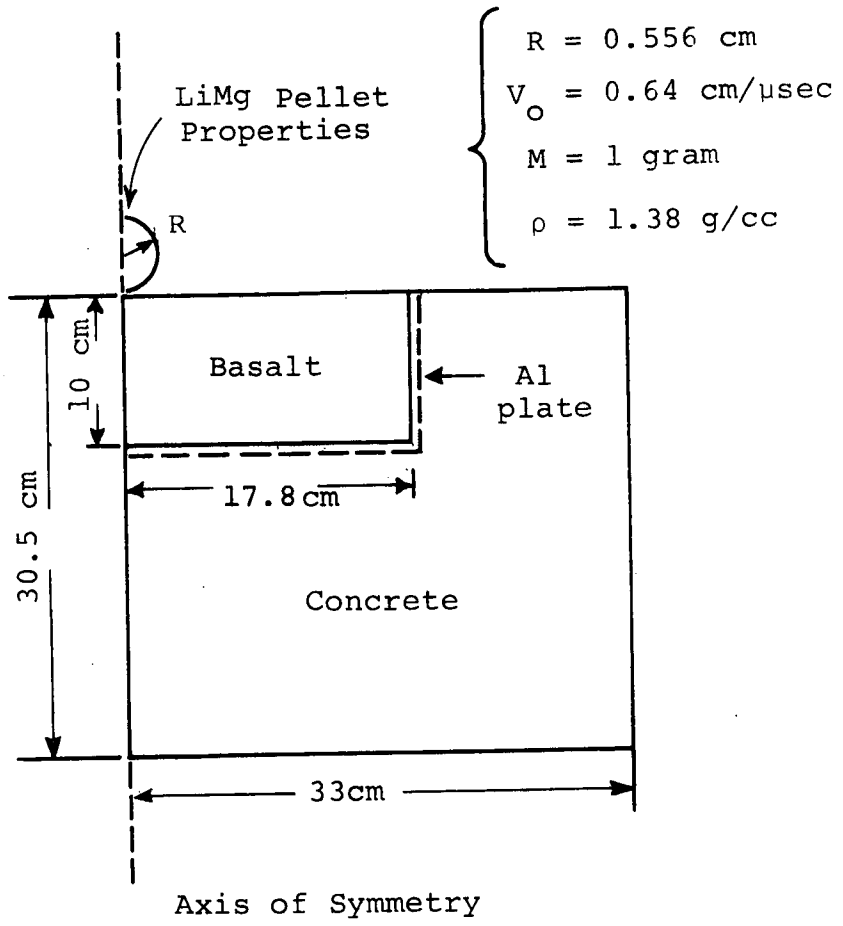

Basalt Properties

Bulk Modulus K_o = 0.492 Mb

Shear Modulus G_o = 0.295 Mb

Poisson's Ratio σ = 0.25

Pwave Velocity C_p = 0.56 cm/μsec

Initial Density ρ = 2.82 g/cc

Figure 2.1 Pellet impact into basalt geometry.

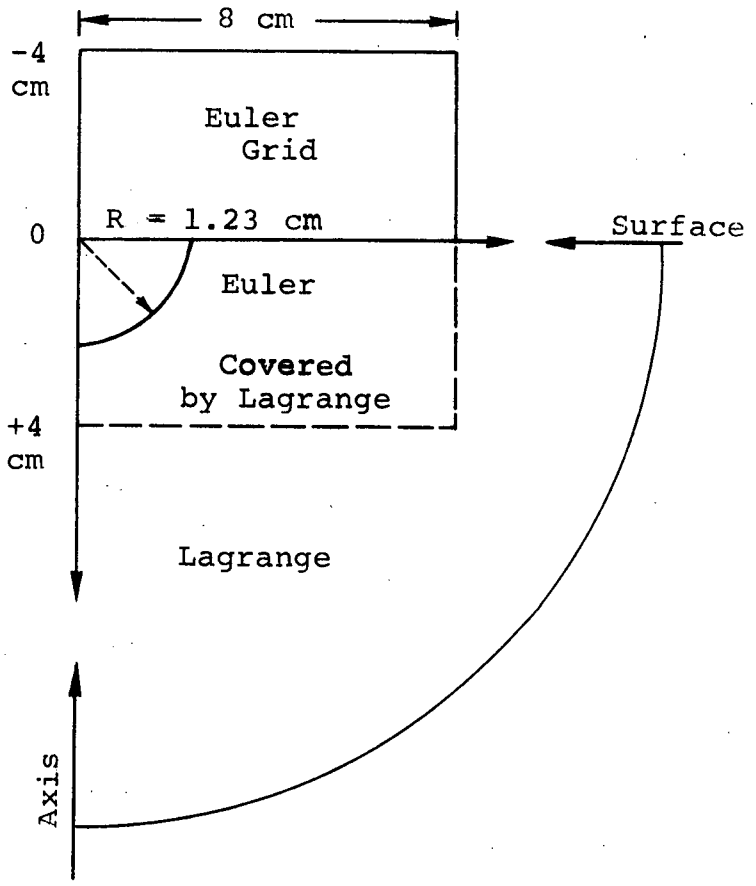

Figure 2.2 Geometry of Euler-Lagrange grid for pellet impacting basalt.

that region inside the radius, R = 1.23 cm. A number of Euler cells covered by the Lagrange grid will be uncovered during the course of the calculation as the interface between the Lagrange grid and the uncovered Euler grid moves and distorts.

The Euler cells (or zones) are "space fixed" so that the material flows through them and does not restrict the computational time step by zone "tangling." The material in the Euler grid is treated hydrodynamically and has no strength properties. This approximation is quite accurate for this case because the stress deviators and strength properties of the real case are overwhelmed by the large hydrodynamic forces inside the radius, R = 1.23 cm.

The Lagrange grid is "material fixed" with each zone moving and distorting with the enclosed mass element. The complete stress tensor acts in this grid with the resulting elastic-plastic flow being consistent with the selected yield and cracking models.

The zones of the Euler grid were originally each 0.1 x 0.1 cm squares to obtain fine resolution during the early impact phase. These were later dezoned to become 0.2 x 0.2 cm squares corresponding to 21 vertical lines (rows) and 41 horizontal lines (columns) fitting into the Euler region square of Figure 2.2. The Lagrange grid was composed of radial straight lines (rows) and circles (columns) fitting into the Lagrange region of Figure 2. The radial thickness of the innermost zones was 0.2 cm with this value increasing by 7 percent per column. The angular width of all Lagrange zones was 0.08722 radians corresponding to a radial fan of 18 rows extending from the vertical (downward) to the

horizontal surface direction. The number of columns was 34, extending to a radius of about 26 cm. The reflected shock from this outer boundary does not occur in the time frame of the calculation.

2.3 Equations of State

The form for the equation of state of the basalt is given in Appendix A. The coefficients are in Table A1. The strength parameters that will be given do not apply to the basalt in the Euler region. The LiMg was given the same equation of state as the strengthless basalt except that a density of 1.38 applies. The rest of the discussion applies to the Lagrange region basalt.

Experimental data used to characterize the Hugoniot are derived from Ahrens (Reference 2) for stresses from 50 kbar to 200 kbar. High pressure data from 350 kbar to 2 Mbar were derived from Isabel, et al., Reference 3.

Figure 2.3 shows the fit of pressure vs. relative volume to both sets of data; Figure 2.4 shows the fit to the lower pressure data.

2.4 YIELD MODEL

The yield surface used is the Mohr-Coulomb model (Reference 4), given by $Y = 0.6 + 0.744P$ (kbar) with an ultimate limit of 18 kbar. There is a lower yield surface Y_o = 250 bars to which the material relaxes with a time constant T = 30 μsec. This lower yield surface corresponds to an assumed shear strength of 125 bars at the concrete-aluminum boundary of the experimental basalt block. The time corresponds to a shear wave relief transit across the block. Figure 2.5 displays these yield surfaces.

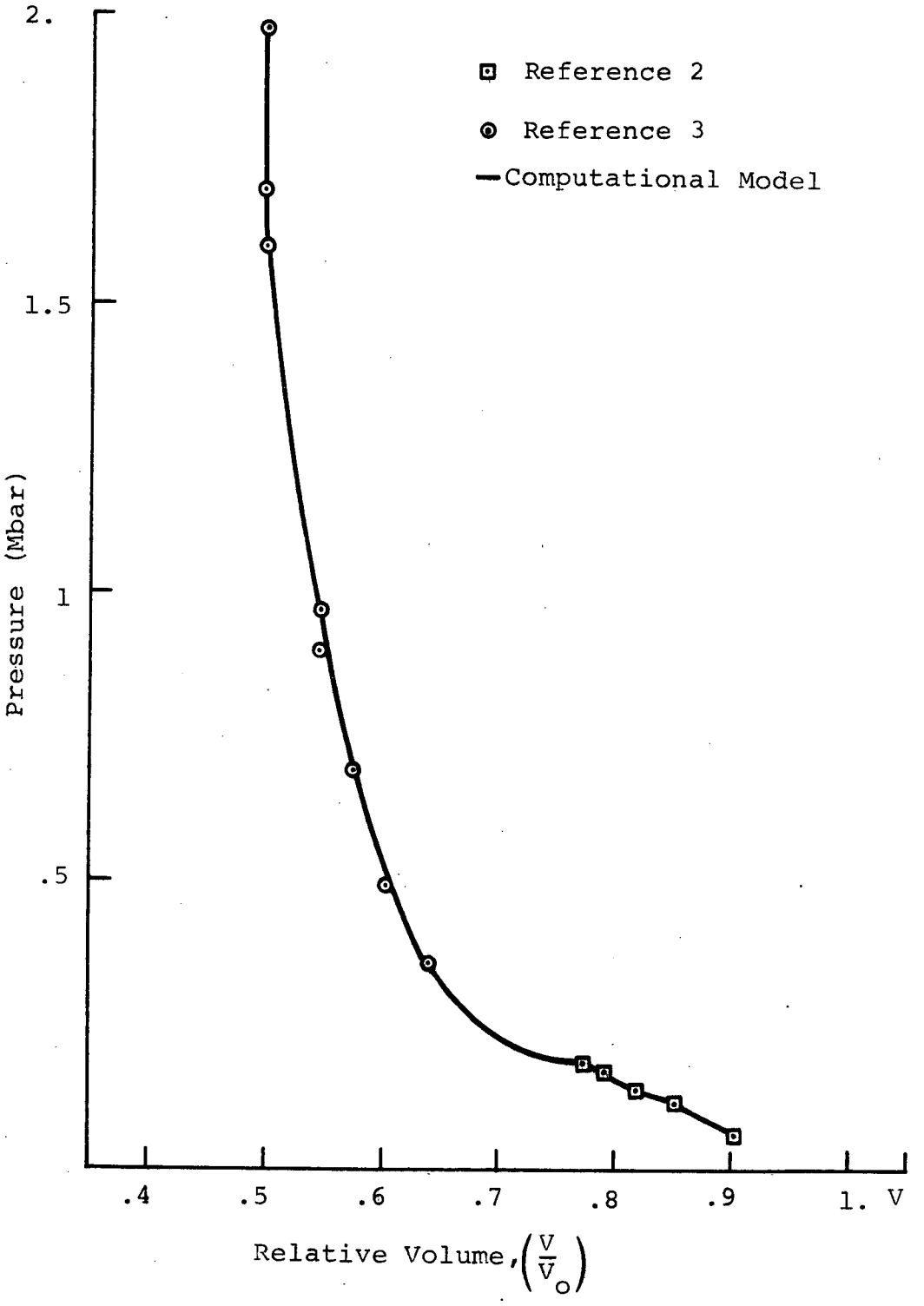

Figure 2.3 Equation of state comparison.

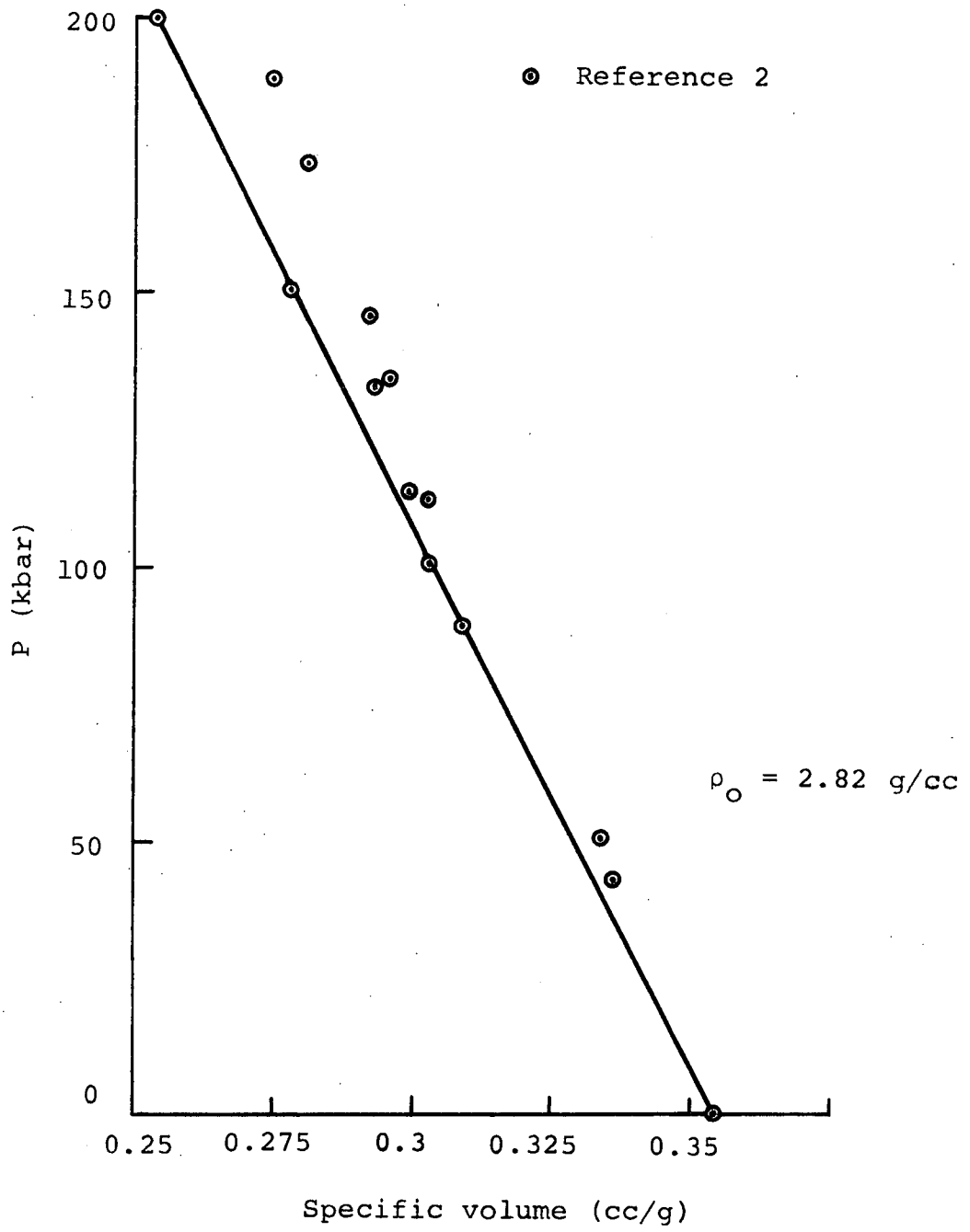

Figure 2.4 Comparison of experimental data to equation of state model.

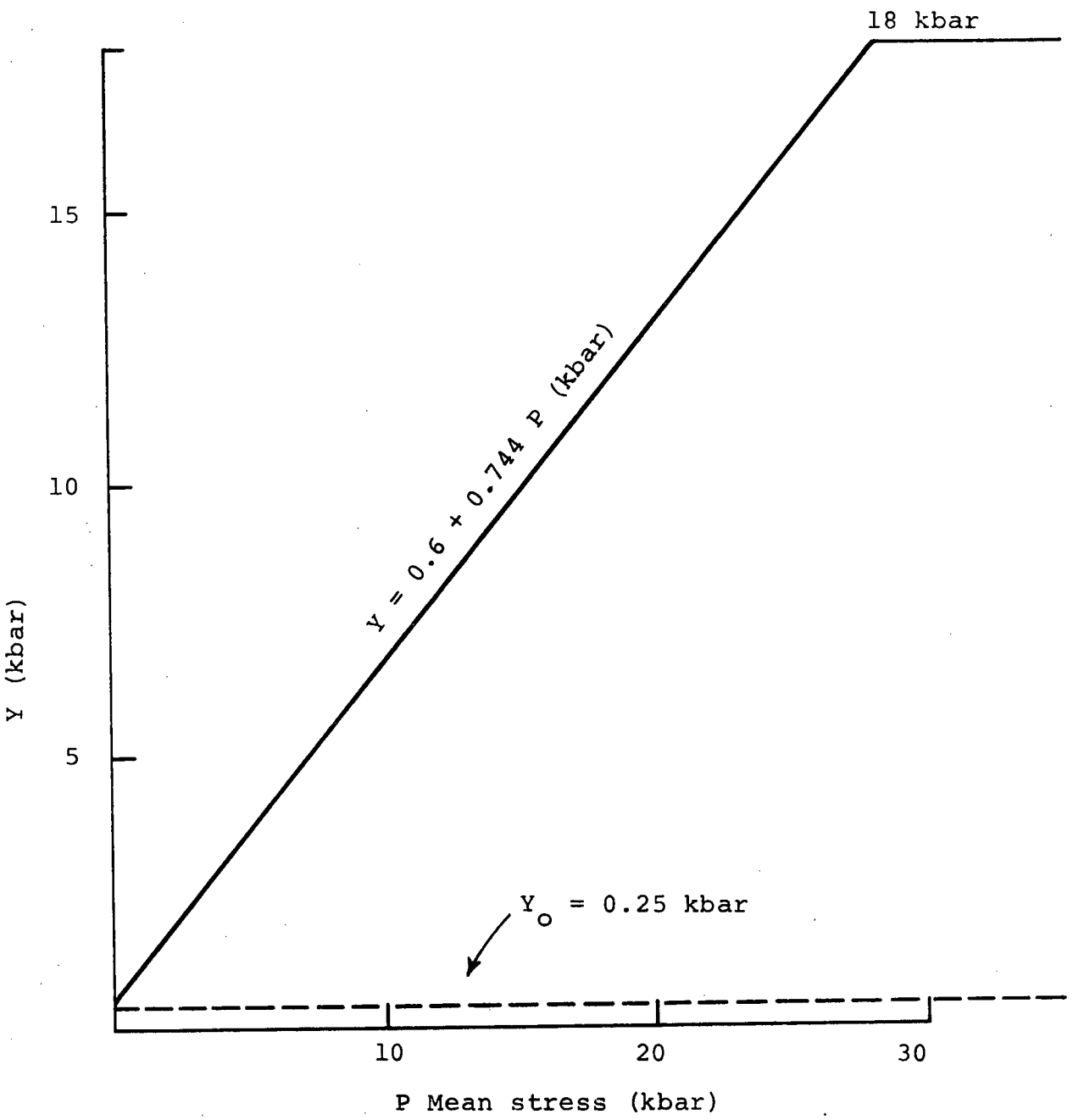

Figure 2.5 Yield strength versus mean stress.

In one-dimensional strain, $\sigma_1 = -(1 + 4/3\ \mu/k)P$ and $\sigma_2 = -(1 - 2/3\ \mu/k)P$ where

σ_1 = longitudinal stress (positive value = tension
σ_2 = transverse stress (positive value = tension
μ = shear modulus
k = bulk modulus

For this case, yielding occurs when $\sigma_1 - \sigma_2 = Y$, where $\sigma_1 - \sigma_2 = 2\mu P/k = 1.2P$. The intersection of this loading path with the initial yield surface occurs at P = 1.31 kbar as shown on Figure 2.6. The experimental curves for the yield surface of Divide basalt and Sabana basalt (both Reference 7) and Westerly granite (Reference 6) are shown on Figure 2.7 together without assumed yield surface.

2.5 ORIGINAL CRACKING MODEL

The basic notion behind the original cracking model was that upon exceeding some tensile stress state, the stress, σ_i, that exceeds this state, P_{min}, is set to zero. Using the following resolution of stress into the sum of the mean stress (pressure) P and deviatoric stress, S_i, the following condition describes cracking in one principal axis direction. If

$$\sigma_1 < P_{min}$$

or

$$\sigma_1 = -P + S_1 > P_{min}$$

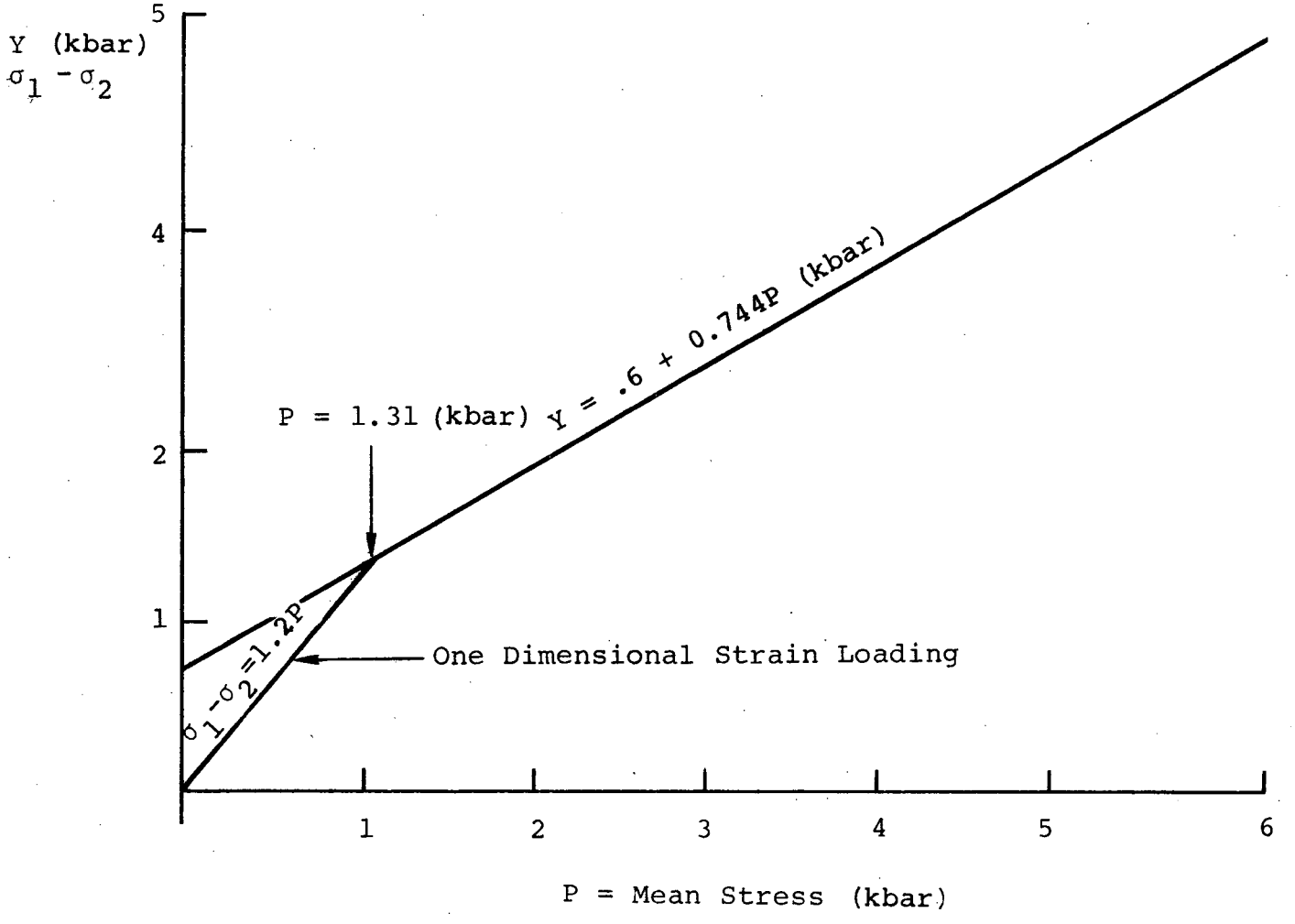

Figure 2.6 Intersection of one-dimensional strain loading path with yield surface.

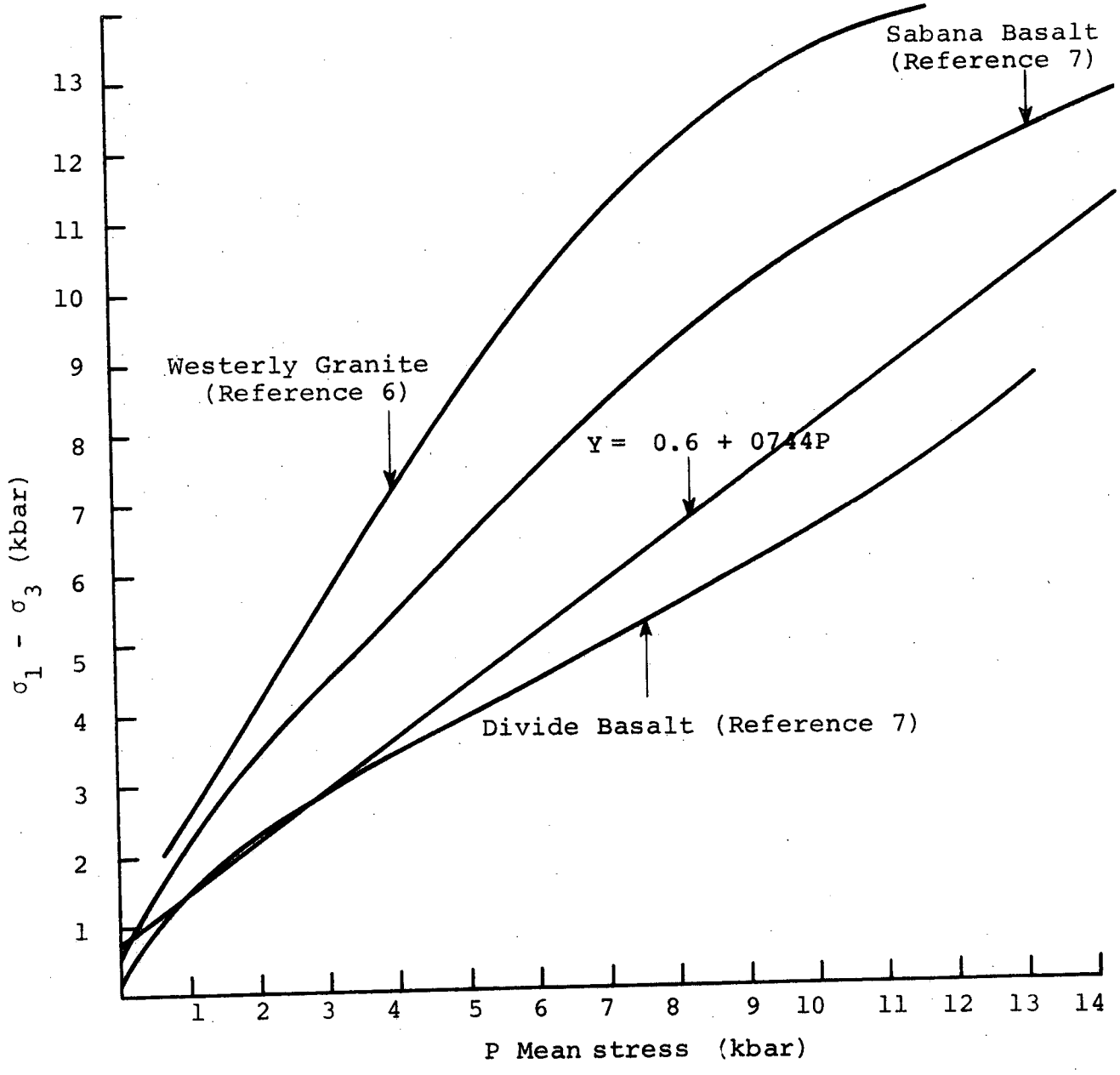

Figure 2.7 Experimental fracture data.

and

$$\left.\begin{matrix}\sigma_2 \\ \sigma_3\end{matrix}\right\} < P_{min}$$

then

$$\sigma_1' = 0$$

$$\sigma_2' = \sigma_2 + \tfrac{1}{2}(S_1 - S_1')$$

$$\sigma_3' = \sigma_3 + \tfrac{1}{2}(S_1 - S_1')$$

and

$$S_1' = P$$

Primes are adjusted values; unprimed are old values. The conditions to be met before cracking occurs are

$$P = -1/3(\sigma_1 + \sigma_2 + \sigma_3)$$

and

$$S_1 + S_2 + S_3 = 0$$

after adjustment of σ_1, so that

$$\sigma_1' = 0$$

$$P = -1/3\ (\sigma_1' + \sigma_2' + \sigma_3')$$

$$P = -1/3\left[\sigma_2 + \tfrac{1}{2}(S_1 - S_1') + \sigma_3 + \tfrac{1}{2}(S_1 - S_1')\right]$$

$$P = -1/3\ (-2P - S_1')$$

since

$$S_1' = P.$$

If two stresses fail, say

$$\left.\begin{matrix}\sigma_1 \\ \sigma_2\end{matrix}\right\} > P_{min}$$

then both are set equal to zero and

$$\sigma_1' = 0$$

and

$$\sigma_2' = 0$$

This gives

$$\sigma_3' = \sigma_3 + (S_1 - S_1') + (S_2 - S_2')$$

$$\sigma_3' = -3P$$

The case for all three to fail is to set all stresses to zero and all stress deviators to zero. The material is then assumed to act hydrodynamically for all times.

2.6 SELECTION OF ORIGINAL CRACKING MODEL PARAMETERS

There are several processes of failure of rocks during shock loading processes. Among the various means of failure are vaporization caused by high energy density, comminution of rock, plastic flow, fracture and microfracturing.

Short (Reference 5) has discussed the failure of granodiorite caused by nuclear explosion and using a calculation of Butkovich as a guide has determined the curve of Figure 2.8 as a guide to failure of a rock because of shock loading. The attenuation of peak pressure is indicated on the figure as a function of range and several pressure levels at which different failure processes occur.

Short's analysis was used as a guide to the first failure model adopted for the pellet impact problem because these mechanisms are a function of the rock's minerals.

As noted, it has been assumed that the basalt acts hydrodynamically inside the radius R = 1.23 cm in the Euler section of the basalt (see Figure 2.2). The peak stresses in this region were expected to be 60 kbar and larger with basalt failing immediately upon shock passage. As the compressive shock progressed outward into the Lagrange grid, it was assumed that basalt was preconditioned by the processes noted on Figure 2.8 and Reference 5, that its subsequent tensile strength was reduced in the manner displayed on Figure 2.9. The 150-bar maximum value was thought to be reasonable; the minimum value of 50 bars avoided certain round-off errors in the calculation and otherwise would have been set to zero for very high preconditioning pressures. As will be seen

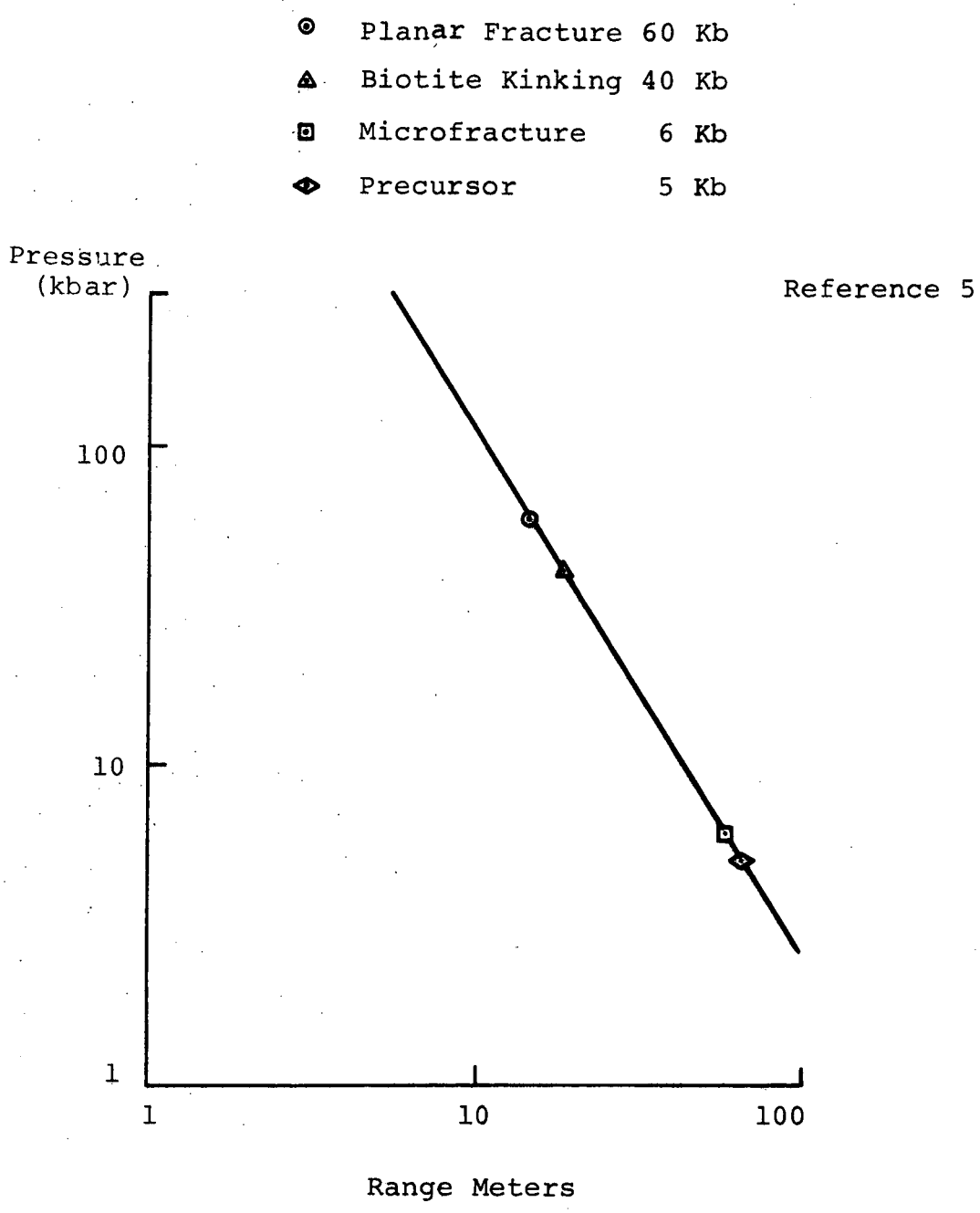

Figure 2.8 Failure regimes induced by shock.

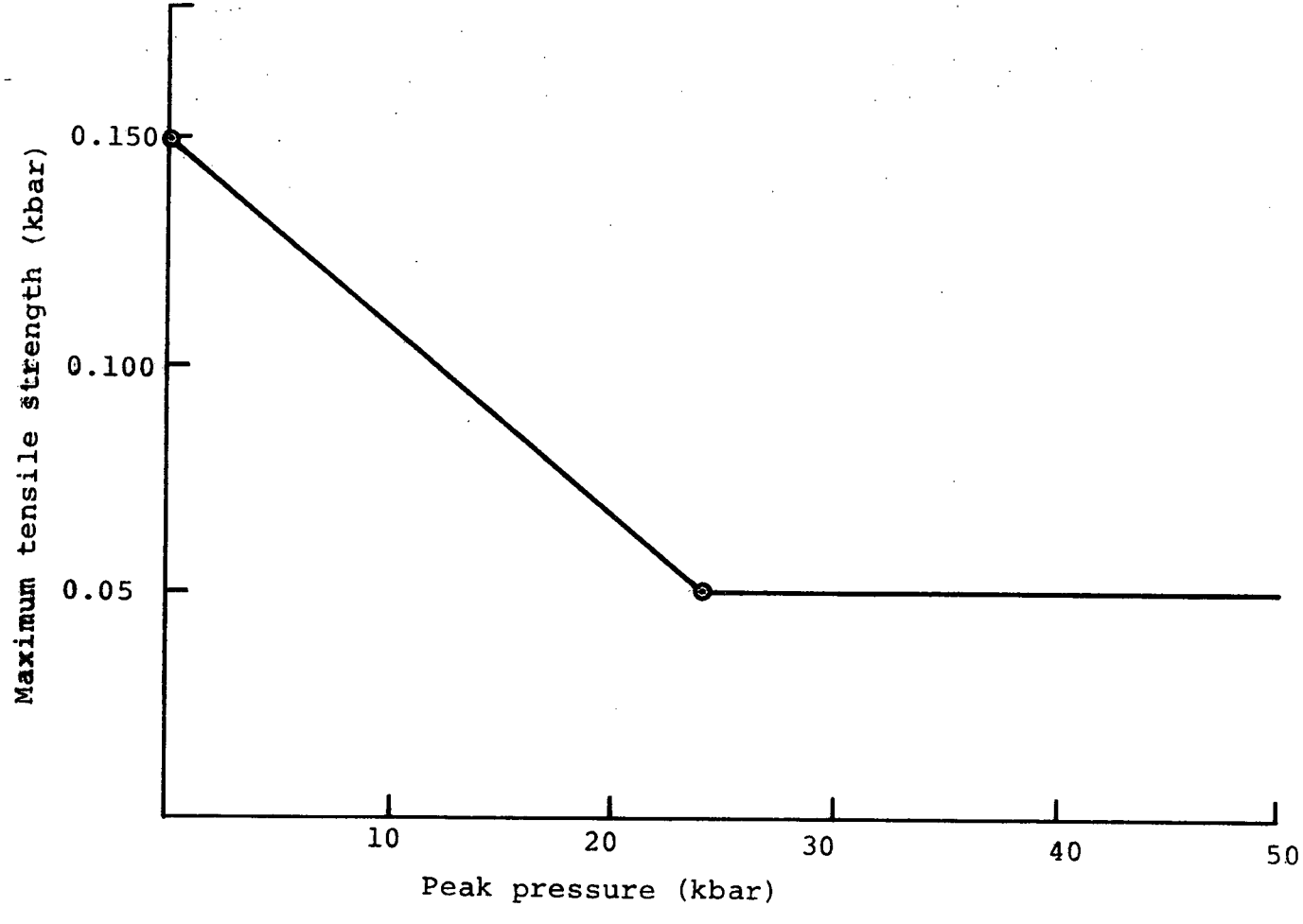

Figure 2.9 Maximum tensile stress versus peak pressure.

later, the predicted results were unsatisfactory with respect to predicting crater size and shape. The results of this original model are reported in paragraph 2.7.

2.7 ORIGINAL CRACKING MODEL RESULTS

The calculated results predicted by the ELK code were satisfactory with respect to peak pressures and early crater growth as will be seen later. However, the predicted cracking from the crack model was disappointing, producing a pattern that did not correlate to the experiment.

In Figure 2.10, a small section of the Lagrange grid is shown at t = 22 μsec when the shock front was at a radius of about 13 cm (beyond the extent of the grid that is shown). The stationary Euler grid is not shown. It can be seen that the original inner boundary of the Lagrange grid (not to be confused with the crater) has been pushed outward from R = 1.23 cm to about 1.8 cm at this time. The surface lip suggests that the current crater splash radius is about 1.9 cm. The stress levels in this region are low, indicating that the high velocity splash phase of the crater process is almost over. This was confirmed by examining the printouts at a time of t = 16 μsec which showed that the crater lip was at a radius of about 1.8 cm. Figure 2.11, corresponding to Figure 19 of Reference 1, is a radiograph of the experiment at t = 13.6 μsec. The ½-inch fiducial markers on this figure can be used to confirm that the experimental splash radius is about 1.8 cm which correlates well with the computed value.

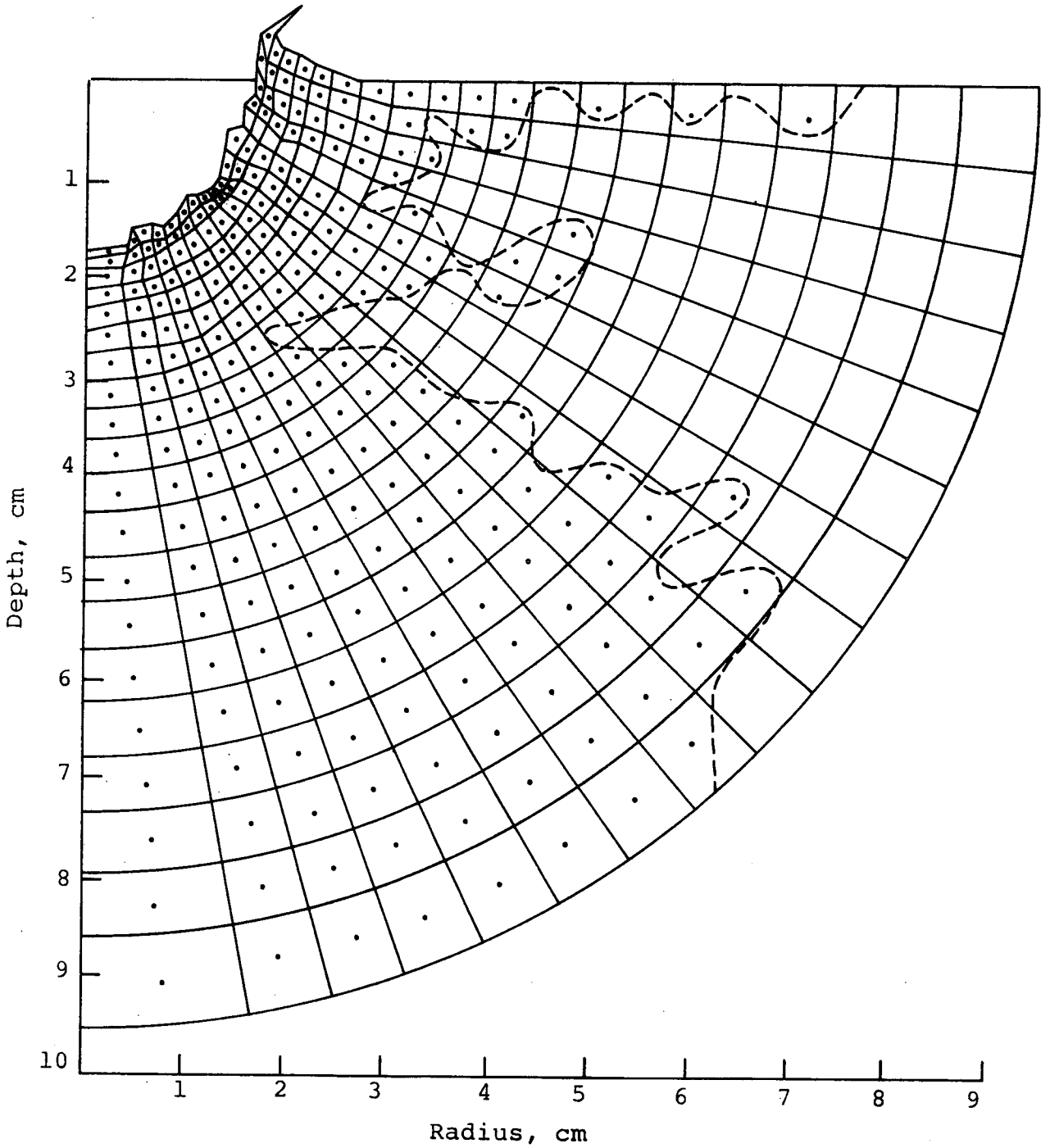

Figure 2.10 Pellet impact Lagrange grid at t = 22 μsec. The dotted zones contained in the dashed line have cracked.

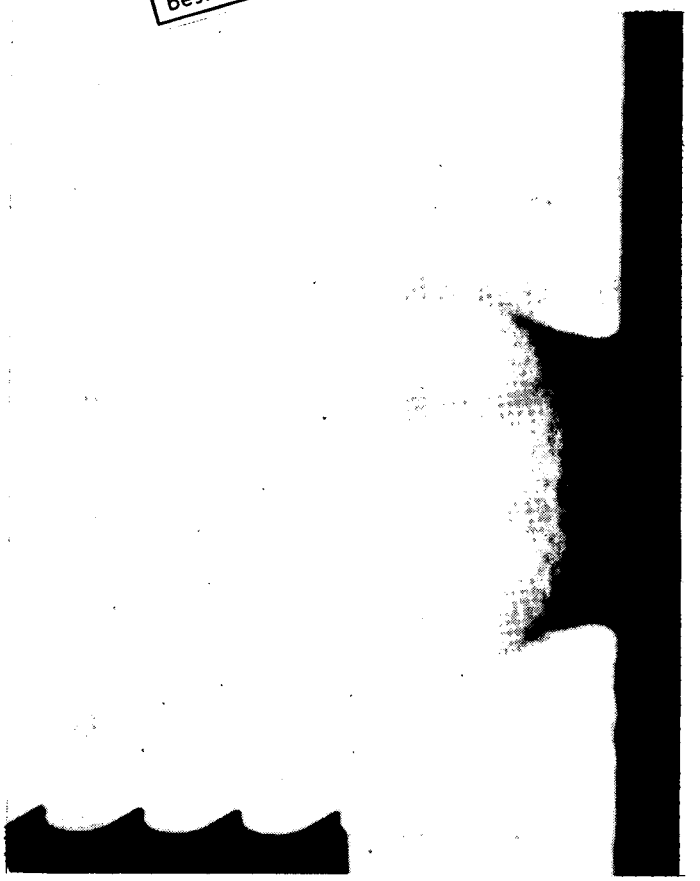

Figure 2.11 Radiograph of target ejecta 13.6 μsec after impact (shot 395-17).

The final crater will be substantially larger than the transient splash crater because of low-speed ejecta of the tensile cracked basalt. Regions of basalt, surrounded by connected cracks and adjacent to a free surface can be expected to be removed at late times.

The dotted zones of Figure 2.10 contained in the dashed line have cracked in the code simulation. The conoid pattern centered downward on the axis is at variance with the experiment as will be seen. This particular pattern resembles that computed and observed experimentally by Wilkins, Reference 8, for the case of a high-velocity steel bullet impacting high-strength ceramic. This can be seen, for example, in Figure 18 of the Wilkins article. The important features of his cracking model for this case were that a zone cracked when (a) a 3-kbar tension was achieved, (b) the zone either was adjacent to a free surface or to a previously cracked zone, and (c) with a time delay corresponding to an assumed crack propagation velocity.

Except for the value of tensile strength, feature a of the Wilkins model corresponded to the subject model. The other two features, if present in the subject, apparently would have produced a more ray-like character to the cracking pattern in the basalt.

It would have been instructive to redo this computation with Wilkins' features b and c added. This was not done. It was thought that a natural rock, with pre-existing microcracks, dilatancy and planes of weakness was sufficiently different from a homogeneous ceramic that the effort would be better spent in attempting to correlate computed parameters of the original calculation to the experimental results.

2.8 FINAL CRACKING MODEL--COMPRESSIVE PHASE

The basalt used in the experiment was quite competent and was estimated to be similar to Westerly granite with respect to strength properties. The compressive fracture radius will be estimated on this basis.

Figure 2.12, taken from Swanson's report of Reference 9, displays the compressive fracture yield surface of Westerly granite. On this figure, $J_1 = 3P$. At the shock front in the basalt, $\sigma_1 - \sigma_2$ loads along the path $\sigma_1 - \sigma_2 = 1.2P$ for the chosen values of shear and bulk modulus. This path is shown as the dashed line on Figure 2.12. The intersection of this path with the fracture surface, A, is out of the range of the experimental data, but extrapolates to occur at about P = 40 kbar. Thus, the compressive pulverization region boundary is expected to occur at the 40 kbar peak pressure contour that was predicted by the calculation.

The contours of the pressure peak that had been achieved in the time interval up to 22 μsec are shown in Figure 2.13, and consequently will apply to all times for the region of space shown. The compressive-failure crater is thus expected to extend to a depth of 2 cm with a slightly smaller radius. The experimental crater depth of about 2.4 cm and the radiograph of the splash crater radius do not contradict this prediction.

2.9 FINAL CRACKING MODEL--TENSILE PHASE

A correlation was discovered between the code results, the final crater and the cracking pattern in the basalt. The

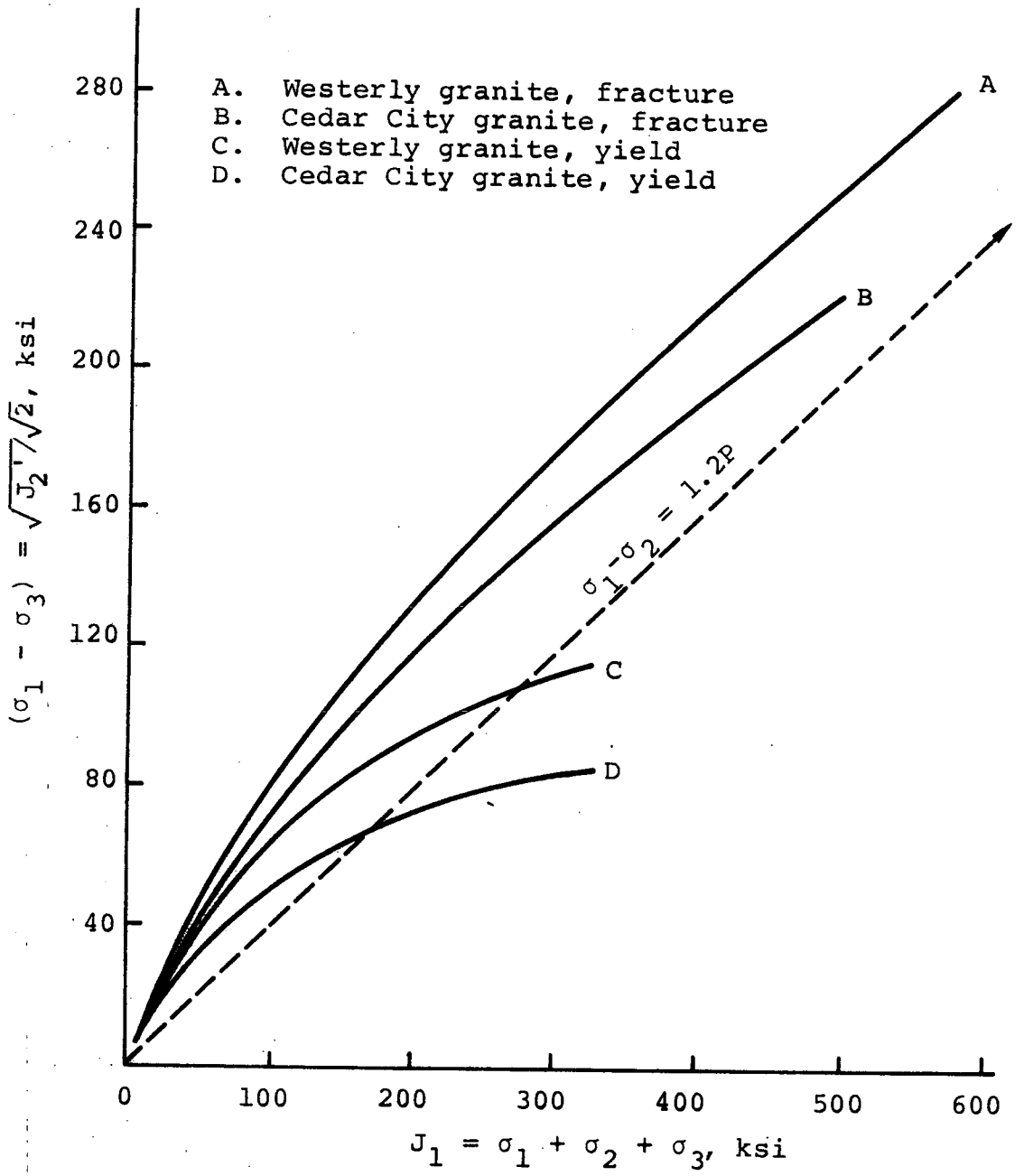

Figure 2.12 Comparison of fracture and yield curves for Cedar City and Westerly granites.

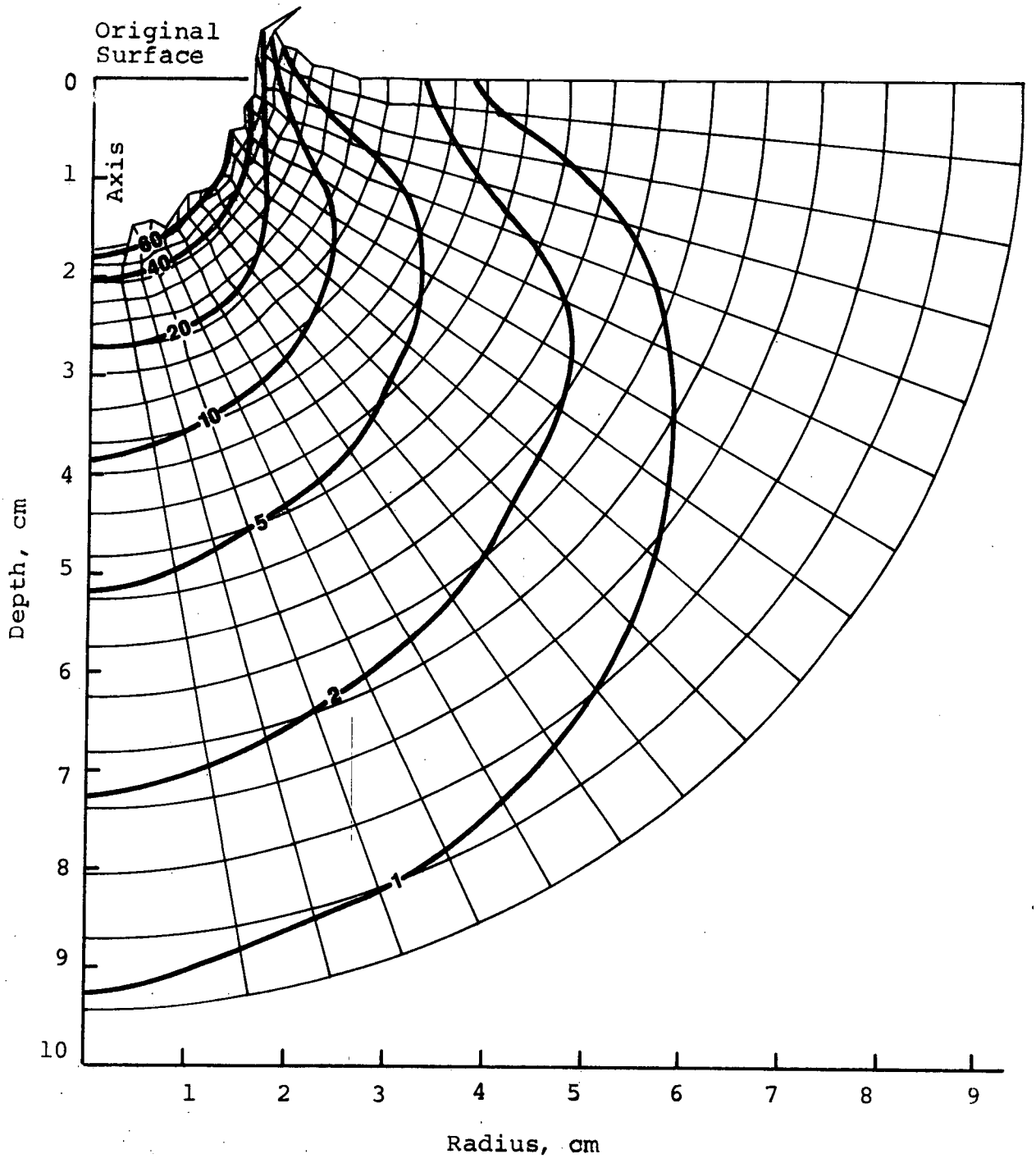

Figure 2.13 Basalt impact calculation. Contours of peak pressure (kbar) achieved over all time overlaying distorted Lagrange grids at 21 μsec.

correlating parameter is suspect, and the corresponding model is not claimed to be complete. Nevertheless, the results are sufficiently encouraging to infer that the model may have a fundamental basis that is not yet understood.

It was noted that the volumetric strain energy, available on the printouts, became negative for certain zones in the calculation and that these zones produced a pattern that could be roughly correlated to the final crater and the underlying crack pattern. In addition, this same correlation successfully predicted the crater width of an experimental nuclear surface burst in competent granite.

The volumetric strain energy of a zone in the code corresponds to the area enclosed by a path in P-V space. Figure 2.14 is a schematic showing how the positive volumetric strain energy accumulated by a load-unload at positive pressure can be lost during decompression at negative pressure. In Figure 2.14, when the area labeled + equals the area labeled -, the volumetric strain energy has returned to zero.

The shaded zones of Figure 2.15 correspond to the zones that have achieved negative volumetric strain energy at some time during the calculation. Four sections of the experimental crater profile are also shown. It can be confirmed that 70 percent of the 85 zones inside the radius of 2.5 cm have been cracked by this criterion. This suggests that the crater depth should be about 2.5 cm, perhaps a little less because of the four uncracked zones on axis in this region.

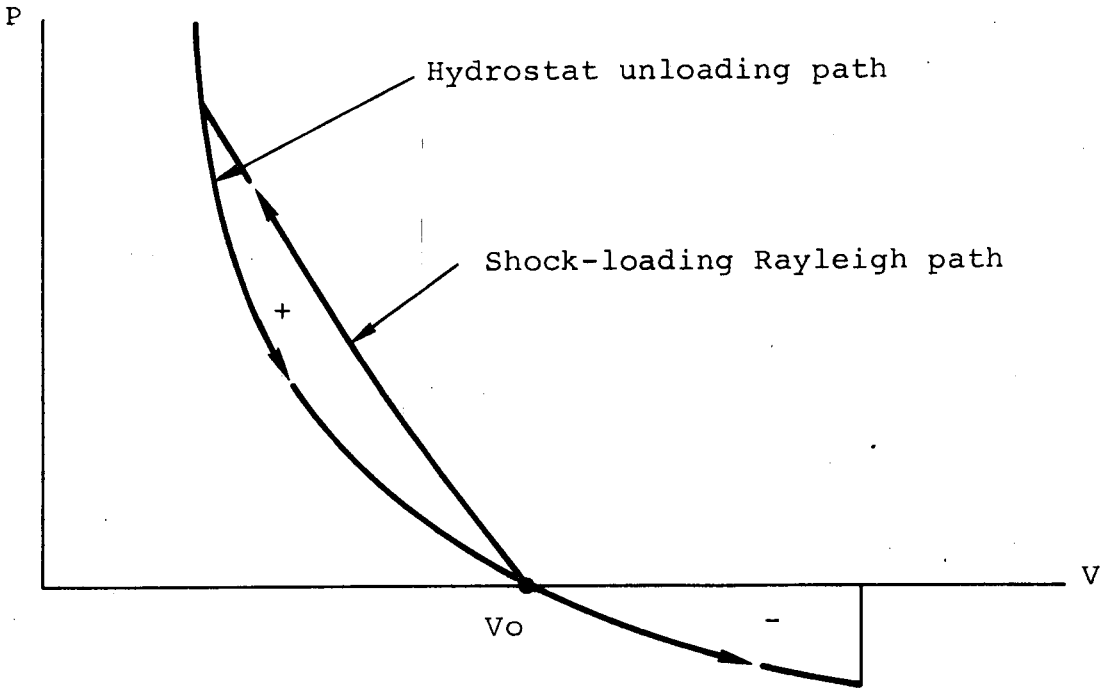

Figure 2.14 A schematic path in P-V space resulting in negative volumetric strain energy.

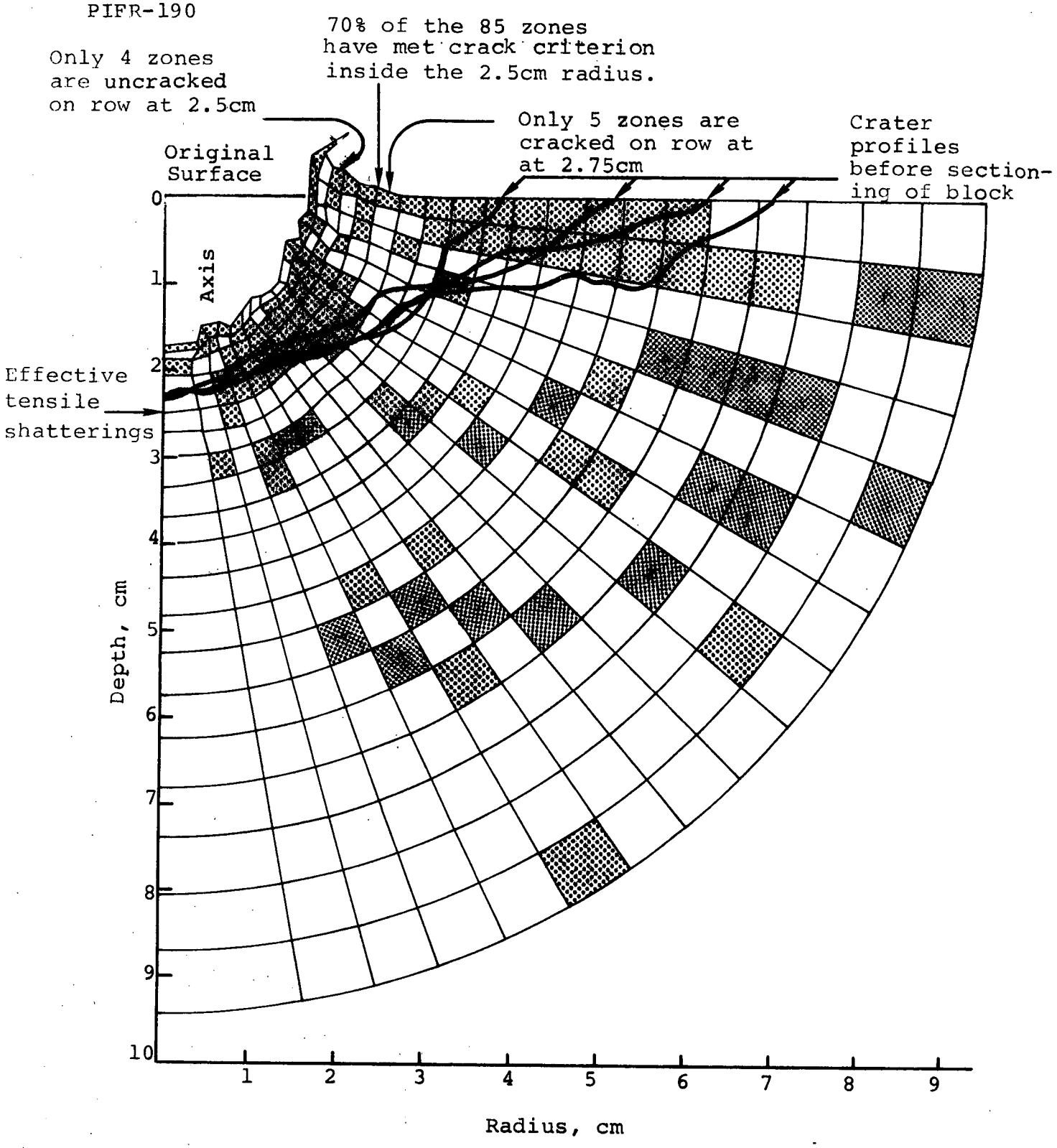

Figure 2.15 Basalt impact calculation. Regions of tensile cracking (shaded) in Lagrange grid at 21 μsec, predicted by volumetric strain-energy model.

The shaded wing area along the surface, undercutting slightly, suggests a crater radius of about 6 cm. The remaining shaded areas will be correlated to the experimental crack pattern. Of particular interest is the scarcity of shaded zones along the axis cone, completely at variance with the original cracking model results.

The basalt block was sectioned and the two halves placed as shown in Figure 2.16 to expose the interior cracks. These were photographed and examined in detail. Because the impact was about 3/4 inches off center, it was possible to identify the cracks caused by the side effects of the finite block. This was not possible with respect to cracks formed by the impedance mismatch at the bottom of the block. These could be identified easily near the bottom surface where they were close-packed. They became less obvious with increasing height and apparently terminated about two inches above the bottom of the basalt block.

The remaining cracks were assumed to be associated with the cratering process and to be correlatable to the model. The more dominant of these cracks were traced and are shown on Figure 2.17.

The crater profiles before sectioning shown on Figure 2.15 were altered by two substantial chips that fell out during the curing process, demonstrating the sensitivity and inherent non-reproducibility to be expected with respect to exact crater shape. Corresponding chips which did not fall out on sectioning are designated A and C in Figure 2.17. Comparison of Regions E, F, and G of Figure 2.17, the observed experimental cracking can be made with the identically labeled areas of Figure 2.18, the tensile-cracked zone pattern calculated and shown on the same scale as

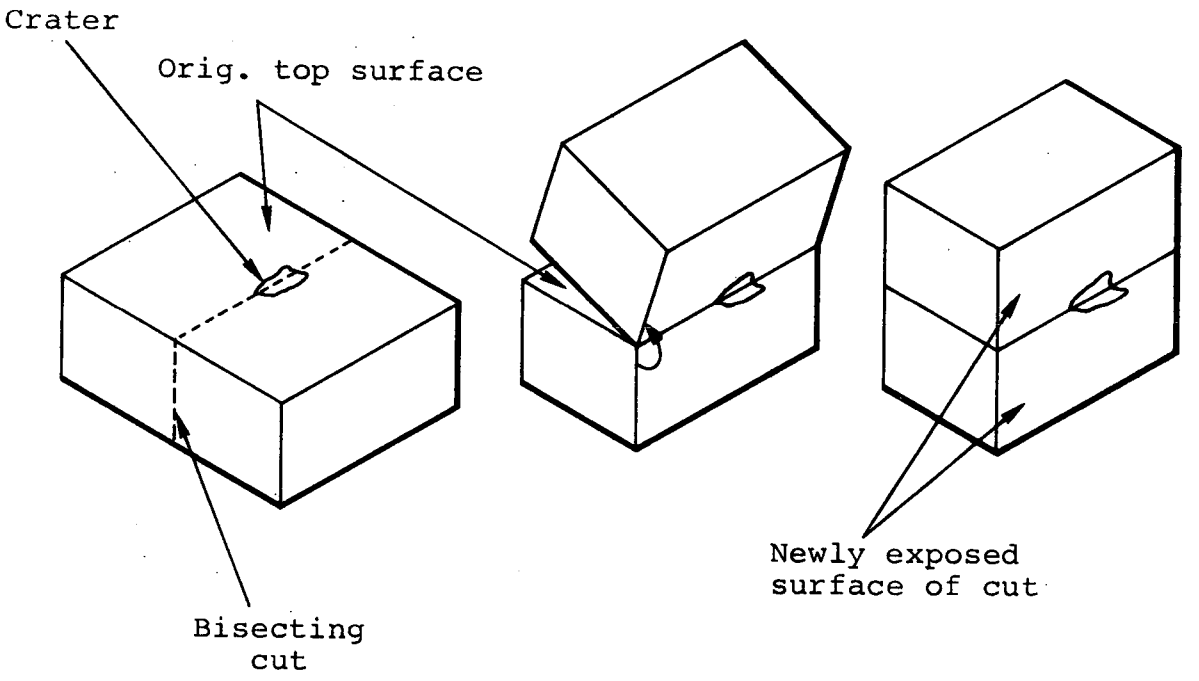

Figure 2.16 Sectioning of basalt block to expose crack pattern.

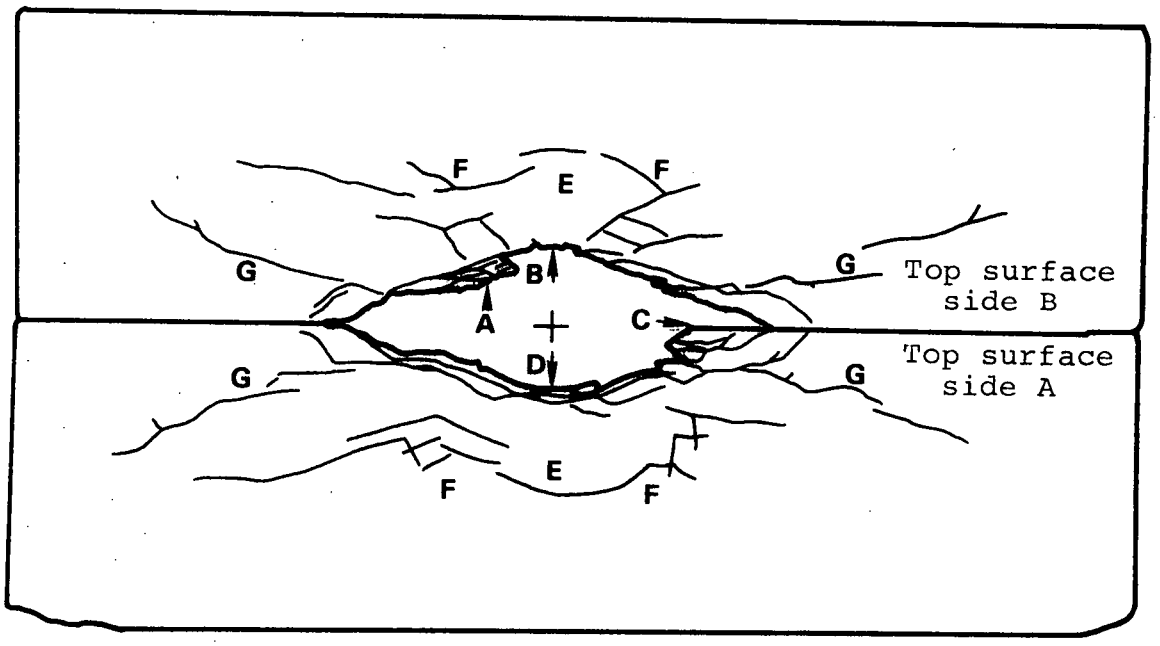

Figure 2.17 Mapping of basalt block cracks.

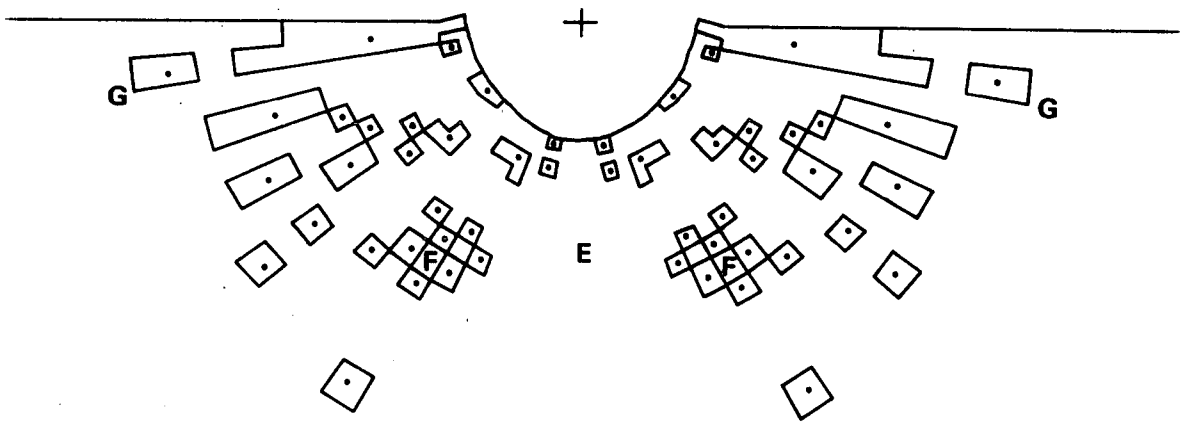

Figure 2.18 Calculated tensile-crack zones to the same scale as Figure 2.17 with the areas E, F, G in the same location.

Figure 2.17. Region E is uncracked by the model and shows the lowest crack density experimentally. Region F shows modest cracking in both cases. The model suggests in region G the ray-like cracking observed.

2.10 CORRELATION TO AN EXPERIMENTAL NUCLEAR SURFACE BURST

The correlation of this model to the results of the basalt-impact experiment prompted a re-examination of the predicted results of a nuclear surface burst calculation over hard rock for which an experimental true crater was known.

The shaded zones of Figure 2.19 have met the volumetric strain-energy criterion for this nuclear case. The experimental crater width is crudely outlined by the straight line. The experimental crater depth corresponds quite satisfactorily to the compressive cracking model previously used. The average experimental crater radius correlates to the width of the shaded region to about the same extent as that of the basalt crater of Figure 2.15.

The peak stress contour encountered by a vertical line passing through the nuclear-crater lip was calculated to be almost an order of magnitude different from the peak stress on the corresponding line calculated for the basalt-impact case. This observation suggests that peak stresses do not govern the crater radius and that the volumetric-strain-energy tensile-cracking model may have a basic validity in contrast to mechanisms based directly on peak compressive stress.

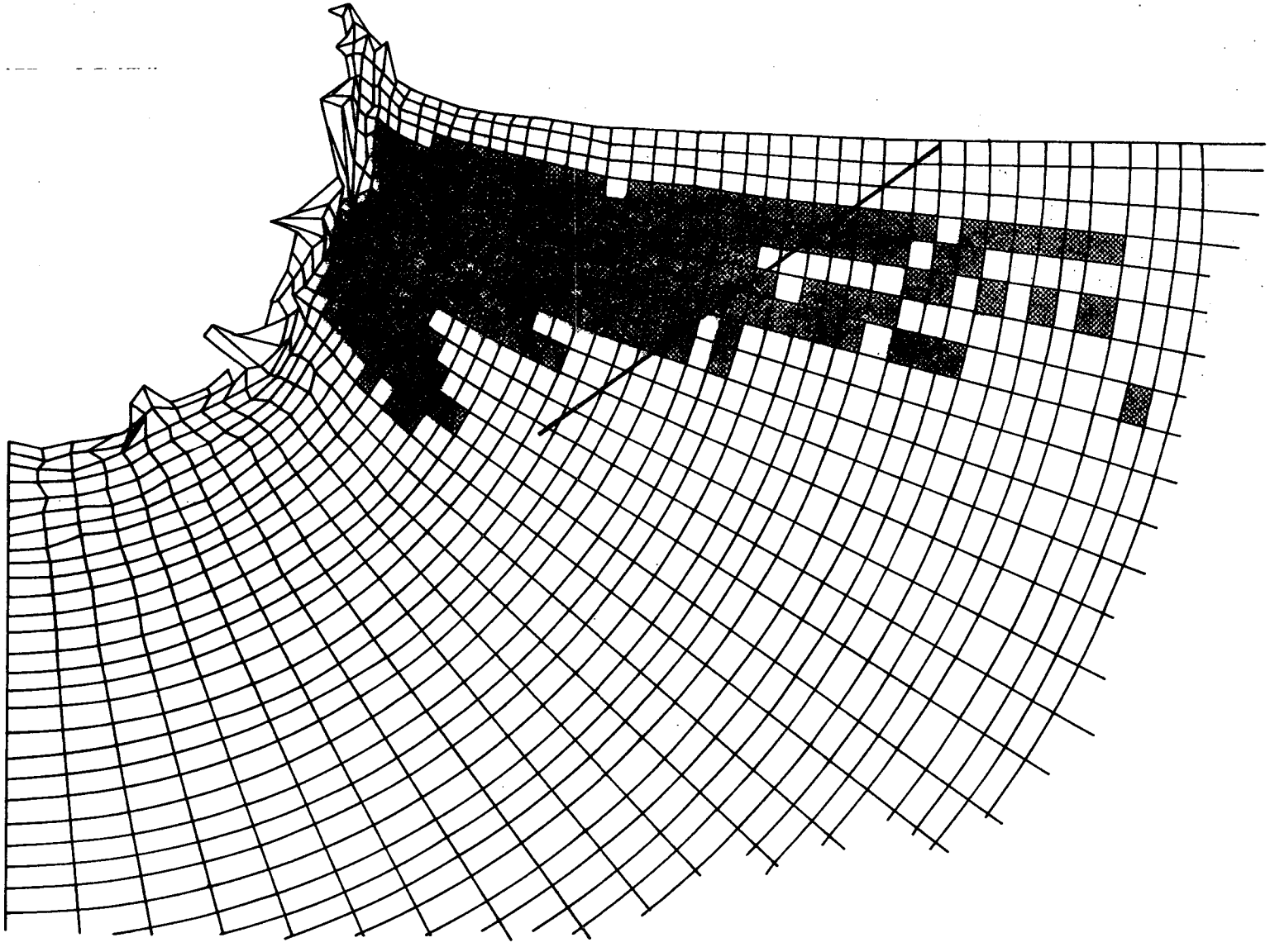

Figure 2.19 Nuclear surface burst calculation. Regions of tensile cracking (shaded) predicted by volumetric strain-energy model.

It must be pointed out that the hard rock of the nuclear experiment was jointed with the crater engulfing many joint dimensions. The asymmetry of this crater was substantial and was attributed to the discrete response of the associated blocks. In spite of the fact that the basalt used in the impact tests was apparently competent with no visible cracks before impact, the final crater asymmetry was similar to that of the nuclear crater. The implications are not clear. The modeling of two media in the computations was quite dissimilar, with different equations of state, elastic moduli and plastic yield surfaces. It may be that the agreement between the experimental and predicted craters by the common model was fortuitious, and additional experiments and calculations would be required before definite validity could be assigned to this model.

2.11 FAILURE OF THE MODEL FOR POROUS ROCK

In the previous examples, the rocks had negligible porosity, so that the load-unload hydrostat is reversible. In applying this model to a porous rock, enhancement of the volumetric strain energy would be expected during the positive pressure phase that would be more difficult to overcome during the negative phase. Because of that consideration, the calculated results of Mine Ore, a 100-ton TNT explosion over Cedar City granite computed for DASA were reexamined. This material was modeled with a 5 percent porosity. As expected, the volumetric strain energy was enhanced, and never became negative in any portion of the grid at any time. An attempt to find a particular value of volumetric strain energy with which to correlate to the crater shape seemed artificial and was not attempted.

SECTION 3
SIERRA MADERA UPTHRUST SIMULATION

3.1 BACKGROUND

The geologic deformation in the central upthrust region of the Sierra Madera crypto-explosion structure indicates that the central upthrust was comprised of inward and upward flow. Wilshire and Howard, Reference 10, and Howard and Offield, Reference 11, present strong arguments and data that support the hypothesis that the Sierra Madera structure was formed by impact cratering.

Figure 3.1, traced from Reference 10, is a cross-section of the Sierra Madera structure. The lithology is described in Reference 10 and in more detail in Reference 12. Surface erosion has obliterated the crater shape, leaving only the ring depression and central uplift pattern of deformation in the strata below the original crater bottom.

Neither the original crater shape nor the impacting energy and mass are known precluding an exact computer simulation of the event. Similarly, the detailed layering and lithology of the material removed by erosion are not known. It was decided therefore, consistent with these inherent uncertainties, to ignore the existing layering and to model the earth material as a homogeneous medium with averaged properties.

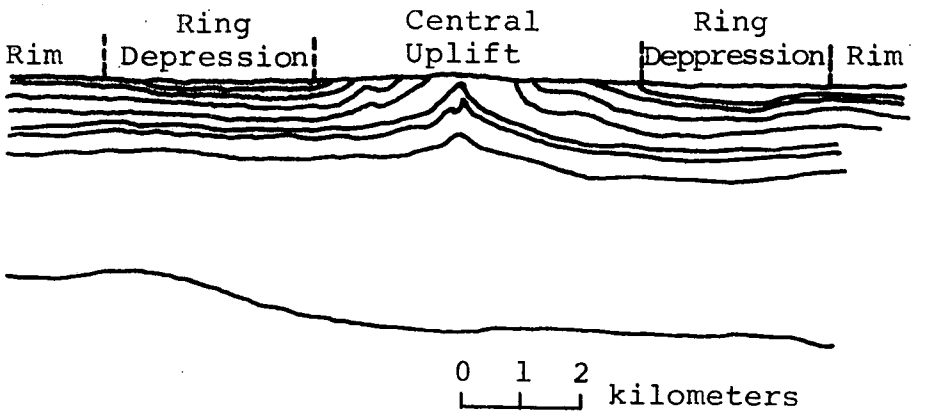

Figure 3.1 Cross section of the Sierra Madera structure showing central uplift surrounded by ring depression of otherwise horizontal strata.

It was not expected that the assumptions of earth properties, impacting mass and velocity would compromise the primary goal of studying the mechanisms and magnitudes associated with upthrust during impact cratering in a Sierra Madera situation.

Before proceeding to this goal, it is instructive to report selected sections of previous studies, DISTANT PLAIN 6 and MINE UNDER, to illuminate some of the mechanisms existing in computer-simulated upthrust cases.

3.2 DISTANT PLAIN NO. 6

The field event, DISTANT PLAIN 6, was a 100-ton sphere of TNT tangent to the surface of heavily layered clay-silt-sand-soil at Watching Hill Site, Suffield Experimental Station, Alberta, Canada. The experimental crater radius was about 40 ft. The maximum depth was about 17 ft with a 1.5-ft central upthrust diminishing the depth below ground zero to about 15.5 ft.

Three computer simulations were performed with differing material properties. The most successful, ELK 31, is briefly described in this paragraph. In the simulation, the weight of the 100-ton charge was allowed to compact the soil beneath to an equilibrium configuration before the charge was detonated. Figure 3.2 displays a portion of the Euler and Lagrange grids at detonation time. The weight of the 100-ton charge induced by gravity in the code had dented the ground surface and modified the material properties in a cone of influence extending downward. The soil had little shear strength. The complete model was based on data supplied by the Waterways Experimental Station. In the simulation, about 50 different material properties were assigned to the various regions of the soil.

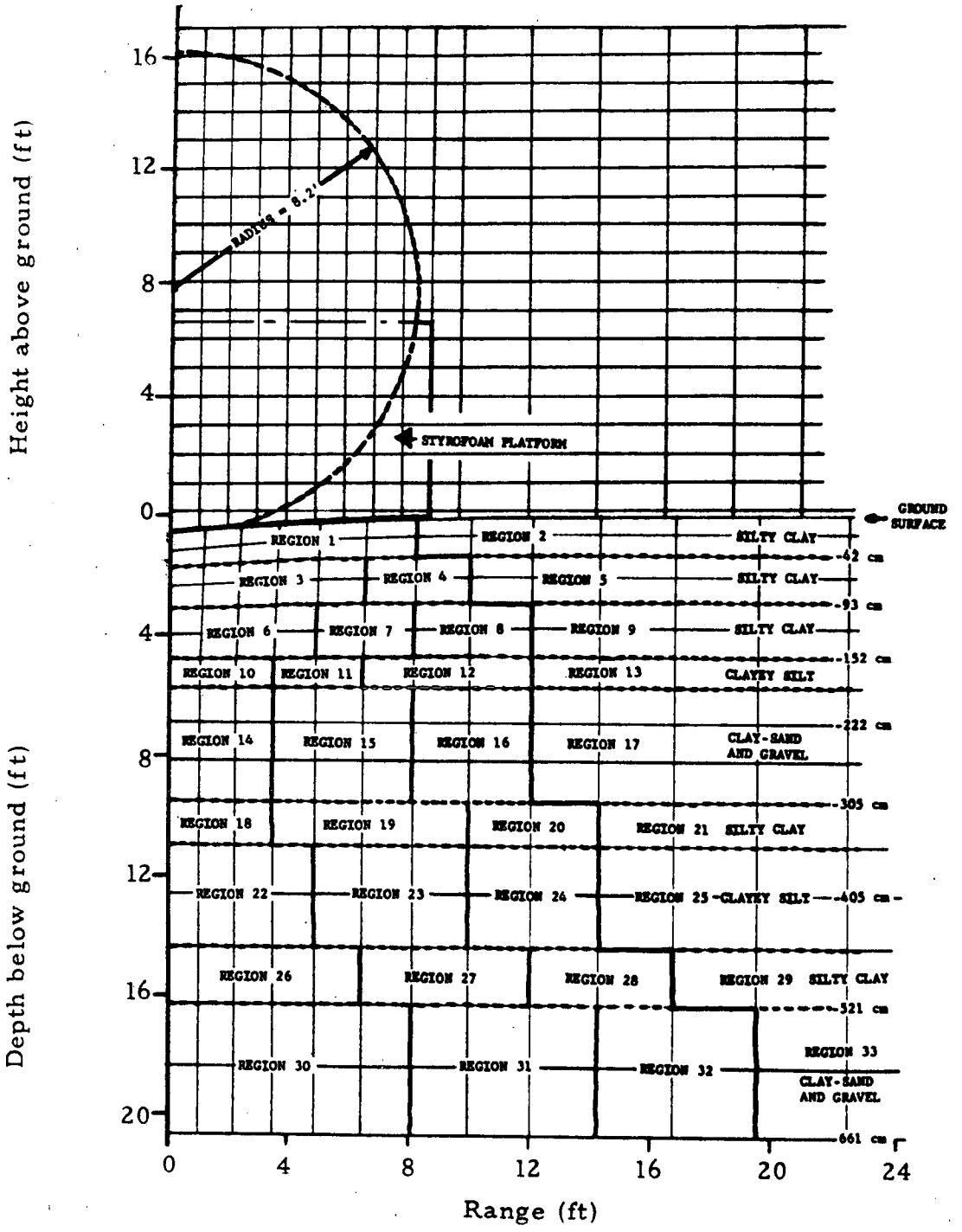

Figure 3.2 Distant Plain No. 6. Theoretical calculation. Euler-Lagrange grid at zero time.

Figure 3.3 shows the computed crater at 220 msec when the crater growth was essentially complete. There was no experimental or computed soil ejecta in this highly compactable case.

The computed upthrust, maximum depth and shape at the crater bottom compared almost exactly with the experiment. The computed crater radius, however, was about 80 percent of the experimental radius. Perhaps the largest error was the absence of a substantial "humped up" crater lip observed in the experiment.

With respect to central upthrust, the responsible mechanism was a vortical soil motion that developed at about 10 msec when the crater depth had reached only about half of its final value.

Figure 3.4 displays the vector velocity field at 220 msec when the crater motion has almost stopped. Though the velocities are dying out at this late time, the vortical pattern is not understood in every detail in this case. The contributing features are:

a. The higher shock impedance in the cone of the precompacted soil below the 100-ton surface level.

b. The release of the gravity-induced weight at ground zero as the H.E. mass dispersed.

c. The general increase in shock impedance with depth (over and above the compaction cone) caused by the decrease of porosity with depth.

d. The shaping of the ground shock front by items 1 and 3 and the shaping of the rarefaction behind the shock by items 2 and 3.

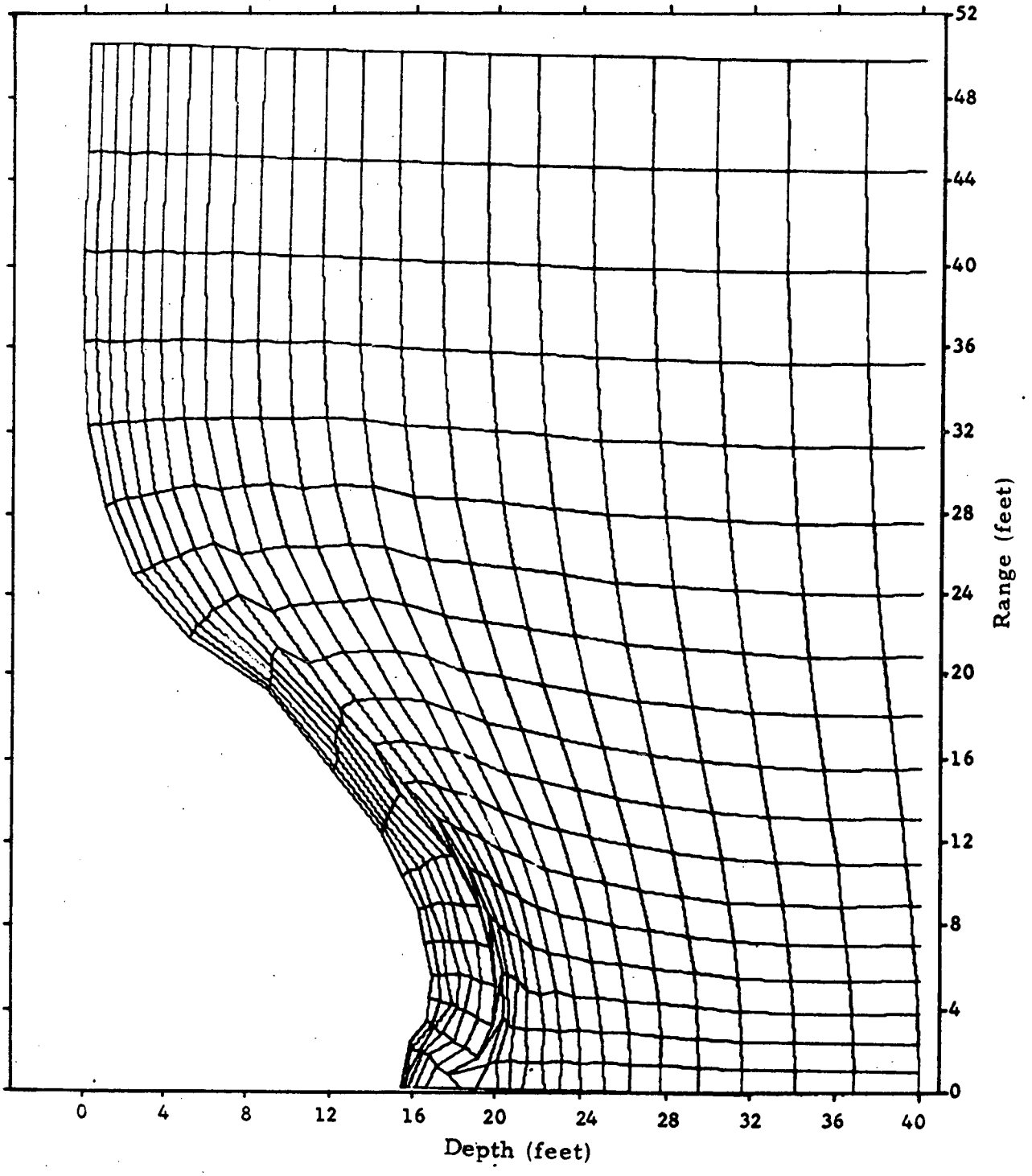

Figure 3.3 Distant Plain No. 6 Theoretical crater calculation: Lagrange grid at t = 220 milliseconds.

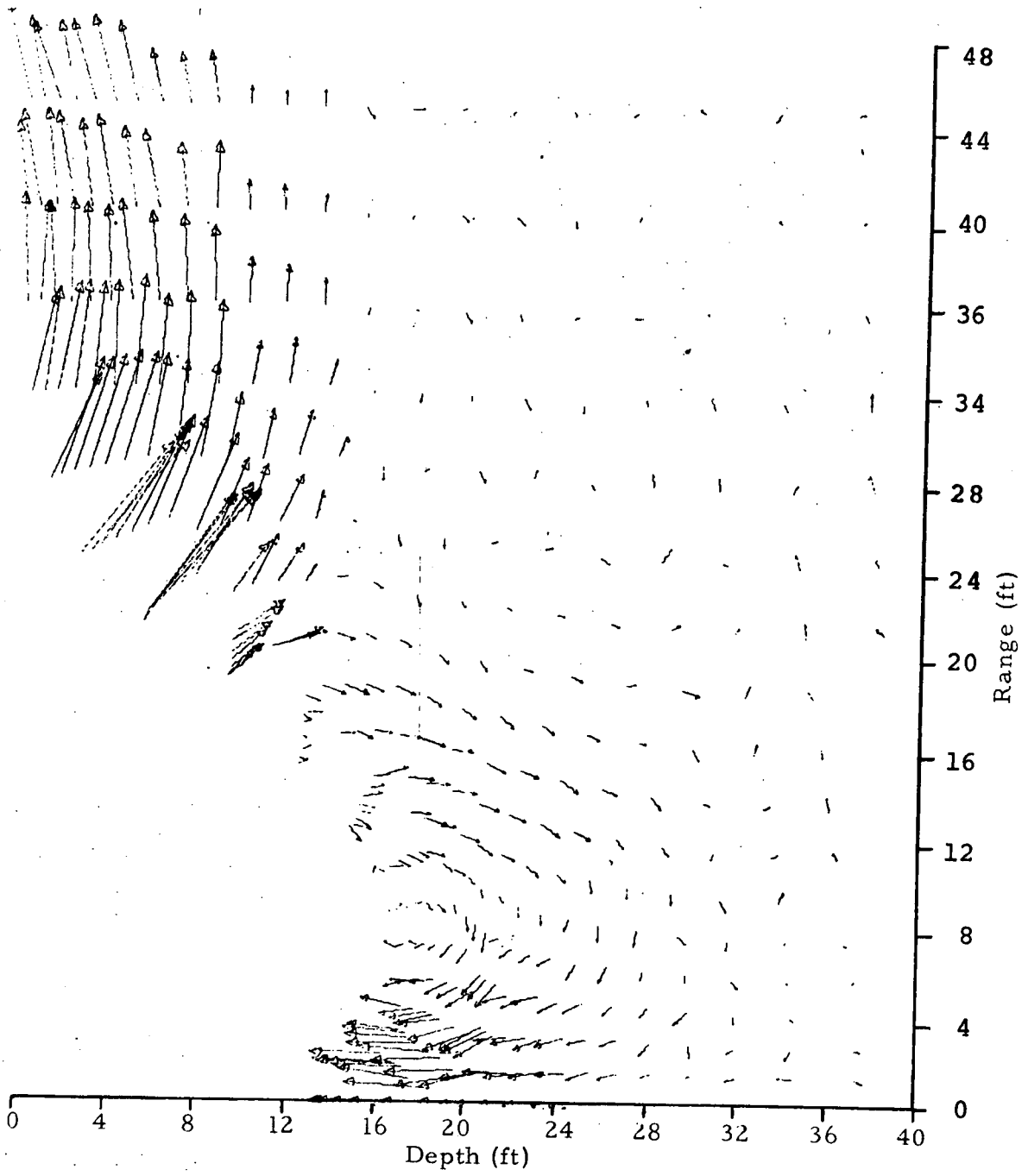

Figure 3.4 Distant Plain 6 theoretical crater calculation: velocity vectors at t = 220 msec

The significance of this calculation is in the fact that the upthrust was initiated by a vortical pattern that developed very early in materials having very little shear strength and was not associated with gravity-induced rebound at late times.

Computational details are reported in References 13 and 14.

MINE UNDER, discussed in the following paragraph, was a calculation of upthrust in a case of homogeneous rock with no gravity in the simulation, a lithology differing greatly from that of the heavily layered, soft soil DISTANT PLAIN 6 simulation with gravity.

3.3 MINE UNDER

Event MINE UNDER was a 100-ton sphere of TNT detonated at the center with a height of burst of 17 ft over Cedar City granite. Computation details are reported in Reference 15.

Although an insignificant crater was formed, this case was chosen because of the very well-defined vortical circulation pattern that was computed in this simple case thus providing an opportunity to investigate an upthrust-inducing mechanism with a minimum of complicating side effects.

Again, the vortical pattern of flow in the earth formed very early in the computation. Figure 3.5 shows the velocity vector field at the time of 8.22 msec. This pattern was well formed at 5 msec and persisted beyond 20 msec. The velocities are quite small as are the displacements for this large height-of-burst case. It is clear, however, that a well-defined central upthrust mechanism is operating.

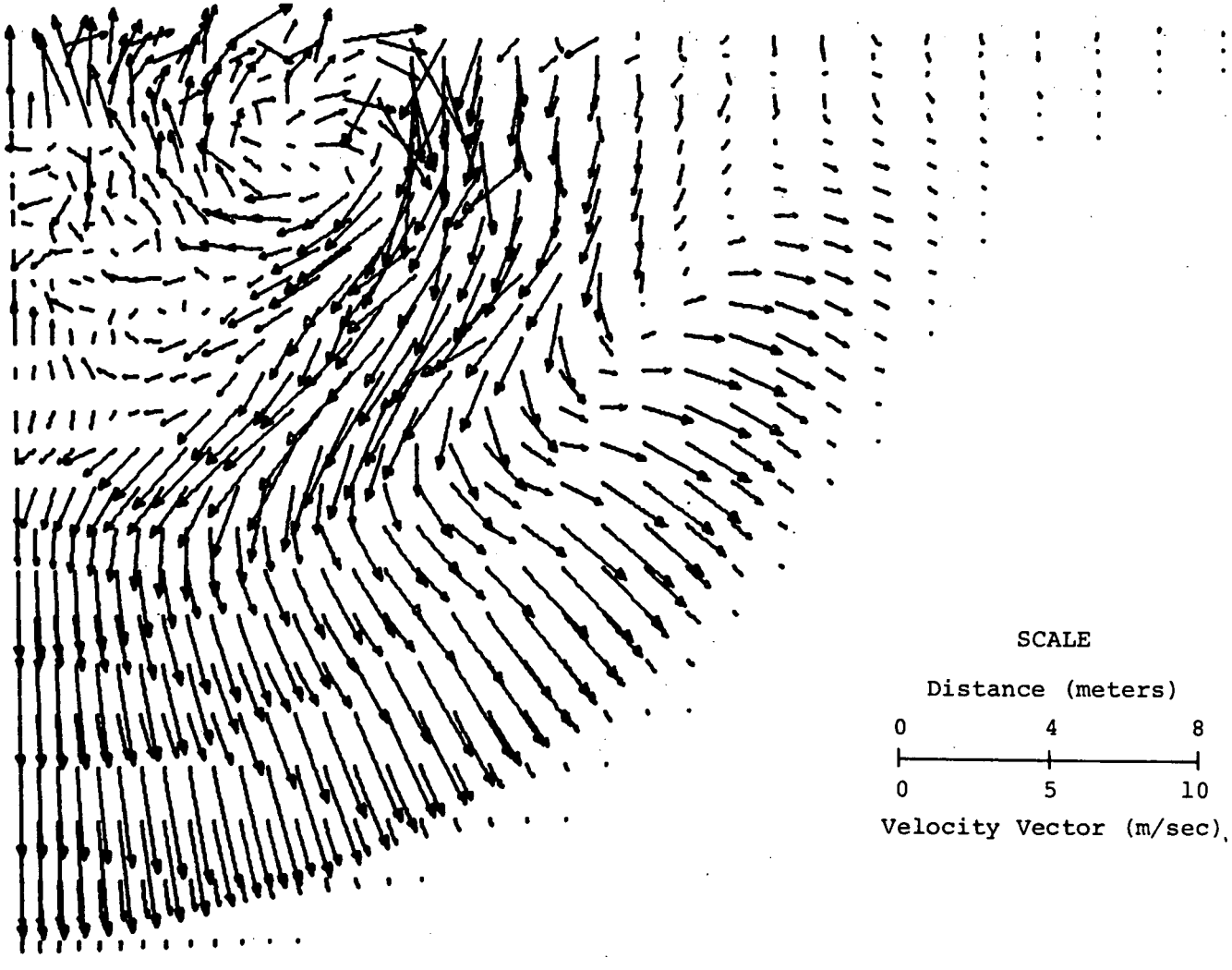

Figure 3.5 Mine Under, t = 8.22 msec velocity vector field.

As noted, gravity is suppressed in this simulation and the rock is homogeneous. The previous discussion of the mechanisms at work in soil is not pertinent.

At the time of 5 msec in the calculation when the vortical pattern in the rock was well established, it was observed that the pressure in the air at ground zero had dropped to 0.06 kbar. The ground shock had progressed to a depth of about 15 meters with a shock pressure of about 0.25 kbar. Strangely enough, the peak pressure anywhere in the grids at this time was located in the surface rock at ground zero. The value 0.64 kbar was significantly higher than that at the other two locations noted, and appeared to be "frozen in" because of a large value of horizontal compressive stress at ground zero.

Figure 3.6 displays the principal stresses in the plane of the figure at 8.98 msec, corresponding to the time of Figure 3.5. It can be seen that the large horizontal compressive stresses still persist in the rock at ground zero, even though in the time interval from 5 to 9 msec, a compressive sound signal in this material propagates about 16 meters.

The vertical stresses in the surface region of rock at ground zero are small, consistent with the surface air pressure. The "locked in" horizontal stresses in this region are slowly being relieved by the upward and outward displacement that is accumulating. The strong downward velocity pattern in the upper region at a horizontal range of about 12 meters has been accentuated by a MACH stem interaction region of high pressure that existed at the surface at an earlier time because of the interaction of the elevated burst with the surface. This effect has accentuated the vortical flow. Nevertheless, an unexpected mechanism was uncovered.

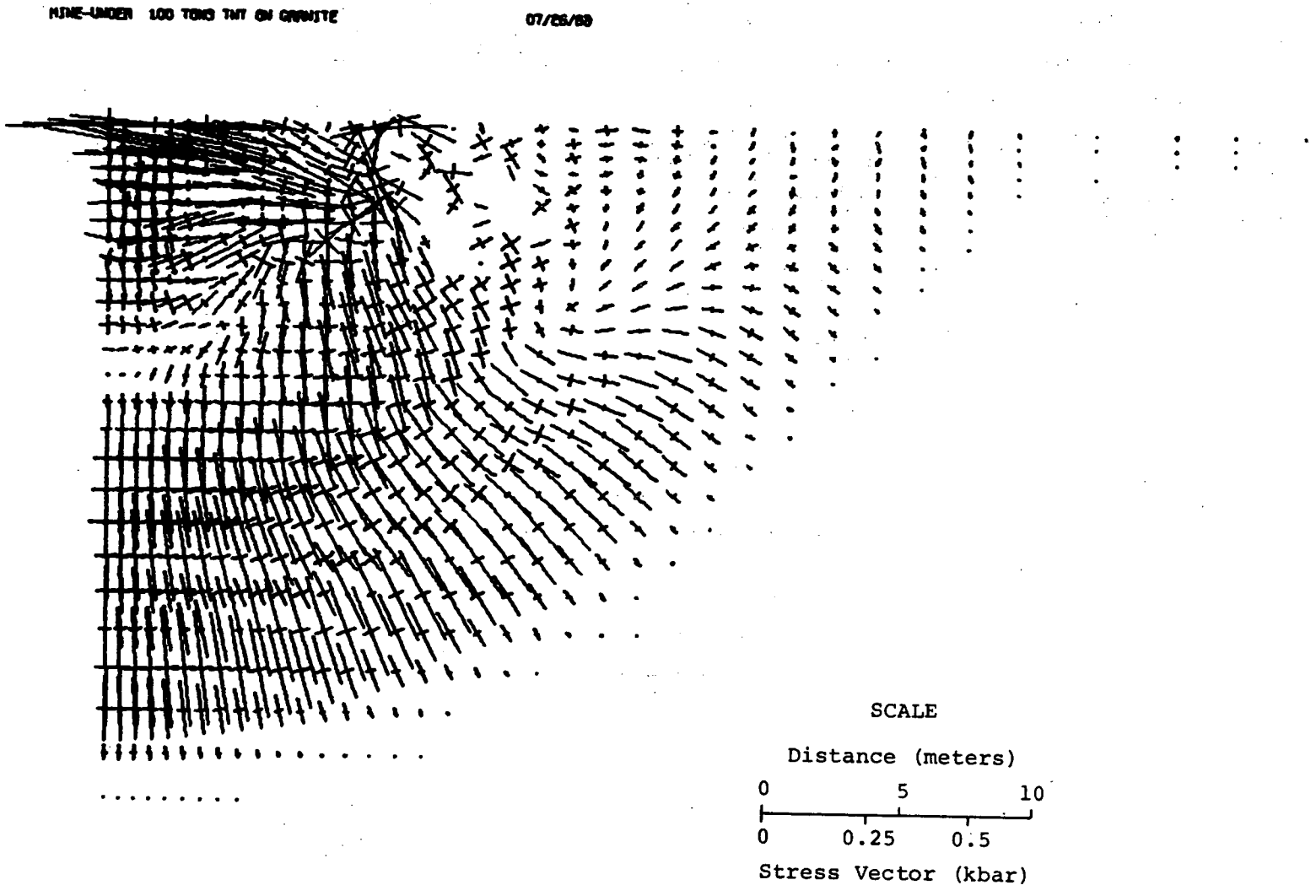

Figure 3.6 Mine Under, t = .8.98 msec. Principal compressive stresses in a plane passing through the axis of symmetry.

An examination of the printouts on the vertical downward axis showed that the rock loaded first elastically to the yield surface, then plastically beyond to the peak stress, with the vertical compressive stress being larger than the horizontal stress by 0.2 kbar, consistent with the assumed yield model. The stress state then relaxed down the unloading path, first elastically with the unloading strains, then plastically as the stress deviators reversed and the yield surface was re-encountered. During subsequent relaxation toward zero pressure, the vertical stresses became tensile, while the horizontal stresses were still compressive with substantial values. The gradient in the horizontal stresses near the surface then accentuated the outward horizontal flow. This, together with the surface upward flow caused by the vertical gradient of the vertical stress, undoubtedly was the dominant mechanism contributing to the upward-outward flow at the surface around ground zero. This surface flow is consistent with an upward-inward return flow at greater depths. However, the MACH stem effect, noted earlier, undoubtedly contributed significantly to the inward flow at depth and cannot be separated from the previous effect.

Two other mechanisms are present that may affect the vortical circulation. The airblast-induced shear wave in the rock is limited to a shear stress of 0.10 kbar by the assumed yield model. This wave contributes to an upward-inward acceleration which will tend to enhance the inward portion of the flow and retard the downward portion of the flow. The contribution of this effect on the total flow pattern of Figure 3.5 is small and cannot be discerned. It would have had a noticeable effect, however, if the MACH stem region had not been present.

The final effect to be discussed regards the upward flow of the material during the upward rebound of the crater. In MINE UNDER, the crater was negligible and the effect was masked. In many rock crater cases, however, the effect to be described can be substantial.

When the crater bottom has reached its maximum depth and starts to proceed upward, a compressive stress develops parallel to the curved crater wall that retards upward motion with a force per unit area proportional to the parallel stress and inversely proportional to the radius of curvature of the crater wall. If the vertical gradient of the vertical stress is strong enough, this bridging effect will be overcome, the wall will buckle with a reversal of curvature, which if it occurs at the bottom, will produce a central uplift. Once started, the uplift flow will continue, relieving the compressive stress that would otherwise accumulate in the wall as the rebounding crater radius diminishes.

3.4 INFERENCE FROM DISTANT PLAIN 6, AND MINE UNDER DISCUSSION

The mechanisms that have been presented for background serve to illustrate the complexities associated with plastic-elastic flow patterns and to serve as a warning that it is not always possible to distinguish mechanisms in terms of cause and effect in highly coupled and interacting flow fields.

Because of its huge size, the Sierra Madera case will be much simpler to analyze than the previous cases. In the Sierra Madera case, substantial flows will occur at great distances for long time periods with the strength of jointed rock being relatively unimportant compared to the gravity-induced overburden pressures released by the crater excavation process.

3.5 SIERRA MADERA COMPUTATIONAL OVERVIEW

The ELK code, previously in connection with the LiMg-basalt-impact case, was utilized in the Sierra Madera simulation. The incoming projectile was assumed to be a basalt sphere with a density of 2.7 gm/cm^3 and a radius of 100 meters. A vertical impact along the axis of symmetry was assumed with an incoming velocity of 30 km/sec. Thus, the projectile mass was 1.127×10^{10} kilograms and the initial kinetic energy was 5.0695×10^{25} ergs (1.2×10^3 megatons). The initial condition corresponded to the projectile being tangent to the ground surface with full velocity. The air shock that would be associated with the incoming projectile in a real case was not included in the initial condition. The subsequent airblast generated by the explosion was of course included as a natural consequence of the code method.

The original Euler zones were square, with a width of 25 meters, small compared to the 200-meter diameter of the projectile. This ensured an adequate resolution of the early impact phases. The earth medium respose in the vicinity of the impact was also computed in the Euler grid, because it was possible to ignore the earth strength properties in the multi-kilobar and megabar high pressure flow near ground zero. As the air and ground shocks diverged from ground zero and as the shock wave width increased owing to dispersion, the fine Euler grid was no longer needed for adequate spatial resolution, and it was rezoned as appropriate. After three such rezonings, the Euler grid was composed of squares, 200 meters on a side. The ground shock pressure attenuated to a value of 20 kbar at a depth of 2 km, where the preexisting overburden pressure was about 0.5 kbar. At this point the Lagrange grid was added with

the subsequent flow taking place in the coupled Euler-Lagrange grids. The portion of these grids in the vicinity of ground zero is shown on Figure 3.7. The Euler grid was dropped at a time of 2.5 seconds when the pressure in this region had relaxed to essentially zero.

At this time, the ground shock had propagated to 10.4 km. The highest pressure in the shock front at this time was 3.8 kbar and was located on the vertical axis below ground zero. At this depth the original overpressure induced by gravity was 2.8 kbar, thus the shock overpressure was only 1 kbar, about one quarter of the total pressure.

Figure 3.8 displays the peak total pressure, peak overpressure and original overburden pressure as a function of depth.

The peak total pressure contours are shown in Figure 3.9. The values were the maximum that were attained over all time, and are not to be confused with isobars at a fixed time. The horizontal dashed lines indicate the original overburden pressures.

At the time of 2.5 seconds, the shock was at a distance of about 12 km and it was then possible to rezone the Lagrange grid to increase computational efficiency without suffering a significant loss in resolution. Every other column (circular arcs in the grid of Figure 3.7) was dropped by a standard code option that blended the appropriate zones, conserving mass, energy and momentum. Calculational speed then was four times as fast and made it practical to reach the very large final time that was required.

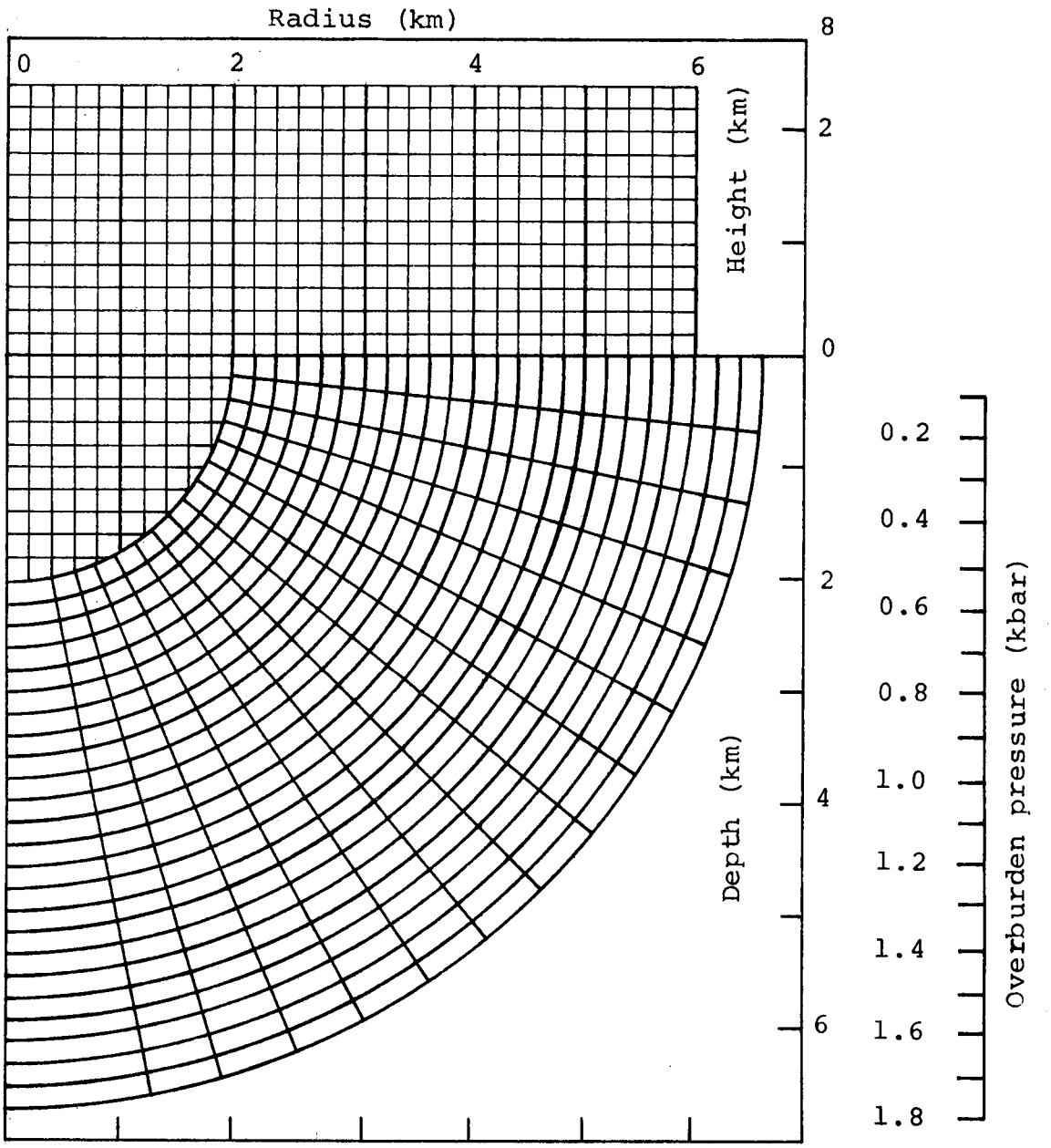

Figure 3.7 A portion of the Euler and Lagrange grids of the Sierra Madera calculation in the vicinity of the impact before Lagrange grid displacement occurs.

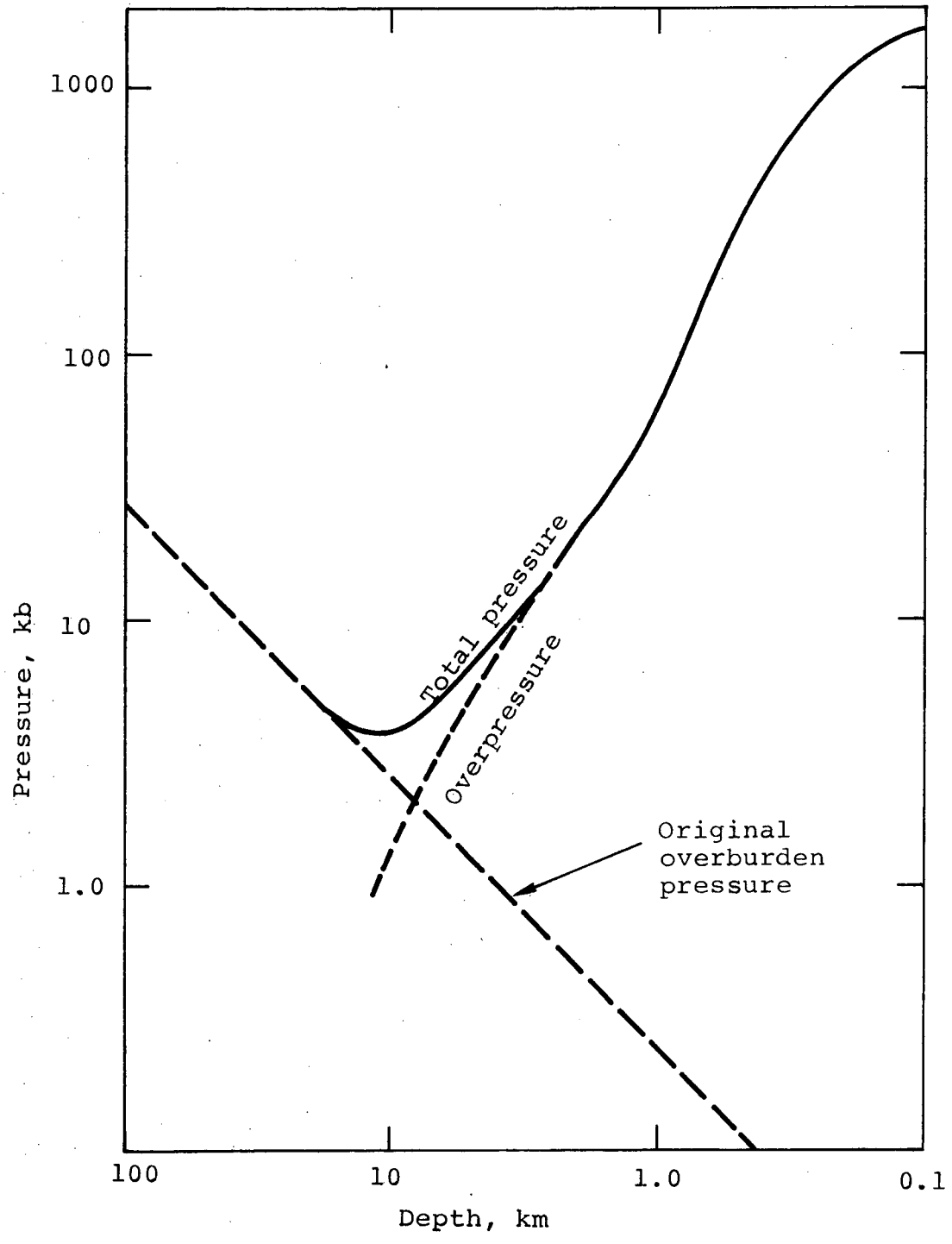

Figure 3.8 Peak pressure encountered on axis, versus depth.

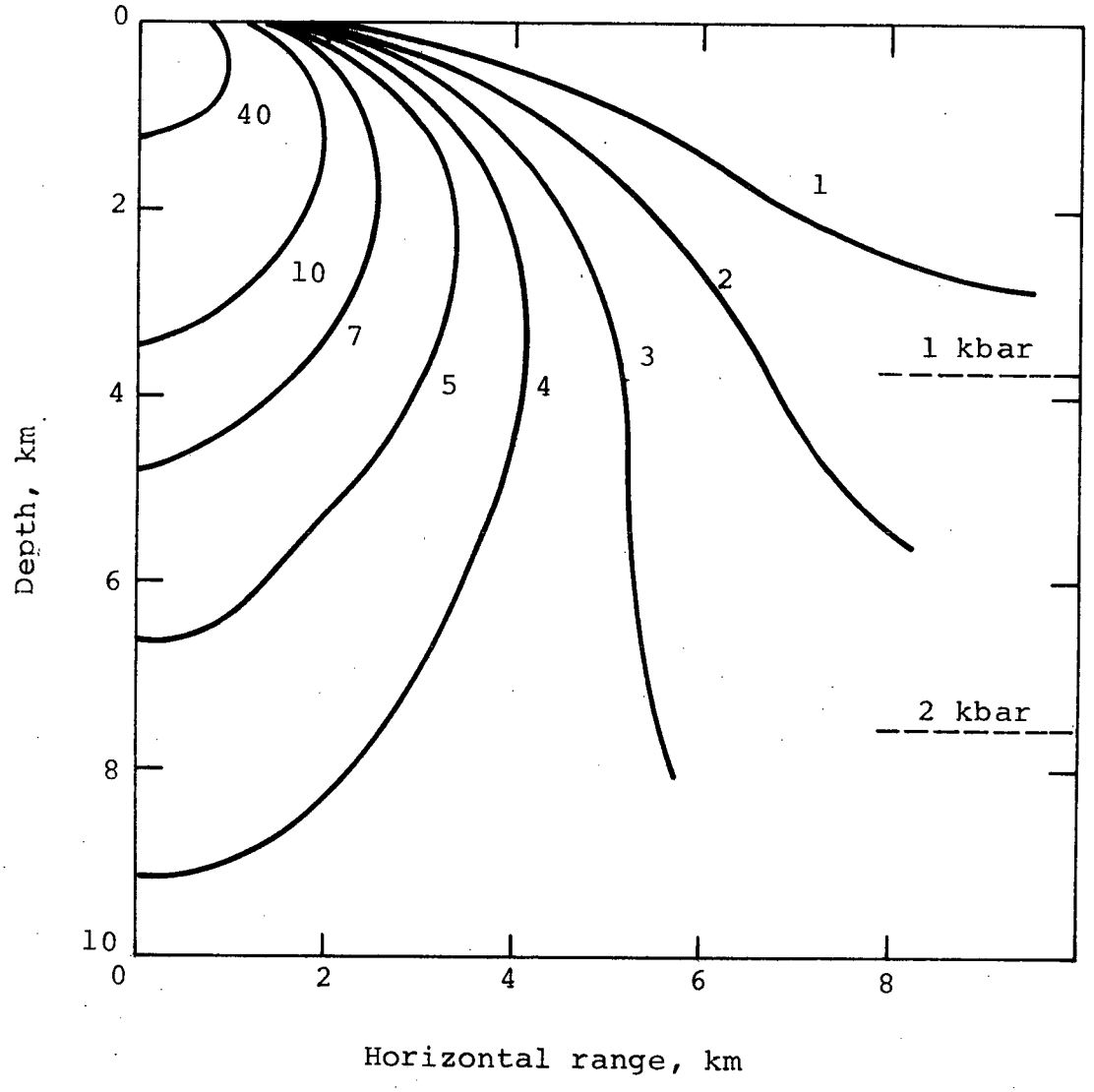

Figure 3.9 Peak total pressure contours attained at any time. The dashed lines indicate the original overburden pressures.

At 5.54 seconds the shock was very weak and had reached about 25 km. The Lagrange zones containing this activity were then dropped from the calculation by defining the grid to extend only to 23 km. This eliminated the possibility that the weak shock could reflect back from any boundary and disturb the crater region of interest.

It had been thought that the upthrust would form in about 10 seconds. After 9.54 seconds it was clear that it would have to be extended to about 30 seconds. At the time of 9.54 seconds, it was observed that the earth activity was trivial outside of a 6-km radius from ground zero. Examination of the printouts revealed that the zones were dominantly hydrodynamic inside a 4-km radius, dominantly elastic-plastic between 4 and 6 km, and purely elastic beyond 6 km. It was also clear that the elastic region would remain so because of the very small velocities and small stress gradients in this region. This enabled all of the zones beyond 6 km to be eliminated by placing a rigid boundary condition at this distance. This change enhanced the computing speed by a factor of about 5 without significantly affecting the cratering process in the interior, and enabled the calculation to proceed to the final time of 30 seconds where the upthrust had tangled the zones to a point where it was difficult to continue. The problem was terminated at this time.

3.6 SIERRA MADERA ROCK STRENGTH MODEL

The rock strength model that was used was as follows:

a. If a zone had ever achieved zero pressure, its shear strength was set to zero for all subsequent time.
b. Otherwise a 200-bar von Mises yield surface applied.

The rationale behind the first assumption was based on the intuitive feeling that joints would open when the overburden was released and that the pre-existing, close-packed blocks would be jumbled in a manner drastically reducing the shear strength. The assumption that the shear strength is reduced to zero can certainly be challenged. In retrospect, it would have been more appropriate to use a real viscosity and a small but finite shear strength to act on the jumbled earth material to damp out the fluid-like behavior during the dying stages of the upthrust activity. This would have made the task much easier with respect to extrapolating to a final shape, in addition to being more realistic with respect to the real phenomena.

3.7 SIERRA MADERA SIMULATION RESULTS

As noted earlier, the Euler grid was dropped from the calculation when it was determined that the material in it would no longer significantly affect a central upthrust response of the Lagrange grid. Thus, the graphs to be shown will be only for the Lagrange region.

At a time of about 3.5 seconds, the Lagrange grid began to rebound inward. At about 5.5 seconds, a circulation started to form inside a radius of about 4 km, which later developed into a well-defined central upthrust pattern.

Grid plots of the active region are shown in Figures 3.10 through 3.16. The fiducial marks on the border are spaced by one kilometer. The original ground surface is indicated by the dashed line. The ground zero point is shown with a + sign. The distorted circular-like arcs were originally at the radii 2.0, 2.4, 2.8, ...km.

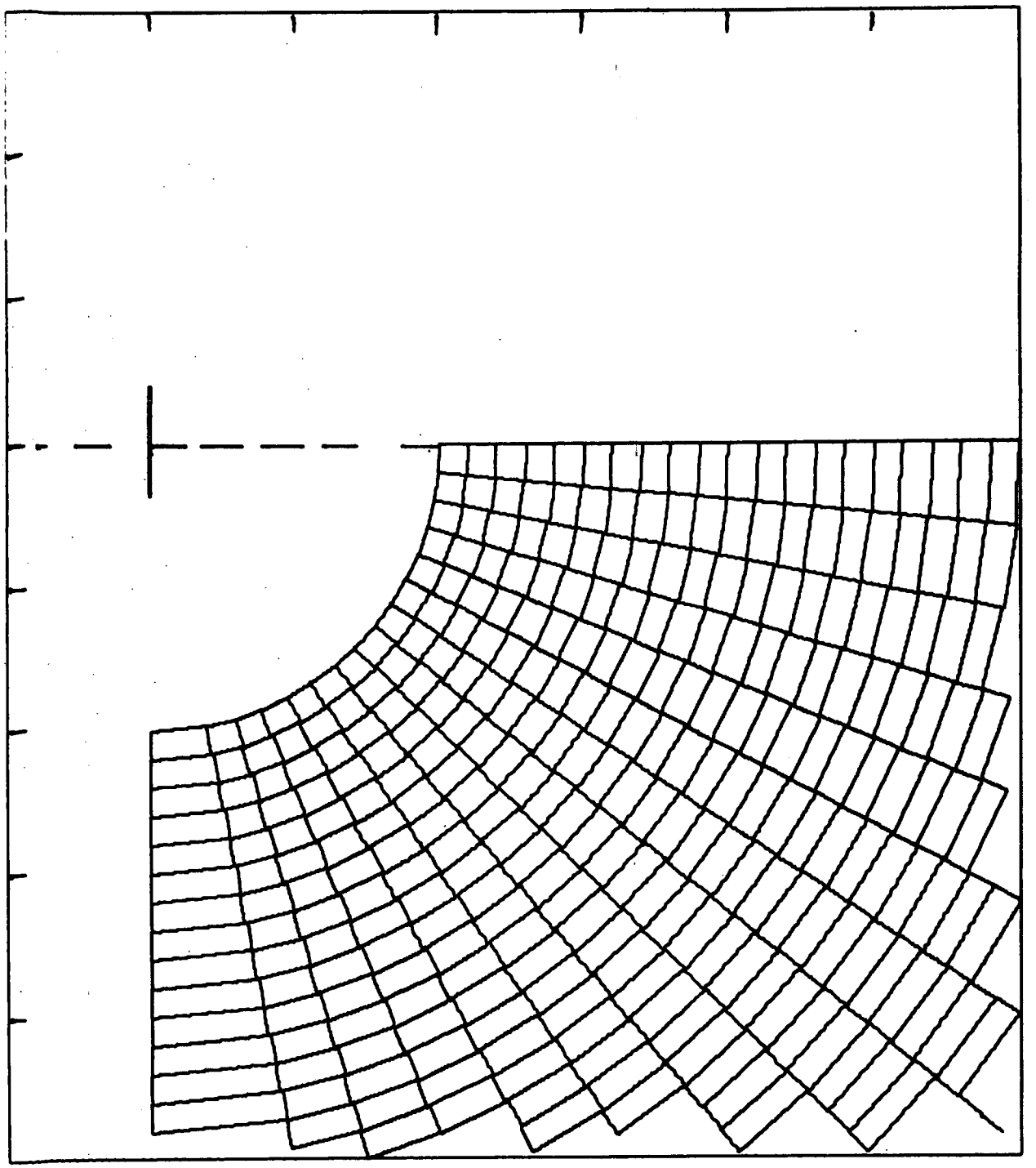

Figure 3.10 Close-in Lagrange Grid before activity. Subsequent figures will have every other column (circular arcs) dropped. See text for scale.

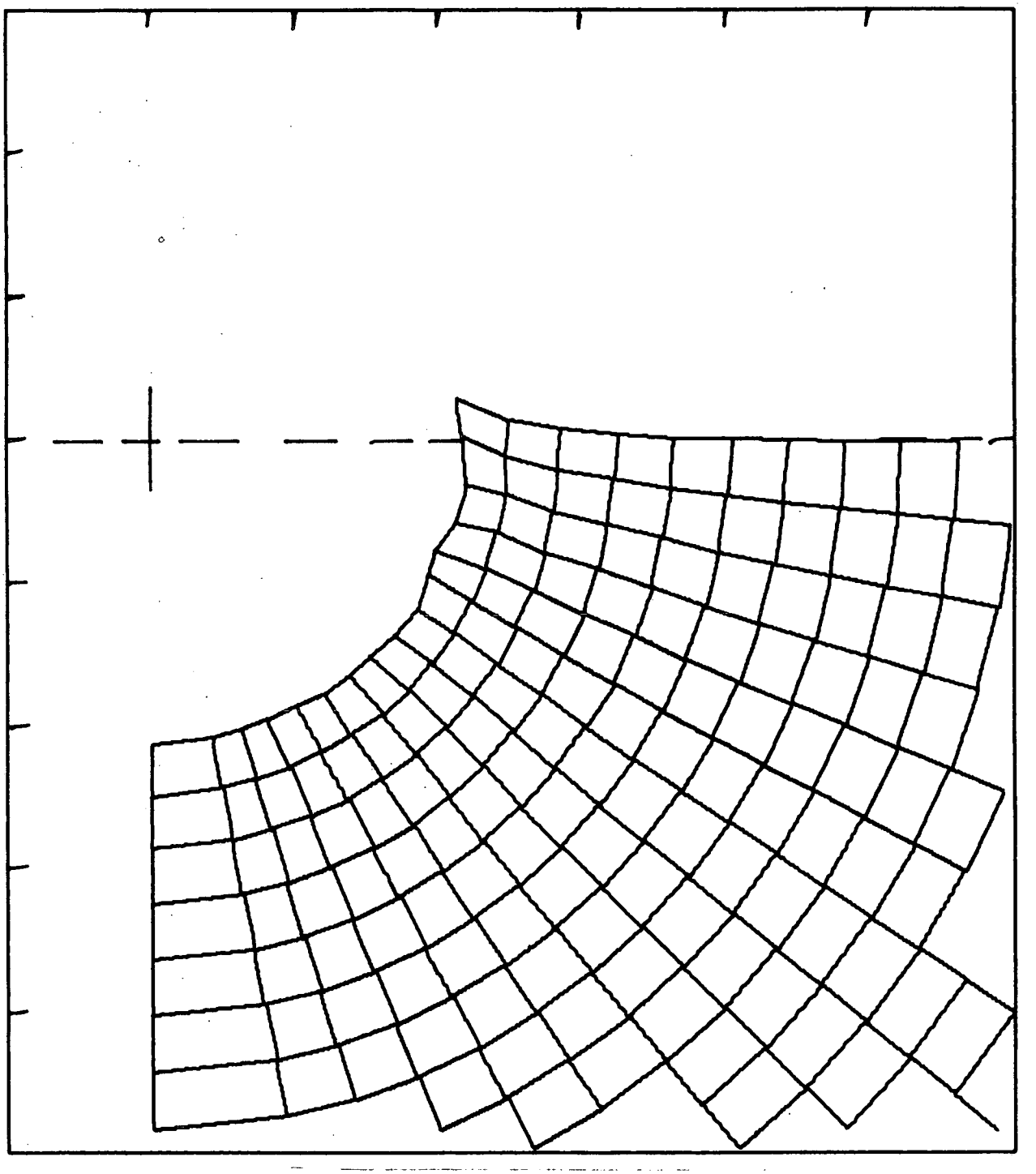

Figure 3.11 Close-in Lagrange grid at 5.6 seconds. See text for scale.

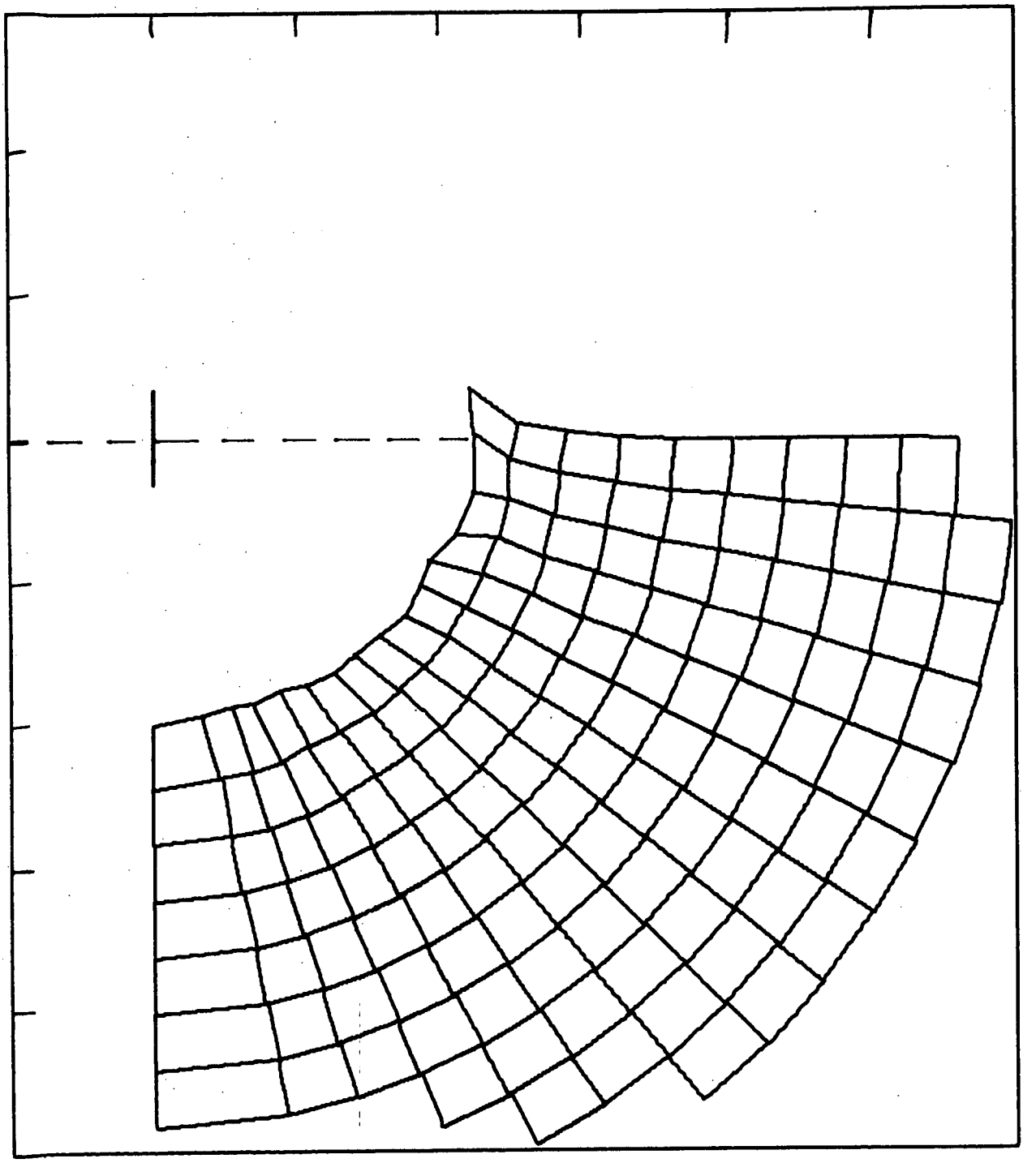

Figure 3.12 Close-in Lagrange grid at 9.6 seconds. See text for scale.

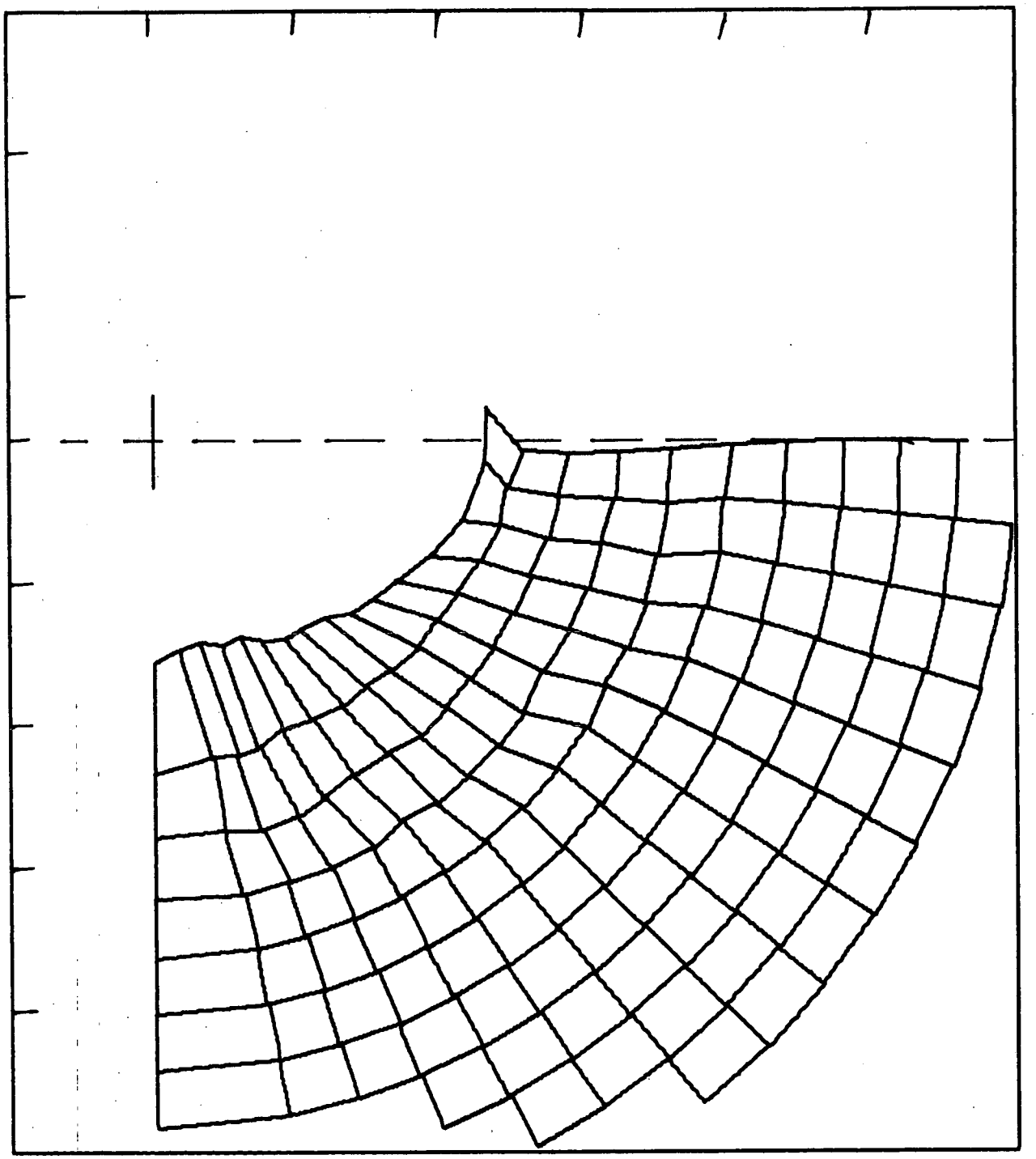

Figure 3.13 Close-in Lagrange grid at 15.1 seconds. See text for scale.

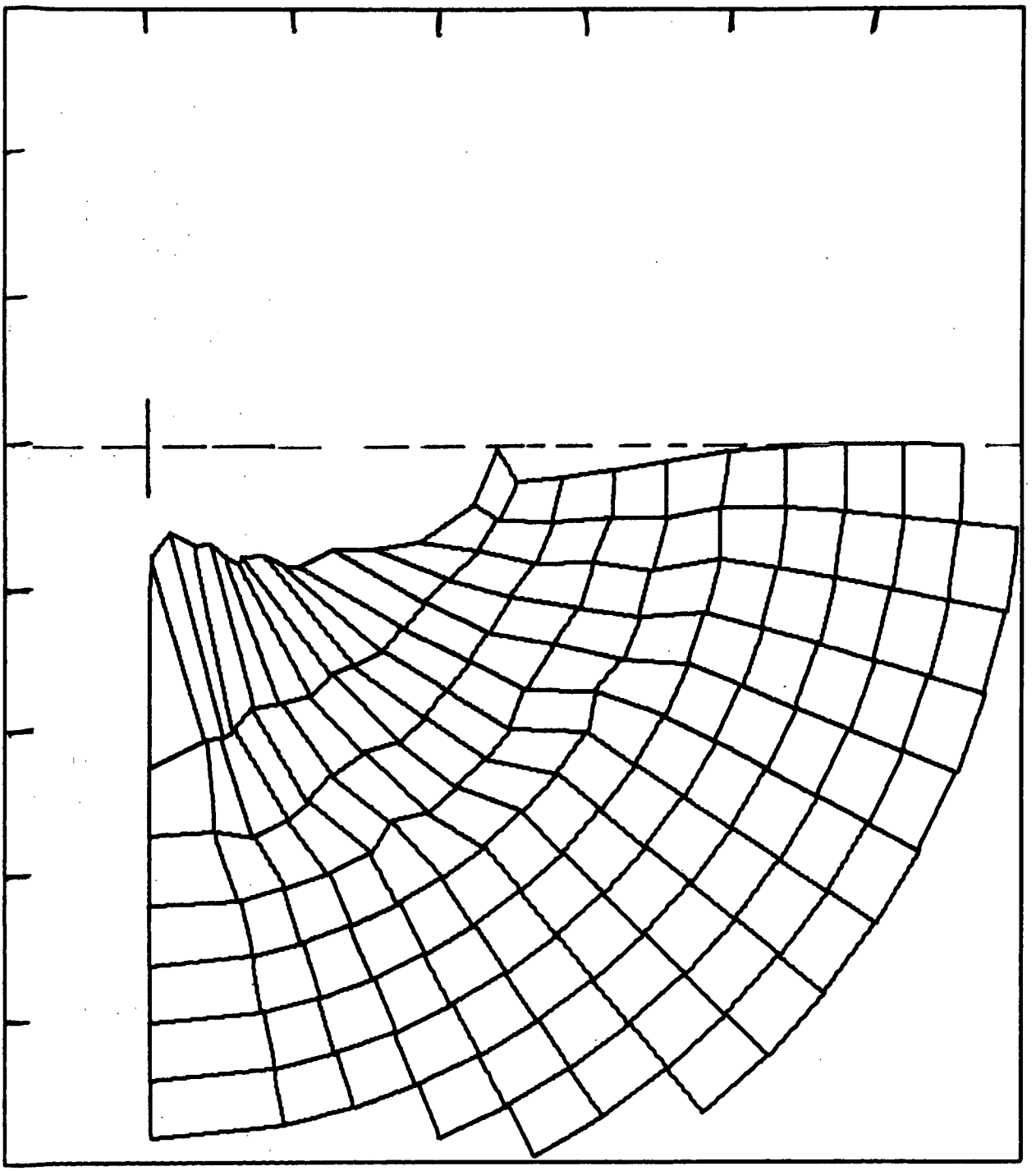

Figure 3.14 Close-in Lagrange grid at 19.5 seconds. See text for scale.

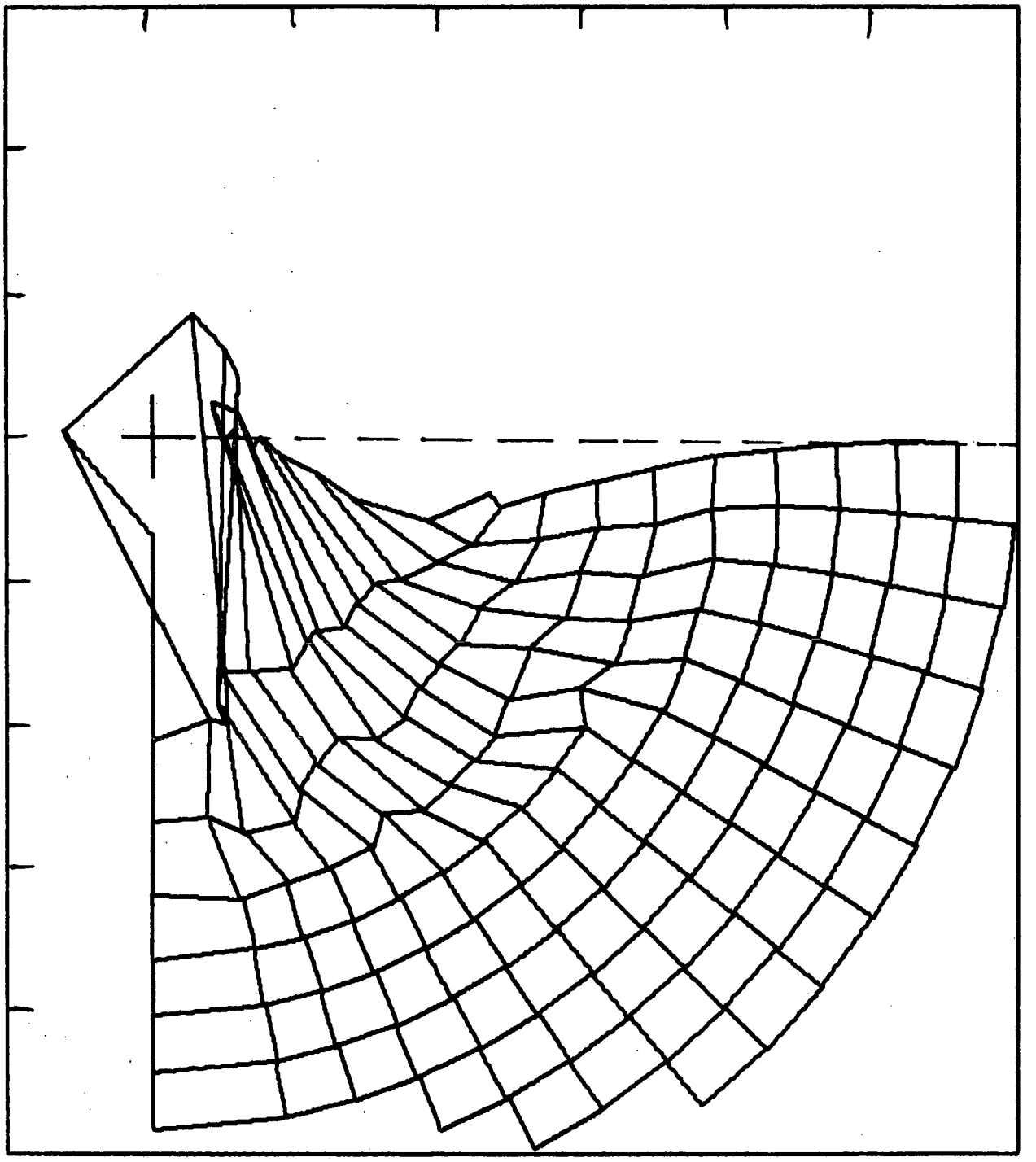

Figure 3.15 Close-in Lagrange grid at 25.2 seconds. See text for scale.

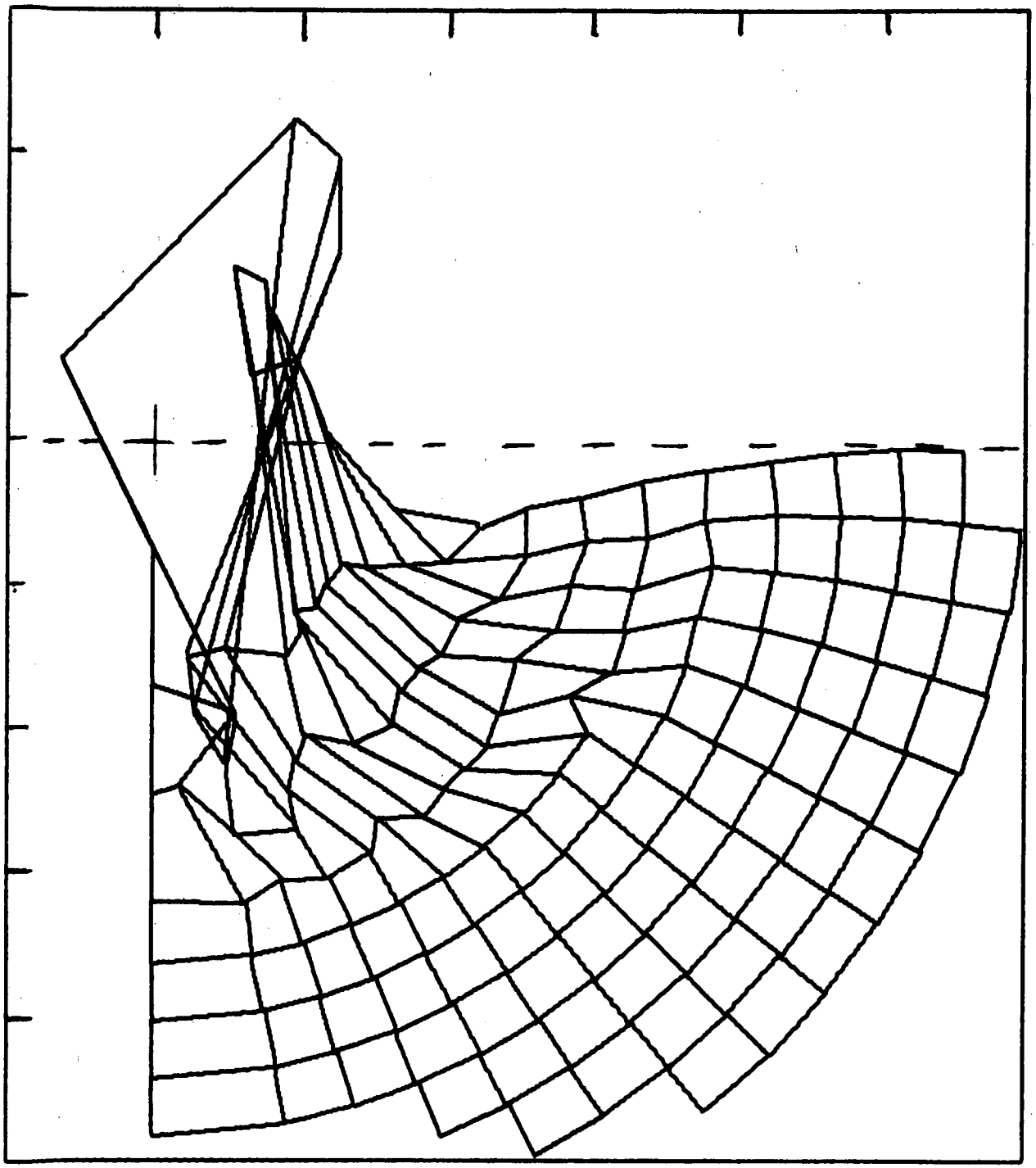

Figure 3.16 Close-in Lagrange grid at 30.0 seconds. See text for scale.

Figures 3.17 through 3.22 show the corresponding velocity vector fields. The fiducial markers are spaced by 1 km, as before, and the velocity scale has been set so that the fiducial spacing also corresponds to a velocity of 0.1 km/sec. As an aid to extrapolate the velocity plots, it can be confirmed that a particle with an initial upward velocity of 0.14 km/sec acted upon only by gravity will proceed upward for 1.0 km.

Figure 3.23 traces the trajectories of selected points, demonstrating the dramatic and violent central upthrust mechanism and the ring depression formation in the subsiding region.

Appendix B includes the time-history plots of the vertical velocity and displacement of selected points. An examination of all these data, including the printouts was conducted to estimate the final elevations of originally horizontal strata, recognizing that an unevaluated error will exist because strengthless earth in reality will come to rest under the action of residual shear strength and viscous forces that were not included in the simulation.

Figure 3.24 is a sketch of a final condition which is compatible with the computed data. Original horizontal layers, spaced by 0.4 km are shown to be distorted, consistent with the computed results and a somewhat subjective extrapolation. An estimated true crater shape is also shown. Fallback was not estimated, hence the apparent crater is not shown. Had a residual shear strength been assigned to the jumbled earth material, it would have been instructive to discard the zones whose ballistic trajectories would clear the crater region, momentarily stop the remaining zones to destroy the remaining momentum, then restart the problem at 30 seconds using the stress equilibrium

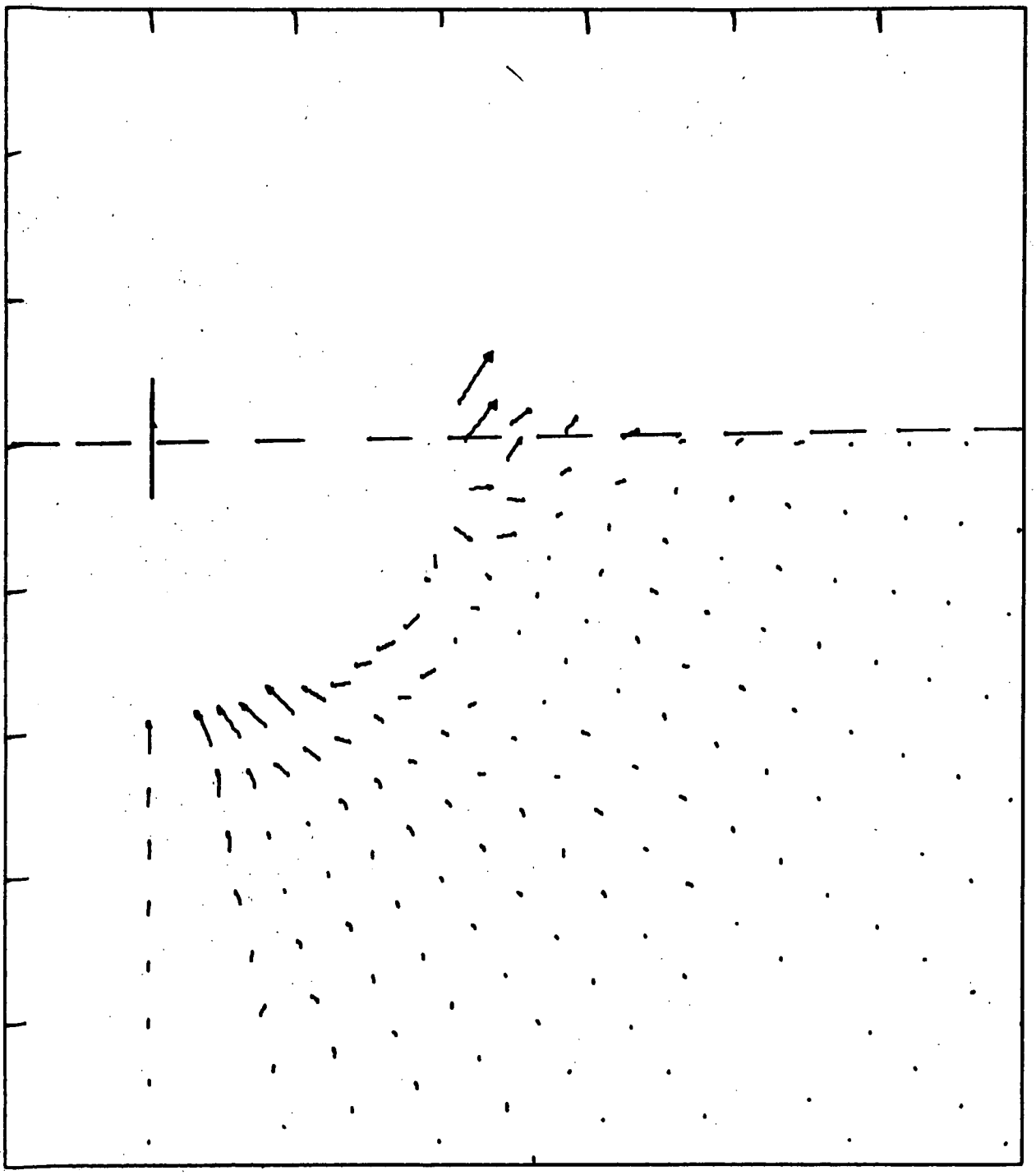

Figure 3.17 Close-in Lagrange velocity vectors at 5.5 seconds. See text for scale.

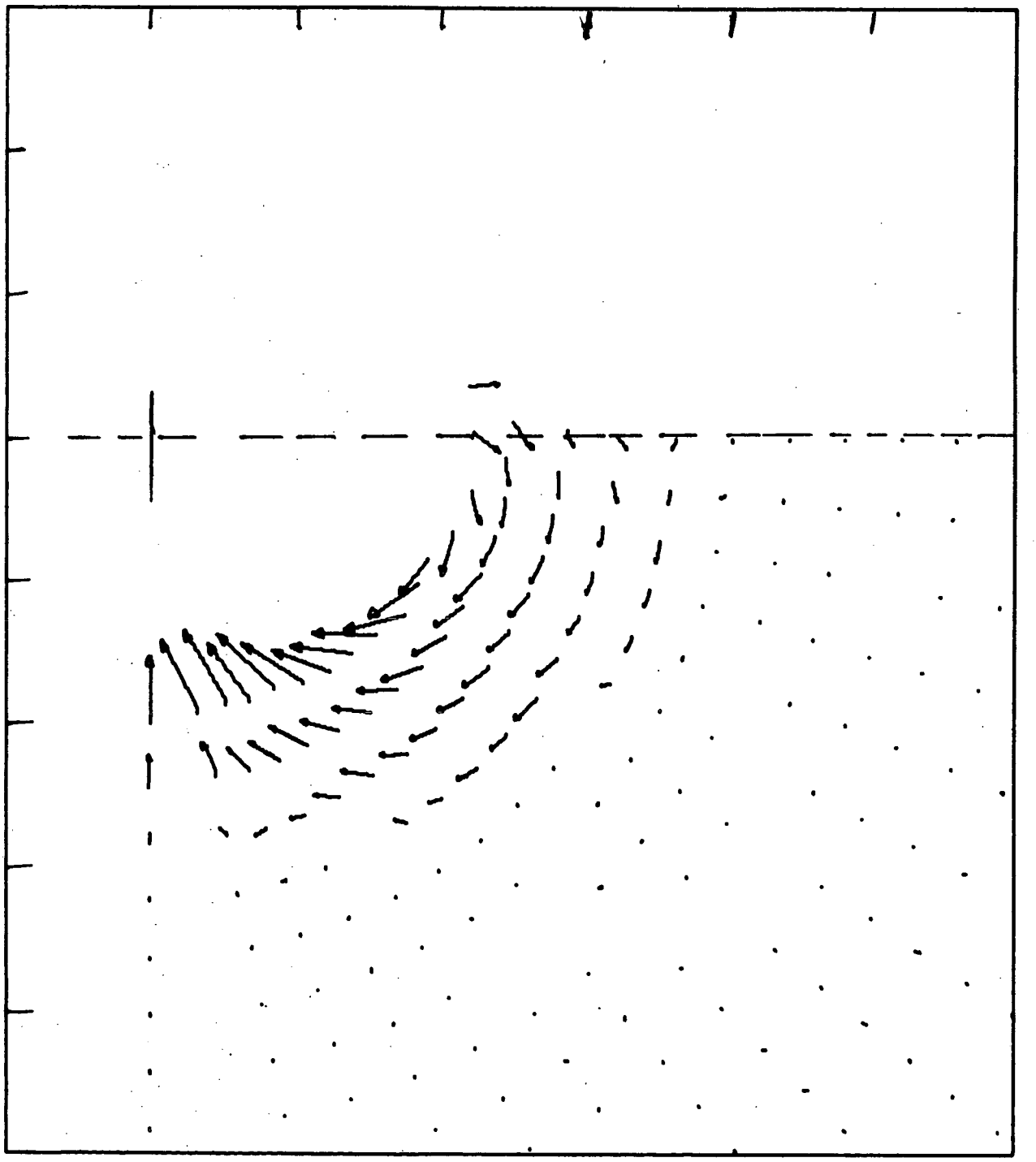

Figure 3.18 Close-in Lagrange velocity vectors at 9.5 seconds. See text for scale.

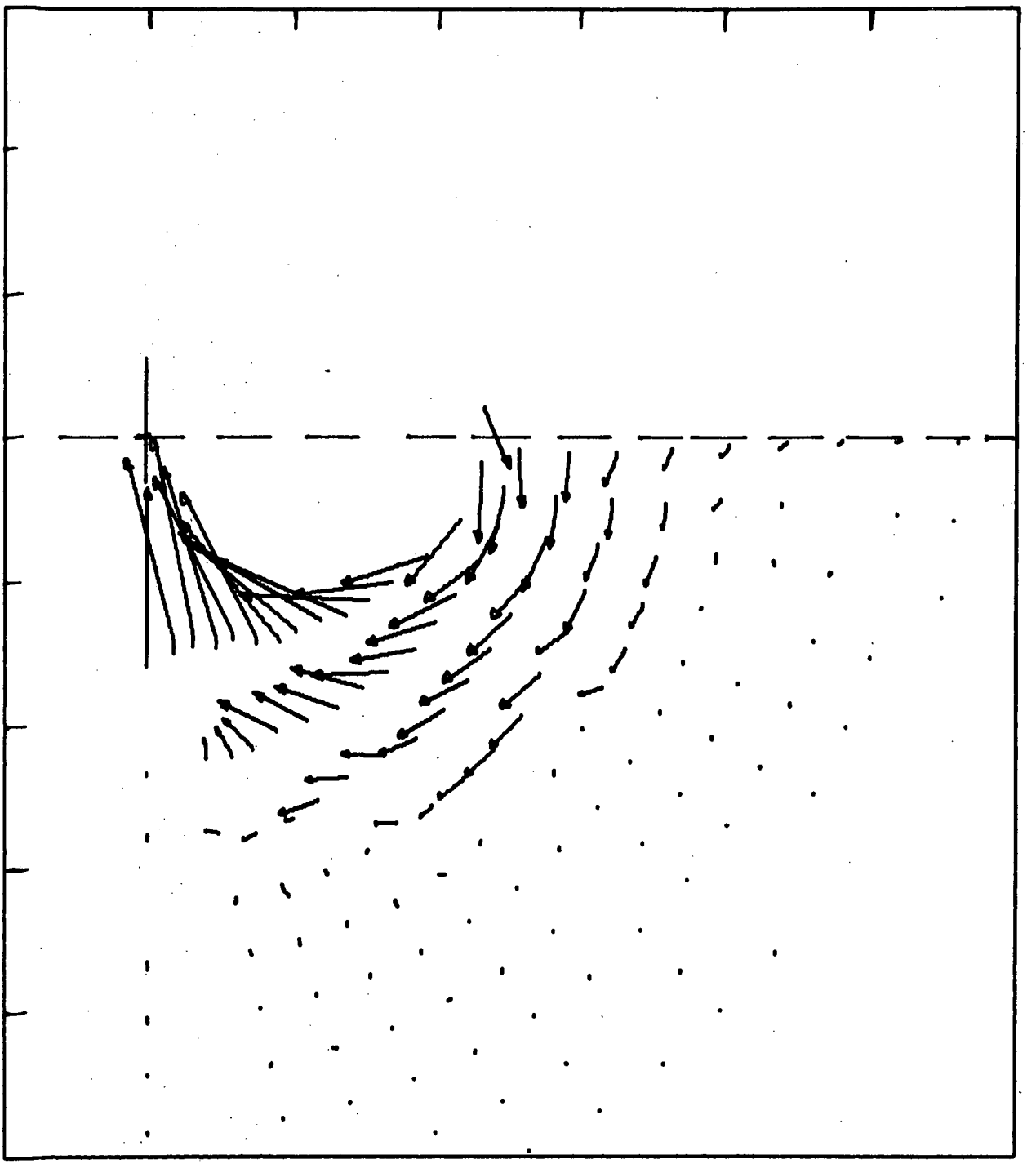

Figure 3.19 Close-in Lagrange velocity vectors at 15.0 seconds. See text for scale.

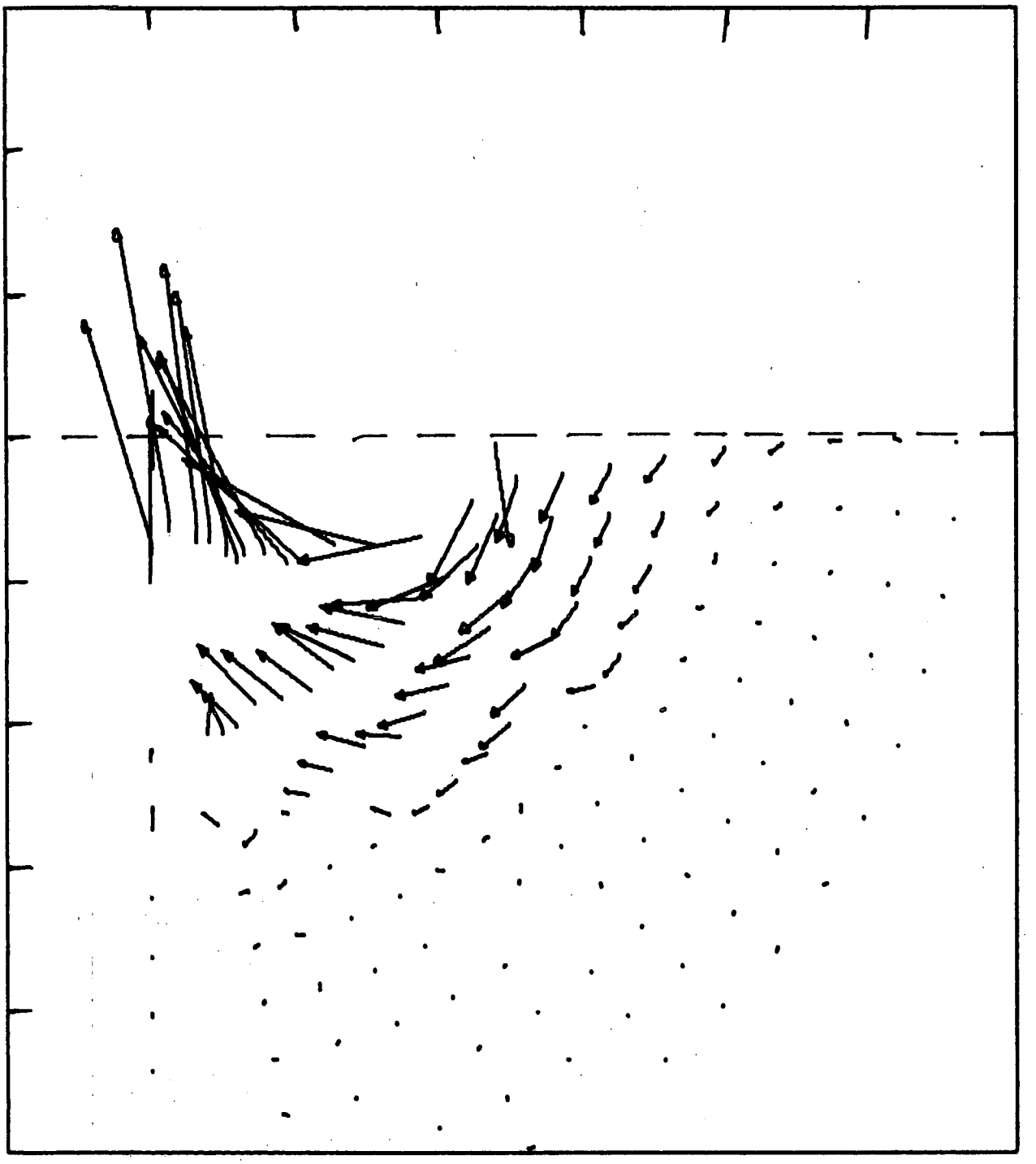

Figure 3.20 Close-in Lagrange velocity vectors at 19.5 seconds. See text for scale.

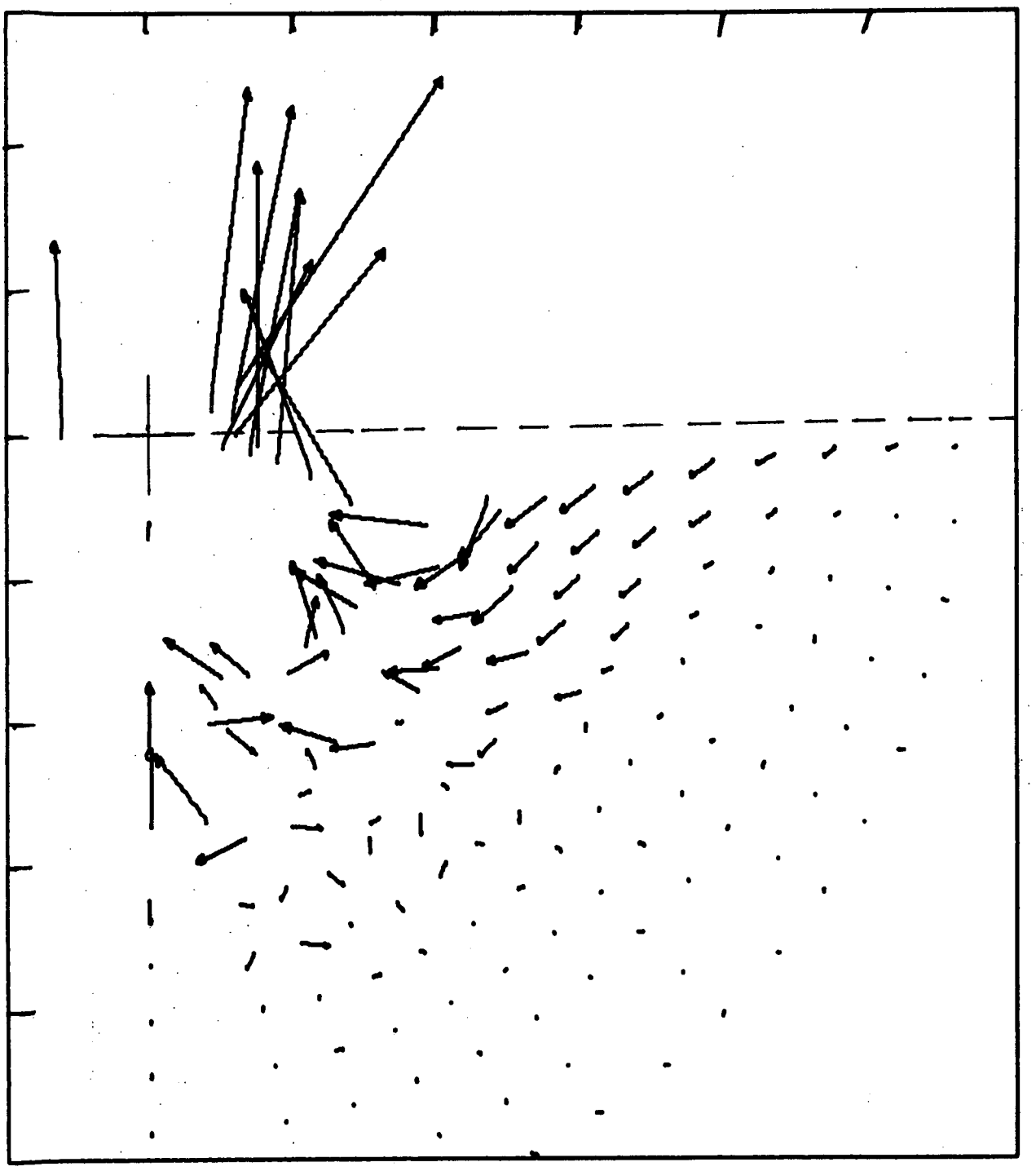

Figure 3.21 Close-in Lagrange velocity vectors at 25.1 seconds. See text for scale.

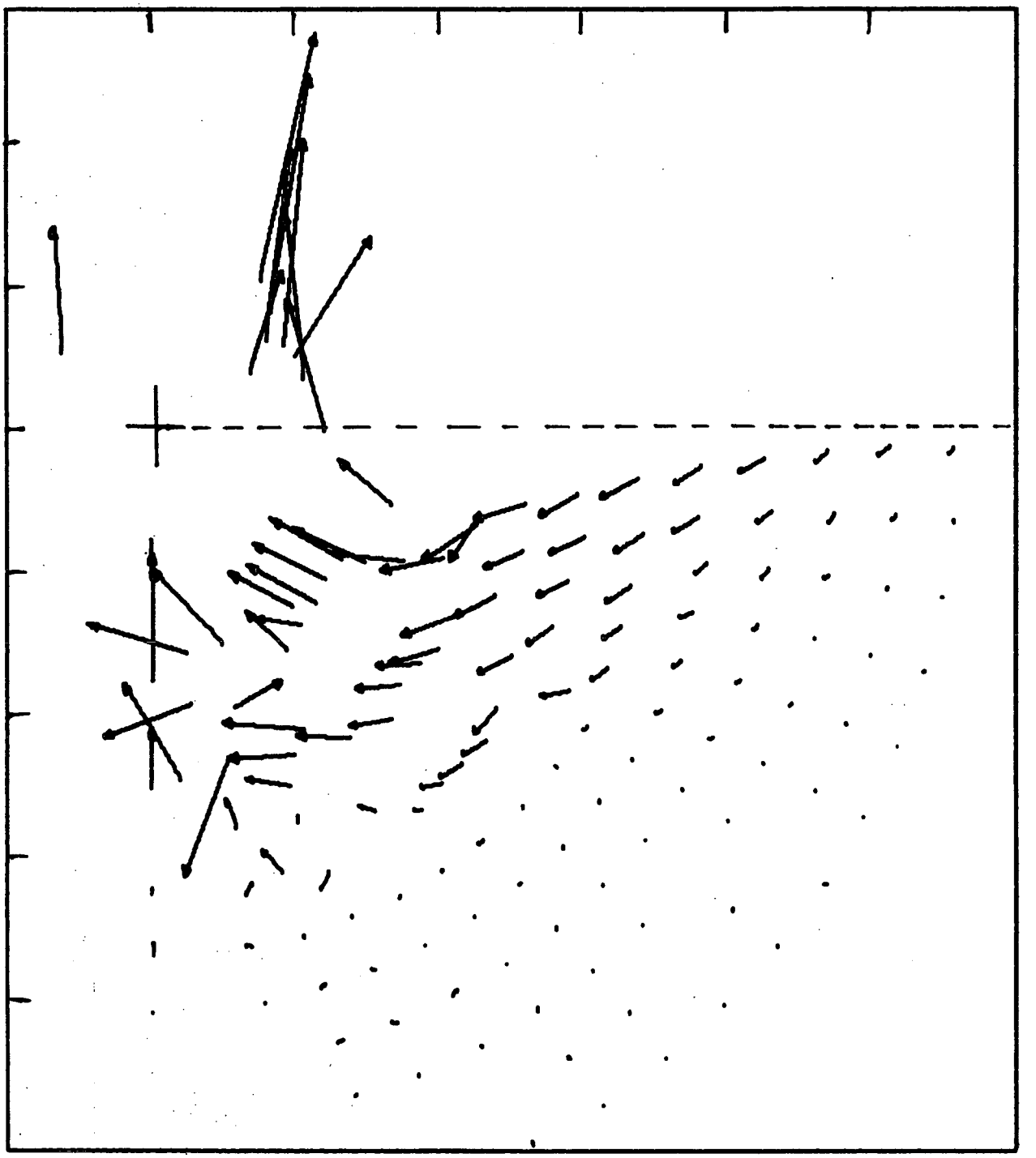

Figure 3.22 Close-in Lagrange velocity vectors at 29.9 seconds. See text for scale.

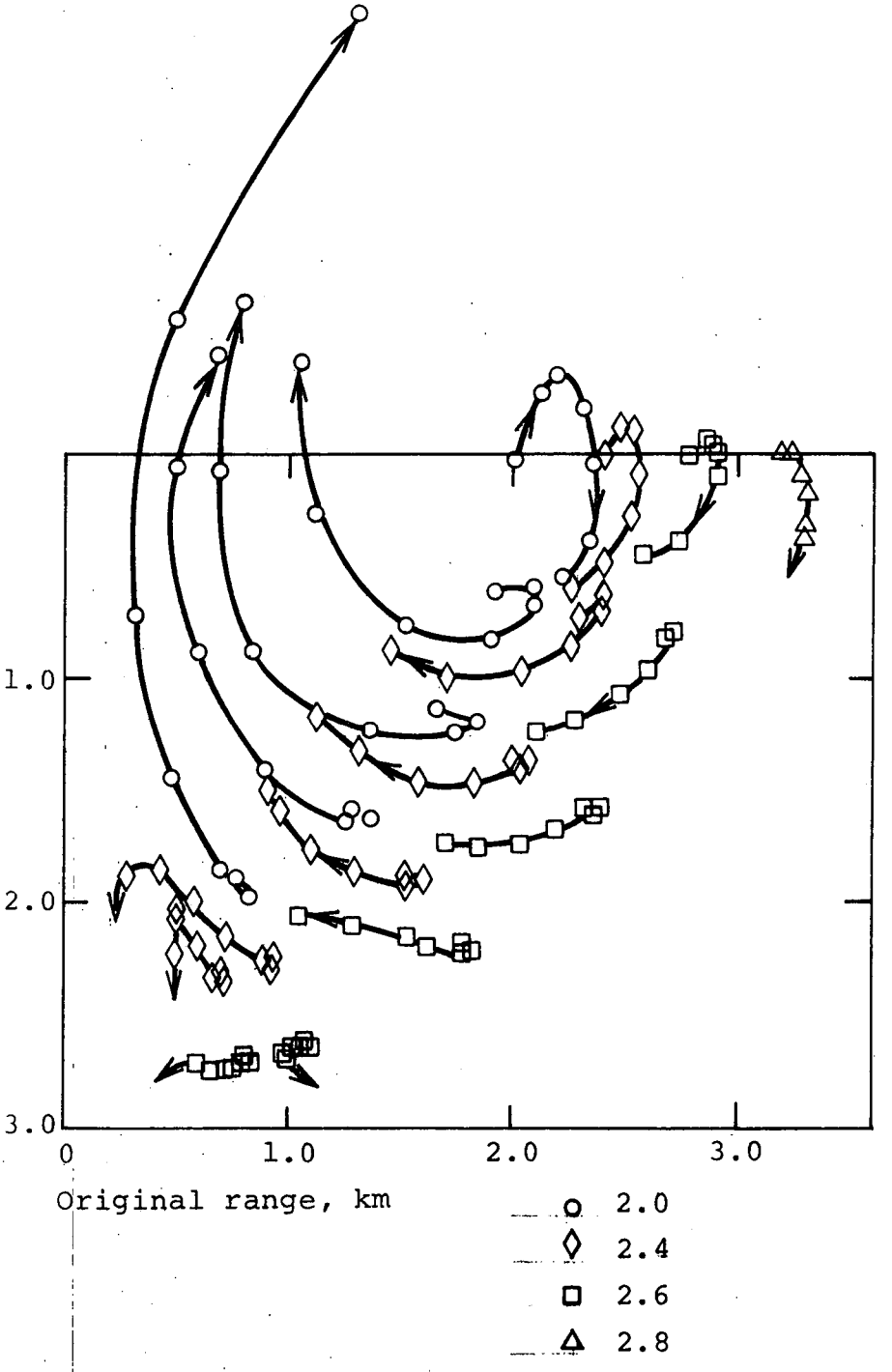

Figure 3.23 Trajectories of selected points to 30 seconds of path. Symbols are spaced by 5 seconds.

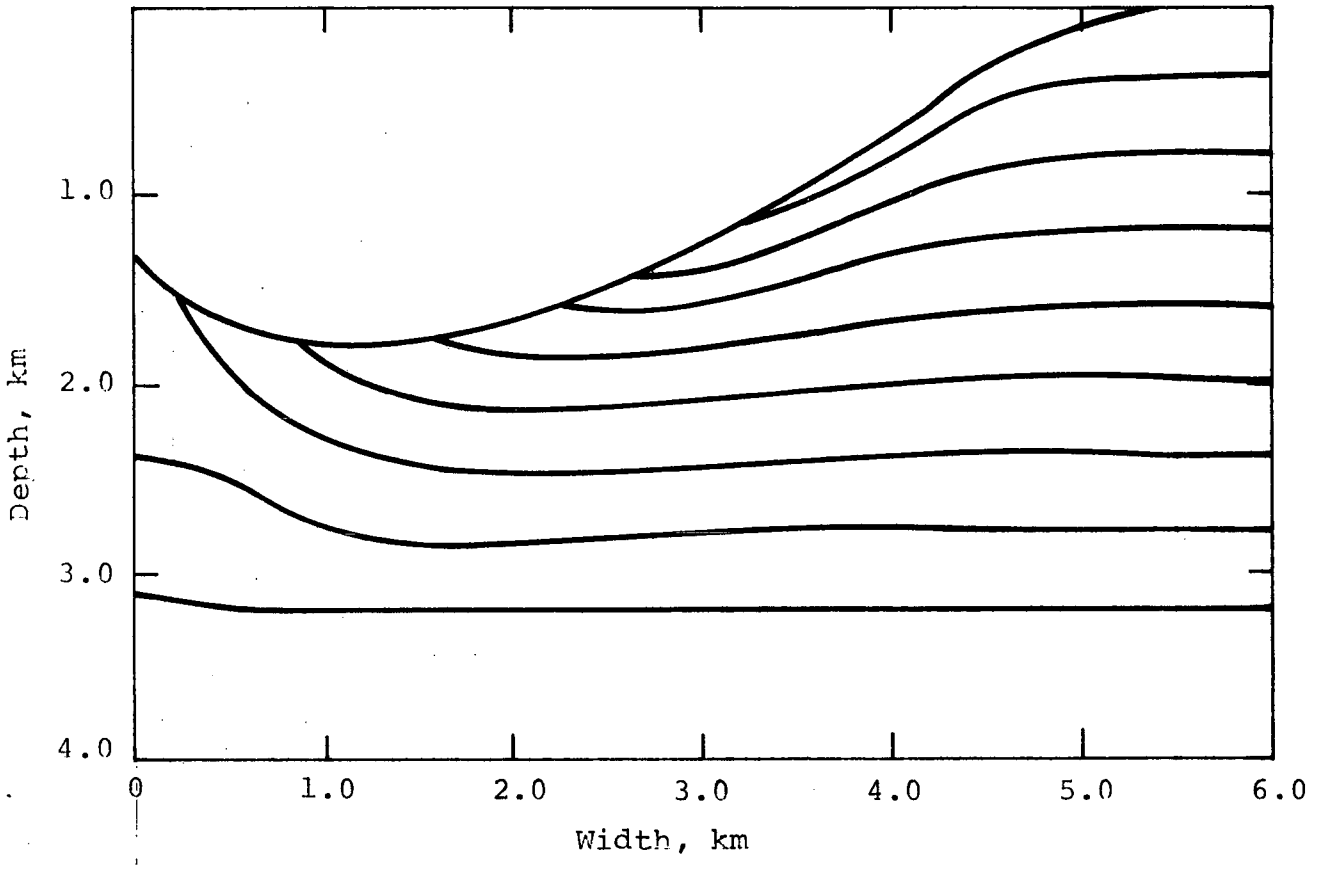

Figure 3.24 Final distortion of initially horizontal strata obtained by extrapolation. The crater shape is crudely estimated. Fall back is not estimated hence, apparent crater is not shown.

option of the ELK code. This would have quickly converged the solution to that of static equilibrium under the influence of gravity, producing an equilibrium crater. The application of this option would be meaningful if the jumbled earth material had a finite shear strength and the material was almost at rest. It was unfortunate that this new option was not available at the time that the calculation was started. Its existence would have been cause to preclude what is now regarded as an unfortunate choice for the strength model.

In spite of these retrospect regrets, the main objective was achieved. The Sierra Madera crytoexplosive structure can be entirely explained on the basis of meteoroid impact. The computed width and magnitude of the upthrust region, and the position and magnitude of the ring depression are in substantial agreement with the real structure.

SECTION 4
CONCLUSIONS AND RECOMMENDATIONS

4.1 LiMG PELLET-BASALT IMPACT CRATER

The compressive cratering phase of the pellet-basalt calculation was in good agreement with experiment and verifies that the code method and compressive material model were quite satisfactory. As previously noted, a comparison of the ejecta lip radius of Figure 2.10 and the radiograph of Figure 2.11 demonstrate that the violent compressive cratering process is being simulated quite well. Not noted earlier, the peak computed pressures shown in Figure 2.13 compare satisfactorily with the data for this experimental case. This can be verified by comparison to the appropriate data of Reference 1.

The tensile cracking phase of the cratering simulation was not as satisfactory. An original "reasonable" cracking model produced results which were at decided variance with the experiment. It was then necessary to discover and apply an unsubstantiated model based on volumetric strain energy. This latter model did predict the crater shape satisfactorily and to some extent the crack pattern beneath. It also predicted correctly the crater of a nuclear explosion over competent granite. It did not predict correctly the Mine Ore crater in weathered porous granite which indicates that this model is far from complete.

With the compressive model well established, any future investigation in this area should concentrate on tensile models, evaluated by the code method. The most expeditious way would be to make a restart tape at the end of the compressive phase. This would provide the initial condition for a series of inexpensive parametric calculations, each starting with the restart tape condition. In this way, a number of models could be evaluated with minimum computing costs. The crack propagation features described by Wilkins (Reference 9) are promising dynamic mechanisms and can be evaluated theoretically only by means of the dynamic code method.

4.2 SIERRA MADERA CONCLUSIONS

The Sierra Madera simulation did achieve its major objective in demonstrating that a meteoroid impact can account for all of the structural features evident in the Sierra Madera geologic structure. The inward-upward flow suggested by Wilshire et al. in Reference 10 did develop and produced a violent central upthrust surrounded by a ring depression much like the true structure. The computed magnitudes perhaps are slightly too small suggesting that the true impact energy was somewhat larger than the 1.2 megatons used to initiate the calculation. The total energy rather than the mass and velocity of the impacting particle determined the response because the release of the overburden by the excavation was the dominant driving force of the central uplift. The ring depression was a consequence of the surface mass subsiding and flowing inward. The vortex-like flow was confined to a surprisingly small volume of earth.

In retrospect, it would have been more accurate and decidedly more expedient to maintain a small shear strength and

real viscosity in the earth region that had been violently "jumbled." This would have resulted in a more accurate extrapolation to the final rest state. The static equilibrium option of ELK, now operational, could have been used to converge rapidly to a final crater shape as noted earlier.

A new option, tested and scheduled for completion in March 1971, would have been especially advantageous in saving computing costs. This new option introduces a finite element linear elastic grid to replace the plastic-elastic grid beyond the radius where the earth response is purely elastic. The zones in this new grid compute a factor of 80 faster than the finite difference zones of their plastic-elastic counterparts. Thus, one would be able to achieve an excellent gain in computing efficiency and be able to achieve the final time without having the large-size zones as were used in the Sierra Madera simulation. These large zones, required to restrict computer costs, somewhat compromised the spatial resolution of the Sierra Madera calculation.

With this last option, it would have been economically feasible to continue the problem beyond 30 seconds. In which case, zones with ballistic trajectories that clear the crater region would be eliminated, after bookkeeping their mass and trajectory. This elimination of these high velocity zones would have avoided the subsequent zone tangling problem and allowed the problem to compute to an unquestionably adequate final time.

REFERENCES

1. D. W. Baum, "Cratering Studies: Lunar Surface Materials," Physics International Company PIFR-118, May 1969.

2. V. G. Gregson, T. J. Ahrens and C. F. Peterson, "Dynamic Properties of Rocks," Stanford Research Institute, AFCRL-63-662.

3. A. H. Jones, W. M. Isbell, F. H. Shipman, R. D. Perkins, S. J. Green, and C. J. Maiden, "Material Properties Measurement for Selected Materials," General Motors Technical Center MSL-68-9 (1968).

4. J. C. Jaeger, "Elasticity, Fracture and Flow," John Wiley and Sons, New York, 1964.

5. N. M. Short, "Effects of Shock Pressures From a Nuclear Explosion on Mechanical and Optical Properties of Granodiorite," J. Geophys. Res., 77, 4, 1195 (1966).

6. W. F. Brace, B. W. Paulding, J. R. C. Scholz, "Dilatancy in the Fracture of Crystalline Rocks," J. Geophys. Res., 71, 16, 3939 (1966).

7. Brown, et al., "The Effect of Pressure on the Strength of Rocks From Two Prospective Routes for an Interoceanic Canal," University of Utah, Army Contract DACW-17-69-C-0030, May 1969.

8. Wilkins, et al., "Light Armor," UCRL-71817. University of California Radiation Laboratory, Livermore, Calif., July 23, 1969.

9. Swanson, S., "Development of Constitutive Equations for Rock," Ph.D. Thesis, Department of Mechanical Engineering, University of Utah, December 1969.

REFERENCES (cont.)

10. H. G. Wilshire, Keith A. Howard, "Structural Pattern in Central Uplifts of Cryptoexplosion Structures as Typified by Sierra Madera," Science, Vol. 162, October 1968.

11. Keith A. Howard, Terry W. Offield, "Shatter Cones at Sierra Madera, Texas," Science, Vol. 162, October 1968.

12. H. G. Wilshire, T. W. Offield, K. A. Howard, and D. Cummings, "Geology of the Sierra Madera Cryptoexplosion Structure," Pecos County, Texas, U. S. Geologic Survey Professional Paper 599-H, in press.

13. Physics International Company Final Report PIFR-21-072, DASA-2360.

14. Physics International Company Final Report, "ELK 40, Prediction Calculation of Ground Motion for Distant Plain, Event 6," DASA-2471, May 1970.

15. Physics International Company Final Report, "Prediction Calculations of MINE UNDER and MINE ORE," DASA-2526, November 1970.

APPENDIX A

EQUATION-OF-STATE MODEL

The equation-of-state model is given the name TAM Equation-of-State. The block diagram of Figure A-1 is included to facilitate the mathematical definition. The following reference statements apply:

ρ_o = reference density, g/cm^3

ρ = stressed state density in successive cycles of computation (g/cm^3)

$V = \rho_o/\rho$ = relative volume

E/ρ_o = internal energy (10^{12} ergs/g)

$\mu = (1/V) - 1$

Region 1. (If no solid-solid phase transition)

$$P_1 = A\mu\delta_1 + B\mu^2\delta_2 + \underbrace{\left[a + \frac{b}{\frac{EV^2}{E_o} + 1}\right] E/V}_{\text{Rock or Soil}} + \underbrace{cE/V}_{\text{steam}}$$

where:

$$\delta_1 = 1 \text{ if } \mu > \left(\frac{1}{HVP} - 1\right)$$

$$\delta_1 = \frac{1}{\mu}\left(\frac{1}{HVP} - 1\right) \text{ otherwise}$$

$$\delta_2 = 1 \text{ if } \mu > 0$$

$$\delta_2 = 0 \text{ otherwise}$$

if solid-solid reversible phase transition is desired, it acts only on the $A\mu$ term of P_1. The method is as follows:

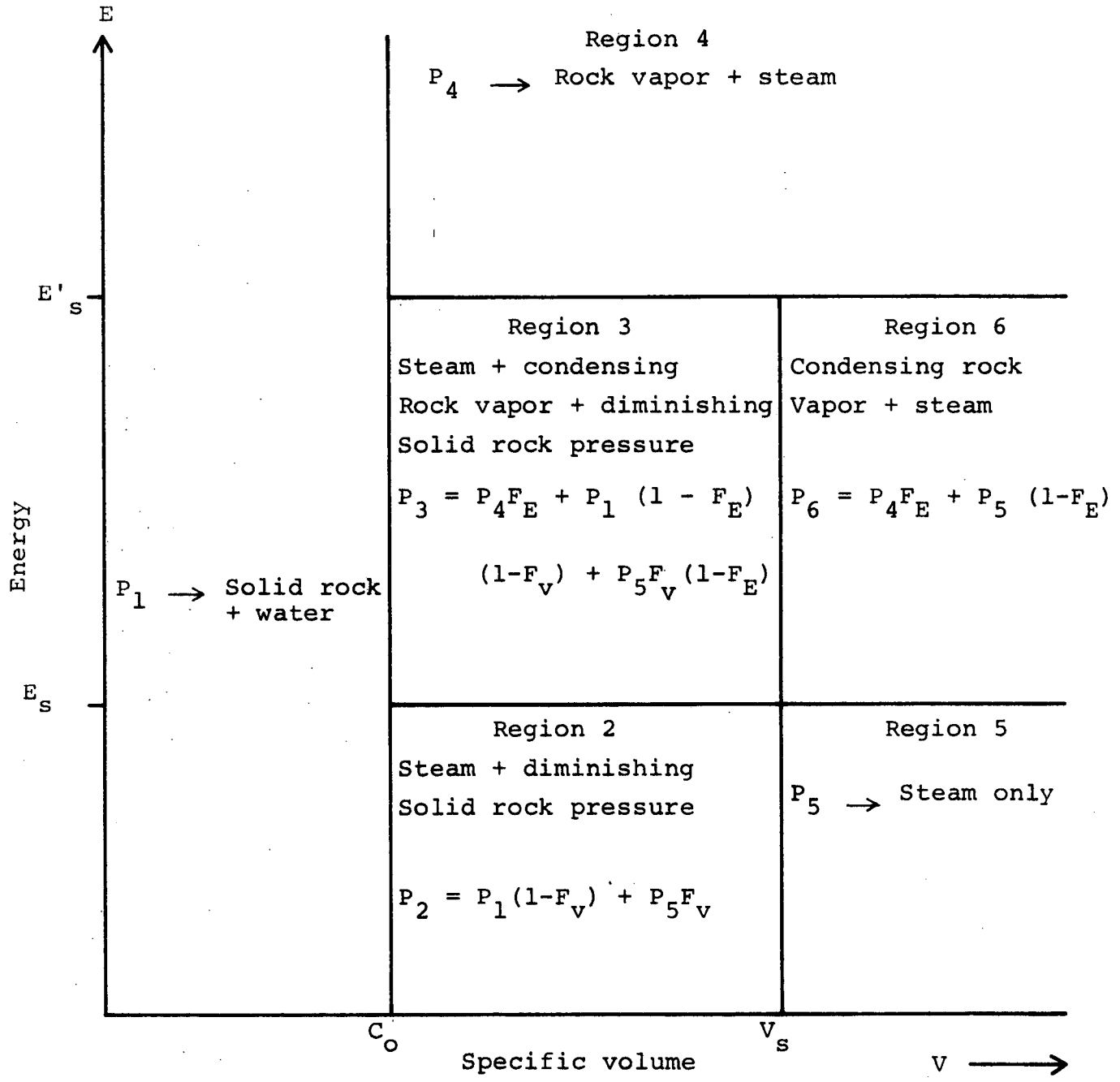

Figure A-1 TAM equation-of-state regions.

7729

$A\mu = A\ (1/V - 1)$ is replaced with $A\ (1/[V + \chi] - 1)$ where χ varies from 0 to C_3 in the following fashion:

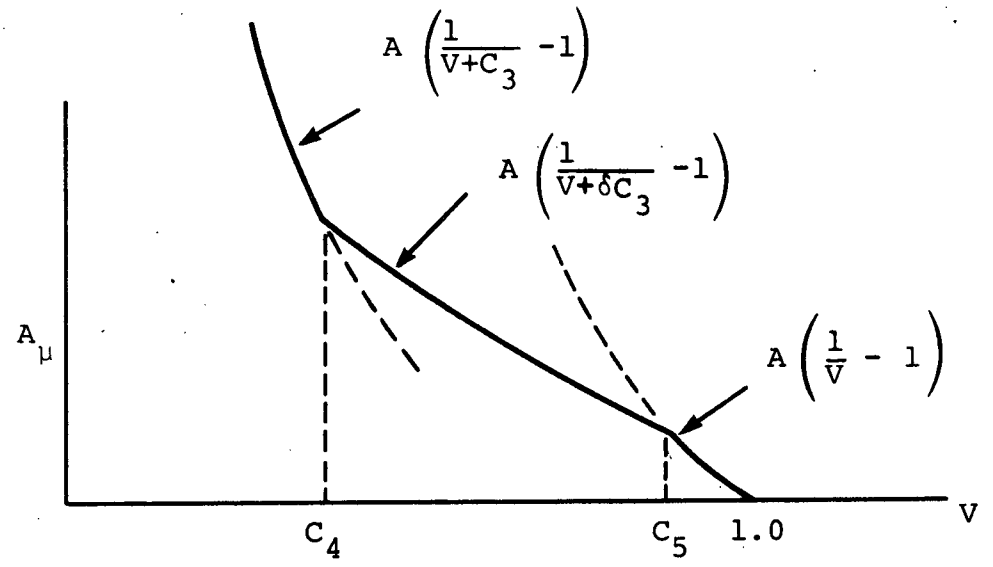

where

$$\chi = \delta C_3 \text{ and}$$

$$\delta = (C_5 - V)/(C_5 - C_4)$$

Recall that only the A term is involved in this model. The values of C_3, C_4 and C_5 are then found by trial and error by using the complete expression for P_1 in the fit of Hugoniot data.

Region 4.

$$P_4 = \underbrace{A\, e^{-5(V-1)} \cdot e^{-5(V-1)^2} + a + \frac{be^{-5(V-1)^2}}{\frac{EV^2}{E_o} + 1}}_{\text{rock vapor}} E/V + C\ E/V_{\text{steam}}$$

Regions 2, 3, and 6 are volume and/or energy weighted mixtures of regions 1, 4, and 5. The weighting factors are

$$FV = (V - C_o)/(V_s - C_o)$$

$$FE = (E - E_s)/(E'_s - E_s)$$

where Figure A-1 shows the weighting method.

The parameters used for the basalt and Sierra Madera media are given in Tables A-1 and A-2 respectively. The application of these parameters using the TAM equation of state gives pressure expressed in megabars.

TABLE A-1
BASALT EQUATION-OF-STATE PARAMETERS

ρ_o	=	2.82
A	=	0.492
B	=	0.2
a	=	0.5
b	=	1.3
c	=	0
E_o	=	0.43
E_s	=	0.094
E'_s	=	0.483
C_3	=	$C_4 = C_5 = 0$
C_o	=	1.0
V_s	=	10^{10}
HVP	=	1.3

TABLE A-2

SIERRA MADERA MATERIAL
EQUATION-OF-STATE PARAMETERS

$\rho_o = 2.7$
$A = 0.4$
$B = 0.6$
$a = 0.5$
$b = 0.6$
$c = 0$
$E_o = 0.72$
$E_s = 0.0675$
$E'_s = 0.378$
$C_3 = C_4 = C_5 = 0$
$C_o = 1.0$
$V_s = 10^{10}$
$HVP = 1.0$

APPENDIX B

TIME HISTORIES

TABLE B-1

ORIGINAL POSITIONS OF SELECTED POINTS

Column	Slant Range (Km)
1	2.
2	2.4
3	2.8
4	3.2

Row	Degrees from Vertical Axis	Row	Degrees from vertical Axis
1	0.	9	50.625
2	11.25	10	56.25
3	16.875	11	61.875
4	22.5	12	67.5
5	28.125	13	73.125
6	33.75	14	78.75
7	39.375	15	84.375
8	45	16	90

Time units are sec.
Vertical units are cm/ sec.
Displacement units are cm.
(+) positive direction is downward for x.
(+) positive direction is outward for y.

The graphs included in this appendix show vertical and horizontal velocities and displacements of selected points. The key to the original position is given in Table B-1.

Because of the rather course zoning and the resulting "noise" no one graph should be given full confidence.

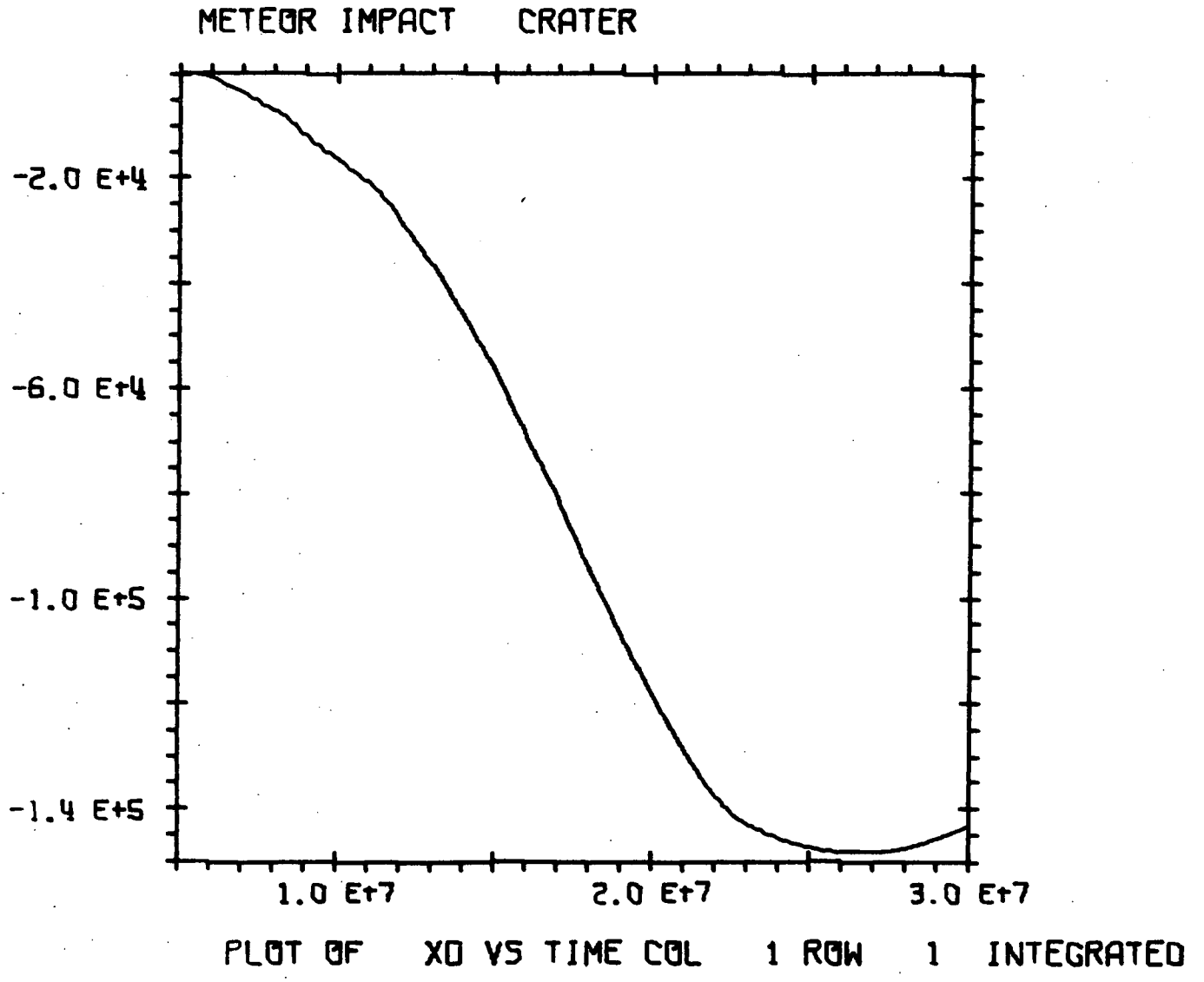
METEOR IMPACT CRATER
-2.0 E+4
-6.0 E+4
-1.0 E+5
-1.4 E+5
1.0 E+7
2.0 E+7
3.0 E+7
PLOT OF XO VS TIME COL 1 ROW 1 INTEGRATED

Figure B-1

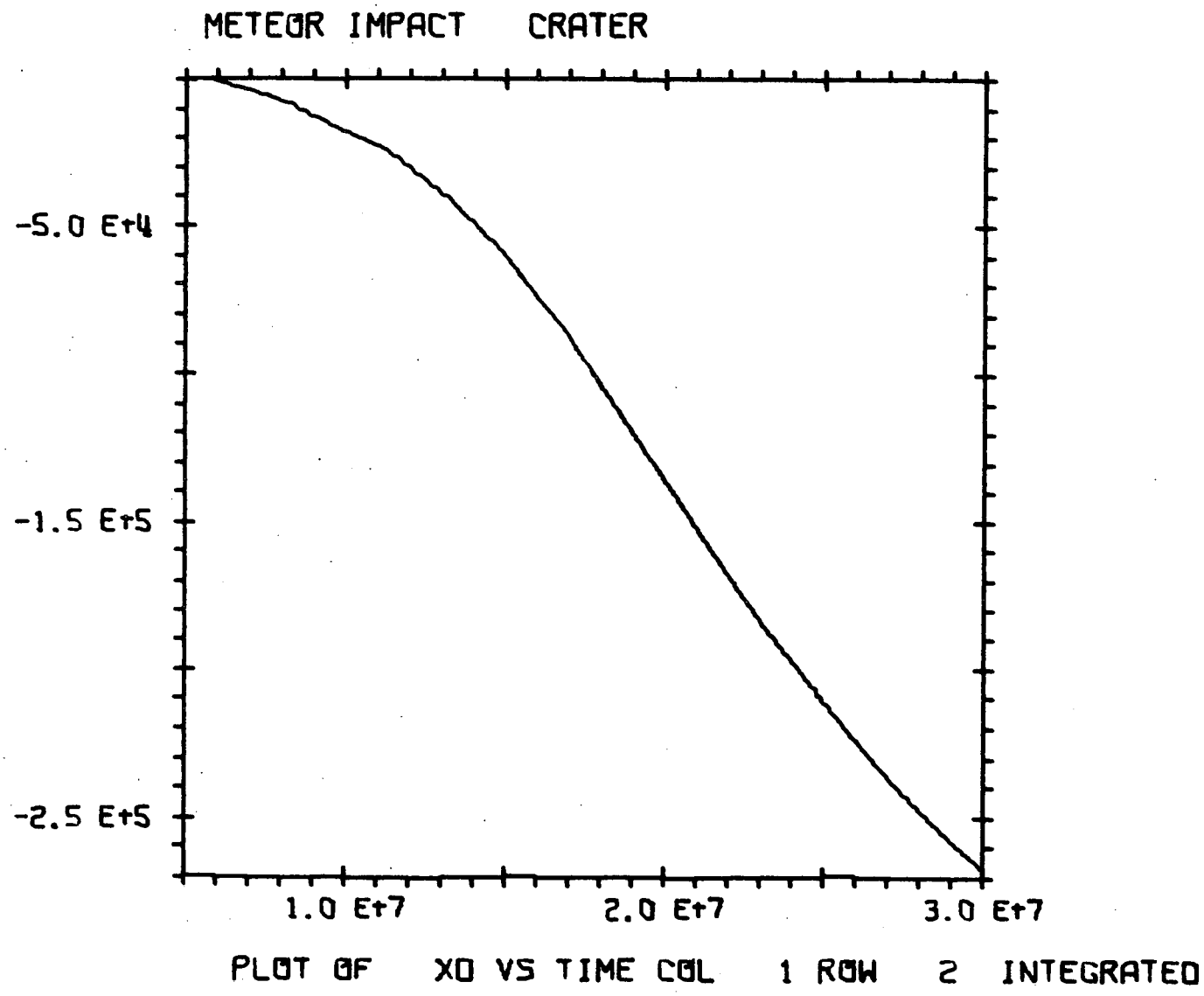
METEOR IMPACT CRATER
-5.0 E+4
-1.5 E+5
-2.5 E+5
1.0 E+7
2.0 E+7
3.0 E+7
PLOT OF XO VS TIME COL 1 ROW 2 INTEGRATED

Figure B-2

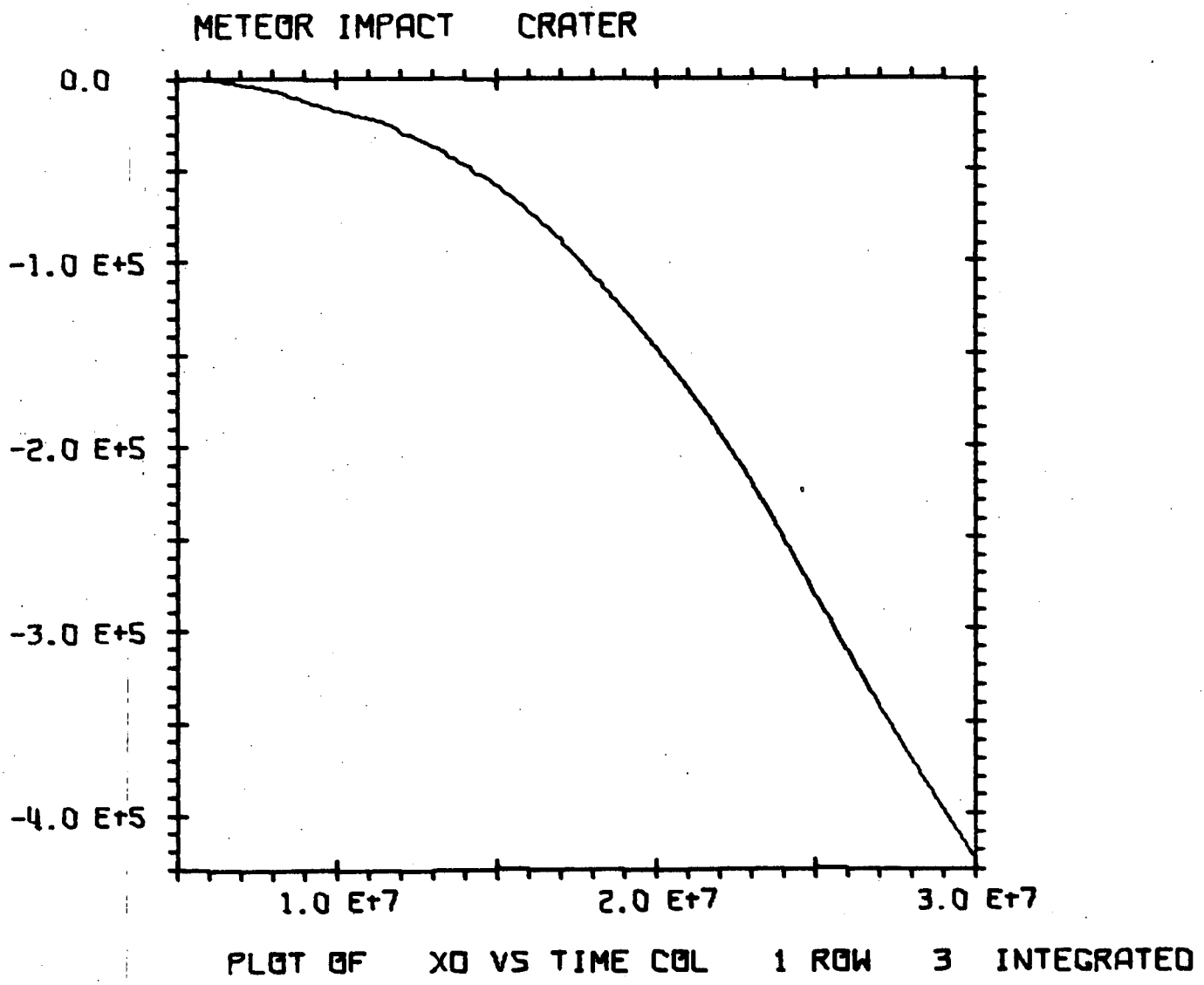
METEOR IMPACT CRATER
0.0
-1.0 E+5
-2.0 E+5
-3.0 E+5
-4.0 E+5
1.0 E+7
2.0 E+7
3.0 E+7
PLOT OF XO VS TIME COL 1 ROW 3 INTEGRATED

Figure B-3

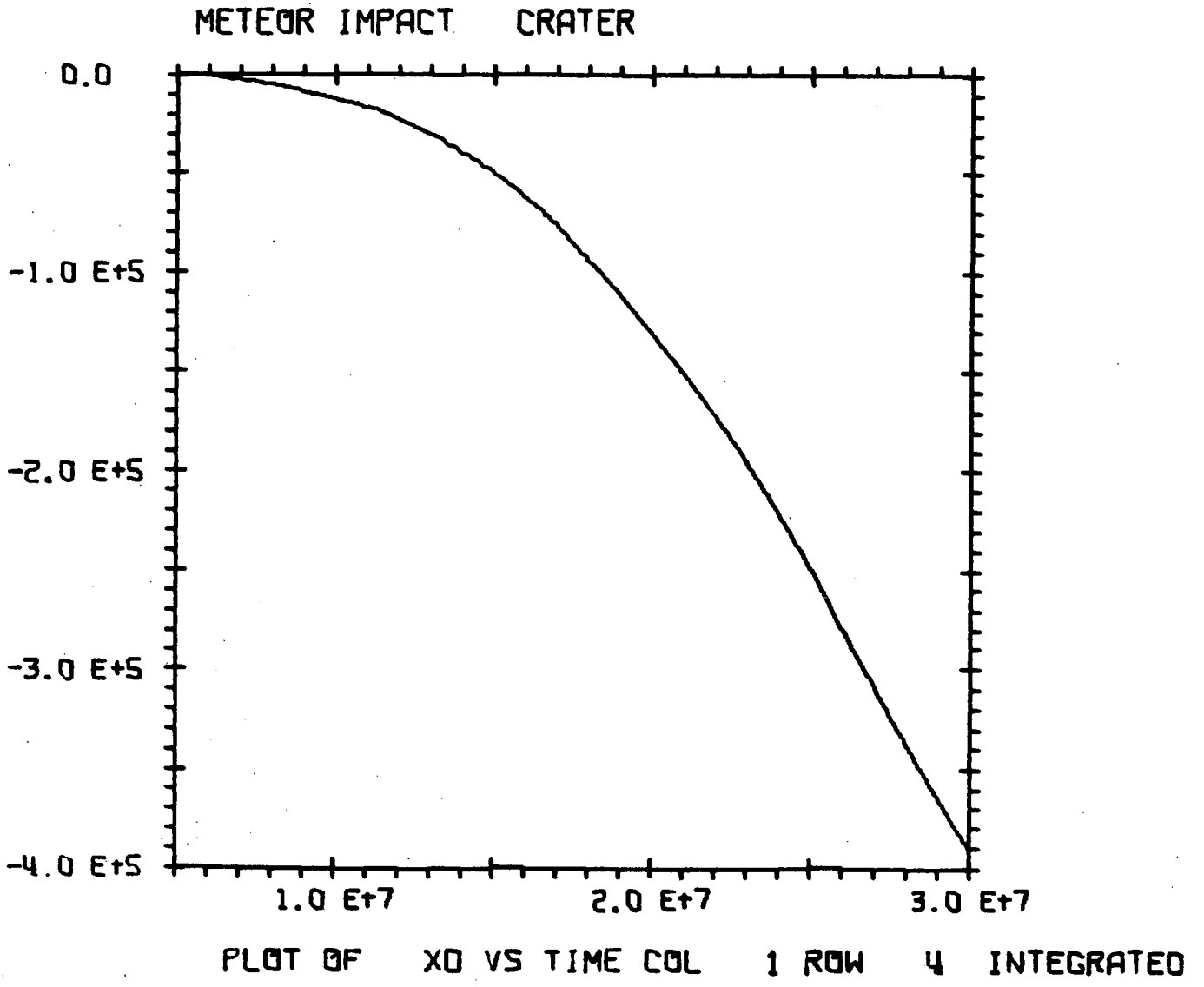
METEOR IMPACT CRATER
0.0
-1.0 E+5
-2.0 E+5
-3.0 E+5
-4.0 E+5
1.0 E+7
2.0 E+7
3.0 E+7
PLOT OF XO VS TIME COL 1 ROW 4 INTEGRATED

Figure B-4

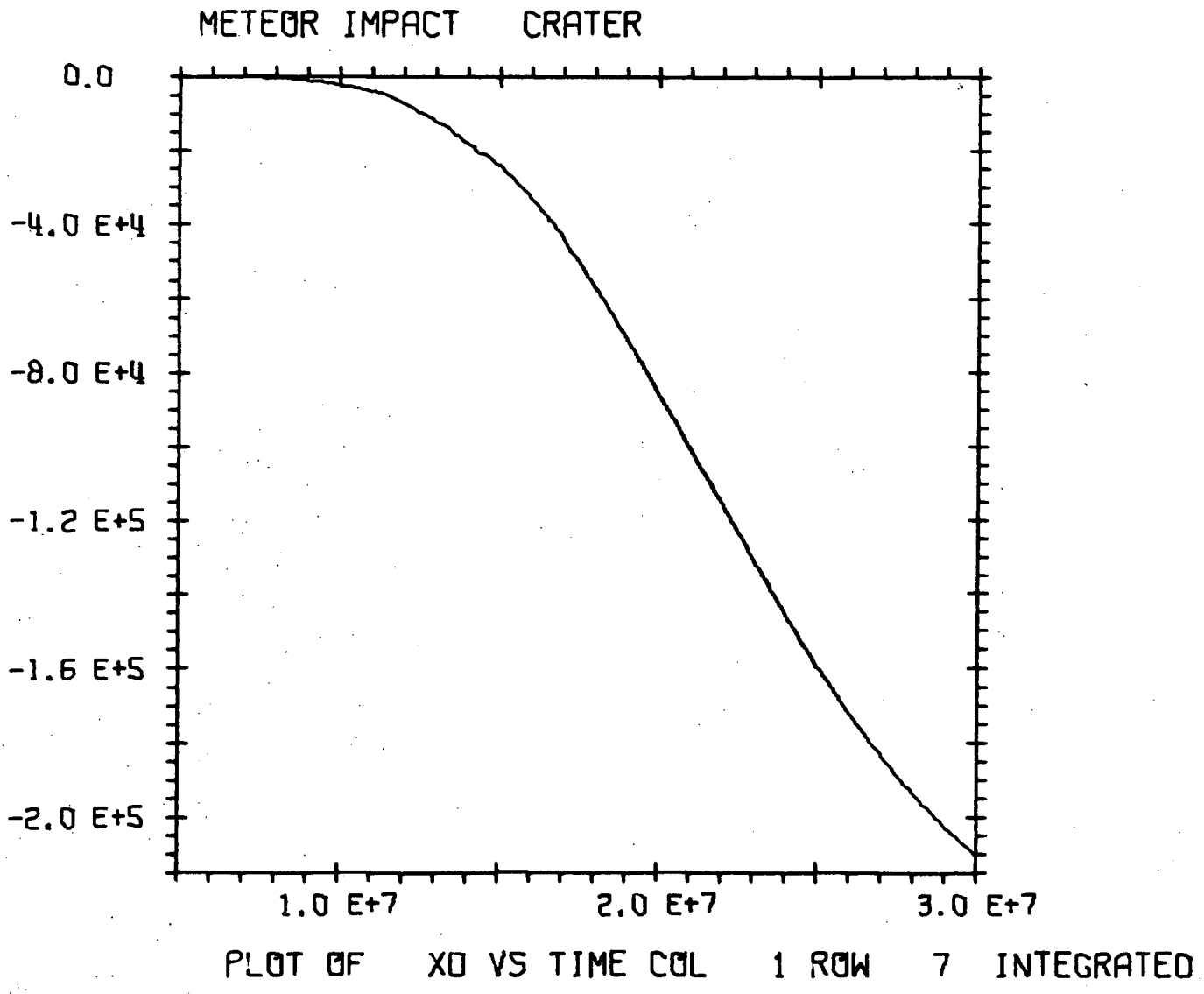
METEOR IMPACT CRATER
0.0
-4.0 E+4
-8.0 E+4
-1.2 E+5
-1.6 E+5
-2.0 E+5
1.0 E+7
2.0 E+7
3.0 E+7
PLOT OF XO VS TIME COL 1 ROW 7 INTEGRATED

Figure B-5

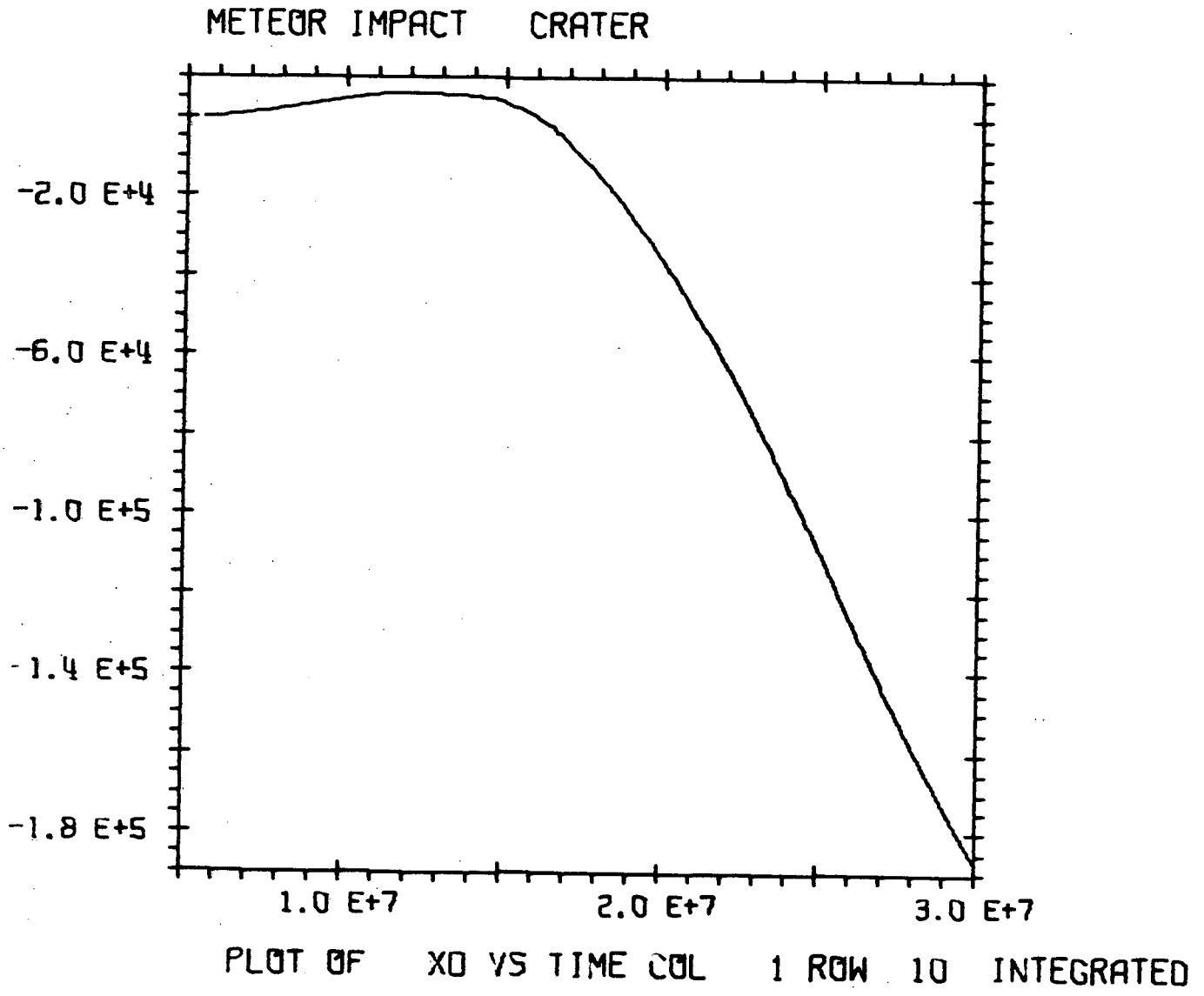
METEOR IMPACT CRATER
-2.0 E+4
-6.0 E+4
-1.0 E+5
-1.4 E+5
-1.8 E+5
1.0 E+7
2.0 E+7
3.0 E+7
PLOT OF XO VS TIME COL 1 ROW 10 INTEGRATED

Figure B-6

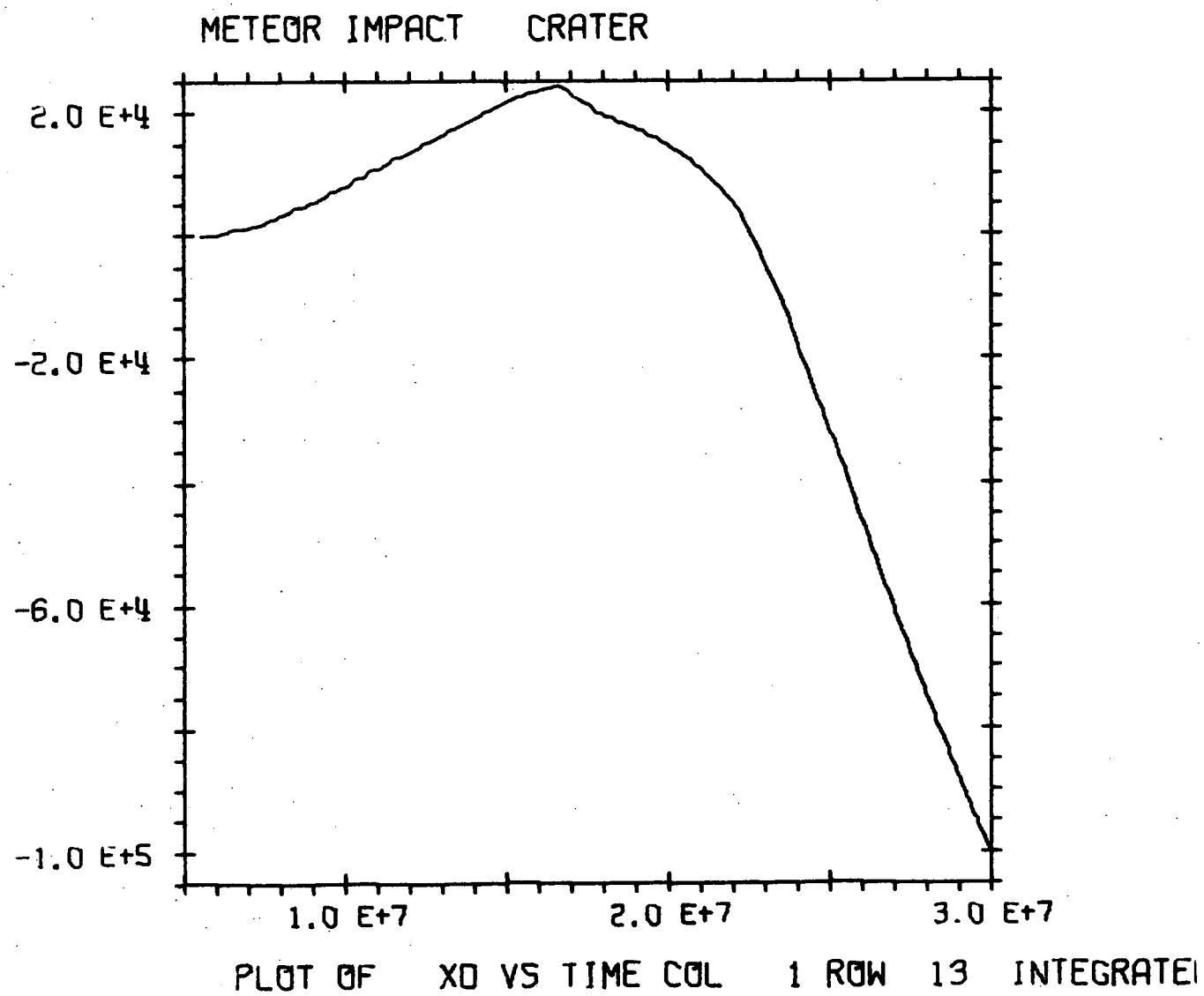
METEOR IMPACT CRATER
2.0 E+4
-2.0 E+4
-6.0 E+4
-1.0 E+5
1.0 E+7
2.0 E+7
3.0 E+7
PLOT OF XO VS TIME COL 1 ROW 13 INTEGRATE

Figure B-7

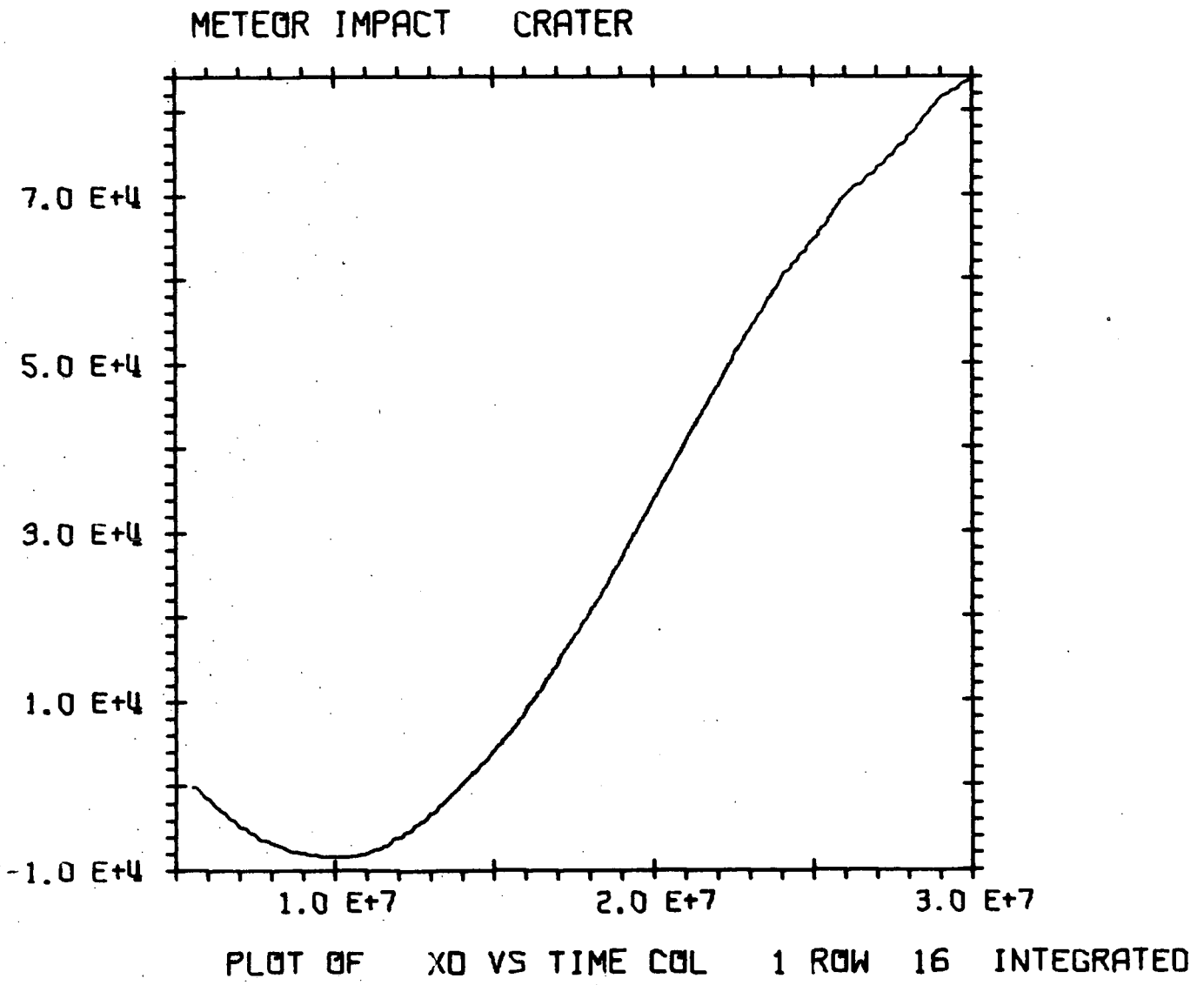
METEOR IMPACT CRATER
7.0 E+4
5.0 E+4
3.0 E+4
1.0 E+4
-1.0 E+4
1.0 E+7
2.0 E+7
3.0 E+7
PLOT OF XO VS TIME COL 1 ROW 16 INTEGRATED

Figure B-8

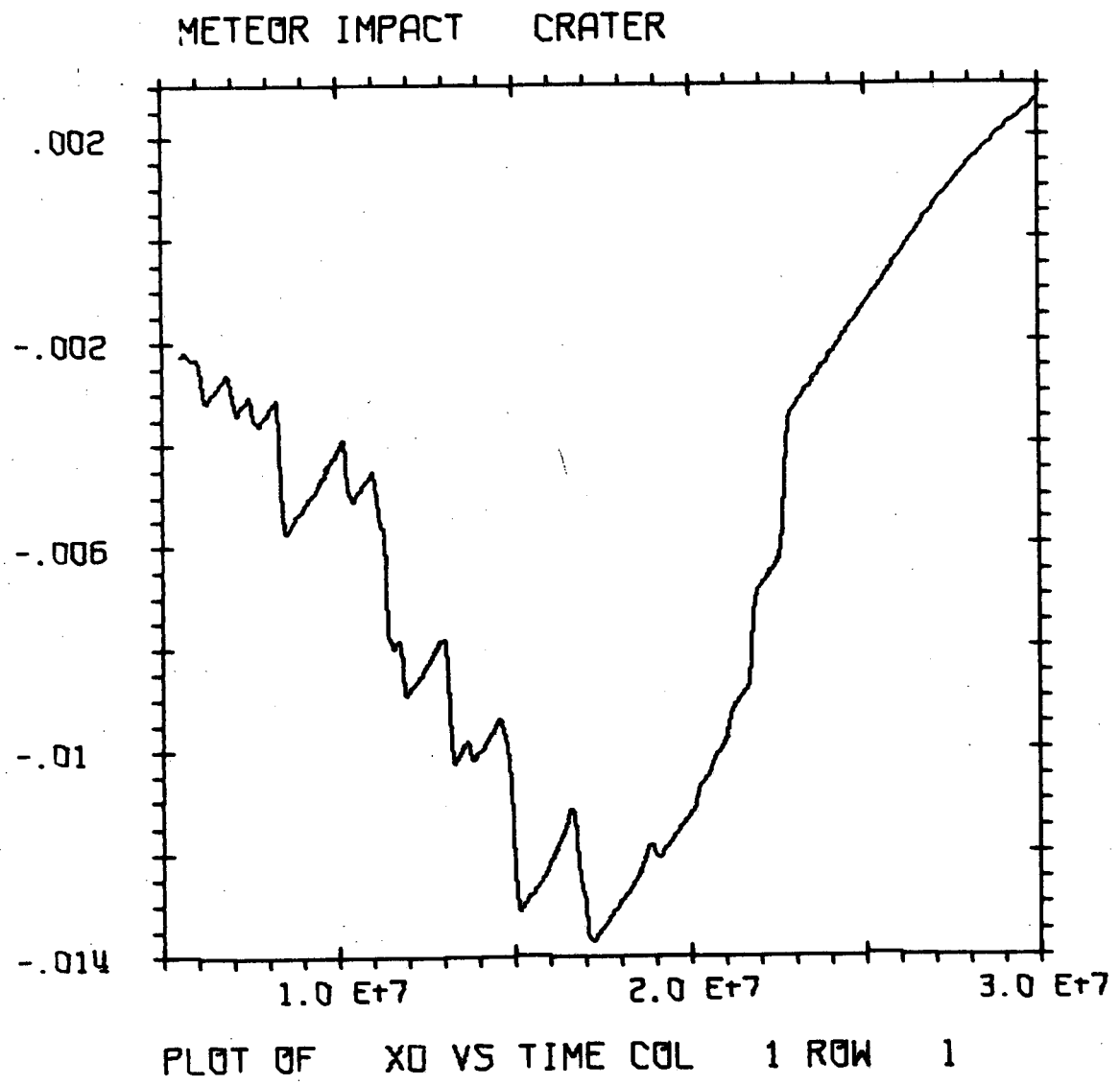
METEOR IMPACT CRATER
.002
-.002
-.006
-.01
-.014
1.0 E+7
2.0 E+7
3.0 E+7
PLOT OF XO VS TIME COL 1 ROW 1

Figure B-9

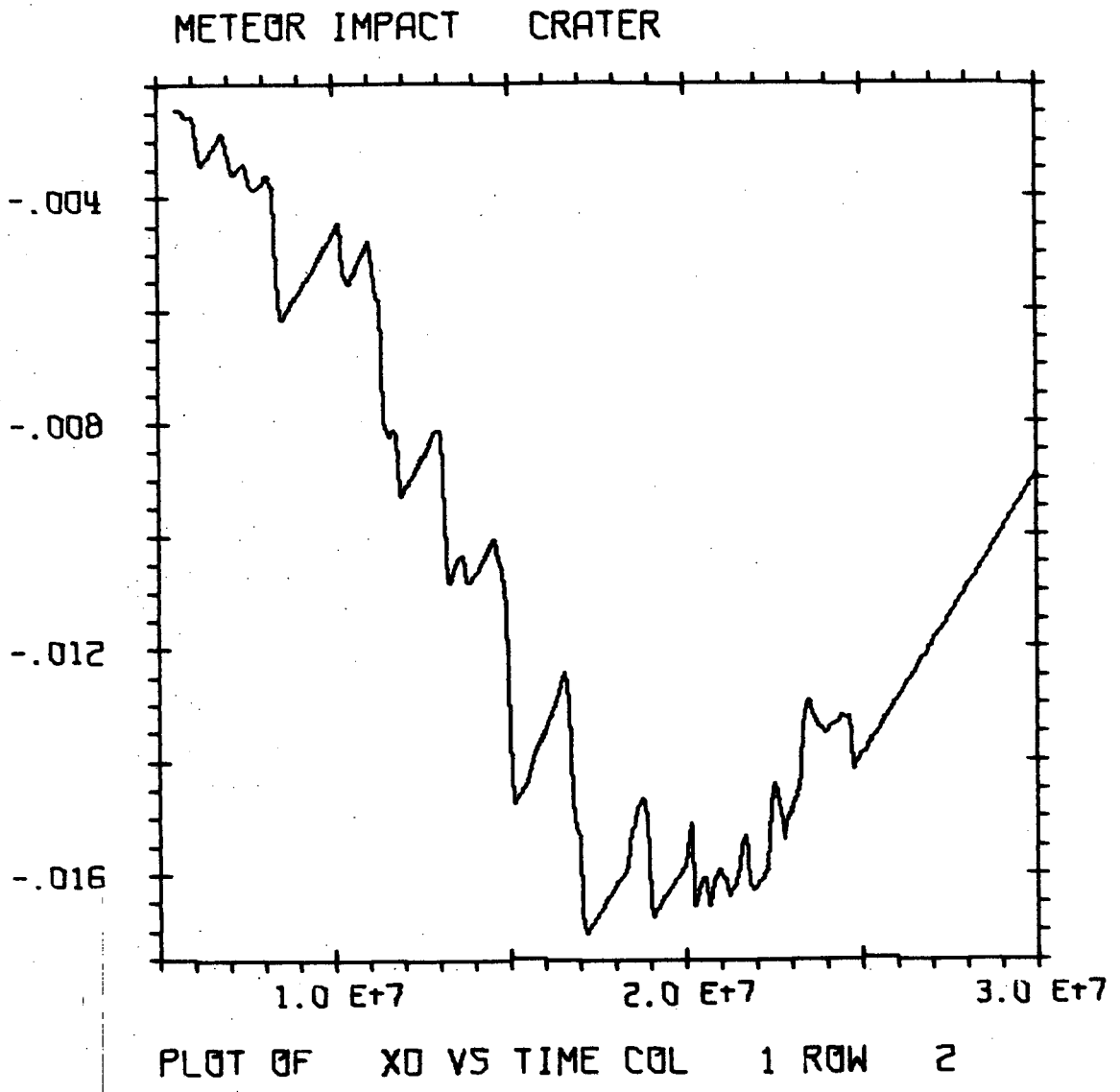
METEOR IMPACT CRATER
-.004
-.008
-.012
-.016
1.0 E+7
2.0 E+7
3.0 E+7
PLOT OF XO VS TIME COL 1 ROW 2

Figure B-10

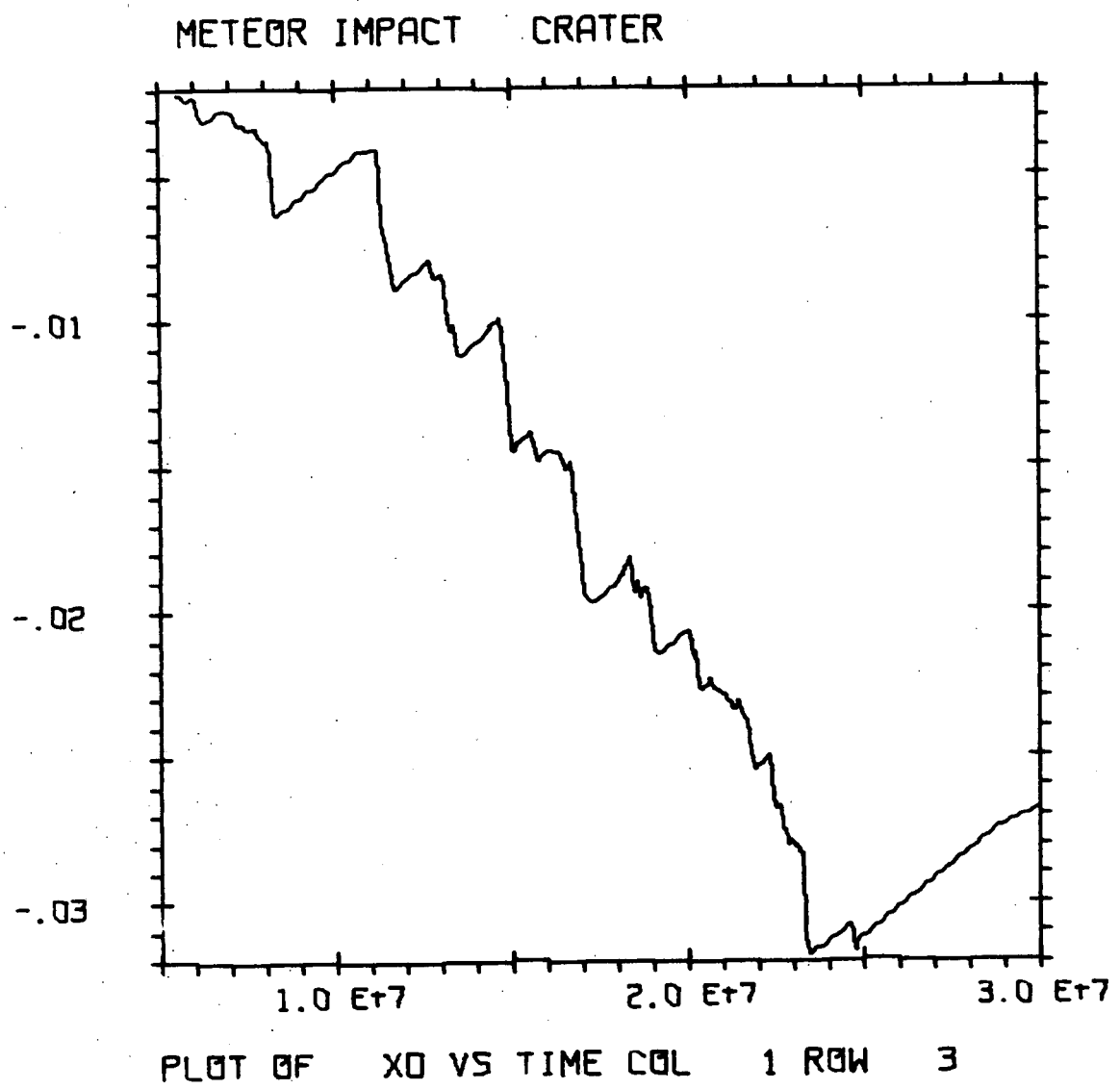
METEOR IMPACT CRATER
-.01
-.02
-.03
1.0 E+7
2.0 E+7
3.0 E+7
PLOT OF XO VS TIME COL 1 ROW 3

Figure B-11

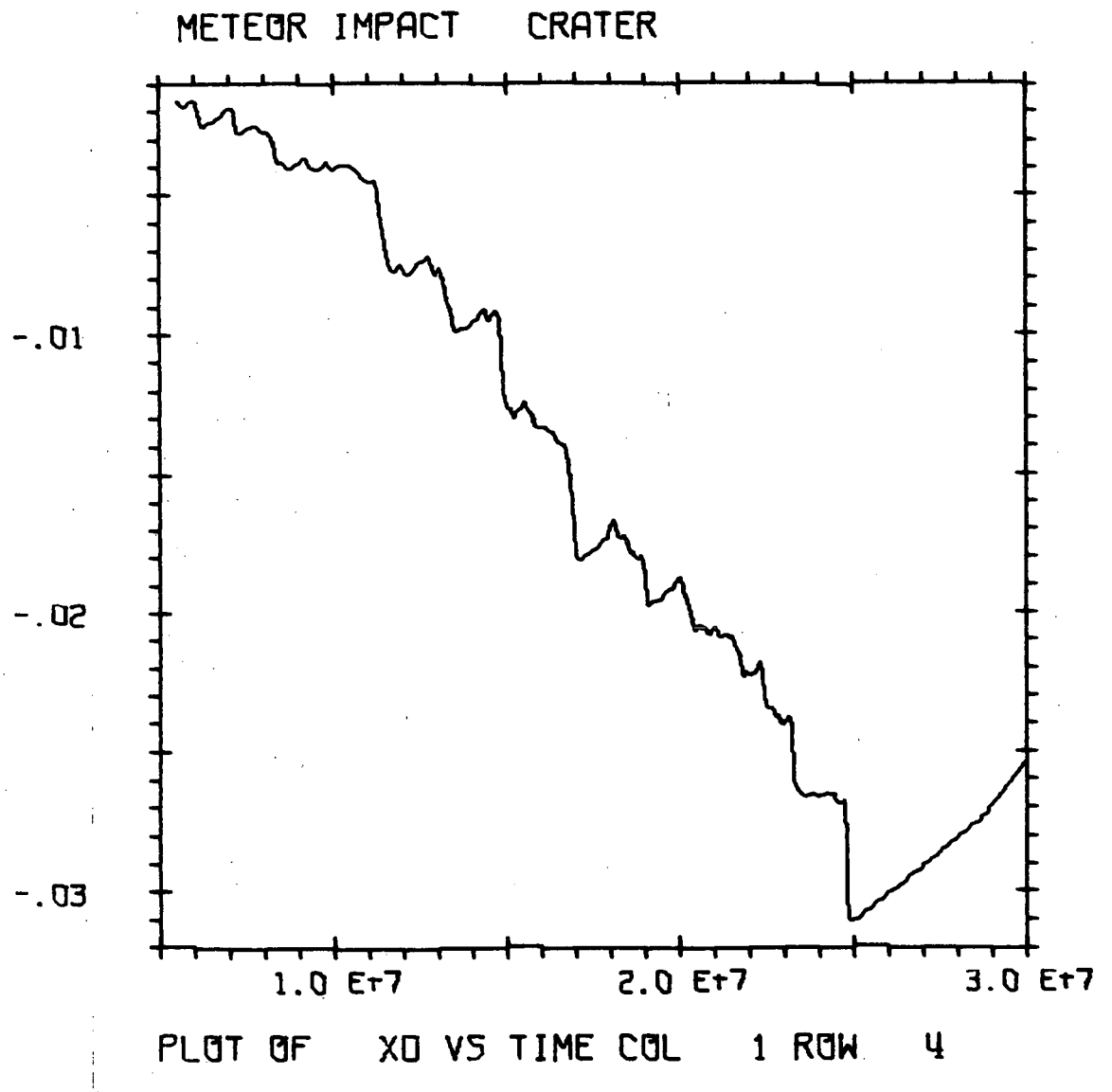
METEOR IMPACT CRATER
-.01
-.02
-.03
1.0 E+7
2.0 E+7
3.0 E+7
PLOT OF XO VS TIME COL 1 ROW 4

Figure B-12

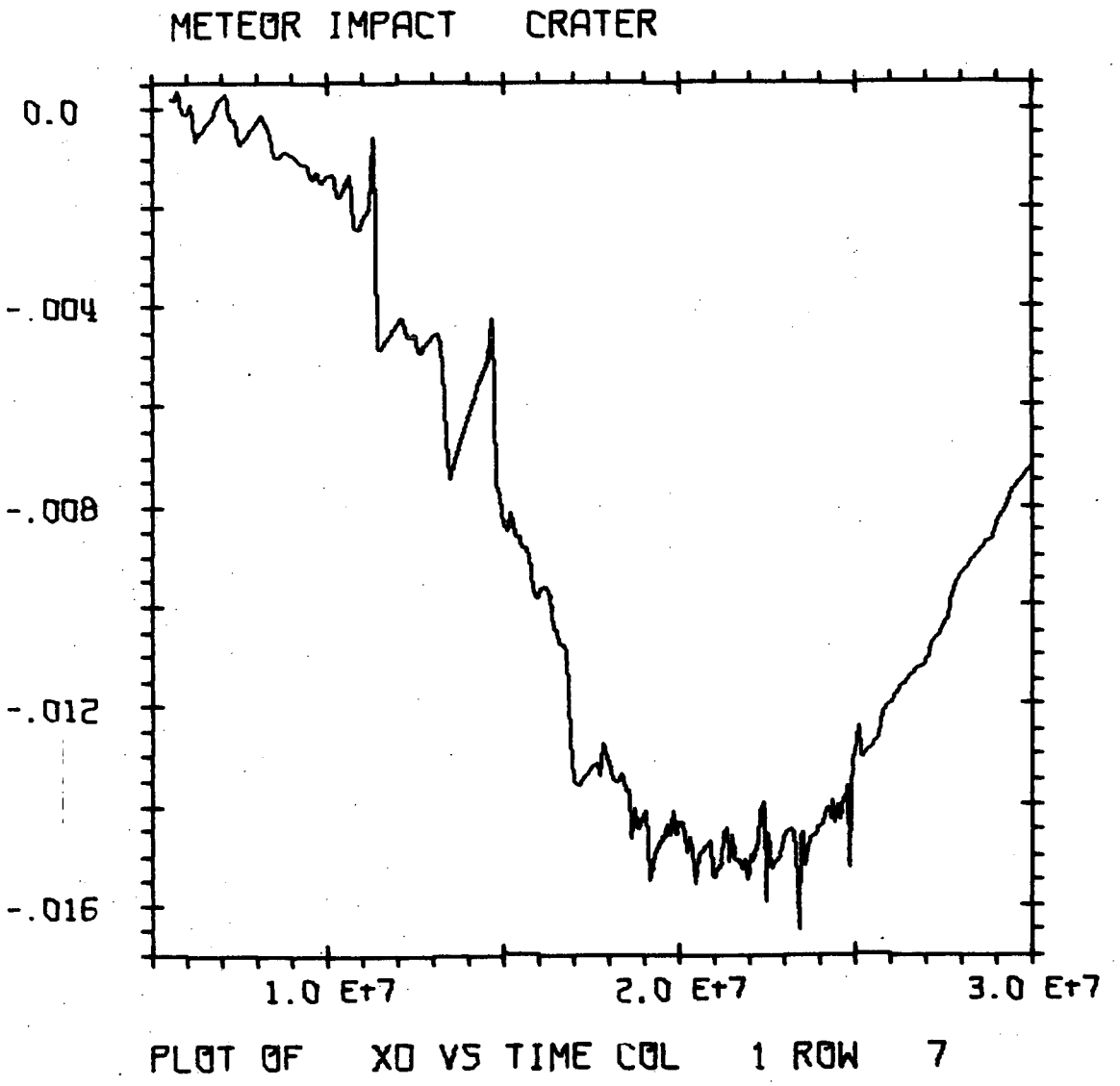
METEOR IMPACT CRATER
0.0
-.004
-.008
-.012
-.016
1.0 E+7
2.0 E+7
3.0 E+7
PLOT OF XO VS TIME COL 1 ROW 7

Figure B-13

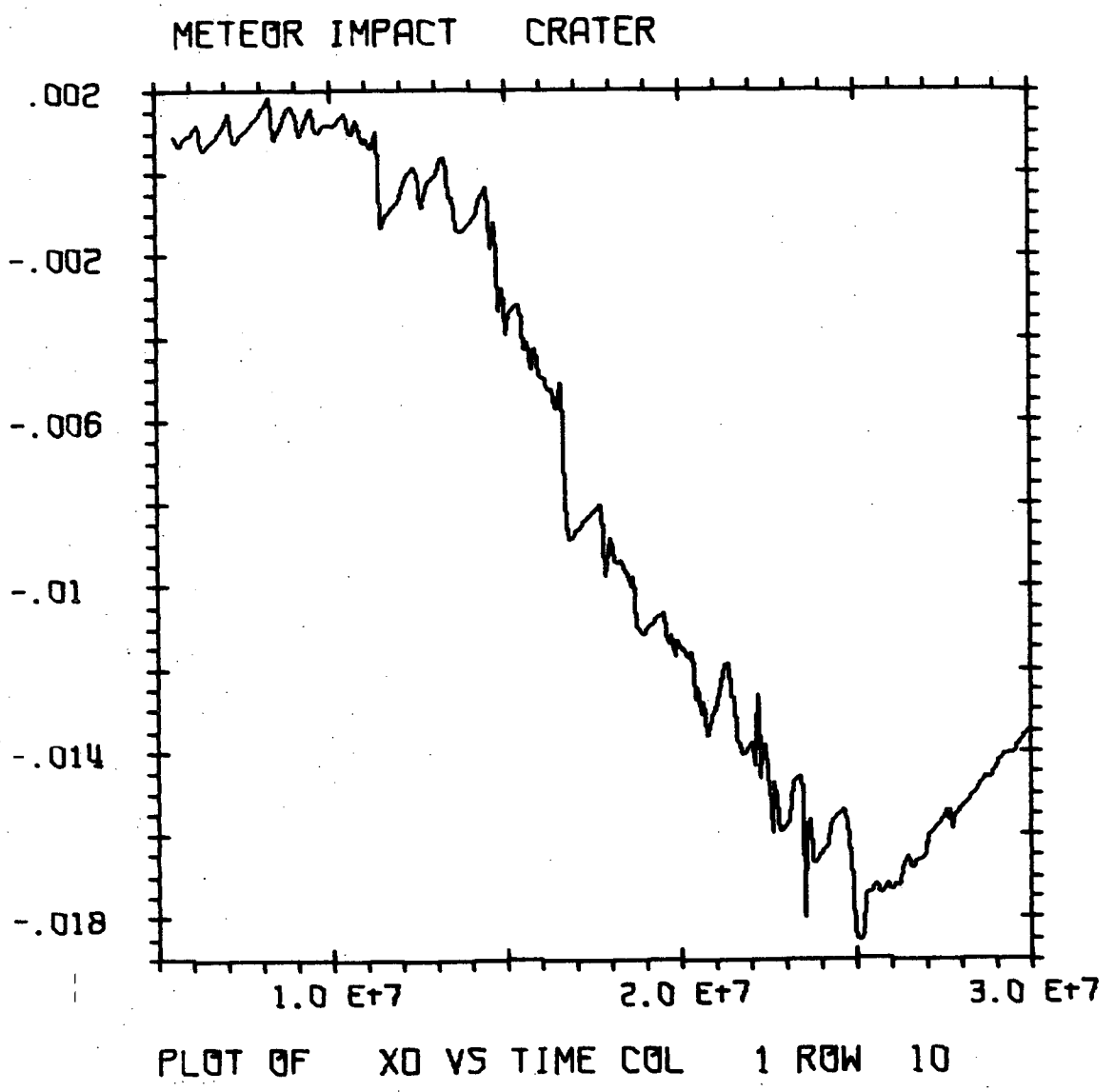
METEOR IMPACT CRATER
.002
-.002
-.006
-.01
-.014
-.018
1.0 E+7
2.0 E+7
3.0 E+7
PLOT OF XO VS TIME COL 1 ROW 10

Figure B-14

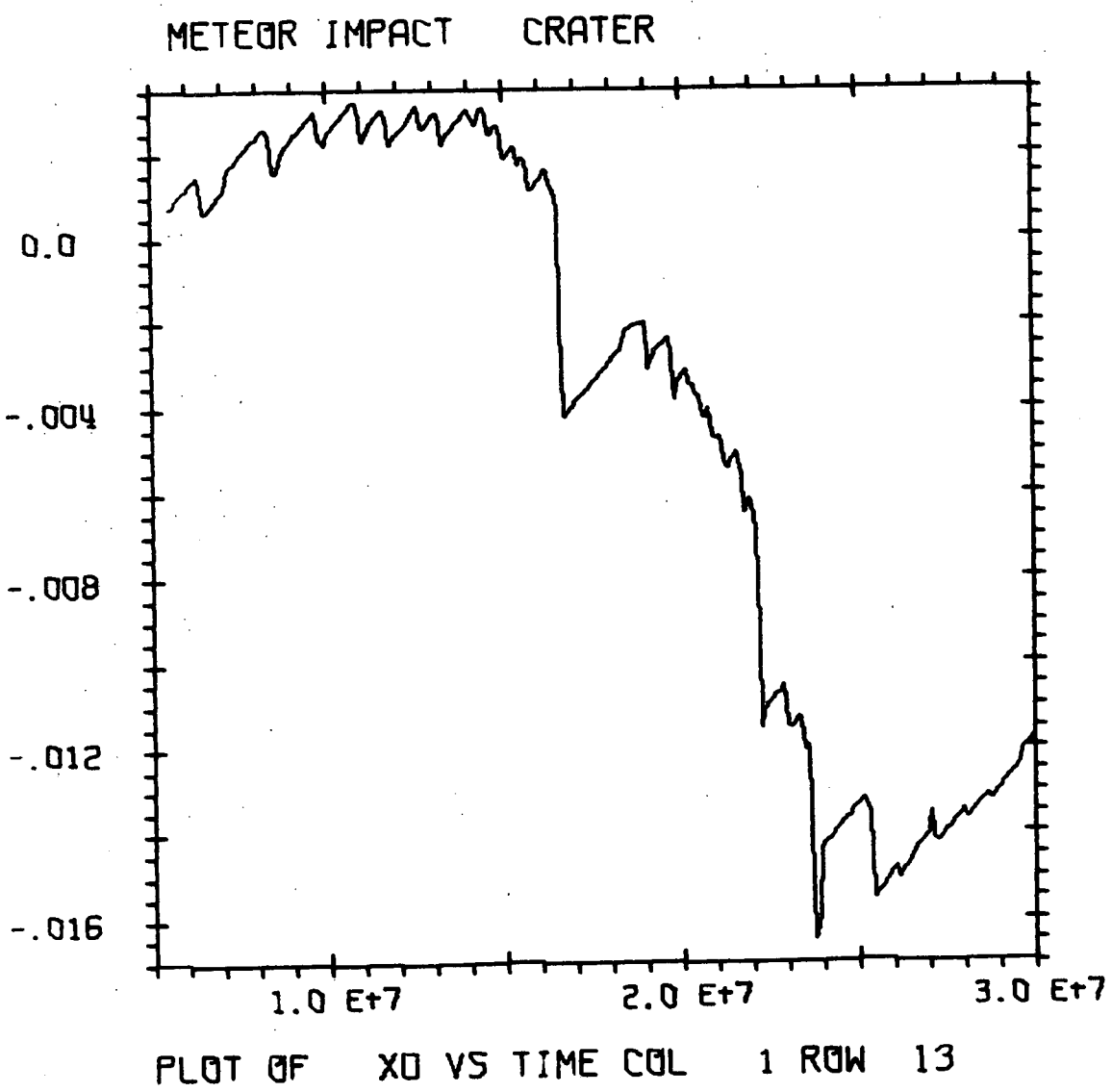
METEOR IMPACT CRATER
0.0
-.004
-.008
-.012
-.016
1.0 E+7
2.0 E+7
3.0 E+7
PLOT OF XO VS TIME COL 1 ROW 13

Figure B-15

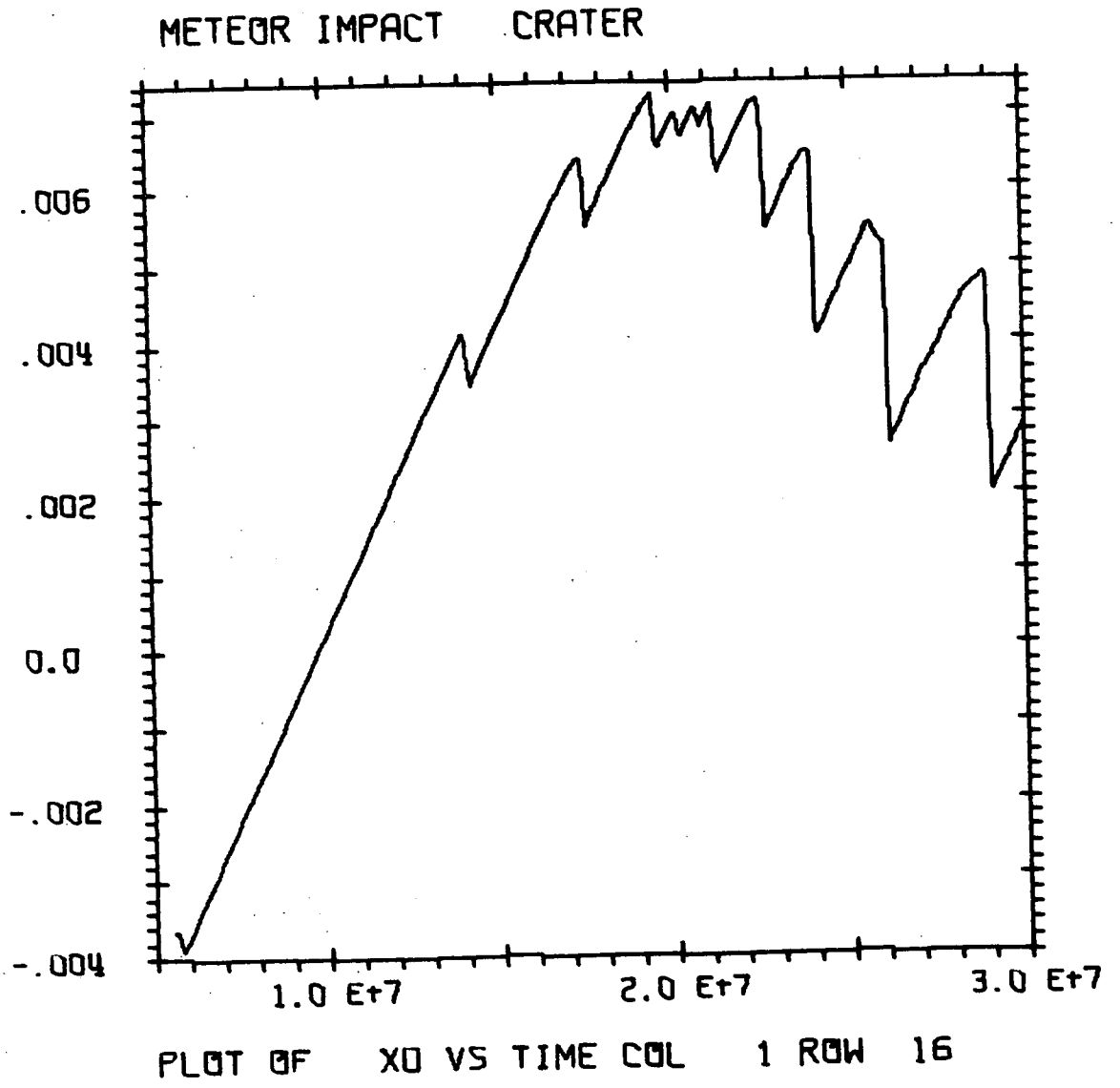
METEOR IMPACT CRATER
.006
.004
.002
0.0
-.002
-.004
1.0 E+7
2.0 E+7
3.0 E+7
PLOT OF XO VS TIME COL 1 ROW 16

Figure B-16

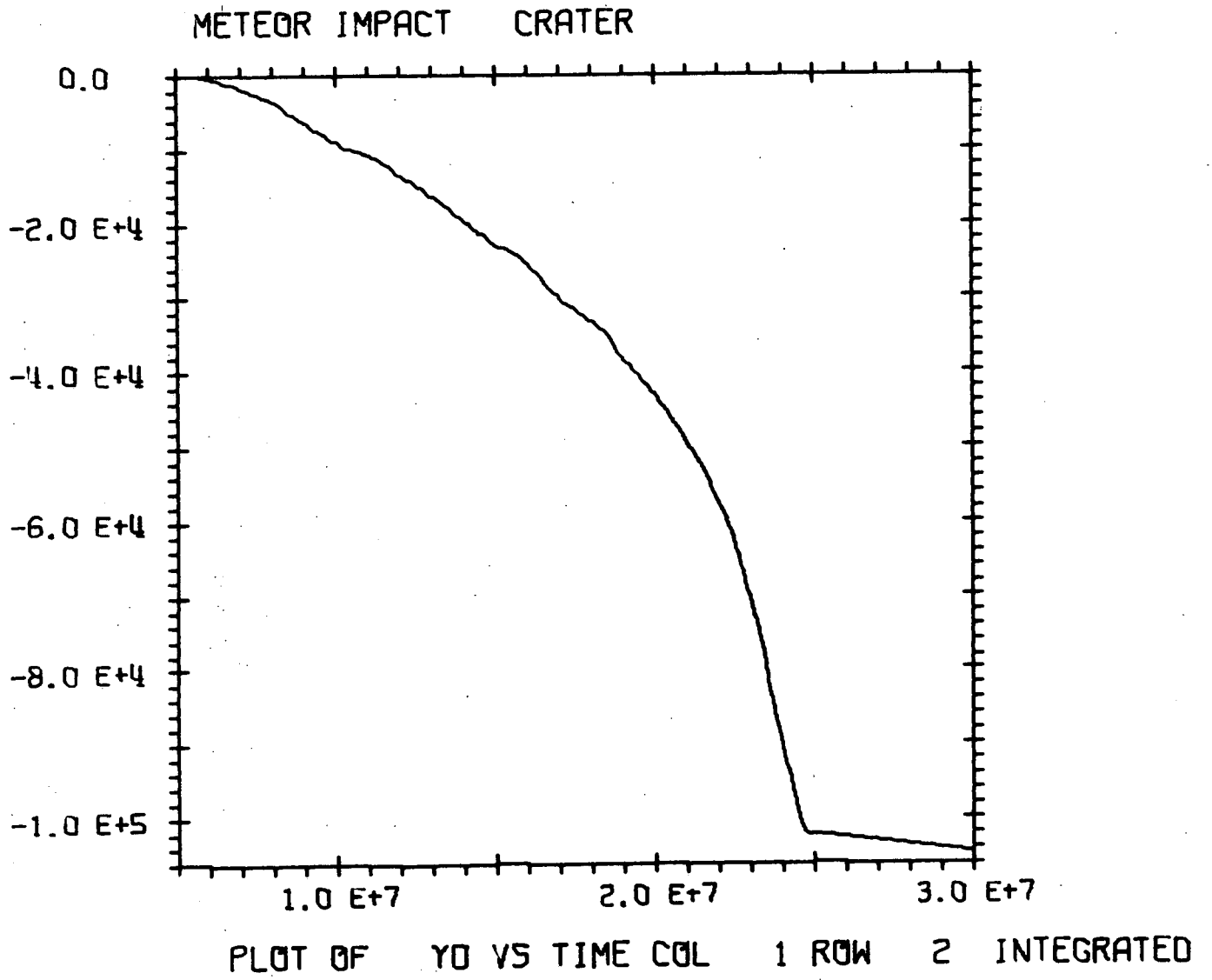
METEOR IMPACT CRATER
0.0
-2.0 E+4
-4.0 E+4
-6.0 E+4
-8.0 E+4
-1.0 E+5
1.0 E+7
2.0 E+7
3.0 E+7
PLOT OF YO VS TIME COL 1 ROW 2 INTEGRATED

Figure B-17

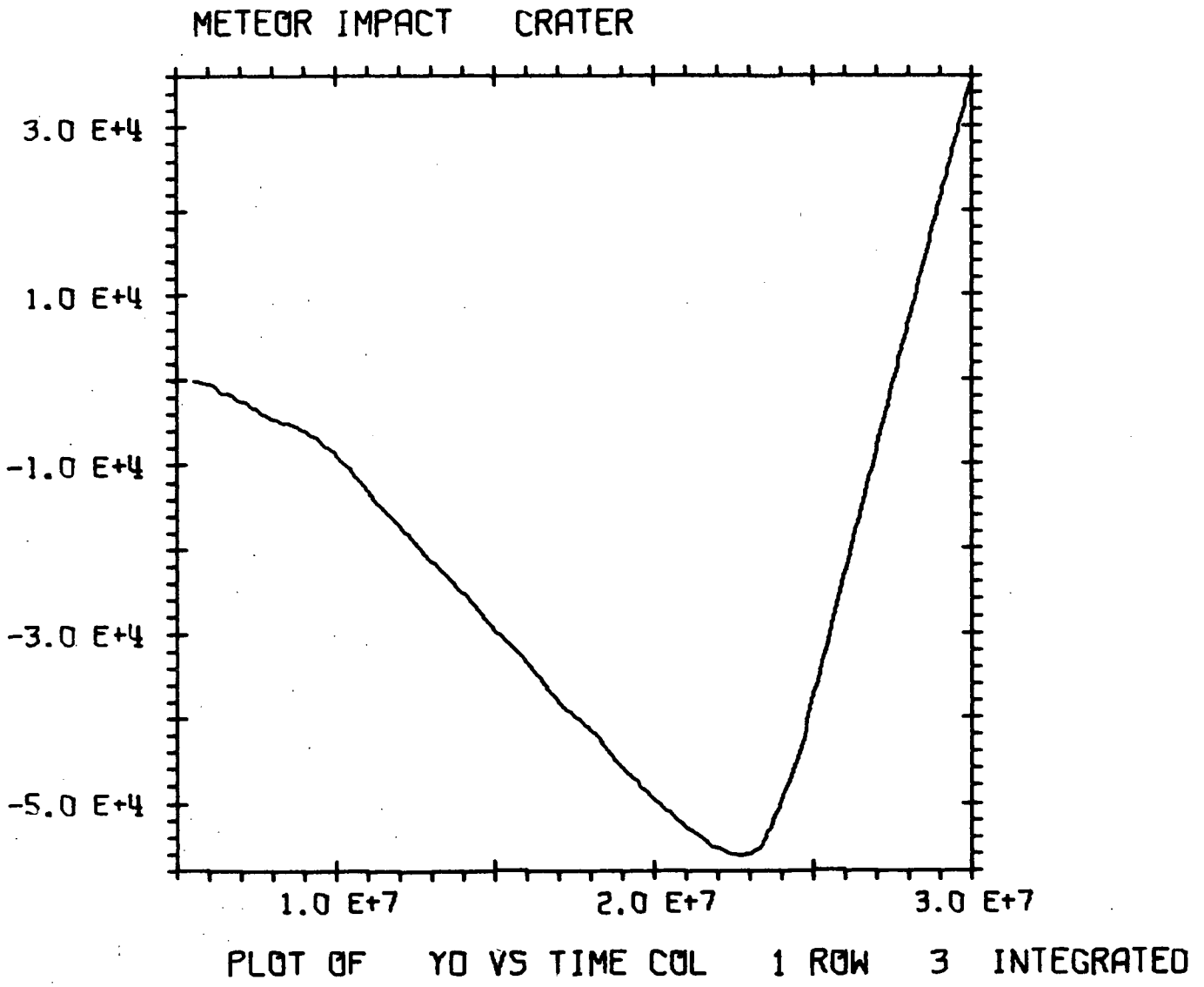
METEOR IMPACT CRATER
3.0 E+4
1.0 E+4
-1.0 E+4
-3.0 E+4
-5.0 E+4
1.0 E+7
2.0 E+7
3.0 E+7
PLOT OF YO VS TIME COL 1 ROW 3 INTEGRATED

Figure B-18

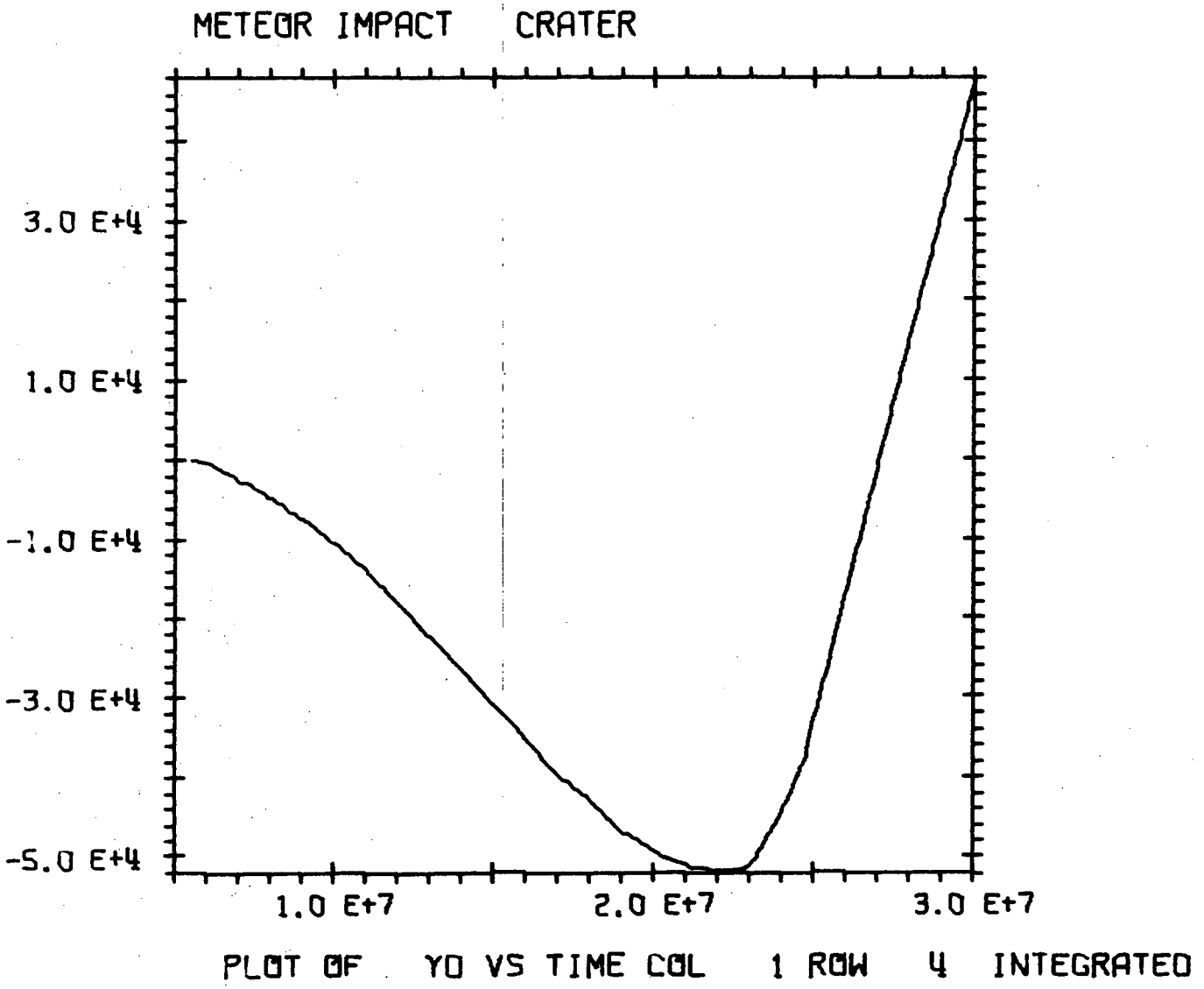
METEOR IMPACT CRATER
3.0 E+4
1.0 E+4
-1.0 E+4
-3.0 E+4
-5.0 E+4
1.0 E+7
2.0 E+7
3.0 E+7
PLOT OF YO VS TIME COL 1 ROW 4 INTEGRATED

Figure B-19

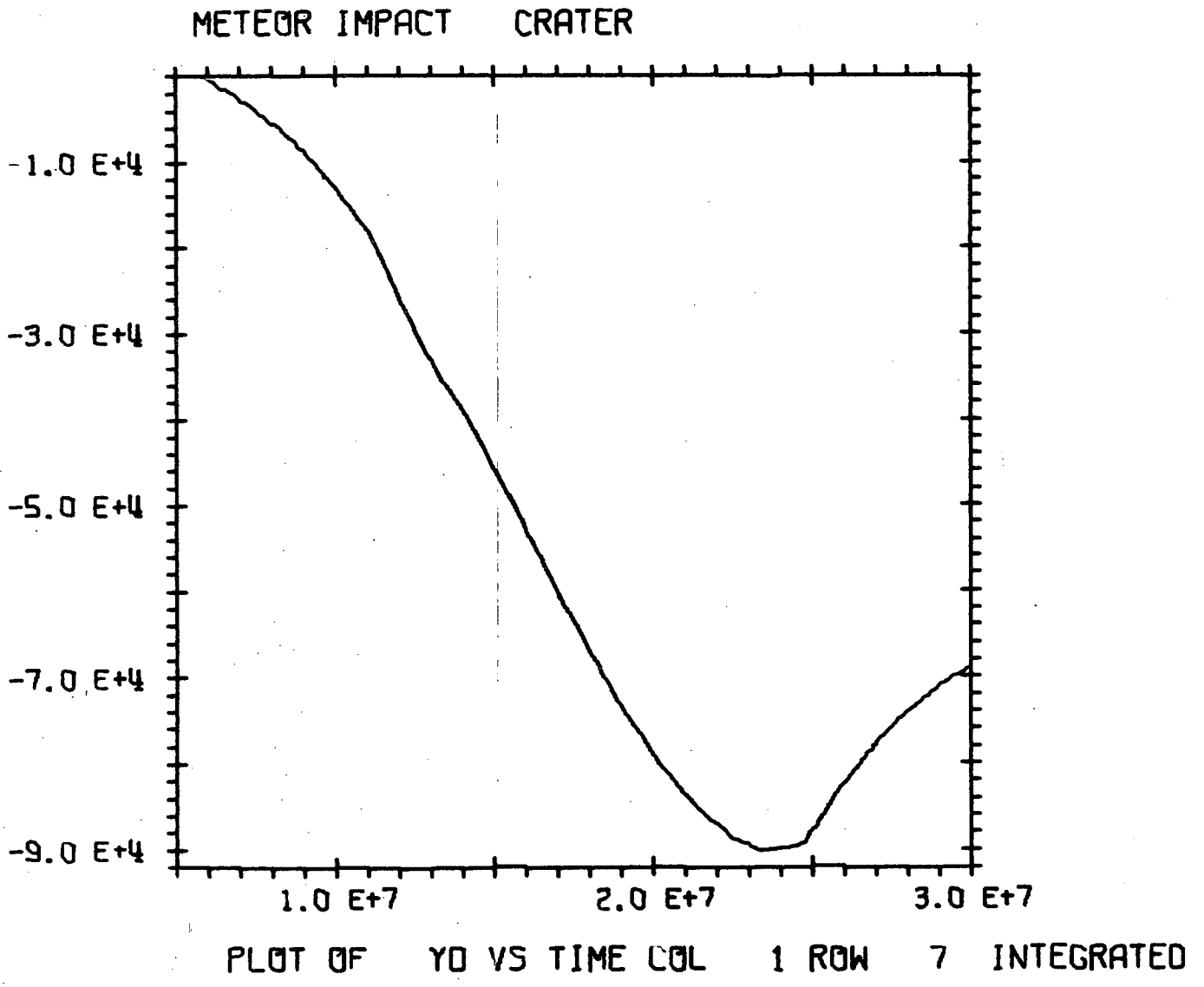
METEOR IMPACT CRATER
-1.0 E+4
-3.0 E+4
-5.0 E+4
-7.0 E+4
-9.0 E+4
1.0 E+7
2.0 E+7
3.0 E+7
PLOT OF YO VS TIME COL 1 ROW 7 INTEGRATED

Figure B-20

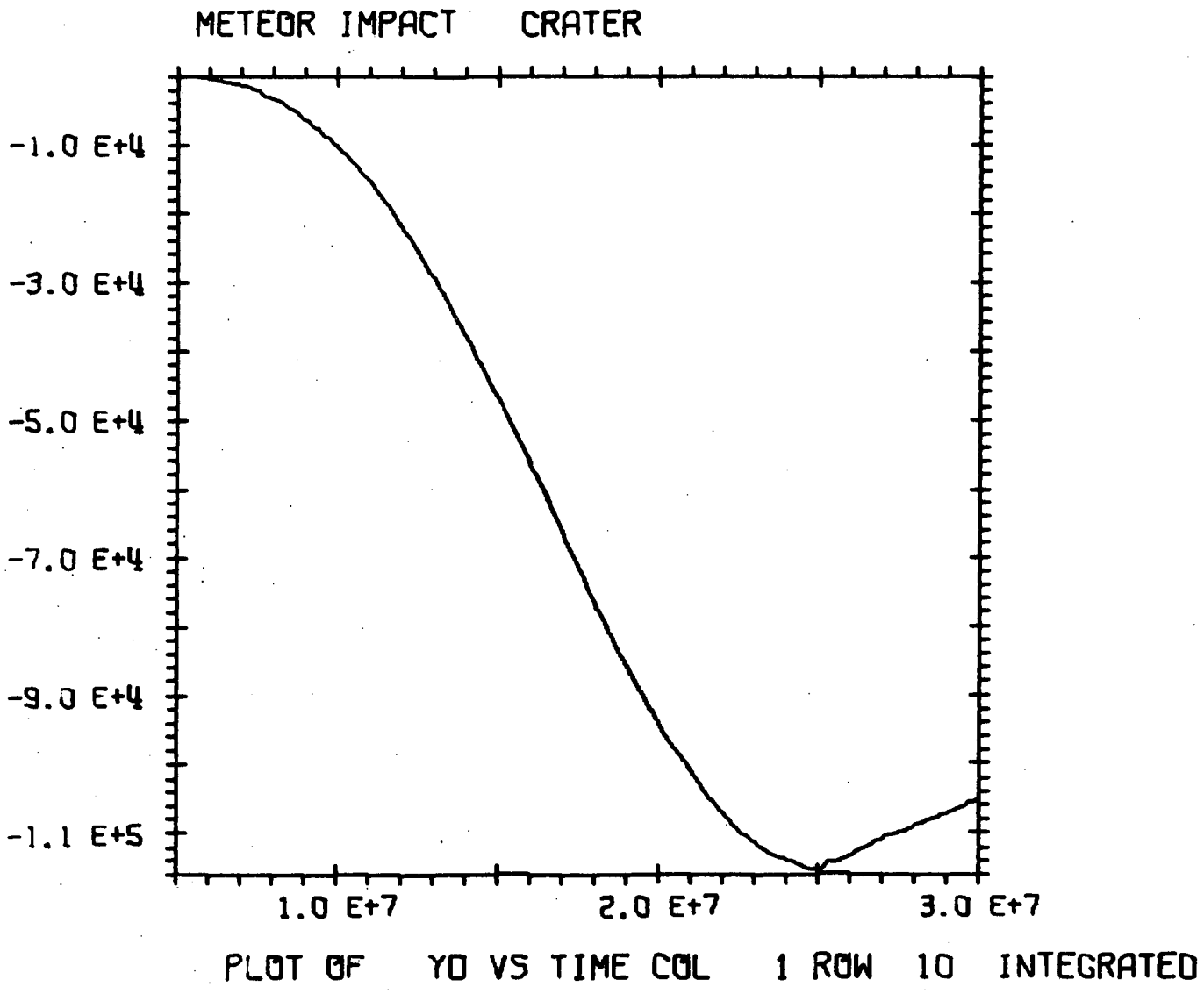
METEOR IMPACT CRATER
-1.0 E+4
-3.0 E+4
-5.0 E+4
-7.0 E+4
-9.0 E+4
-1.1 E+5
1.0 E+7
2.0 E+7
3.0 E+7
PLOT OF YO VS TIME COL 1 ROW 10 INTEGRATED

Figure B-21

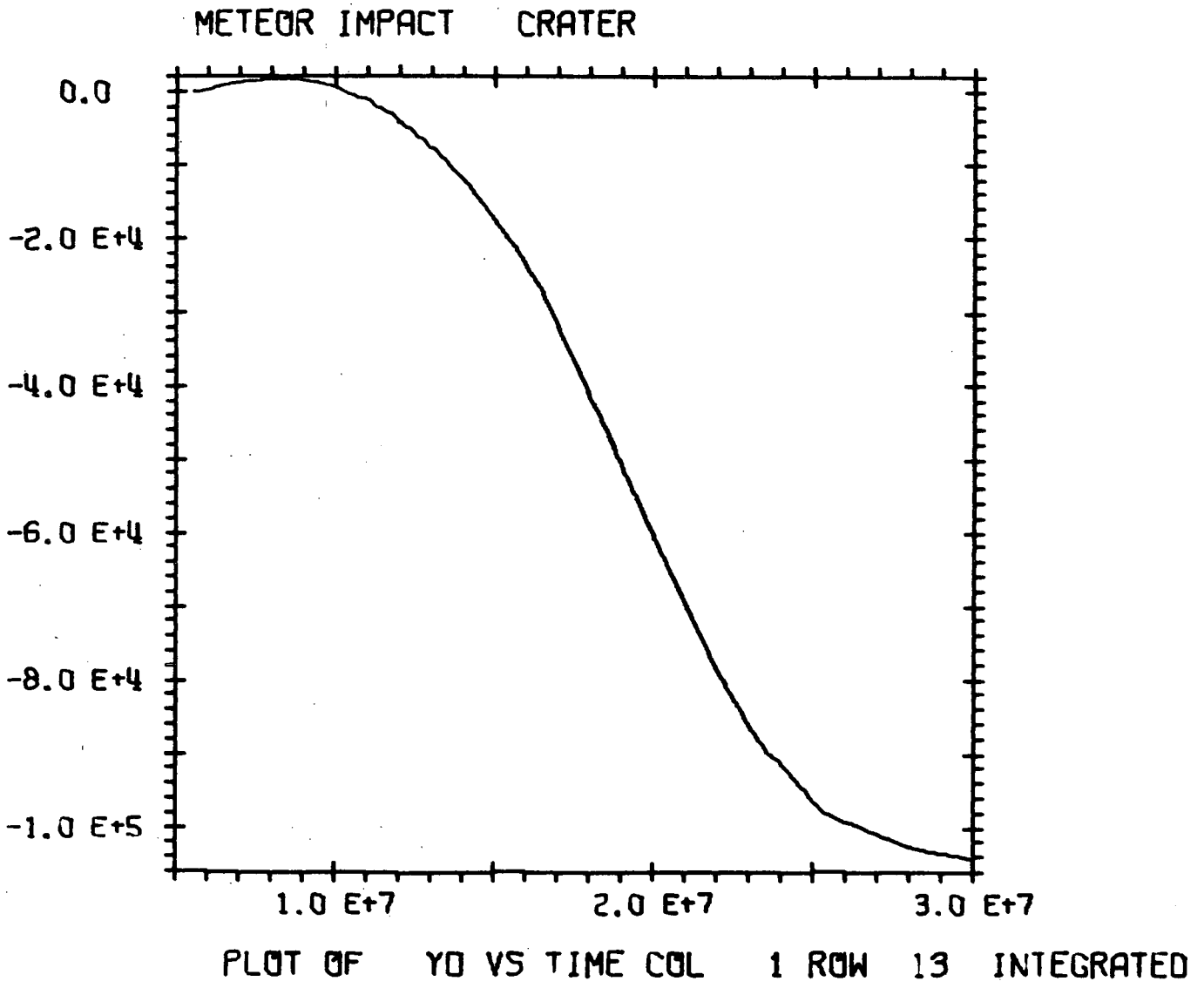
METEOR IMPACT CRATER
0.0
-2.0 E+4
-4.0 E+4
-6.0 E+4
-8.0 E+4
-1.0 E+5
1.0 E+7
2.0 E+7
3.0 E+7
PLOT OF YO VS TIME COL 1 ROW 13 INTEGRATED

Figure B-22

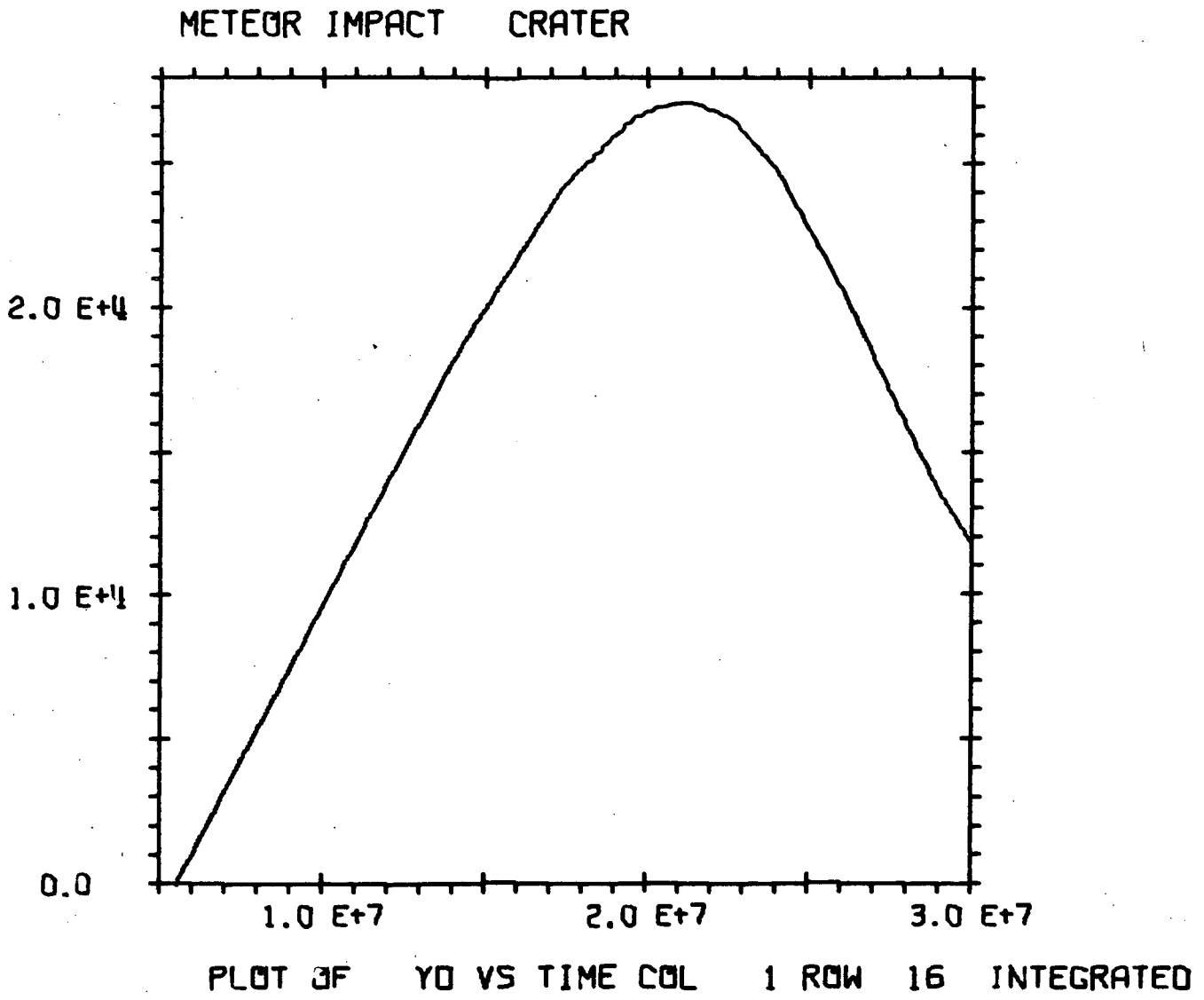
METEOR IMPACT CRATER
2.0 E+4
1.0 E+4
0.0
1.0 E+7
2.0 E+7
3.0 E+7
PLOT 3F YO VS TIME COL 1 ROW 16 INTEGRATED

Figure B-23

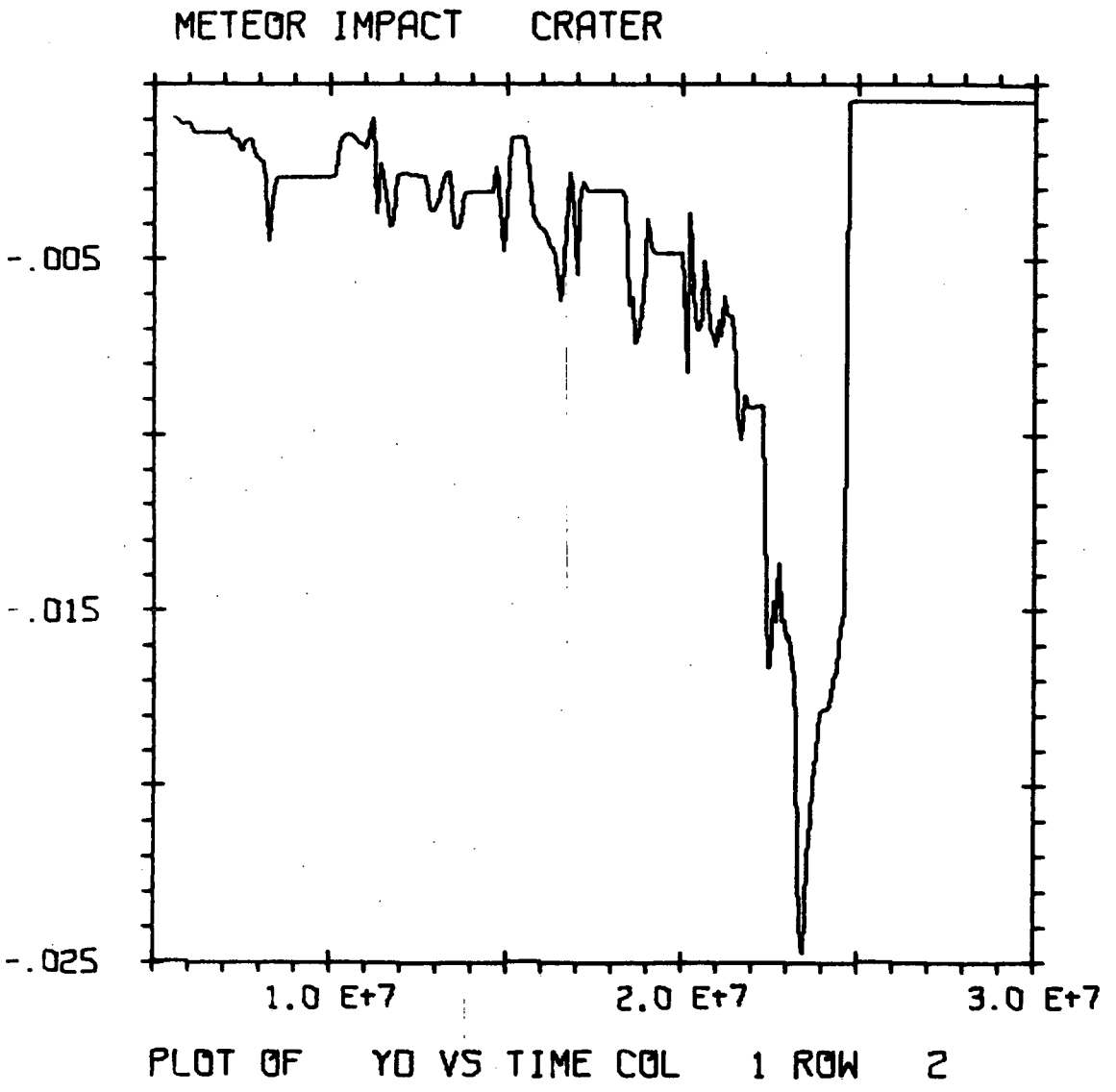
METEOR IMPACT CRATER
-.005
-.015
-.025
1.0 E+7
2.0 E+7
3.0 E+7
PLOT OF YO VS TIME COL 1 ROW 2

Figure B-24

3

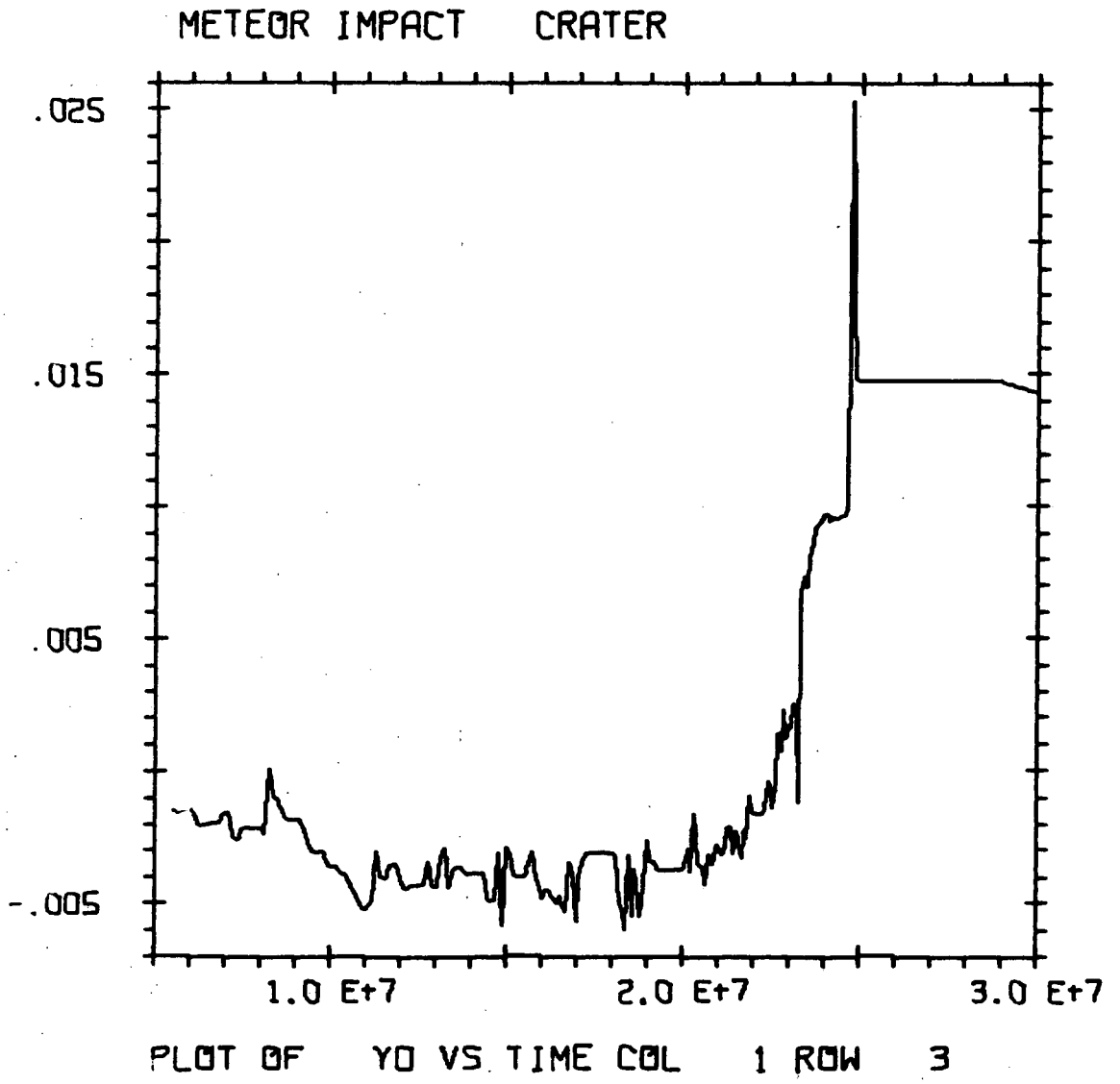
METEOR IMPACT CRATER
.025
.015
.005
-.005
1.0 E+7
2.0 E+7
3.0 E+7
PLOT OF YO VS TIME COL 1 ROW 3

Figure B-25

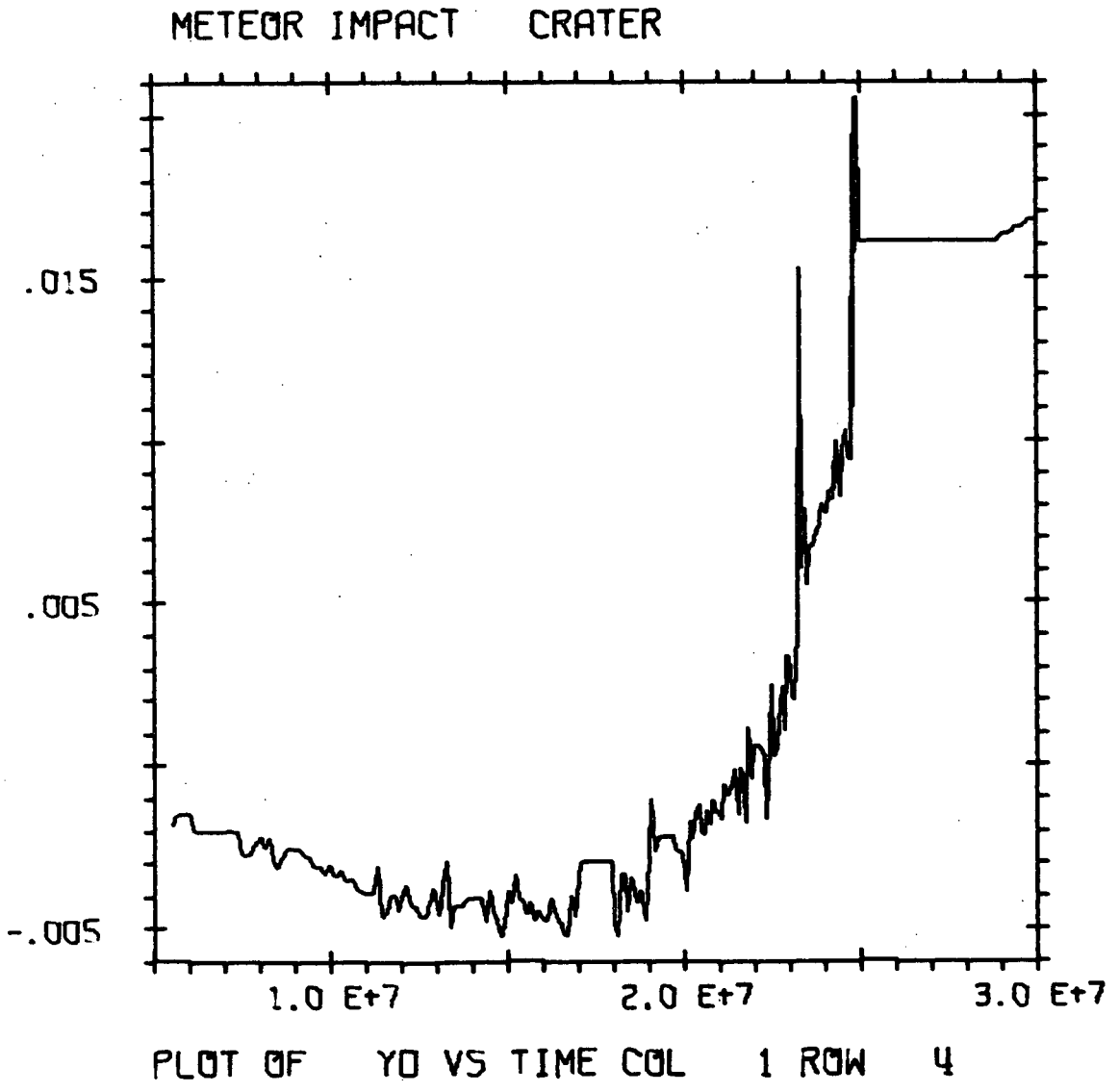
METEOR IMPACT CRATER
.015
.005
-.005
1.0 E+7
2.0 E+7
3.0 E+7
PLOT OF YO VS TIME COL 1 ROW 4

Figure B-26

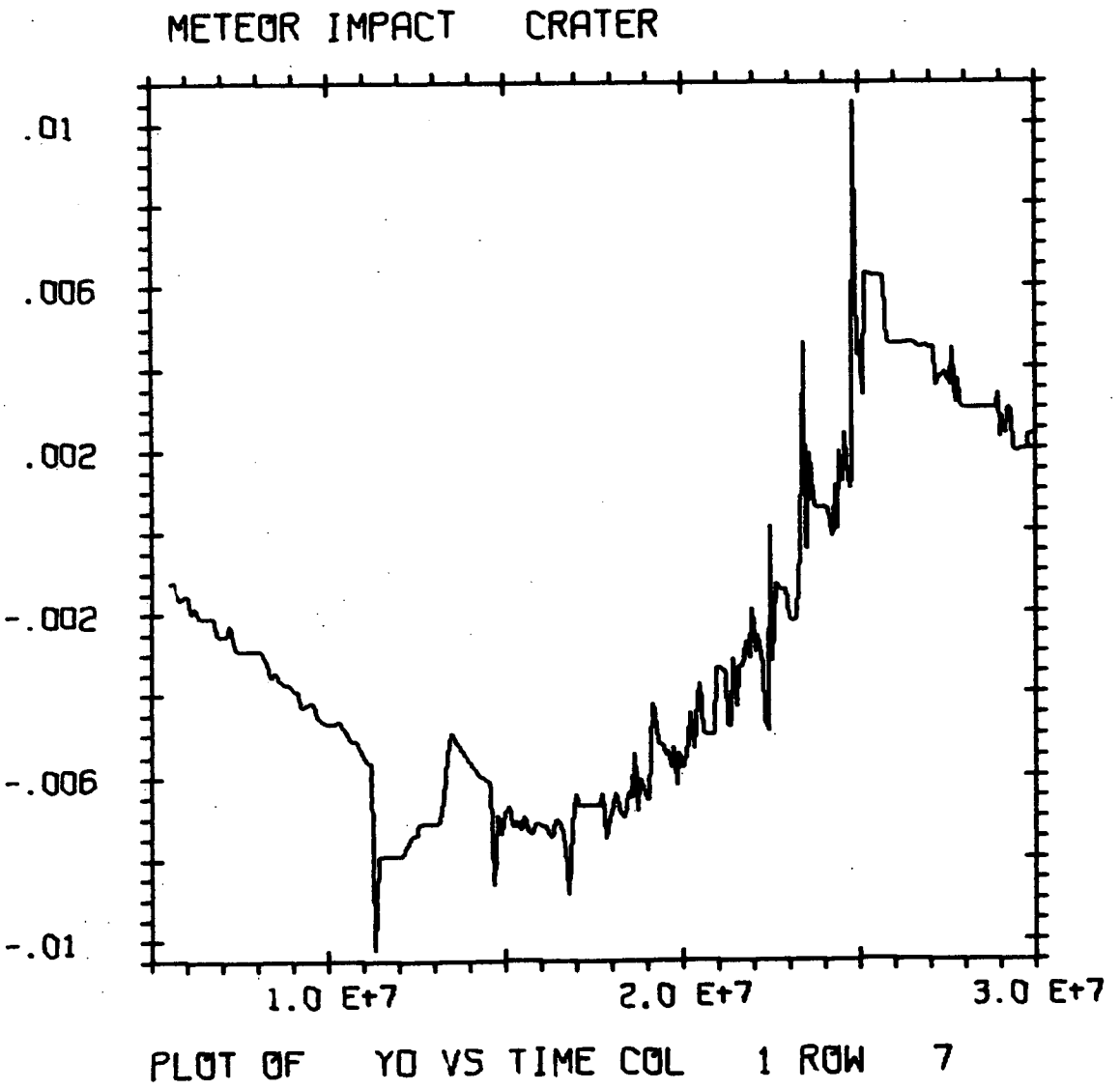
METEOR IMPACT CRATER
.01
.006
.002
-.002
-.006
-.01
1.0 E+7
2.0 E+7
3.0 E+7
PLOT OF YO VS TIME COL 1 ROW 7

Figure B-27

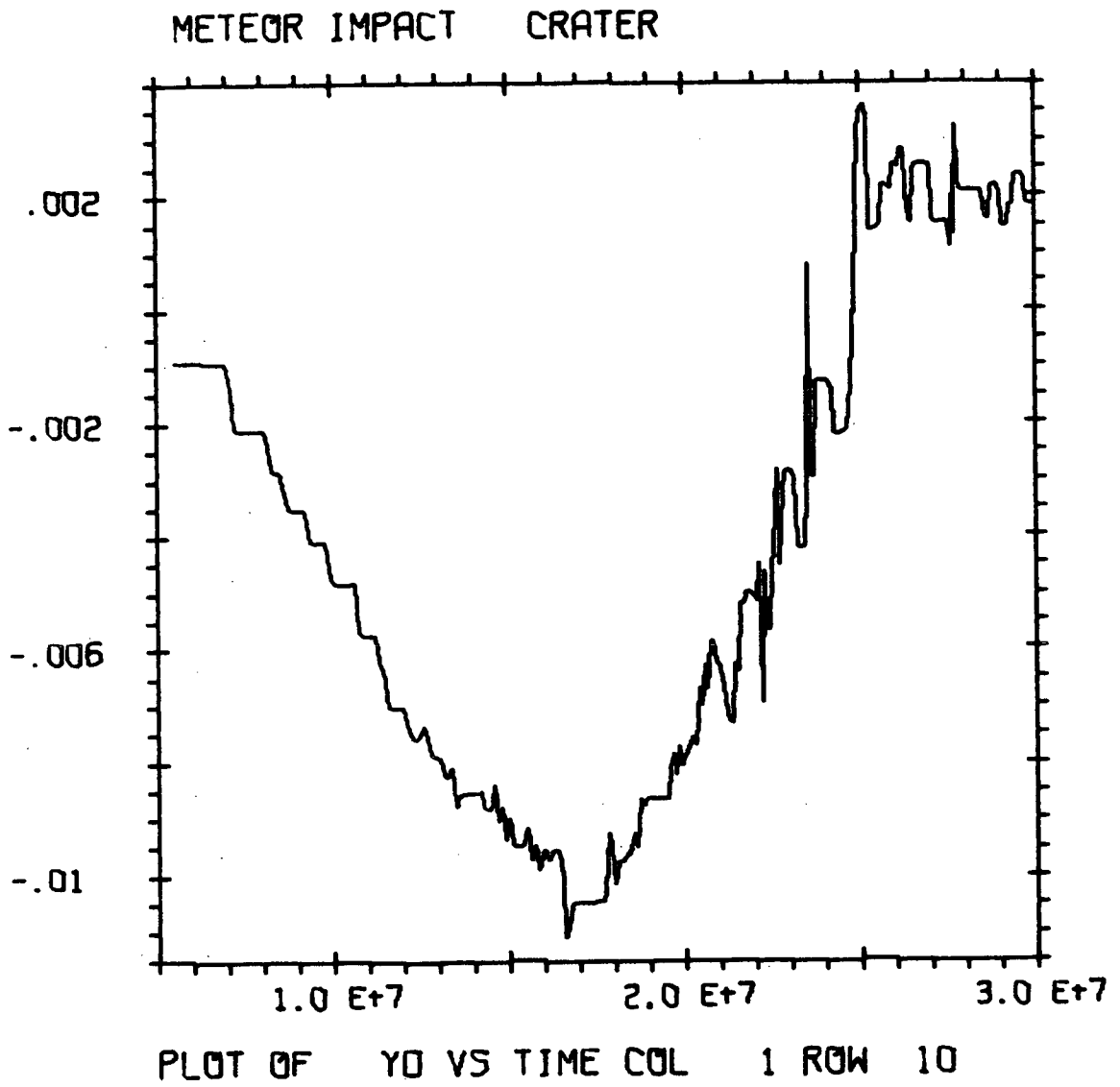
METEOR IMPACT CRATER
.002
-.002
-.006
-.01
1.0 E+7
2.0 E+7
3.0 E+7
PLOT OF YO VS TIME COL 1 ROW 10

Figure B-28

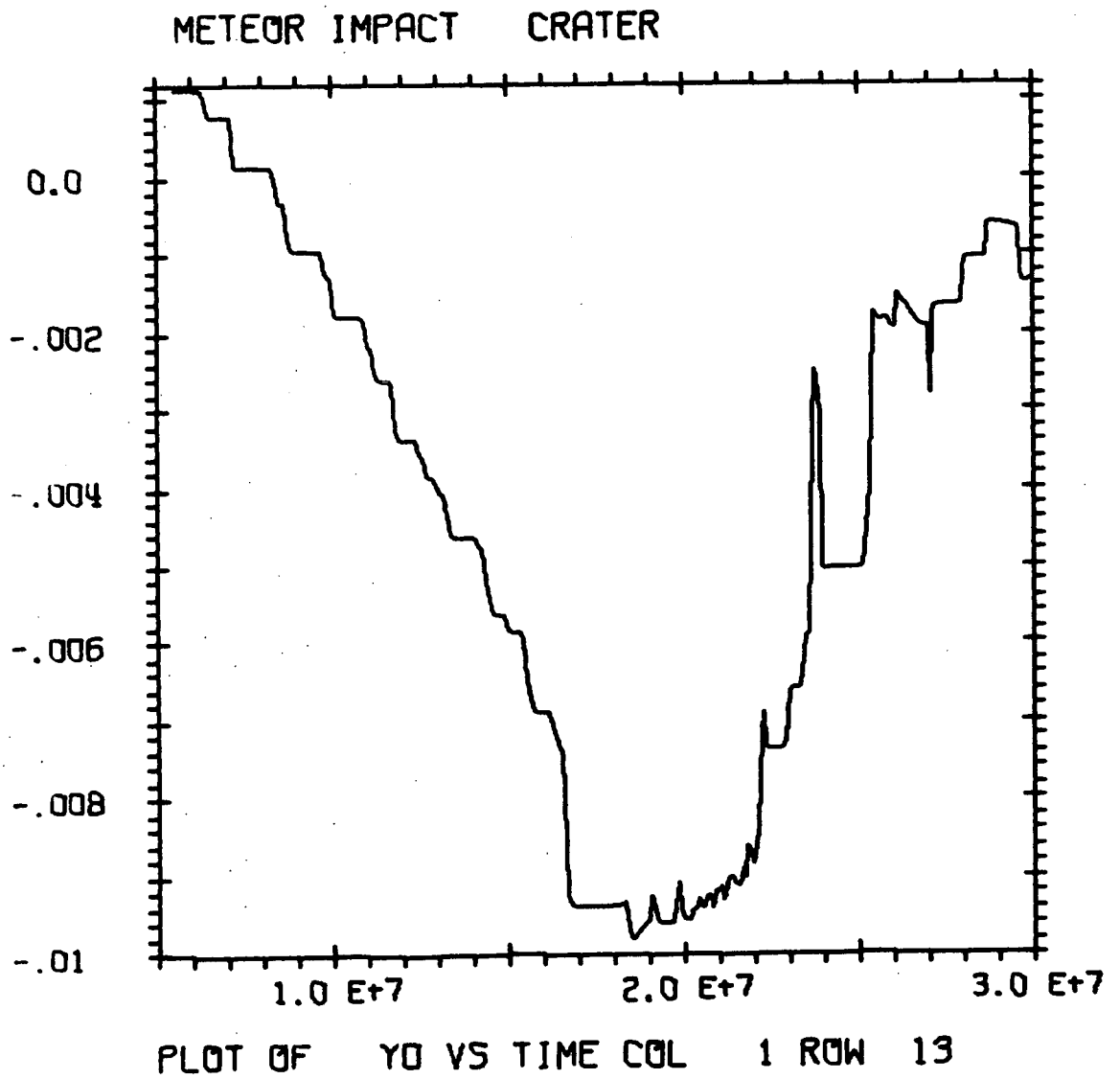
METEOR IMPACT CRATER
0.0
-.002
-.004
-.006
-.008
-.01
1.0 E+7
2.0 E+7
3.0 E+7
PLOT OF YO VS TIME COL 1 ROW 13

Figure B-29

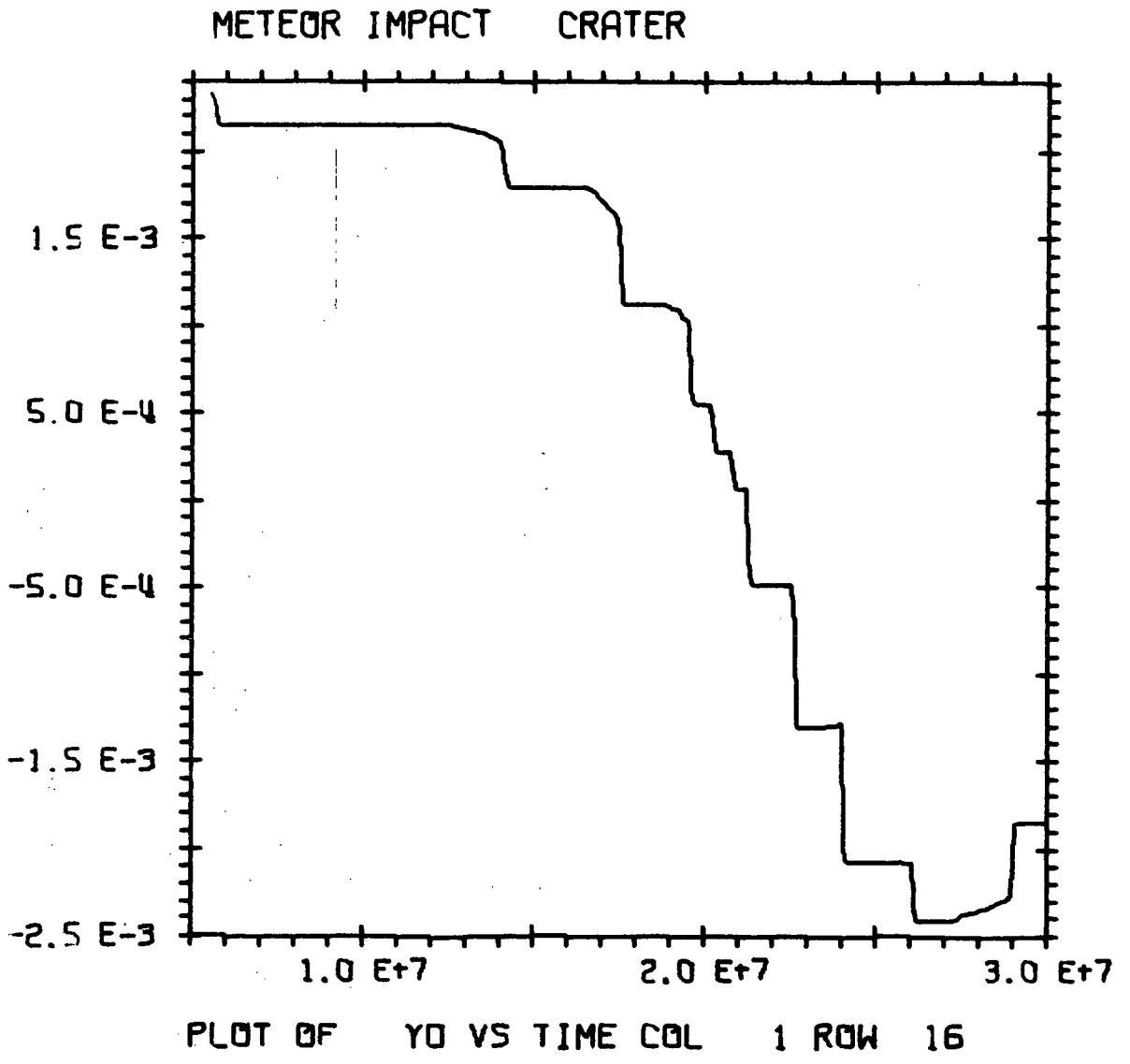
METEOR IMPACT CRATER
1.5 E-3
5.0 E-4
-5.0 E-4
-1.5 E-3
-2.5 E-3
1.0 E+7
2.0 E+7
3.0 E+7
PLOT OF YO VS TIME COL 1 ROW 16

Figure B-30

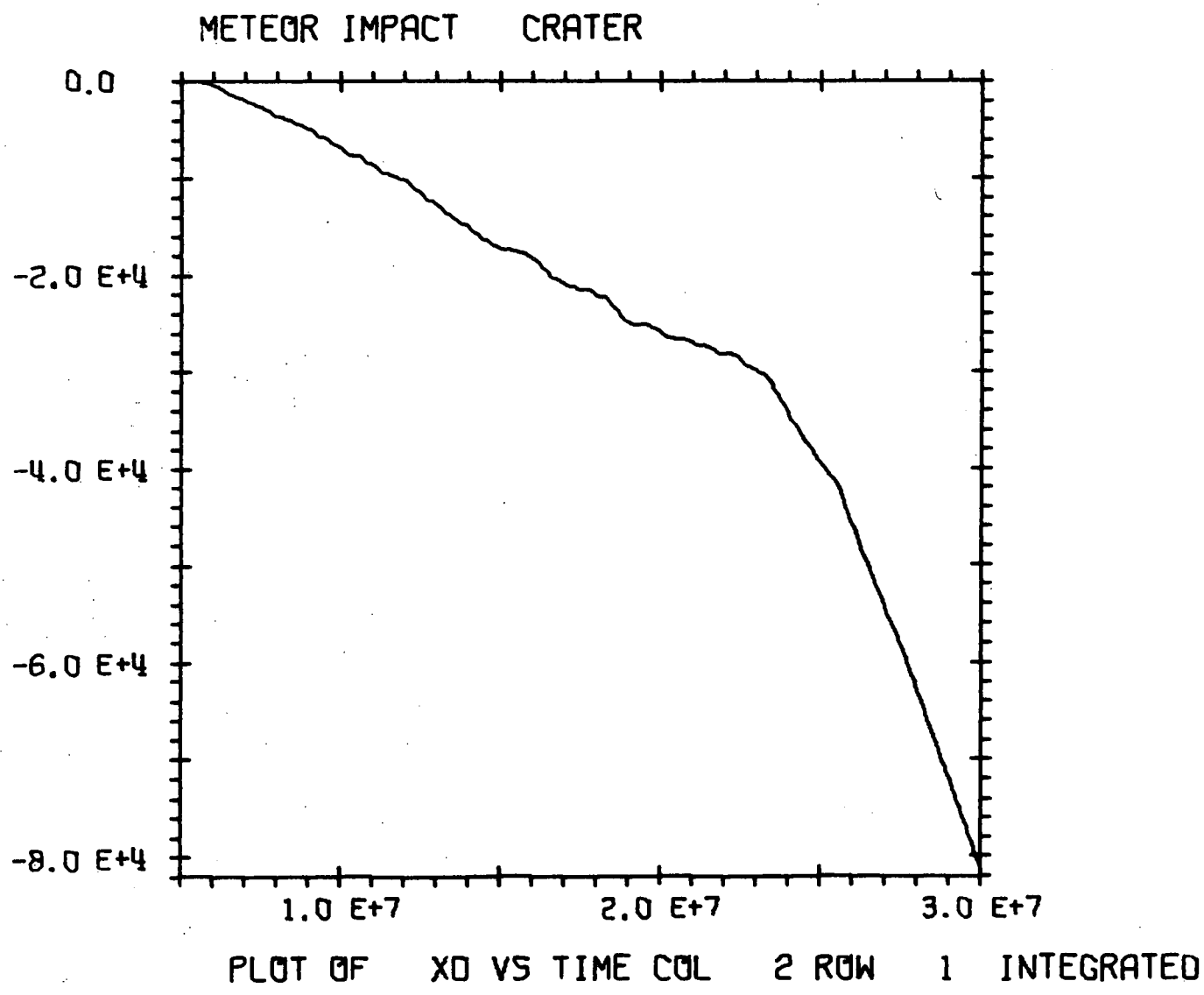
METEOR IMPACT CRATER
0.0
-2.0 E+4
-4.0 E+4
-6.0 E+4
-8.0 E+4
1.0 E+7
2.0 E+7
3.0 E+7
PLOT OF XO VS TIME COL 2 ROW 1 INTEGRATED

Figure B-31

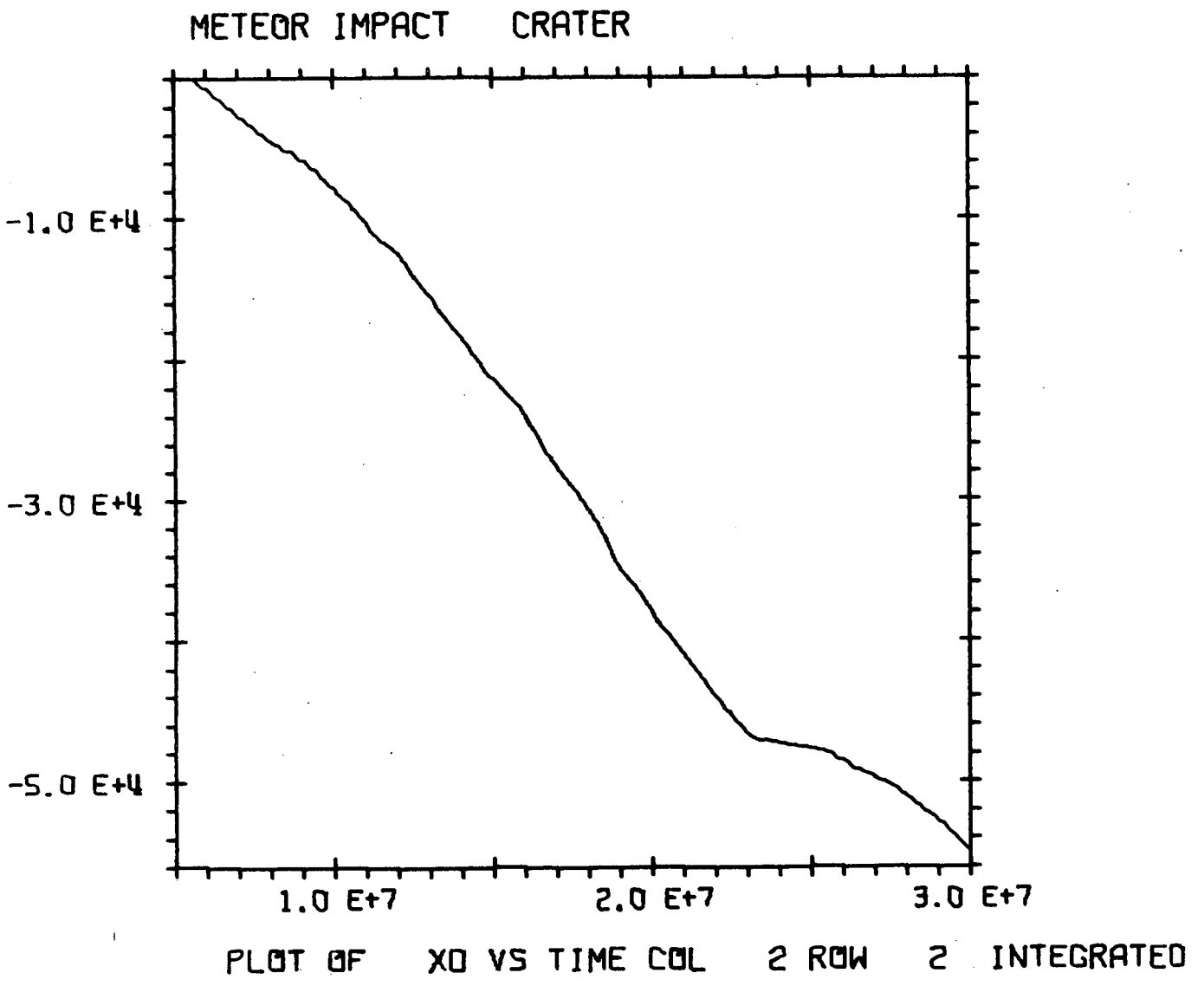
METEOR IMPACT CRATER
-1.0 E+4
-3.0 E+4
-5.0 E+4
1.0 E+7
2.0 E+7
3.0 E+7
PLOT OF XO VS TIME COL 2 ROW 2 INTEGRATED

Figure B-32

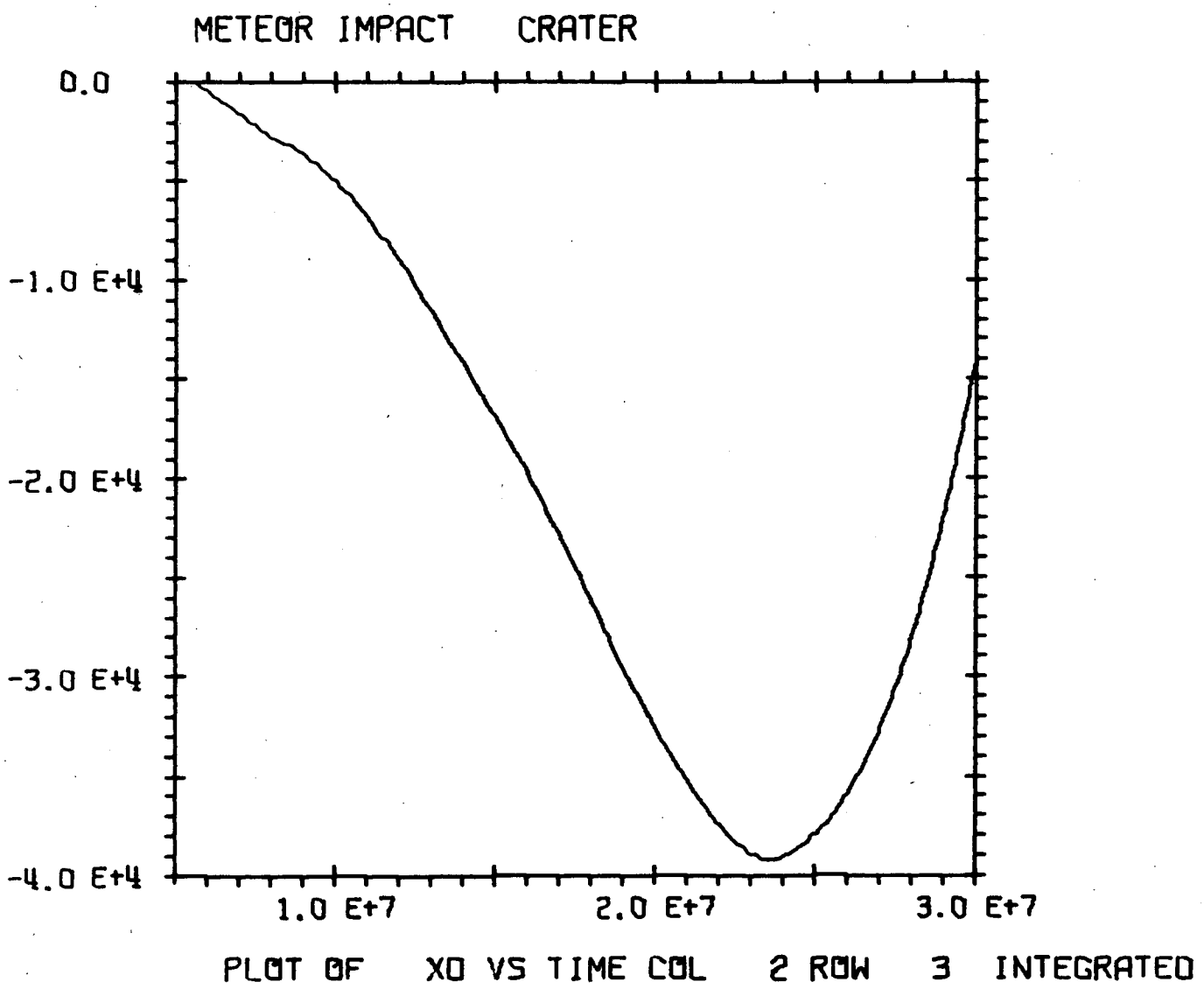
METEOR IMPACT CRATER
0.0
-1.0 E+4
-2.0 E+4
-3.0 E+4
-4.0 E+4
1.0 E+7
2.0 E+7
3.0 E+7
PLOT OF XO VS TIME COL 2 ROW 3 INTEGRATED

Figure B-33

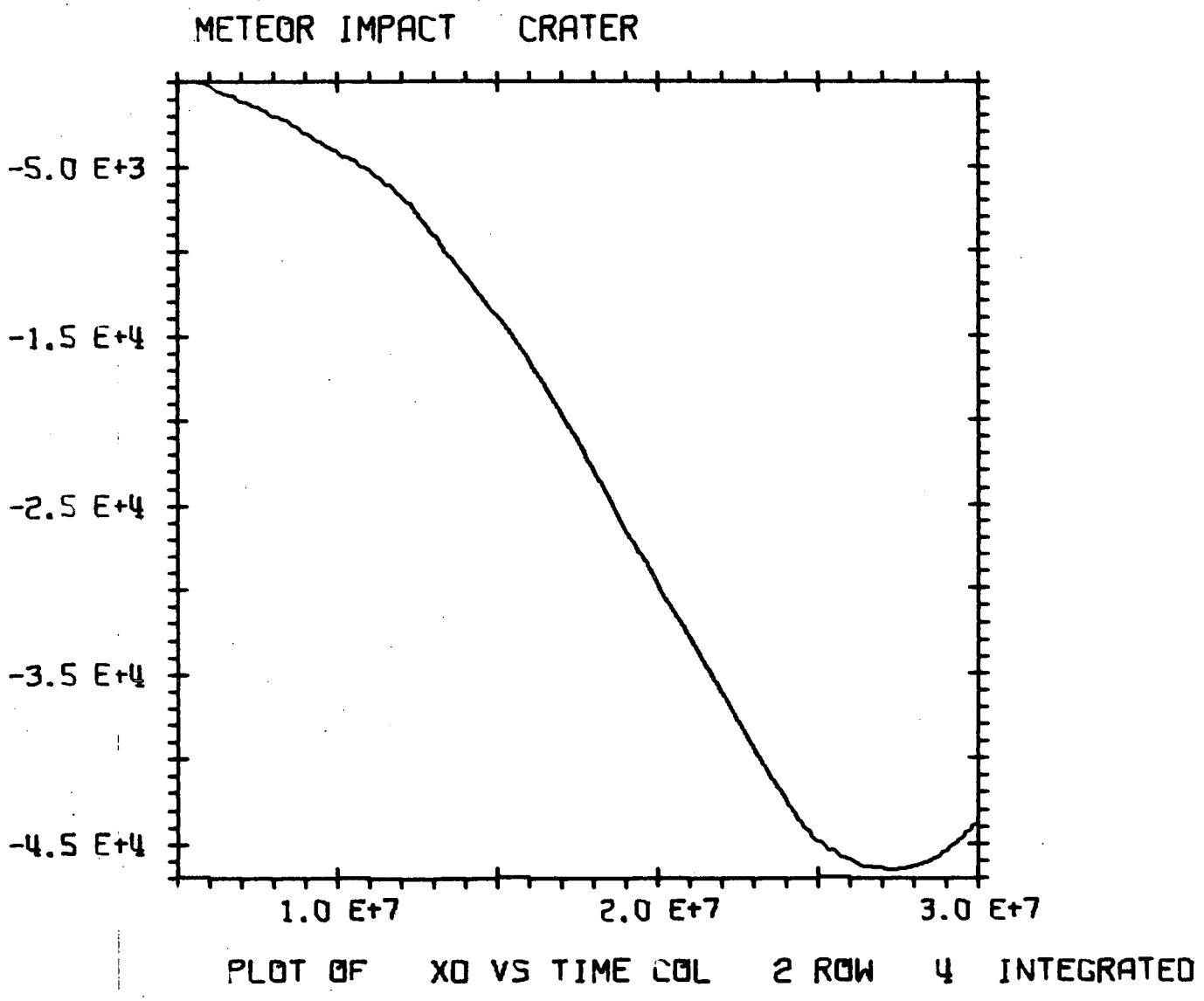
METEOR IMPACT CRATER
-5.0 E+3
-1.5 E+4
-2.5 E+4
-3.5 E+4
-4.5 E+4
1.0 E+7
2.0 E+7
3.0 E+7
PLOT OF XO VS TIME COL 2 ROW 4 INTEGRATED

Figure B-34

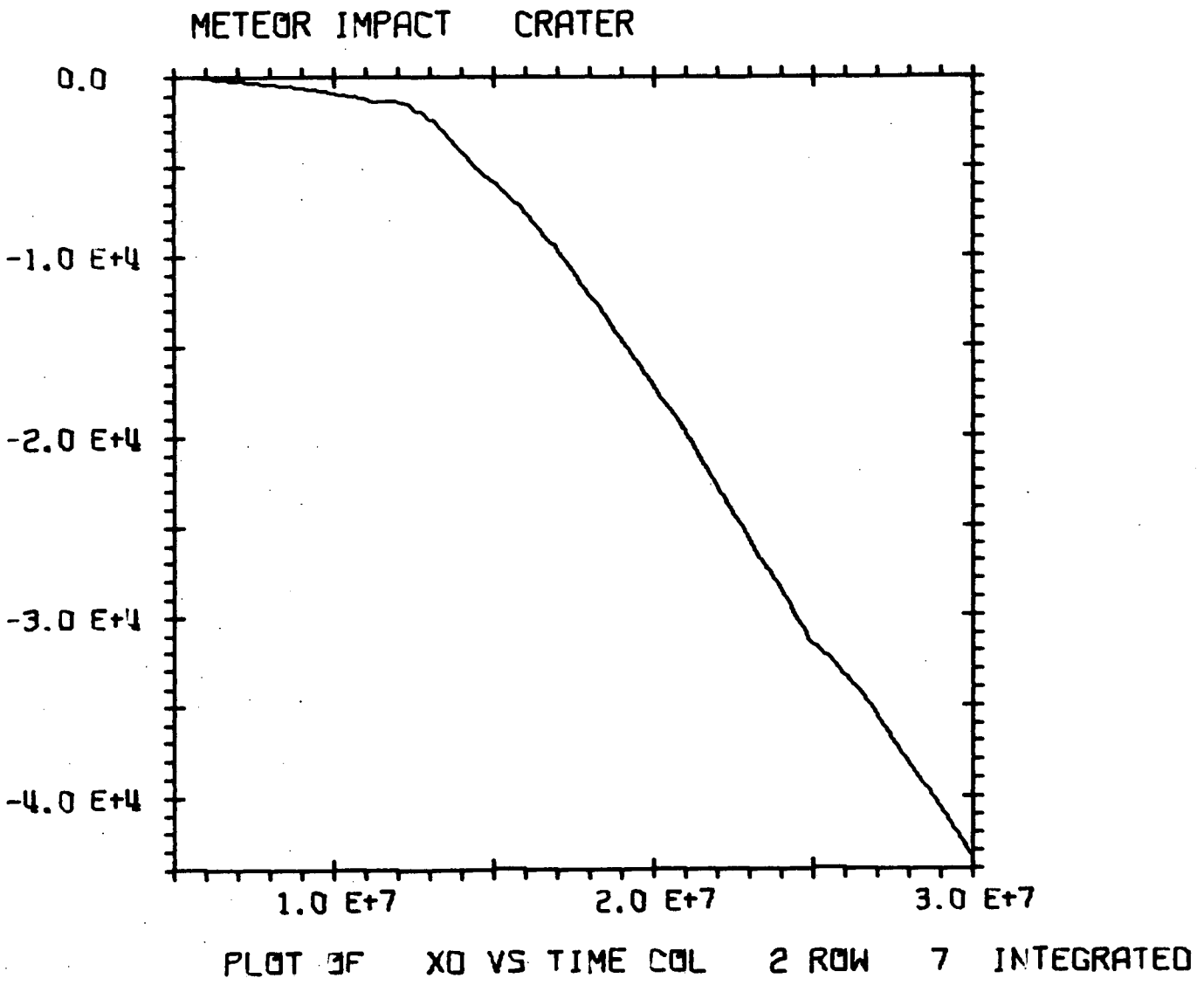
METEOR IMPACT CRATER
0.0
-1.0 E+4
-2.0 E+4
-3.0 E+4
-4.0 E+4
1.0 E+7
2.0 E+7
3.0 E+7
PLOT OF XO VS TIME COL 2 ROW 7 INTEGRATED

Figure B-35

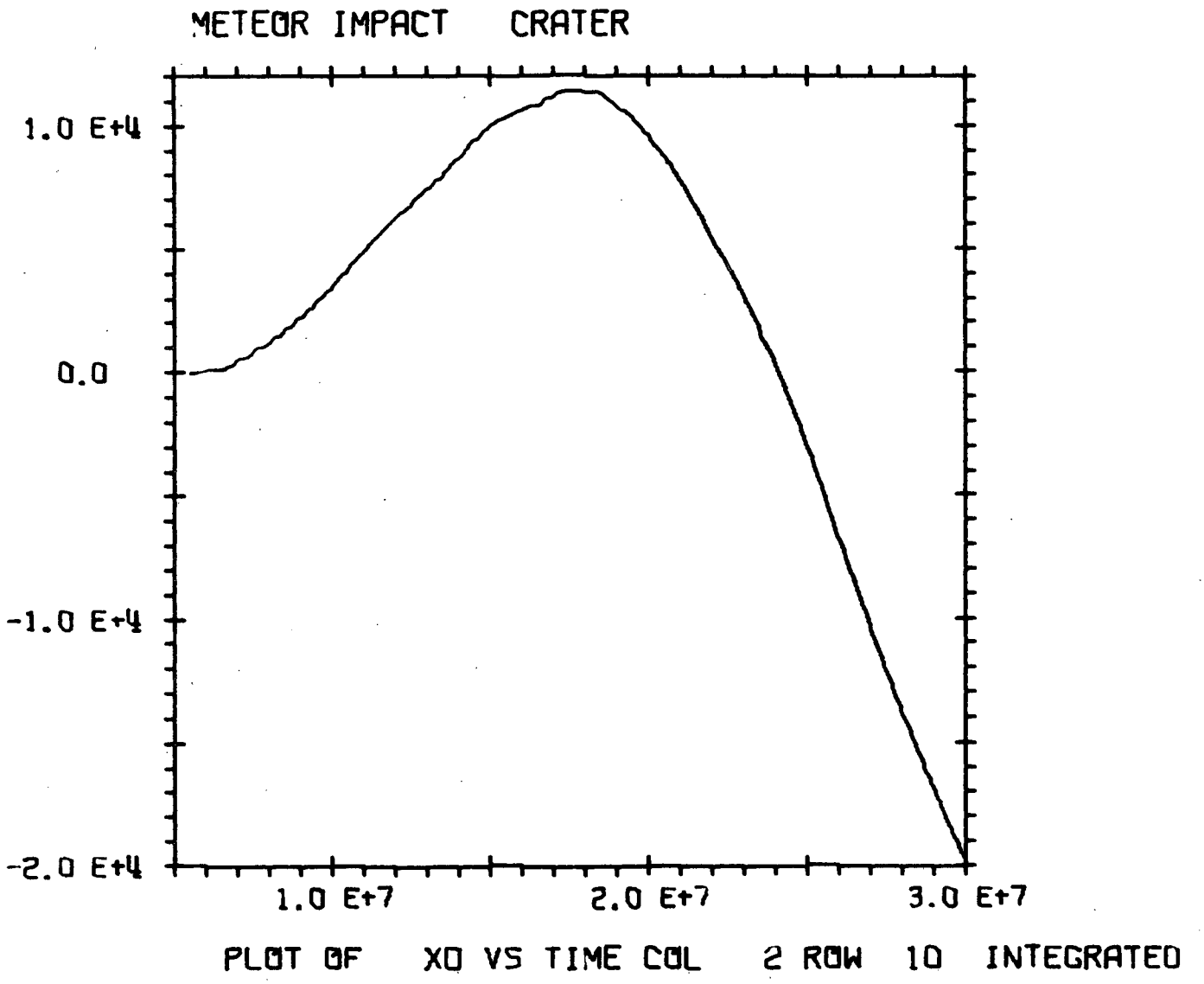
METEOR IMPACT CRATER
1.0 E+4
0.0
-1.0 E+4
-2.0 E+4
1.0 E+7
2.0 E+7
3.0 E+7
PLOT OF XO VS TIME COL 2 ROW 10 INTEGRATED

Figure B-36

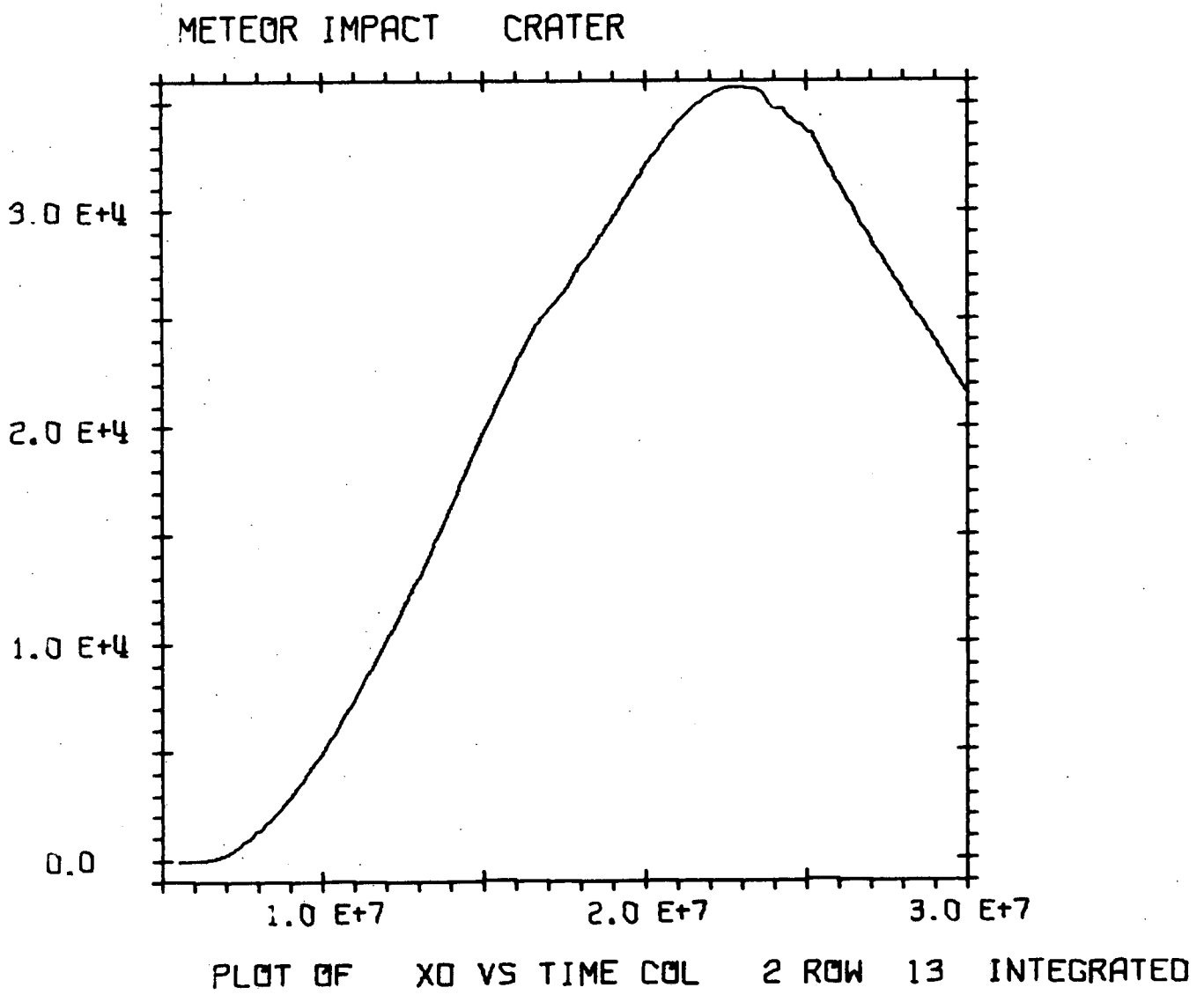
METEOR IMPACT CRATER
3.0 E+4
2.0 E+4
1.0 E+4
0.0
1.0 E+7
2.0 E+7
3.0 E+7
PLOT OF XO VS TIME COL 2 ROW 13 INTEGRATED

Figure B-37

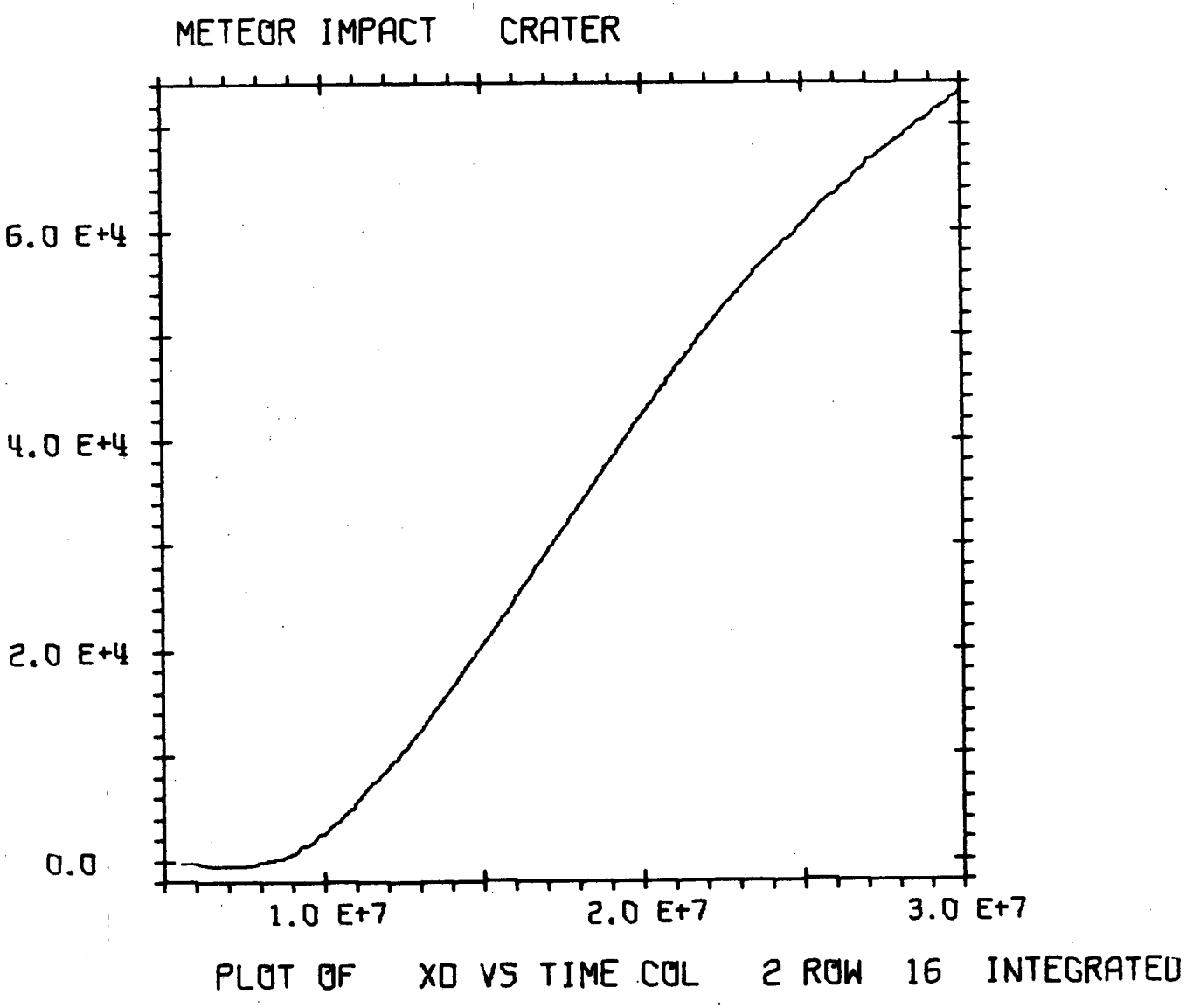
METEOR IMPACT CRATER
6.0 E+4
4.0 E+4
2.0 E+4
0.0
1.0 E+7
2.0 E+7
3.0 E+7
PLOT OF XO VS TIME COL 2 ROW 16 INTEGRATED

Figure B-38

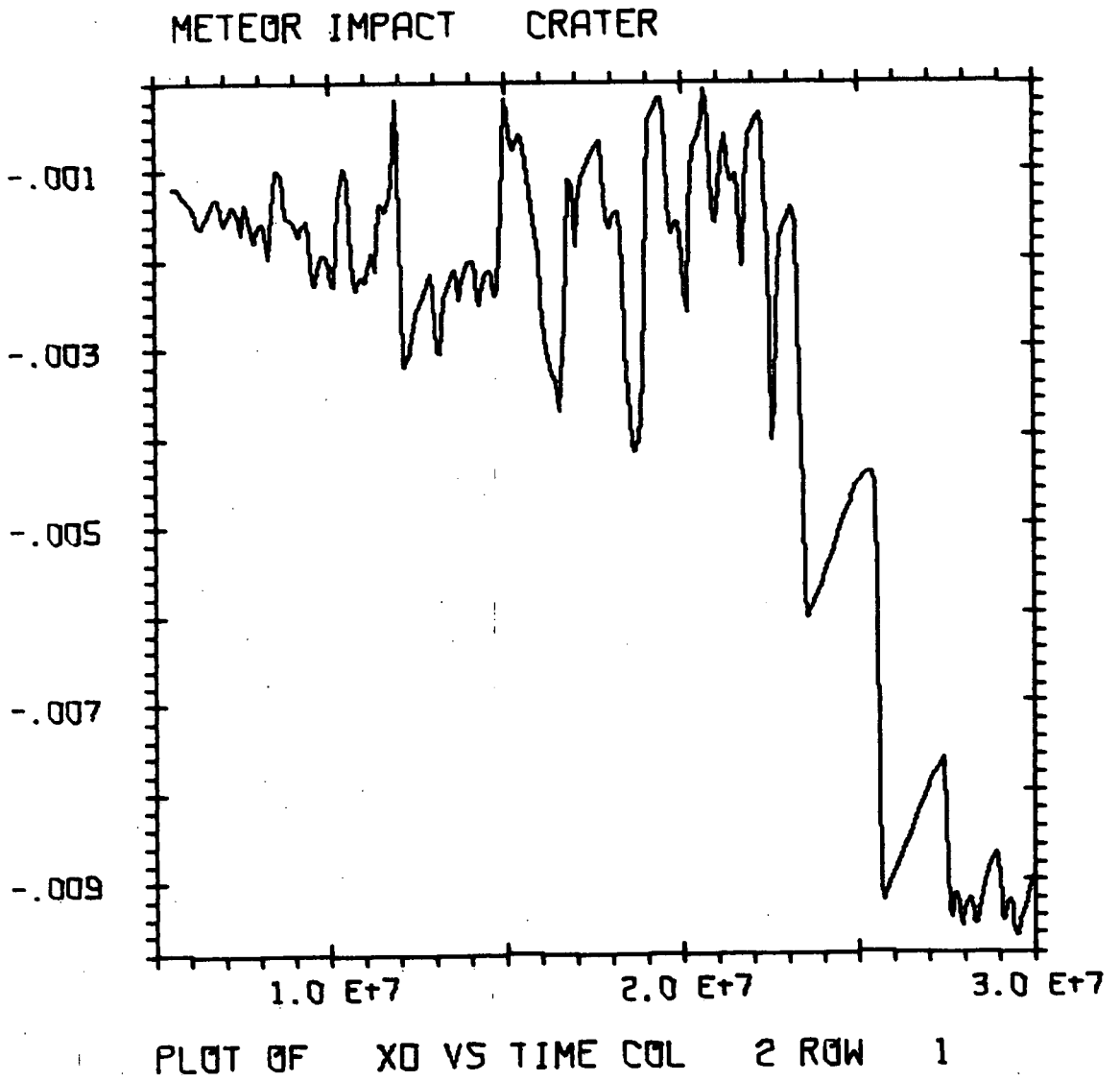
METEOR IMPACT CRATER
-.001
-.003
-.005
-.007
-.009
1.0 E+7
2.0 E+7
3.0 E+7
PLOT OF XO VS TIME COL 2 ROW 1

Figure B-39

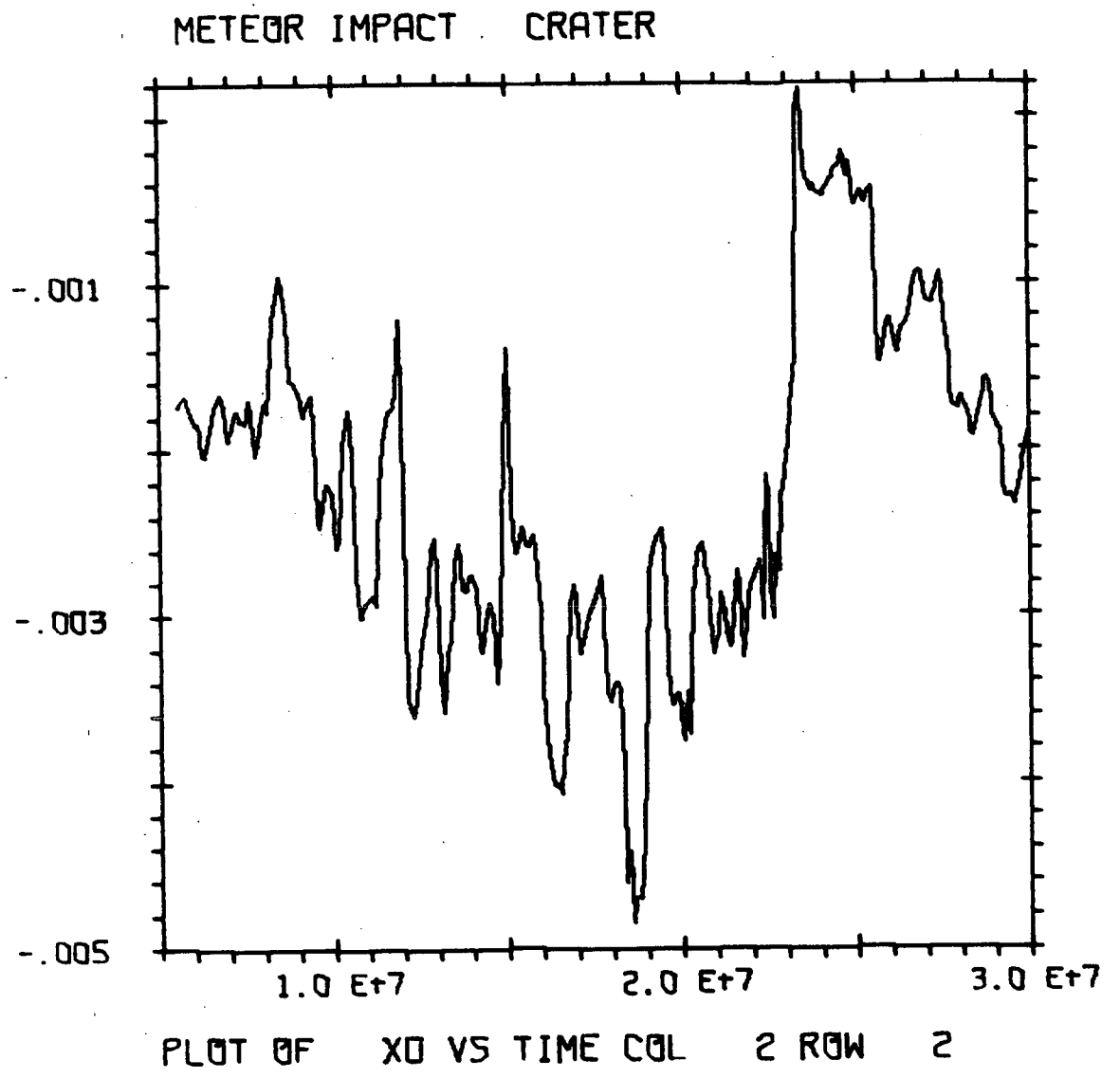
METEOR IMPACT CRATER
-.001
-.003
-.005
1.0 E+7
2.0 E+7
3.0 E+7
PLOT OF XO VS TIME COL 2 ROW 2

Figure B-40

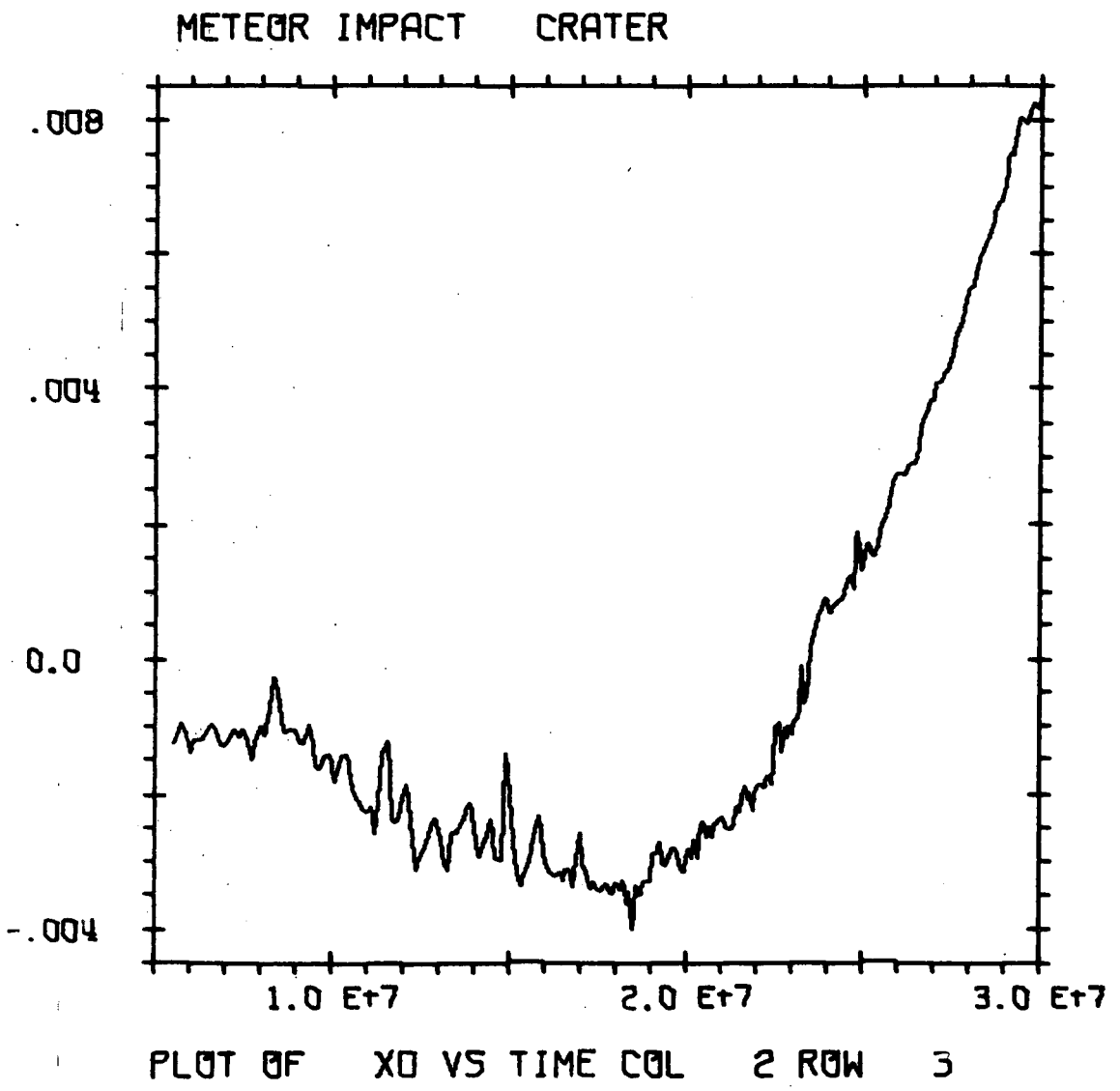
METEOR IMPACT CRATER
.008
.004
0.0
-.004
1.0 E+7
2.0 E+7
3.0 E+7
PLOT OF XO VS TIME COL 2 ROW 3

Figure B-41

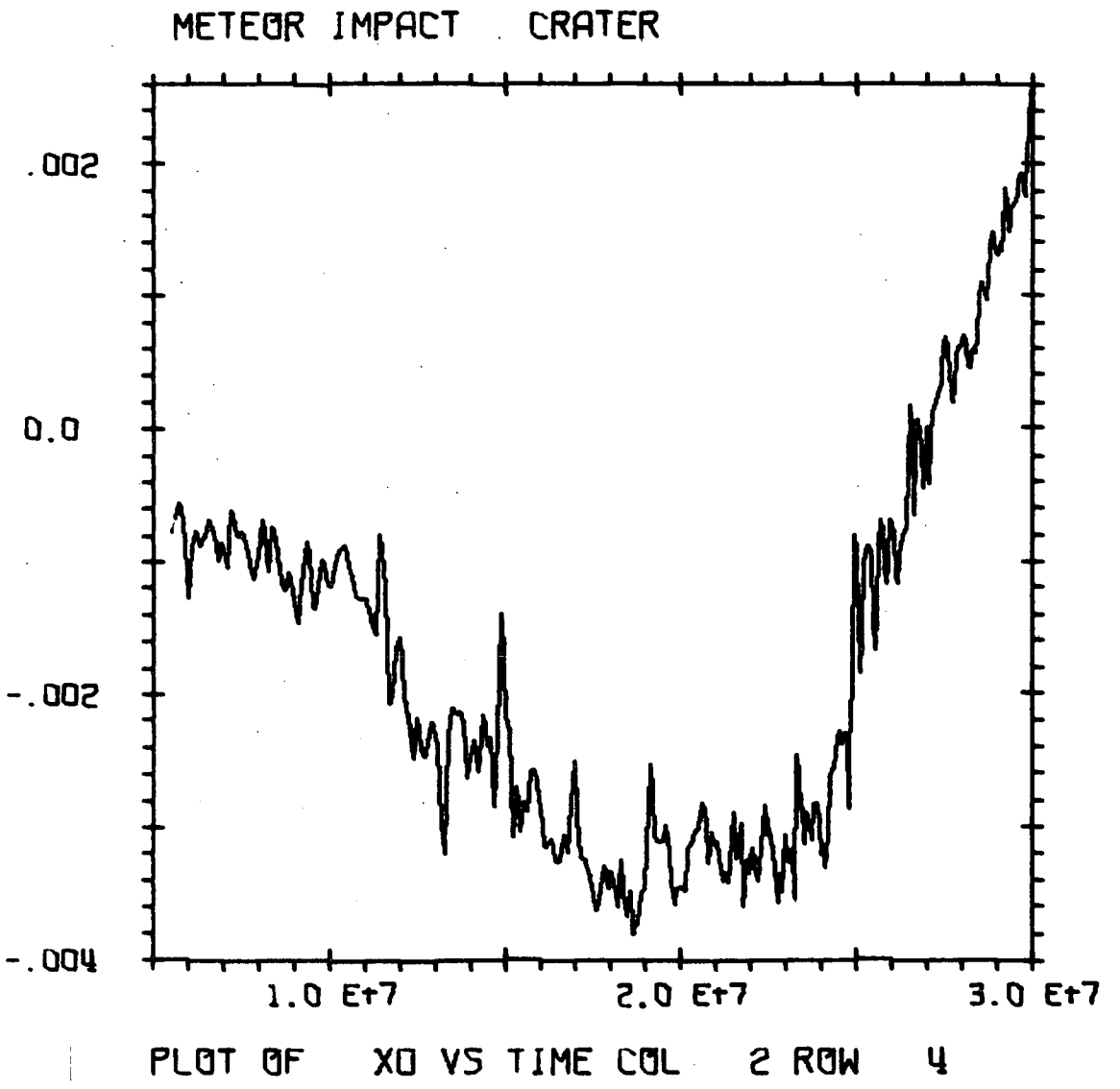
METEOR IMPACT CRATER
.002
0.0
-.002
-.004
1.0 E+7
2.0 E+7
3.0 E+7
PLOT OF XO VS TIME COL 2 ROW 4

Figure B-42

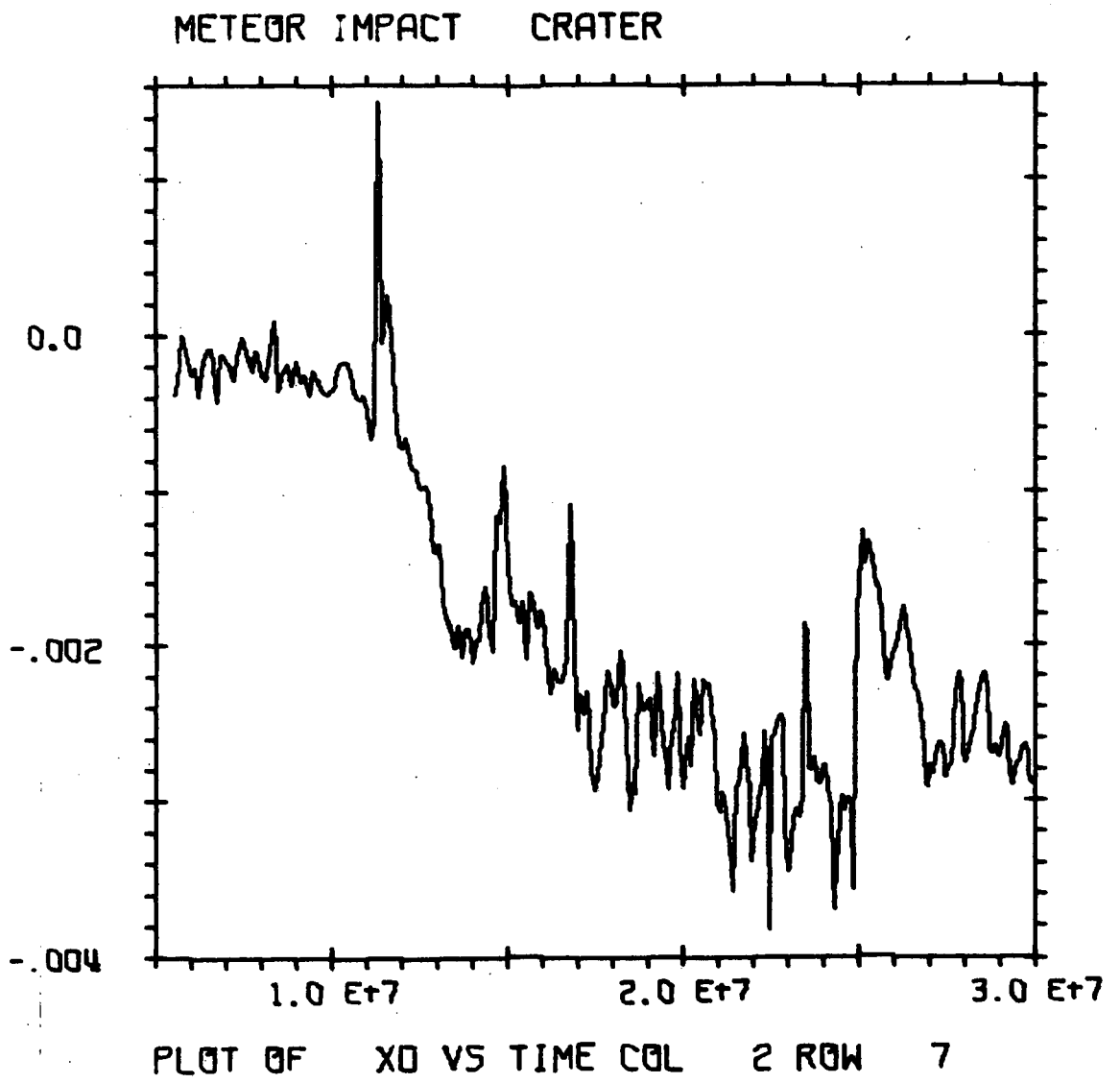
METEOR IMPACT CRATER
0.0
-.002
-.004
1.0 E+7
2.0 E+7
3.0 E+7
PLOT OF XO VS TIME COL 2 ROW 7

Figure B-43

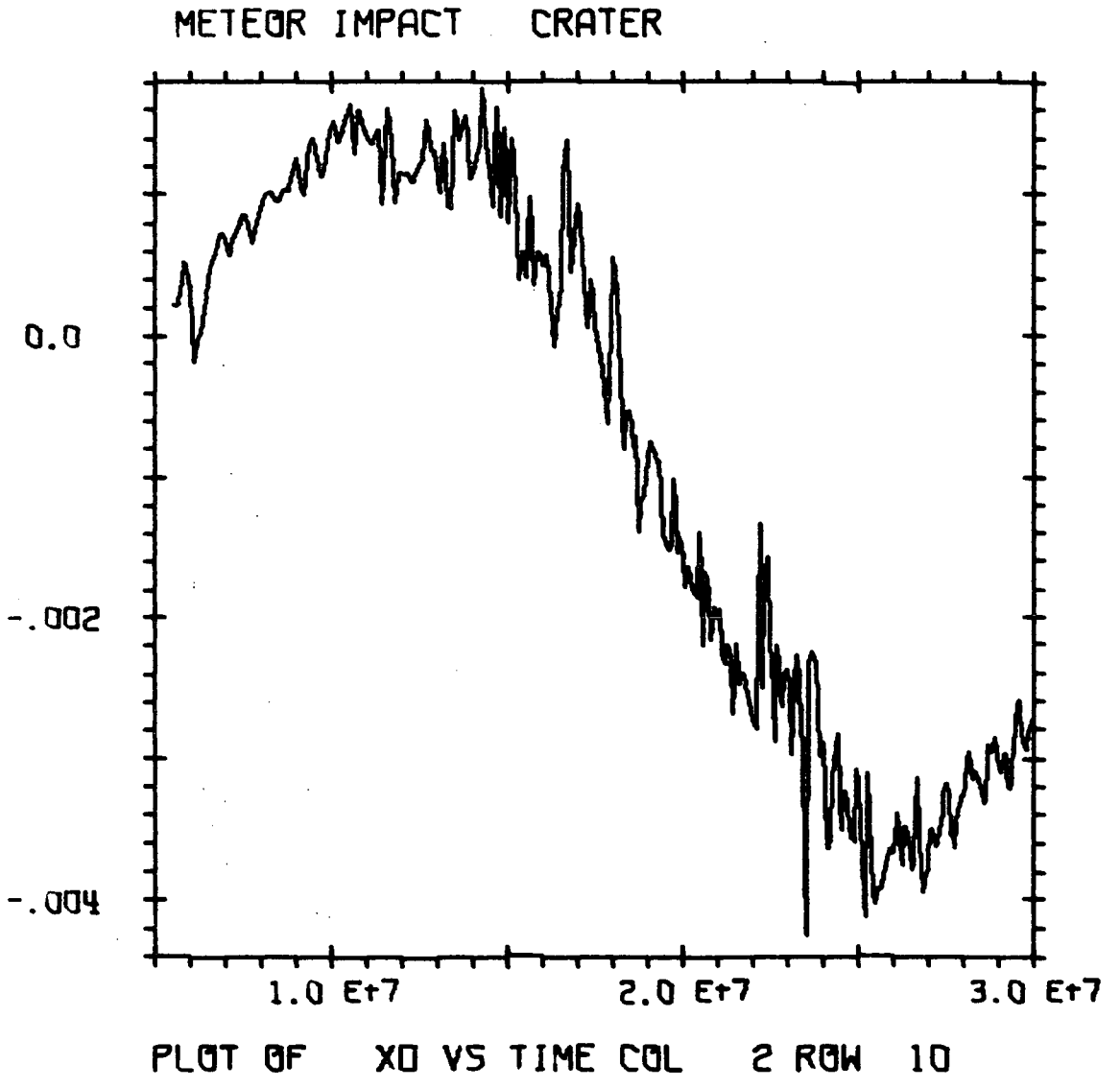
METEOR IMPACT CRATER
0.0
-.002
-.004
1.0 E+7
2.0 E+7
3.0 E+7
PLOT OF XO VS TIME COL 2 ROW 10

Figure B-44

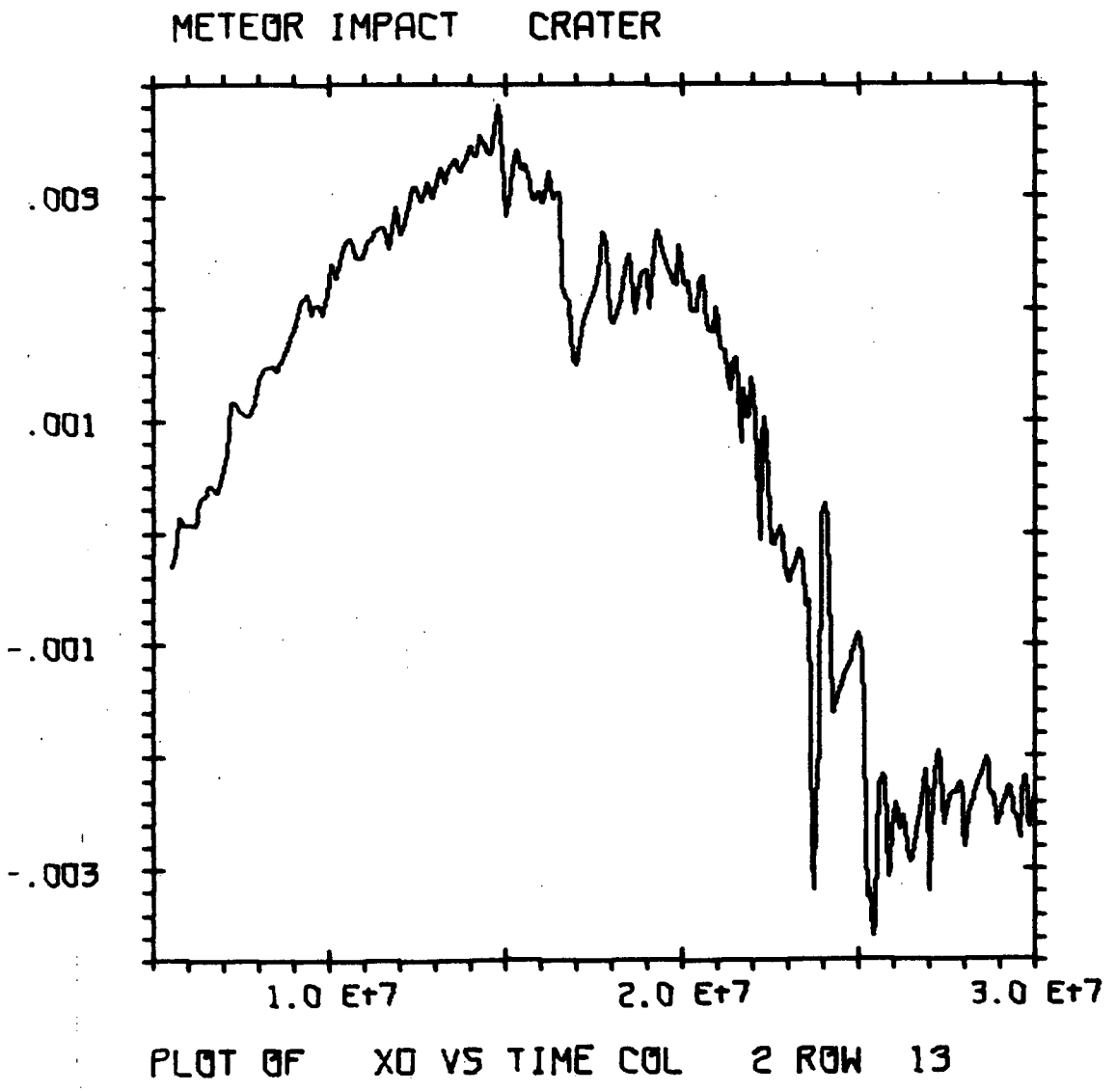
METEOR IMPACT CRATER
.003
.001
-.001
-.003
1.0 E+7
2.0 E+7
3.0 E+7
PLOT OF XO VS TIME COL 2 ROW 13

Figure B-45

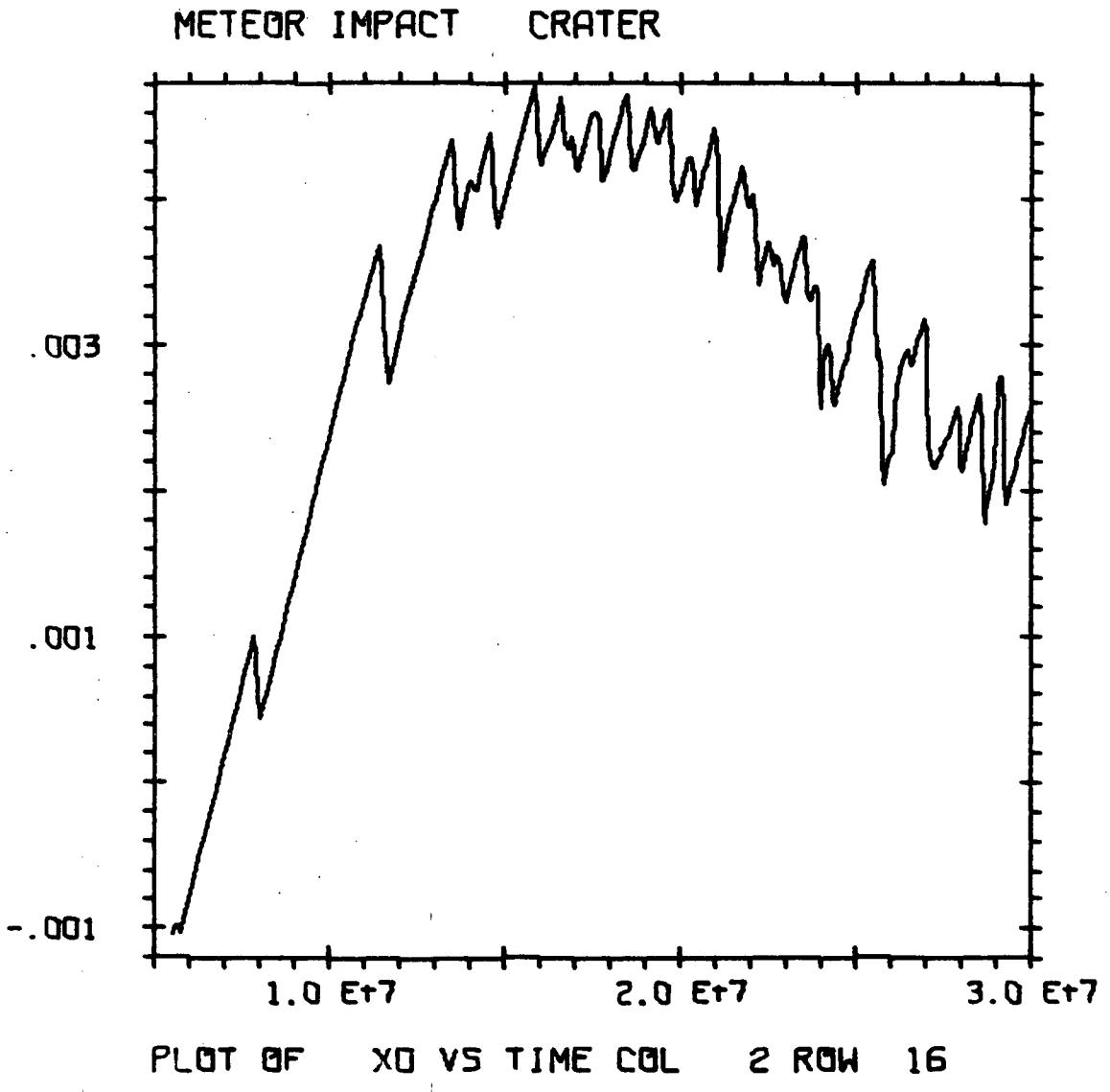
METEOR IMPACT CRATER
.003
.001
-.001
1.0 E+7
2.0 E+7
3.0 E+7
PLOT OF XO VS TIME COL 2 ROW 16

Figure B-46

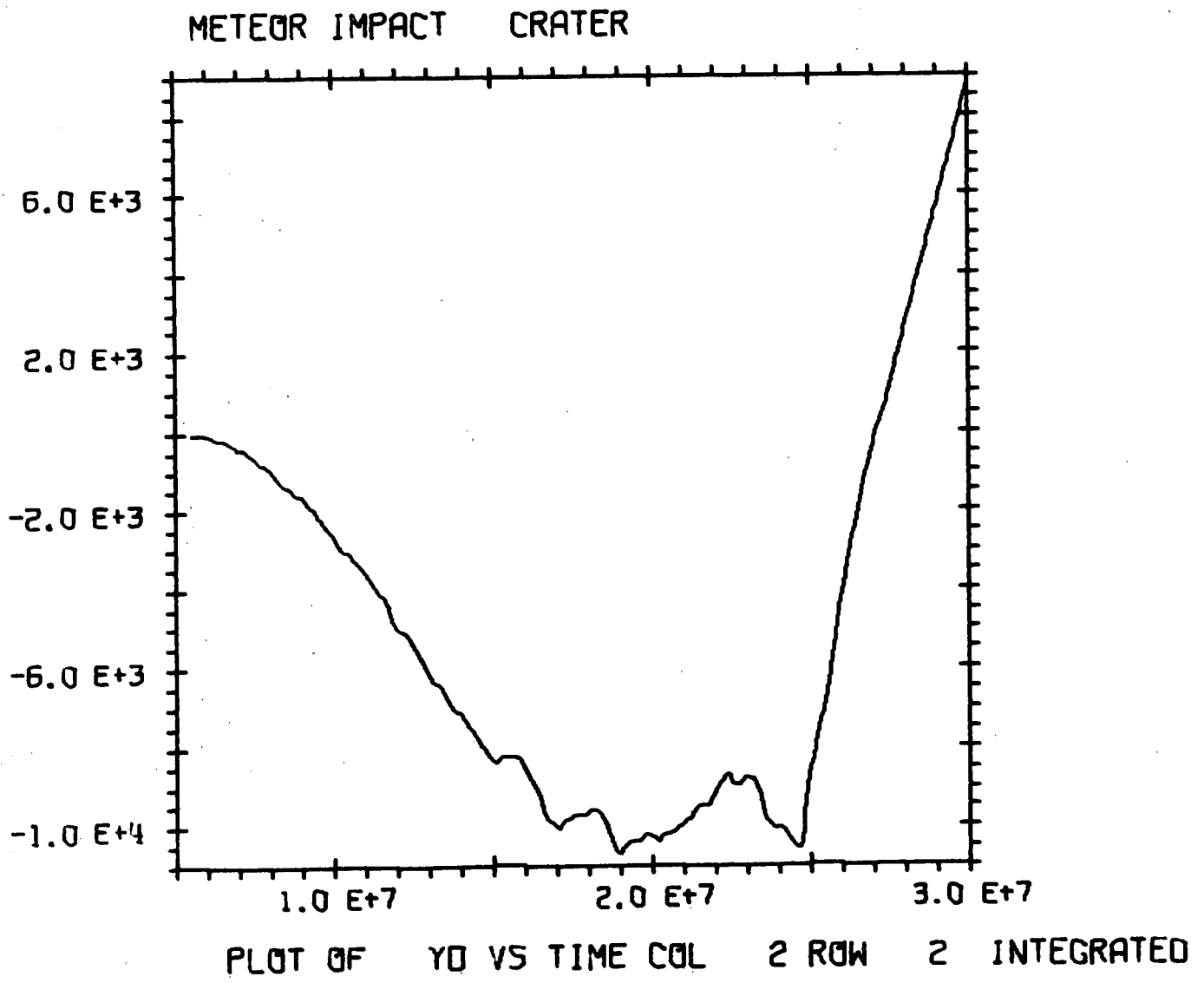
METEOR IMPACT CRATER
6.0 E+3
2.0 E+3
-2.0 E+3
-6.0 E+3
-1.0 E+4
1.0 E+7
2.0 E+7
3.0 E+7
PLOT OF YO VS TIME COL 2 ROW 2 INTEGRATED

Figure B-47

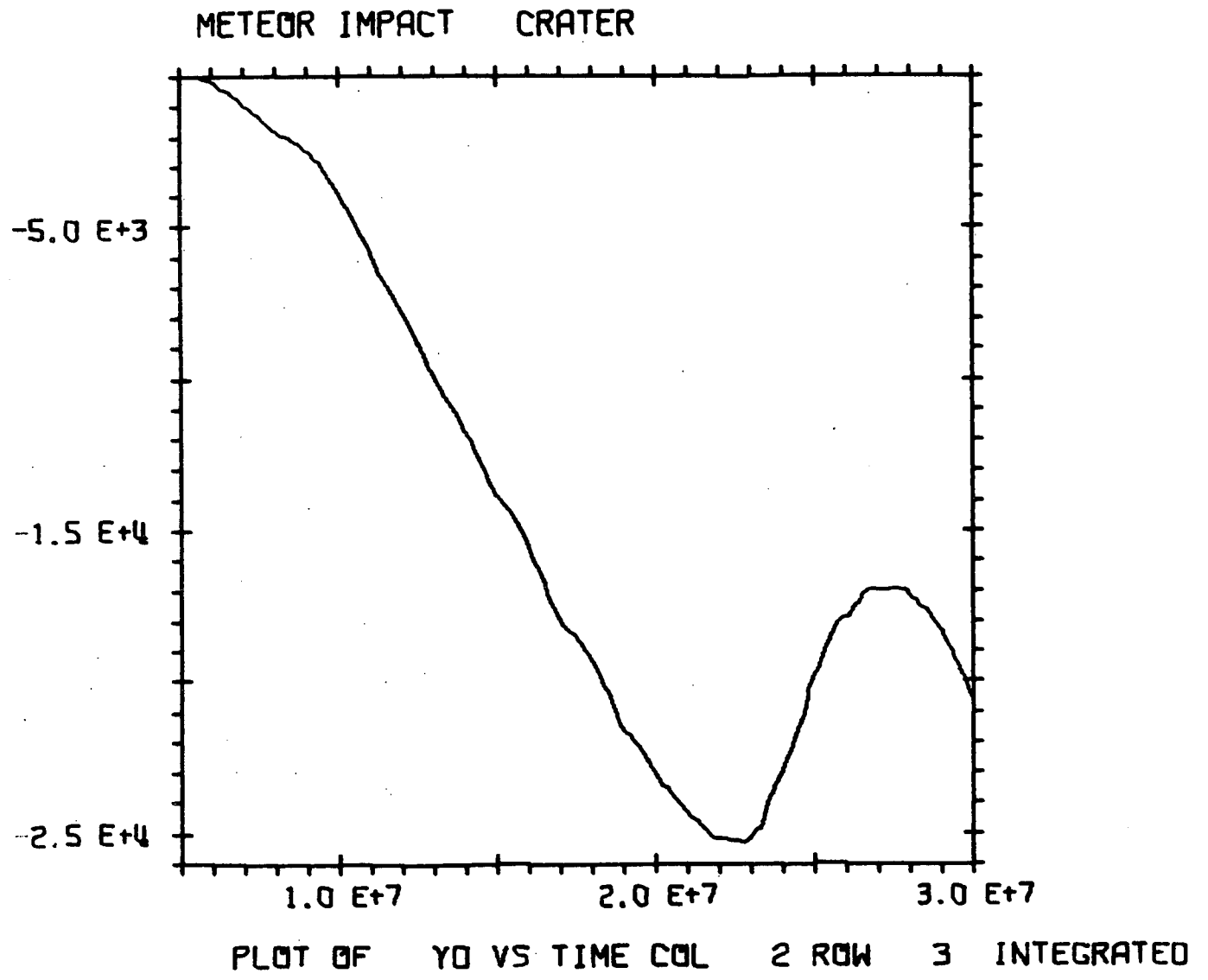
METEOR IMPACT CRATER
-5.0 E+3
-1.5 E+4
-2.5 E+4
1.0 E+7
2.0 E+7
3.0 E+7
PLOT OF YO VS TIME COL 2 ROW 3 INTEGRATED

Figure B-48

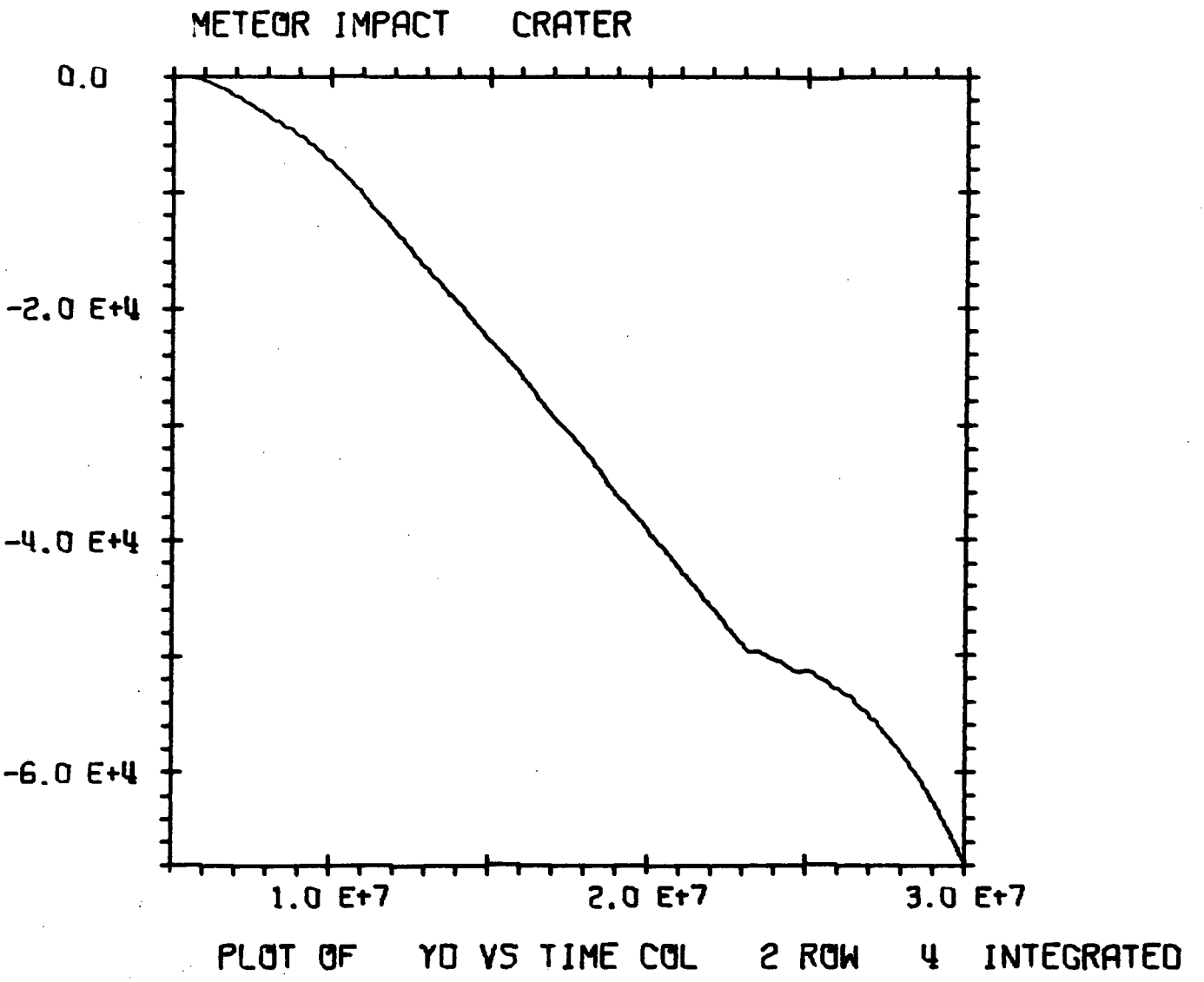
METEOR IMPACT CRATER
0.0
-2.0 E+4
-4.0 E+4
-6.0 E+4
1.0 E+7
2.0 E+7
3.0 E+7
PLOT OF YO VS TIME COL 2 ROW 4 INTEGRATED

Figure B-49

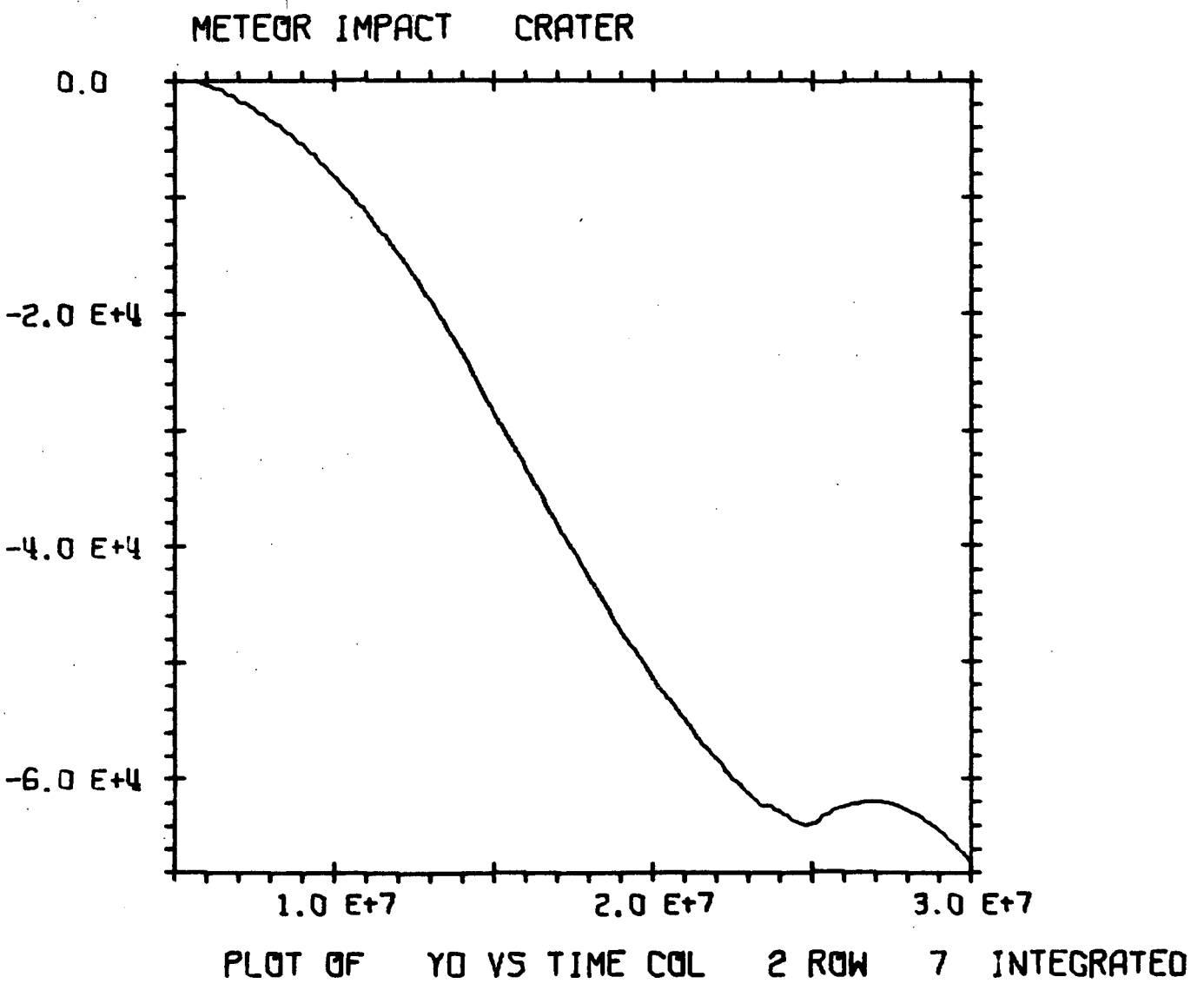
METEOR IMPACT CRATER
0.0
-2.0 E+4
-4.0 E+4
-6.0 E+4
1.0 E+7
2.0 E+7
3.0 E+7
PLOT OF YO VS TIME COL 2 ROW 7 INTEGRATED

Figure B-50

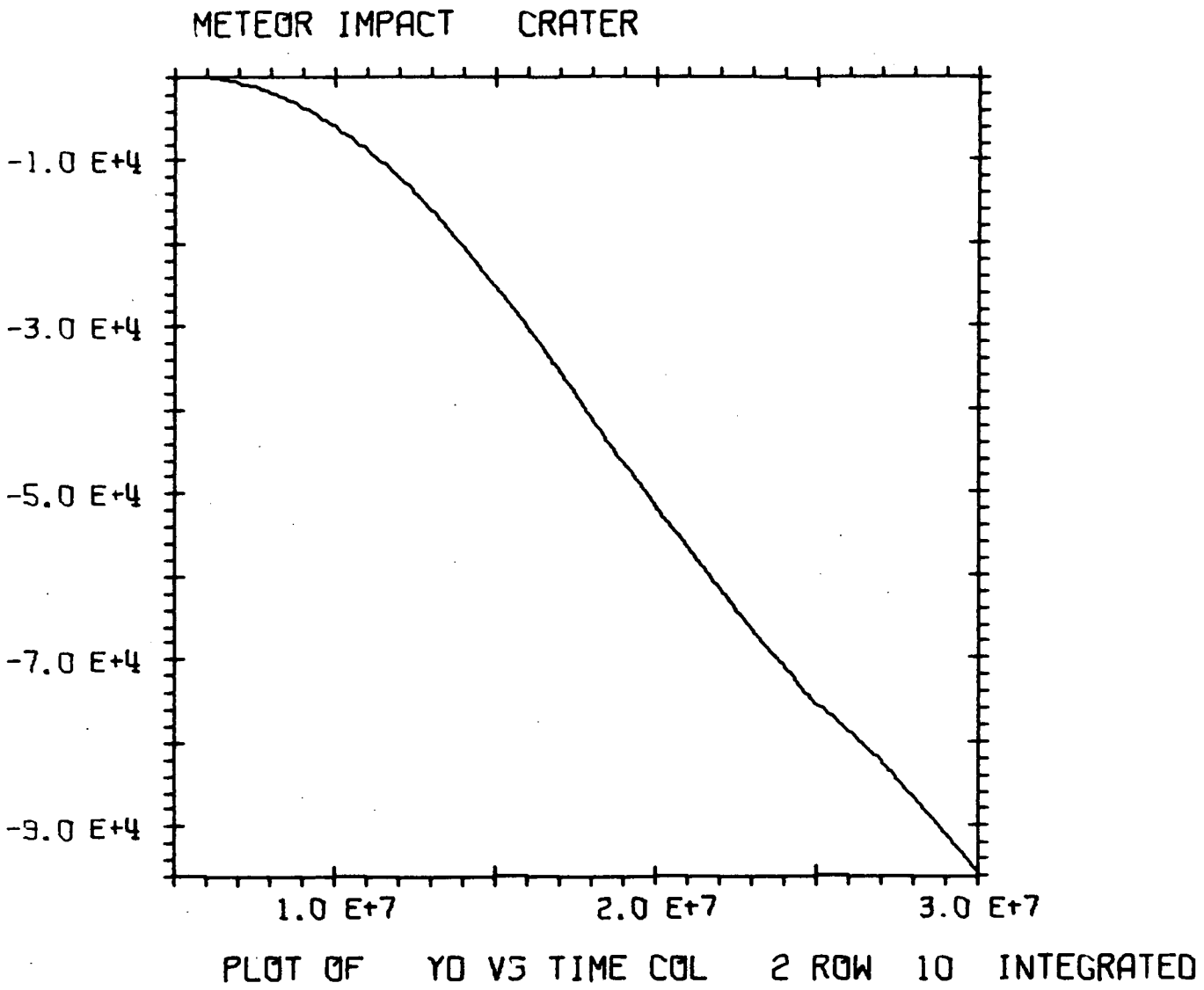
METEOR IMPACT CRATER
-1.0 E+4
-3.0 E+4
-5.0 E+4
-7.0 E+4
-9.0 E+4
1.0 E+7
2.0 E+7
3.0 E+7
PLOT OF YO VS TIME COL 2 ROW 10 INTEGRATED

Figure B-52

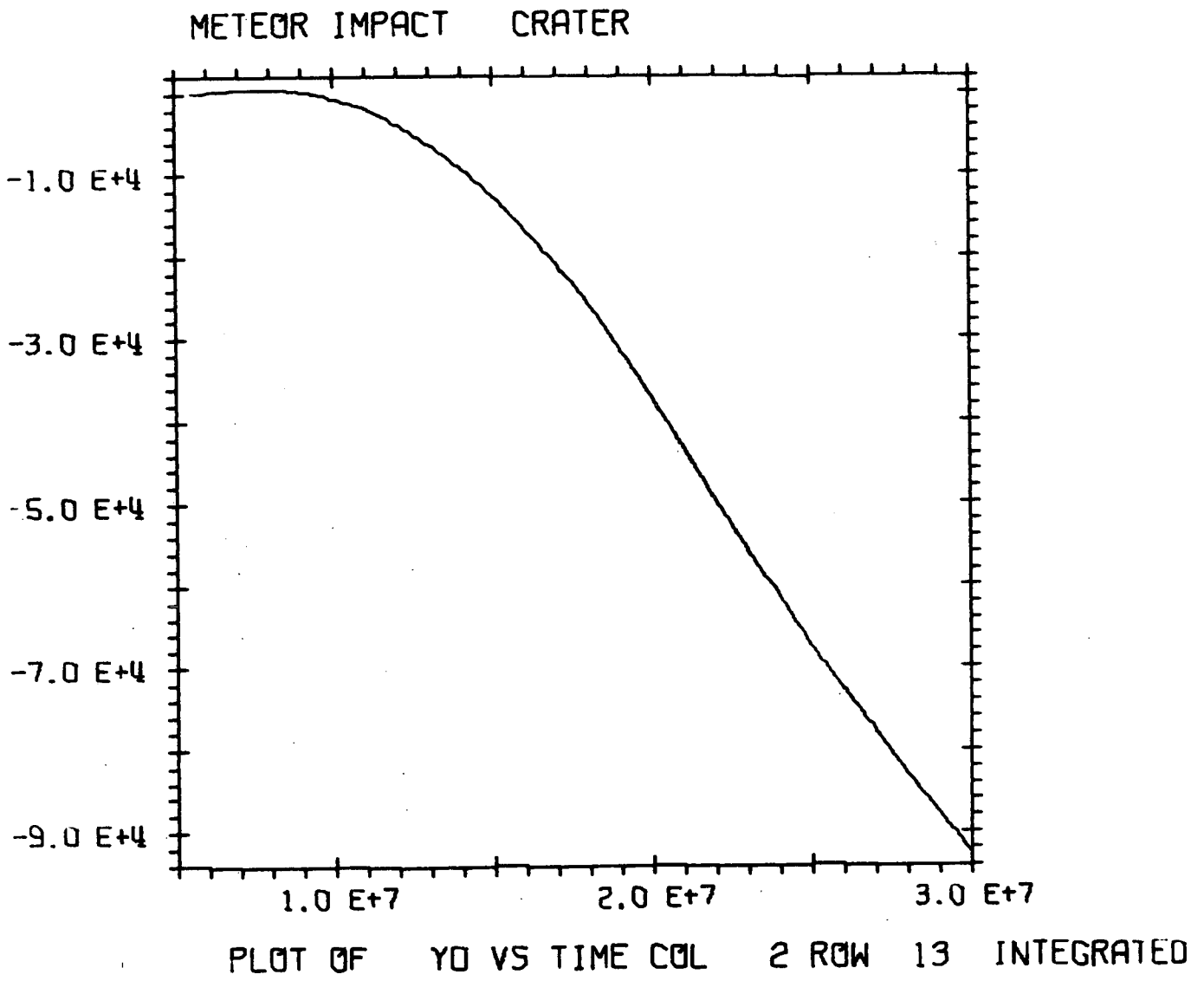
METEOR IMPACT CRATER
-1.0 E+4
-3.0 E+4
-5.0 E+4
-7.0 E+4
-9.0 E+4
1.0 E+7
2.0 E+7
3.0 E+7
PLOT OF YO VS TIME COL 2 ROW 13 INTEGRATED

Figure B-53

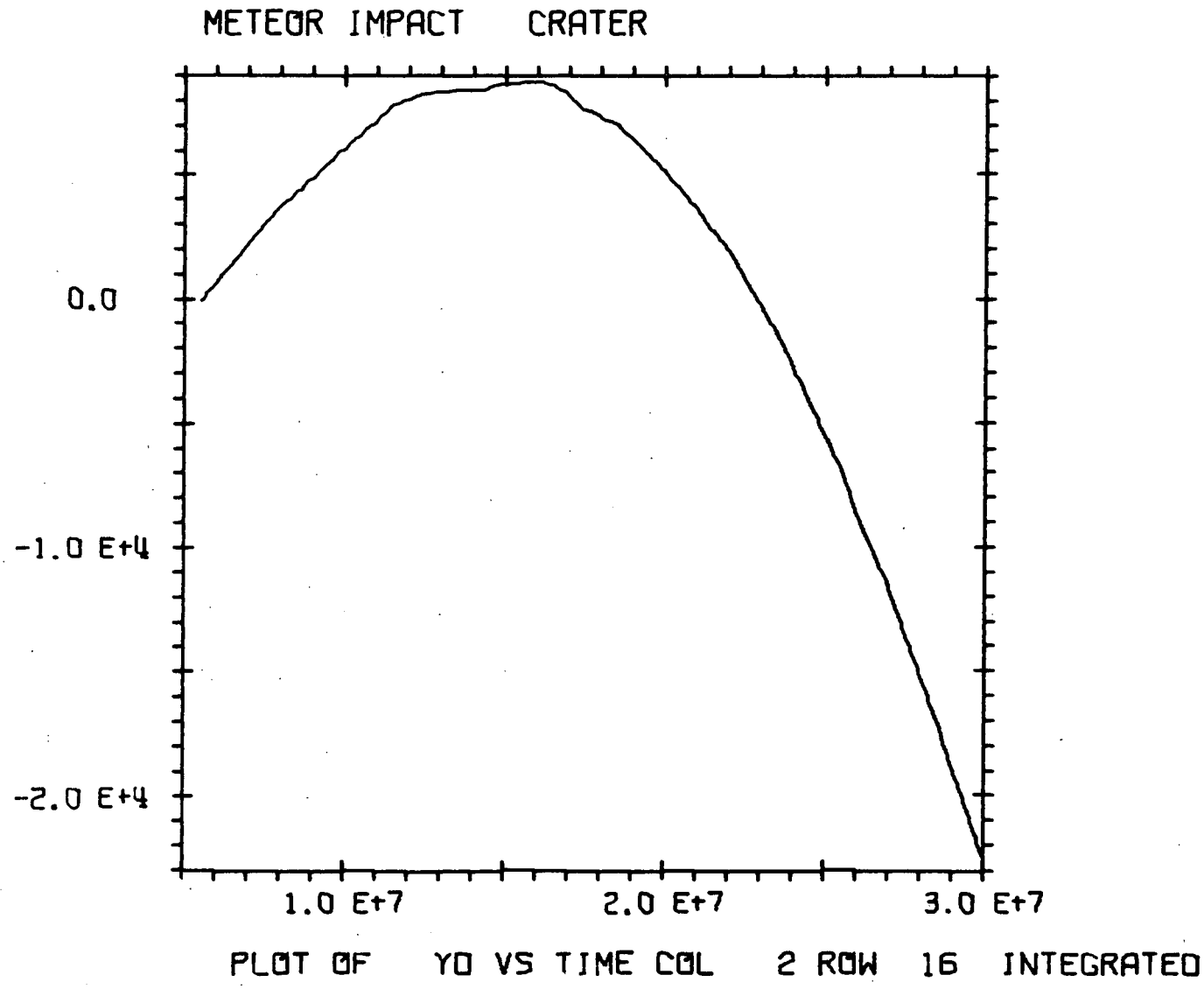
METEOR IMPACT CRATER
0.0
-1.0 E+4
-2.0 E+4
1.0 E+7
2.0 E+7
3.0 E+7
PLOT OF YO VS TIME COL 2 ROW 16 INTEGRATED

Figure B-53

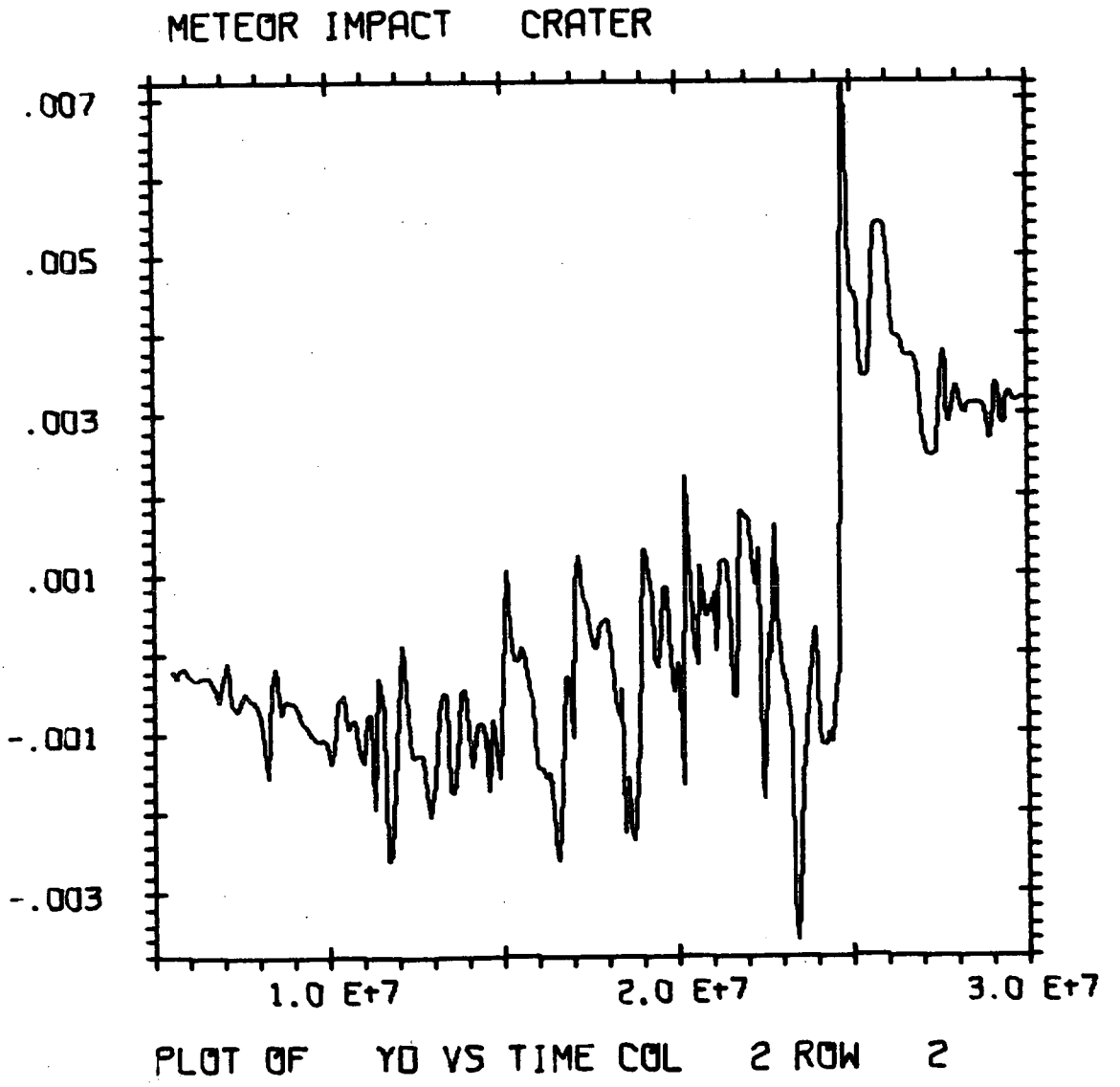
METEOR IMPACT CRATER
.007
.005
.003
.001
-.001
-.003
1.0 E+7
2.0 E+7
3.0 E+7
PLOT OF YO VS TIME COL 2 ROW 2

Figure B-54

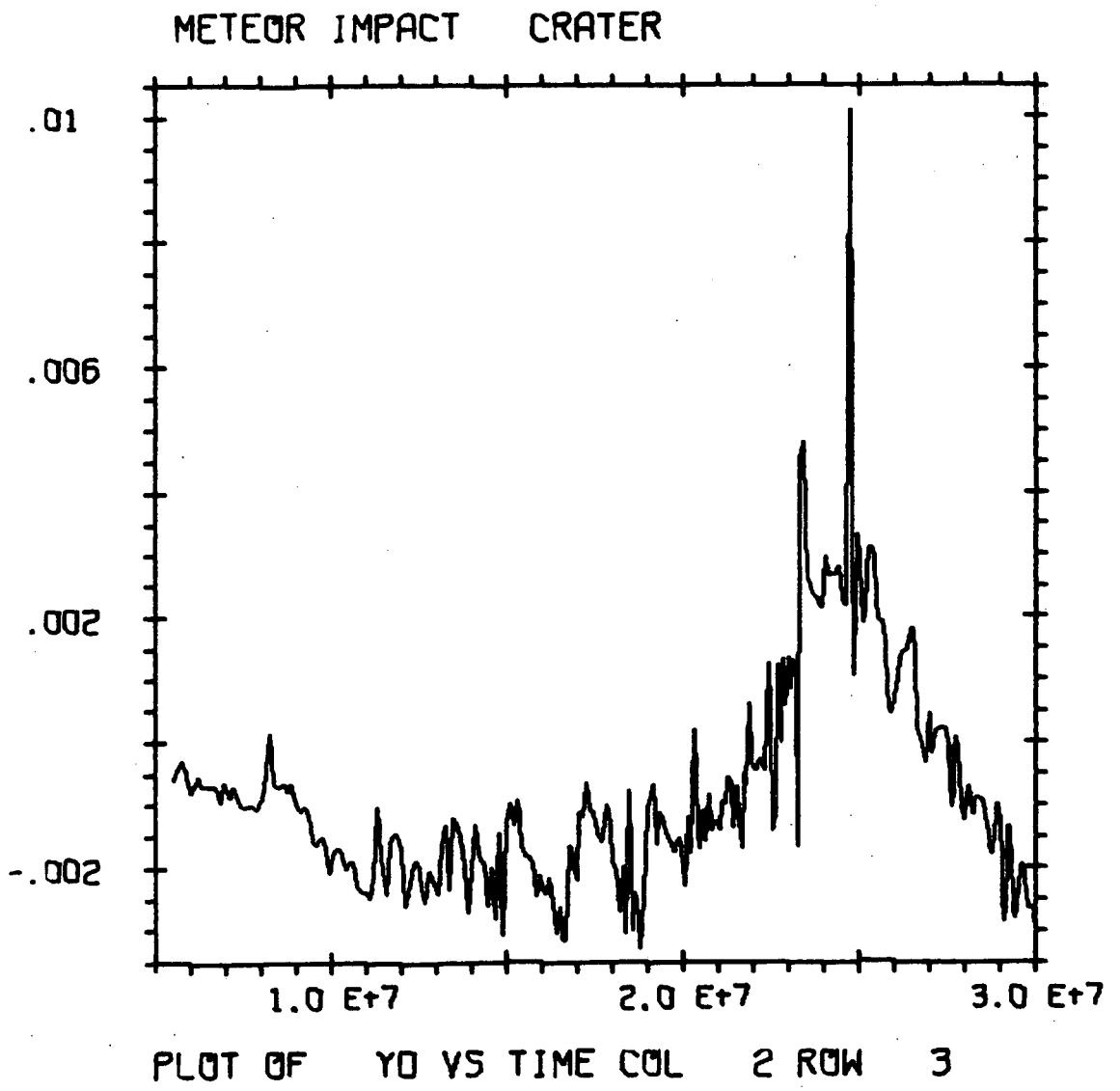
METEOR IMPACT CRATER
.01
.006
.002
-.002
1.0 E+7
2.0 E+7
3.0 E+7
PLOT OF YO VS TIME COL 2 ROW 3

Figure B-55

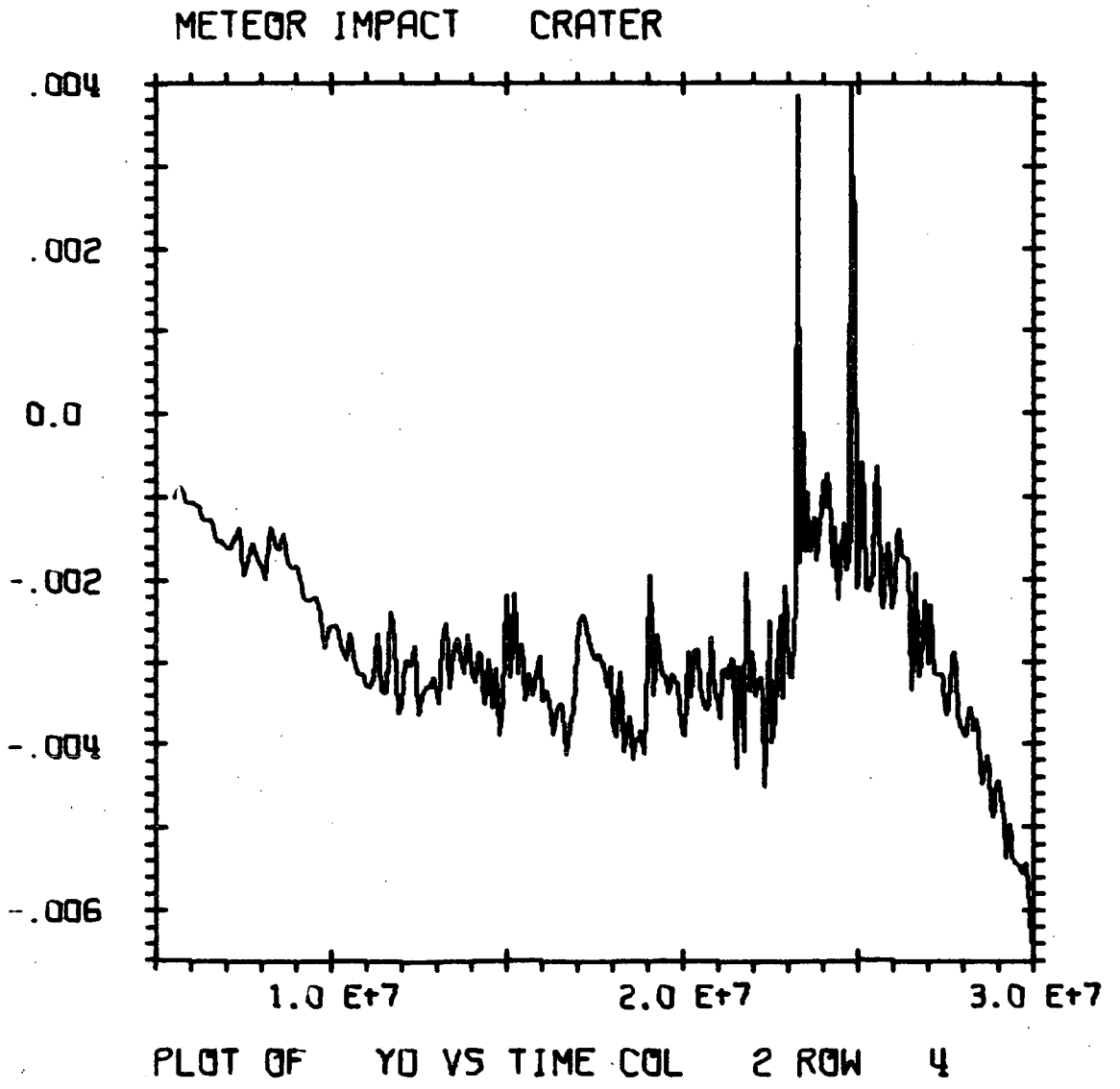
METEOR IMPACT CRATER
.004
.002
0.0
-.002
-.004
-.006
1.0 E+7
2.0 E+7
3.0 E+7
PLOT OF YO VS TIME COL 2 ROW 4

Figure B-56

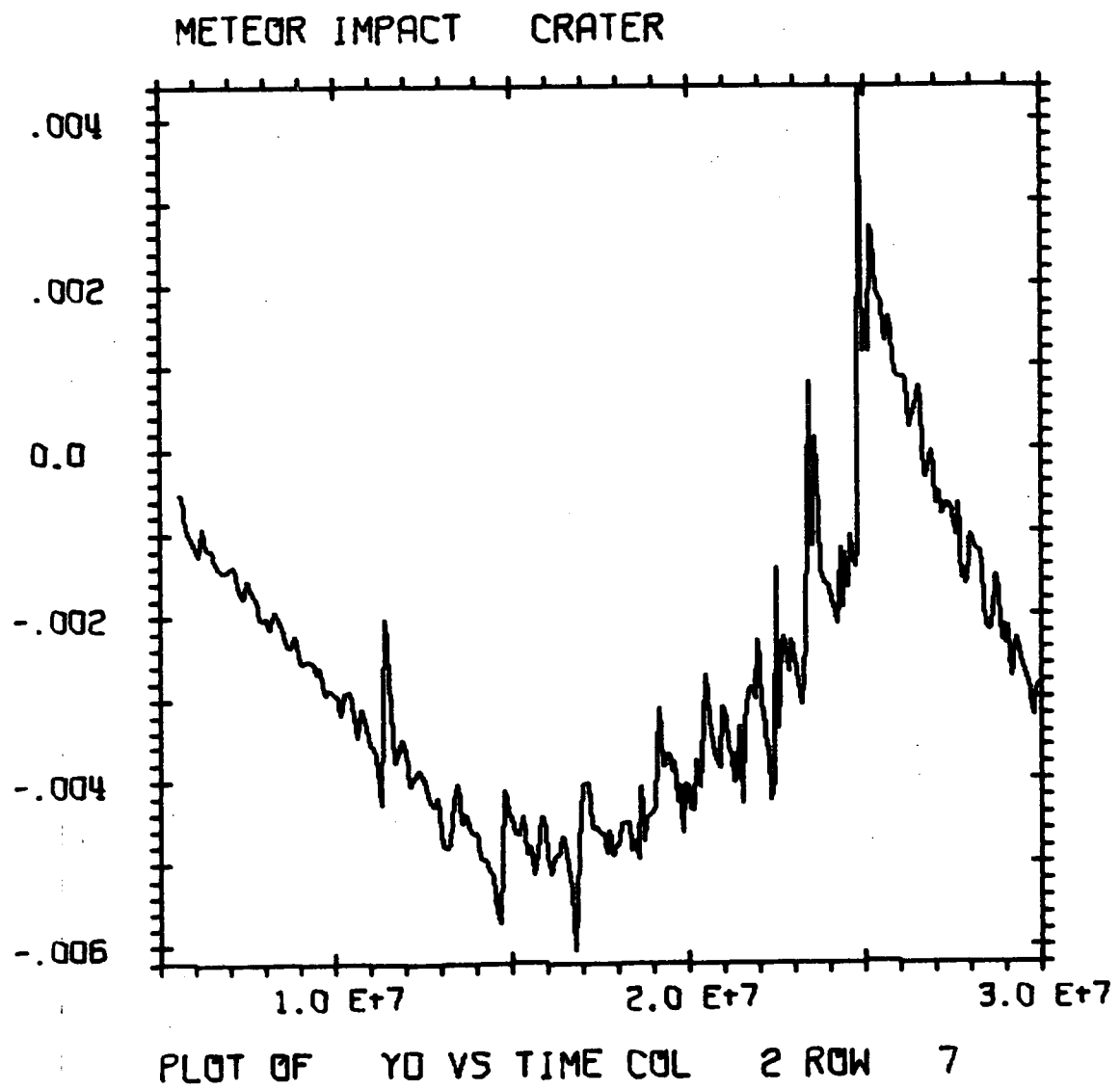
METEOR IMPACT CRATER
.004
.002
0.0
-.002
-.004
-.006
1.0 E+7
2.0 E+7
3.0 E+7
PLOT OF YO VS TIME COL 2 ROW 7

Figure B-57

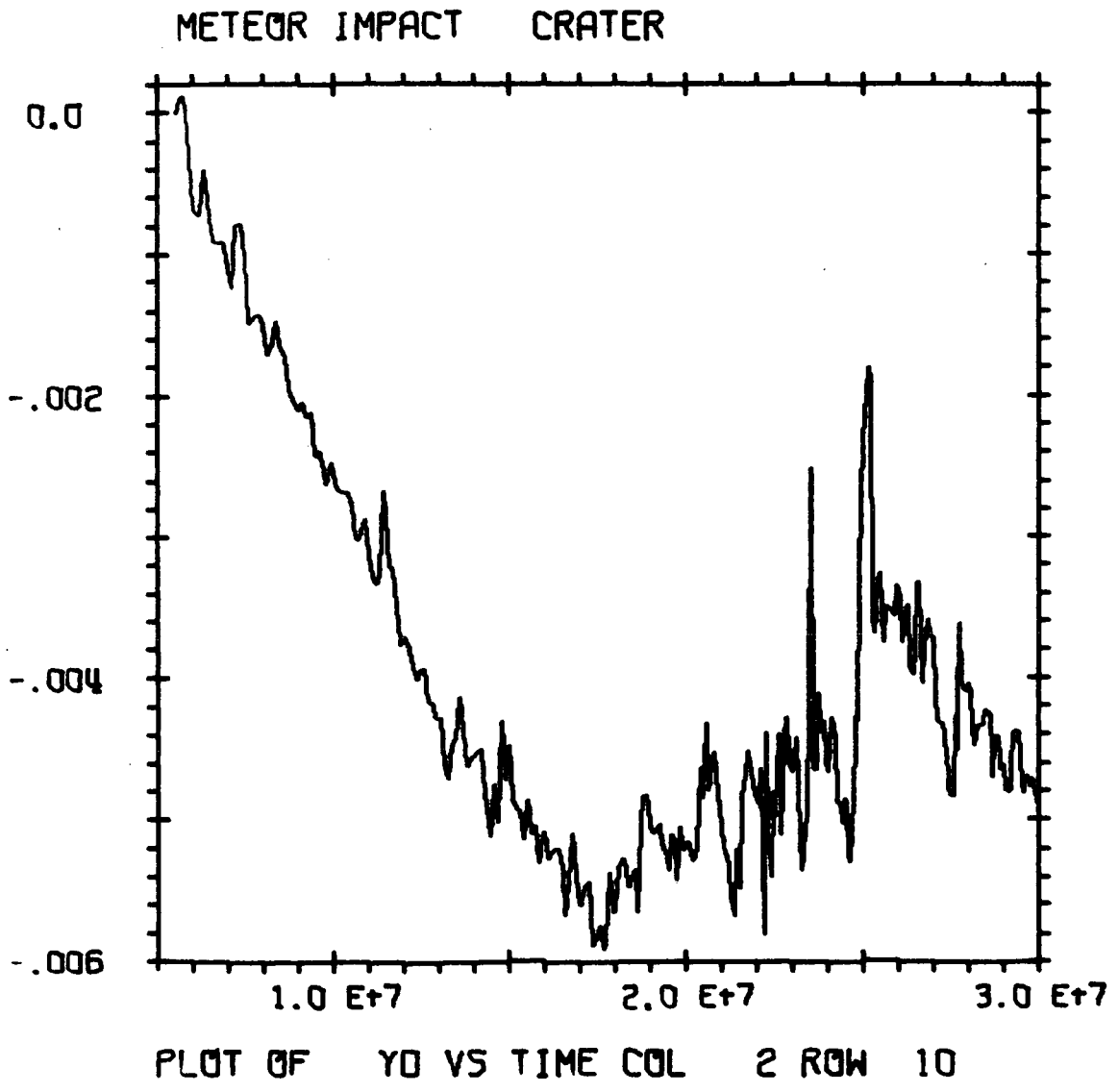
METEOR IMPACT CRATER
0.0
-.002
-.004
-.006
1.0 E+7
2.0 E+7
3.0 E+7
PLOT OF YO VS TIME COL 2 ROW 10

Figure B-58

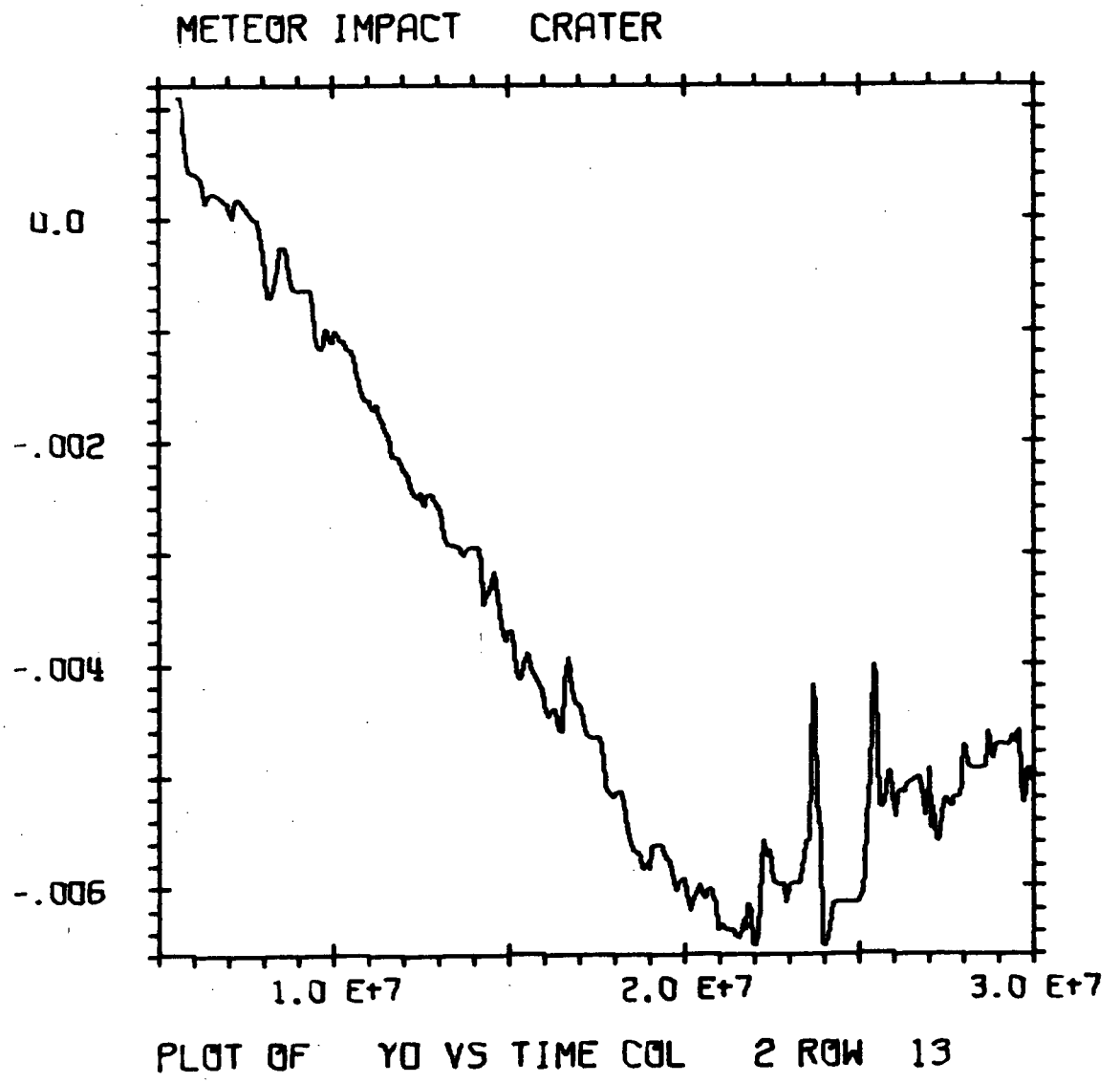
METEOR IMPACT CRATER
0.0
-.002
-.004
-.006
1.0 E+7
2.0 E+7
3.0 E+7
PLOT OF YO VS TIME COL 2 ROW 13

Figure B-59

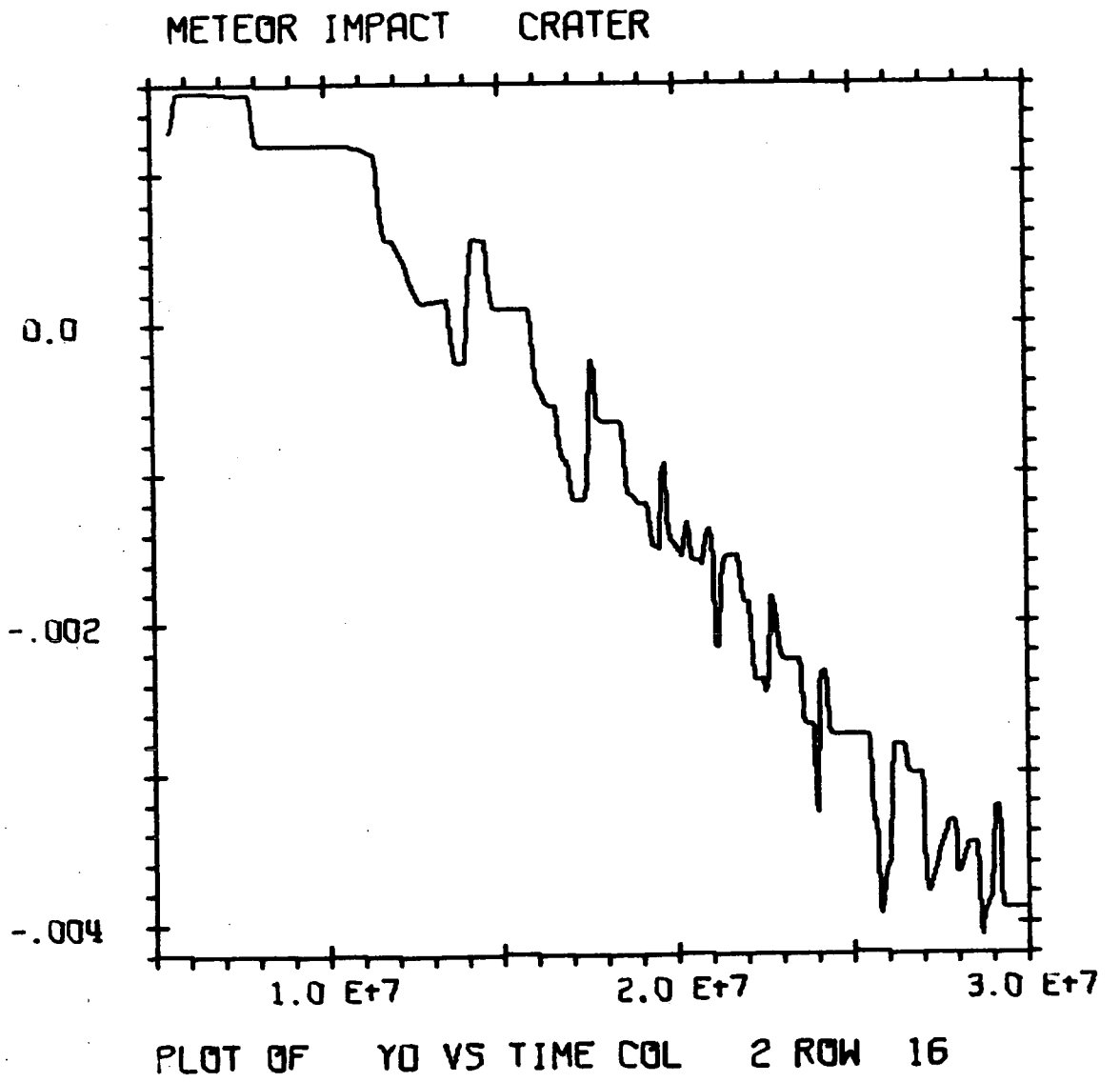
METEOR IMPACT CRATER
0.0
-.002
-.004
1.0 E+7
2.0 E+7
3.0 E+7
PLOT OF YO VS TIME COL 2 ROW 16

Figure B-60

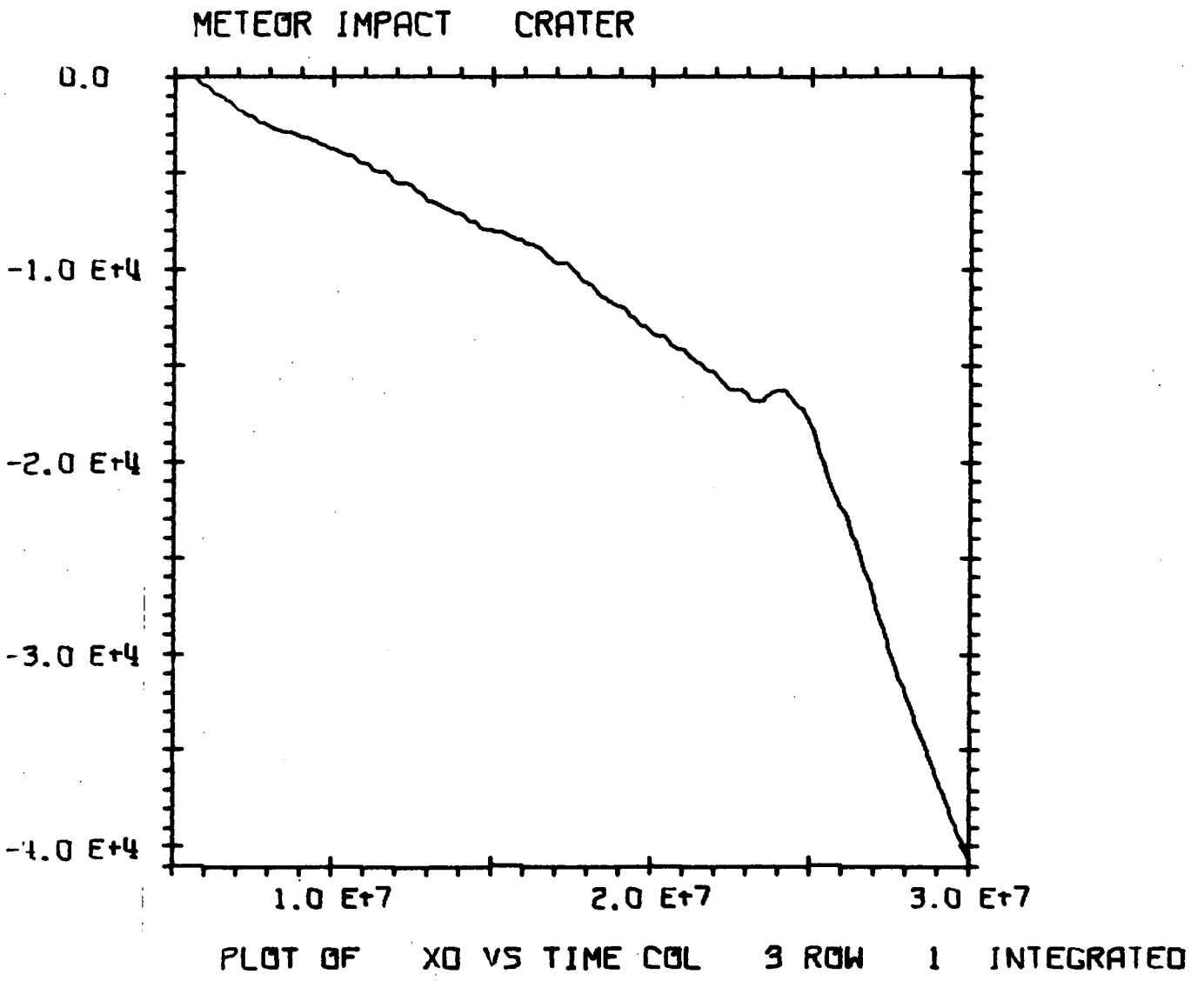
METEOR IMPACT CRATER
0.0
-1.0 E+4
-2.0 E+4
-3.0 E+4
-4.0 E+4
1.0 E+7
2.0 E+7
3.0 E+7
PLOT OF XO VS TIME COL 3 ROW 1 INTEGRATED

Figure B-61

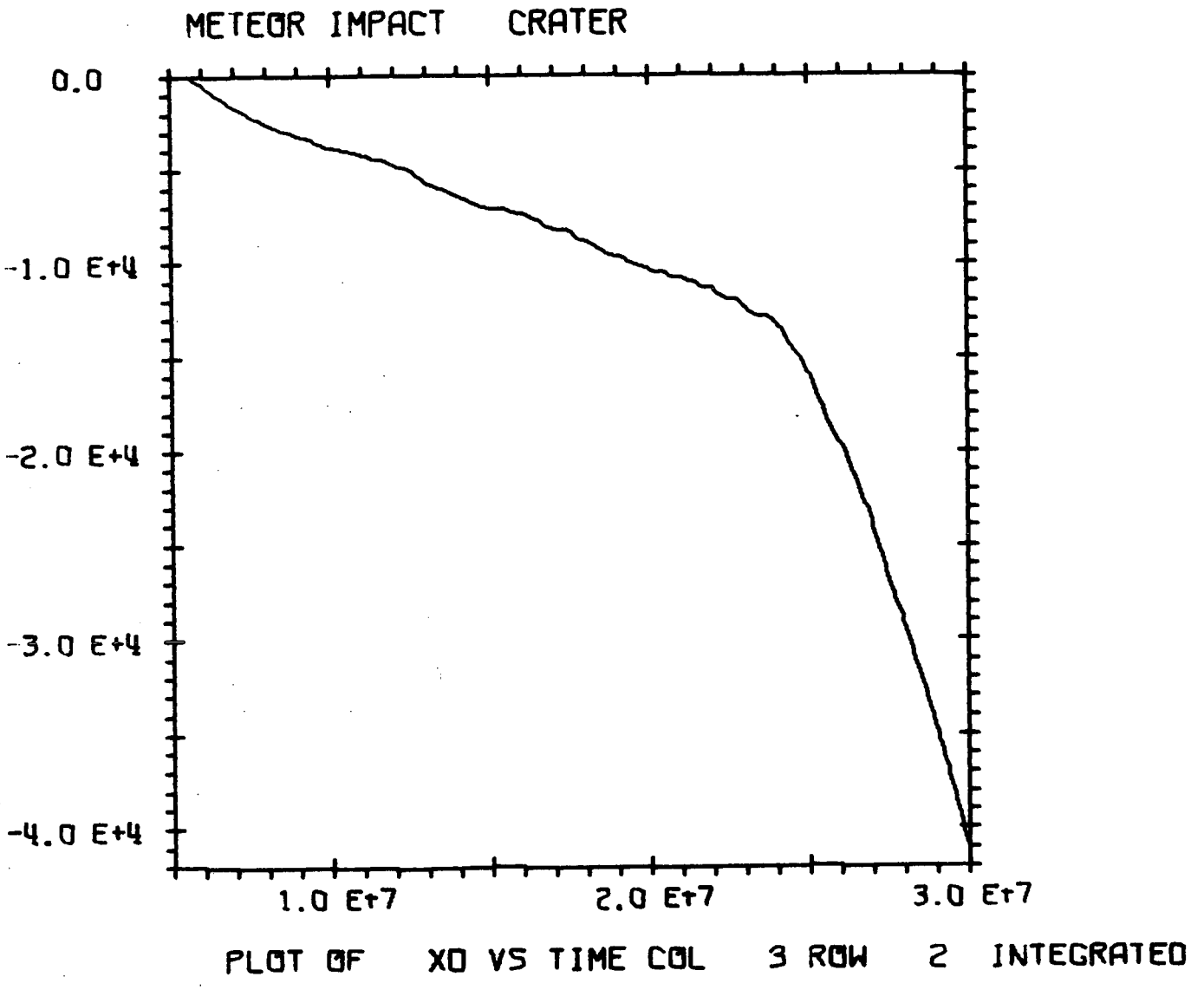
METEOR IMPACT CRATER
0.0
-1.0 E+4
-2.0 E+4
-3.0 E+4
-4.0 E+4
1.0 E+7
2.0 E+7
3.0 E+7
PLOT OF XO VS TIME COL 3 ROW 2 INTEGRATED

Figure B-62

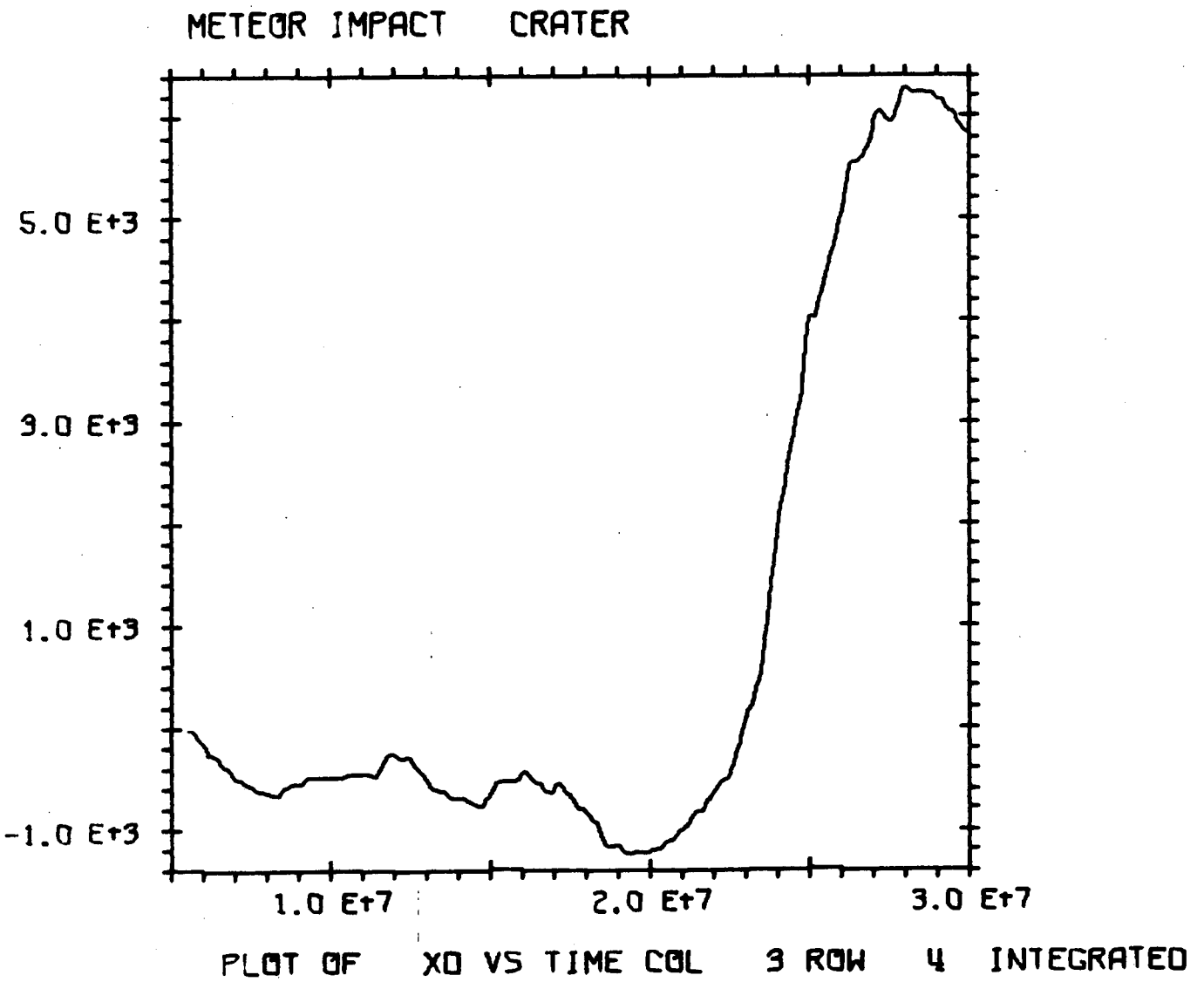
METEOR IMPACT CRATER
5.0 E+3
3.0 E+3
1.0 E+3
-1.0 E+3
1.0 E+7
2.0 E+7
3.0 E+7
PLOT OF XO VS TIME COL 3 ROW 4 INTEGRATED

Figure B-63

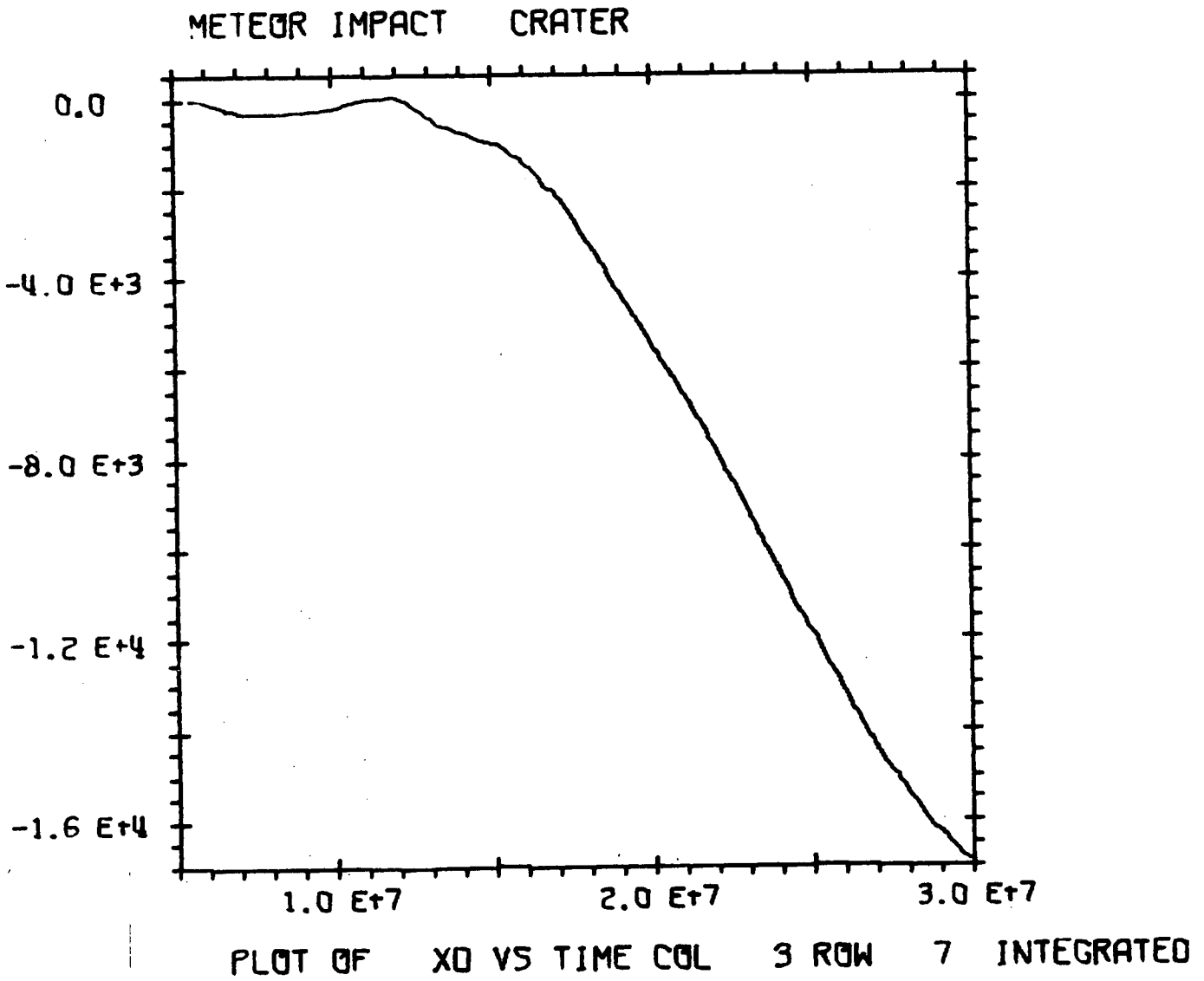
METEOR IMPACT CRATER
0.0
-4.0 E+3
-8.0 E+3
-1.2 E+4
-1.6 E+4
1.0 E+7
2.0 E+7
3.0 E+7
PLOT OF XO VS TIME COL 3 ROW 7 INTEGRATED

Figure B-64

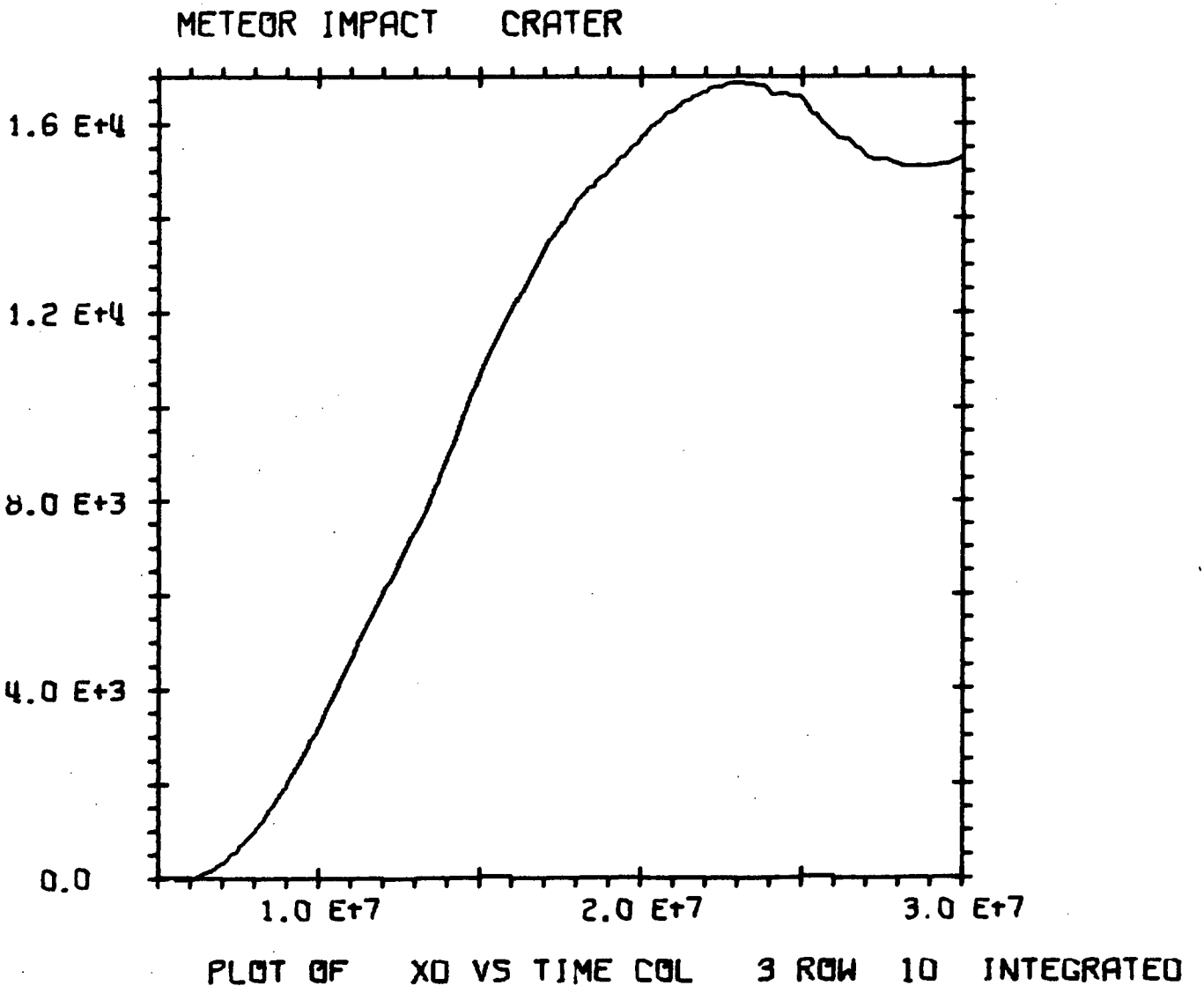
METEOR IMPACT CRATER
1.6 E+4
1.2 E+4
8.0 E+3
4.0 E+3
0.0
1.0 E+7
2.0 E+7
3.0 E+7
PLOT OF XO VS TIME COL 3 ROW 10 INTEGRATED

Figure B-65

4

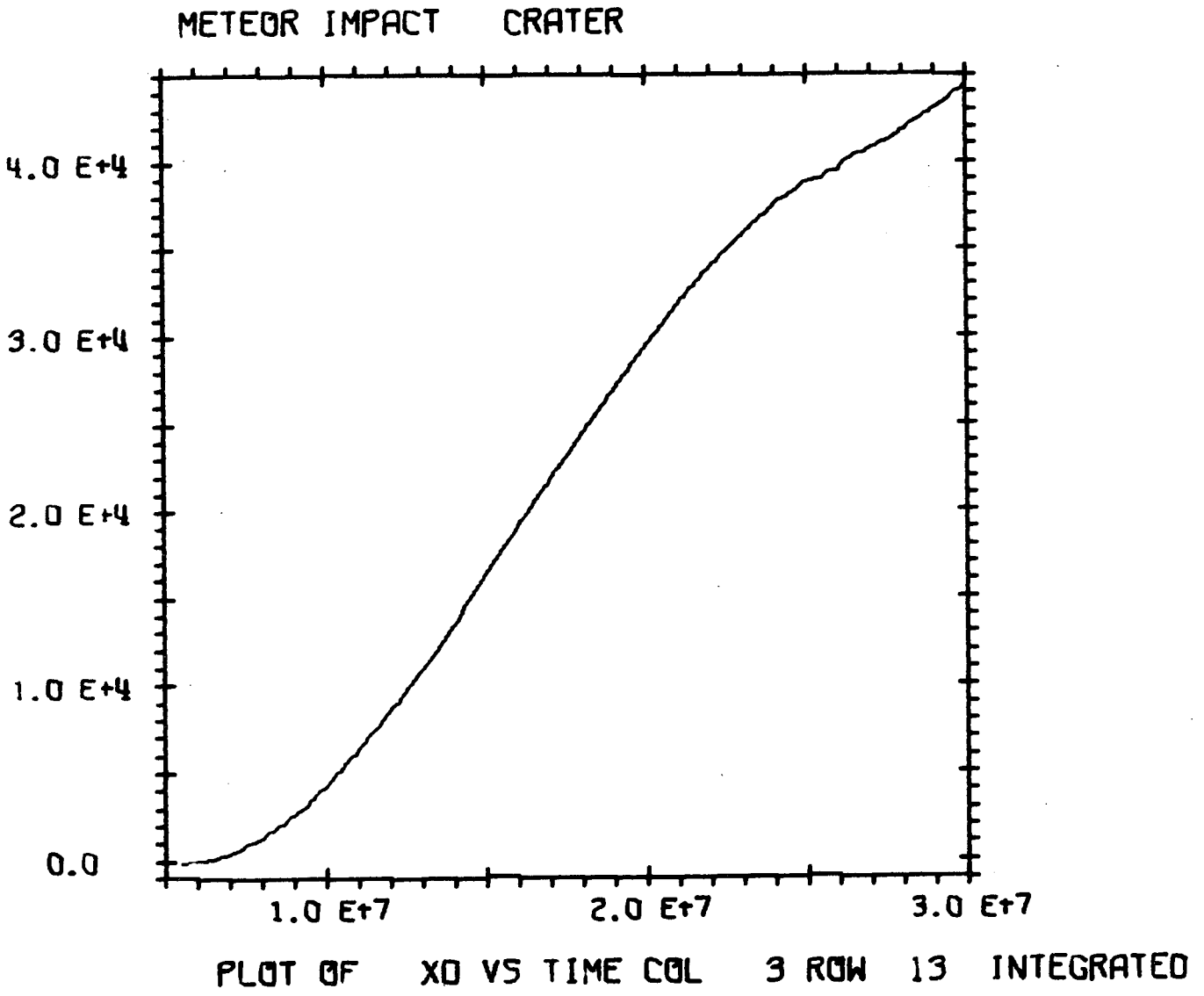
METEOR IMPACT CRATER
4.0 E+4
3.0 E+4
2.0 E+4
1.0 E+4
0.0
1.0 E+7
2.0 E+7
3.0 E+7
PLOT OF XO VS TIME COL 3 ROW 13 INTEGRATED

Figure B-66

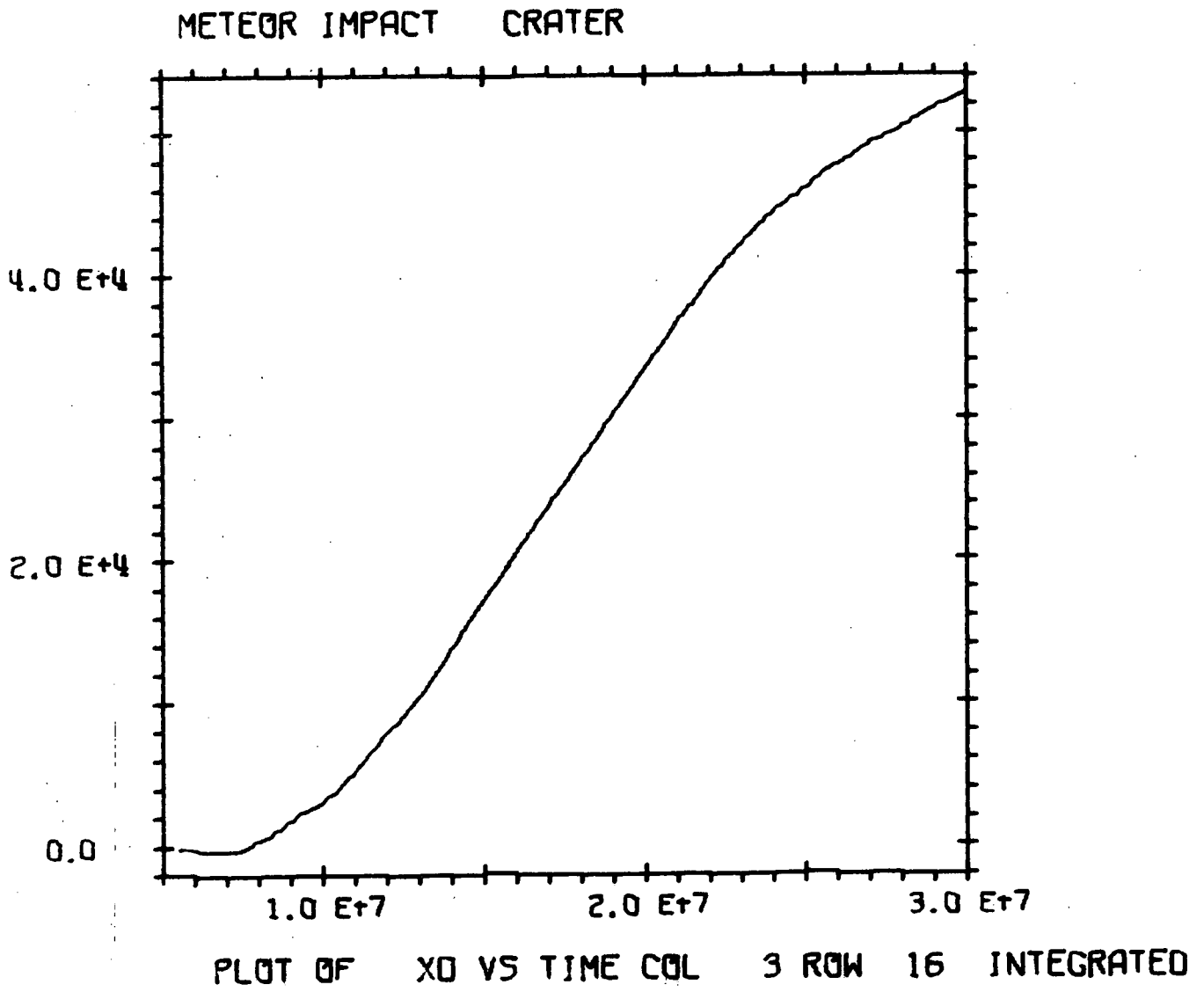
METEOR IMPACT CRATER
4.0 E+4
2.0 E+4
0.0
1.0 E+7
2.0 E+7
3.0 E+7
PLOT OF XO VS TIME COL 3 ROW 16 INTEGRATED

Figure B-67

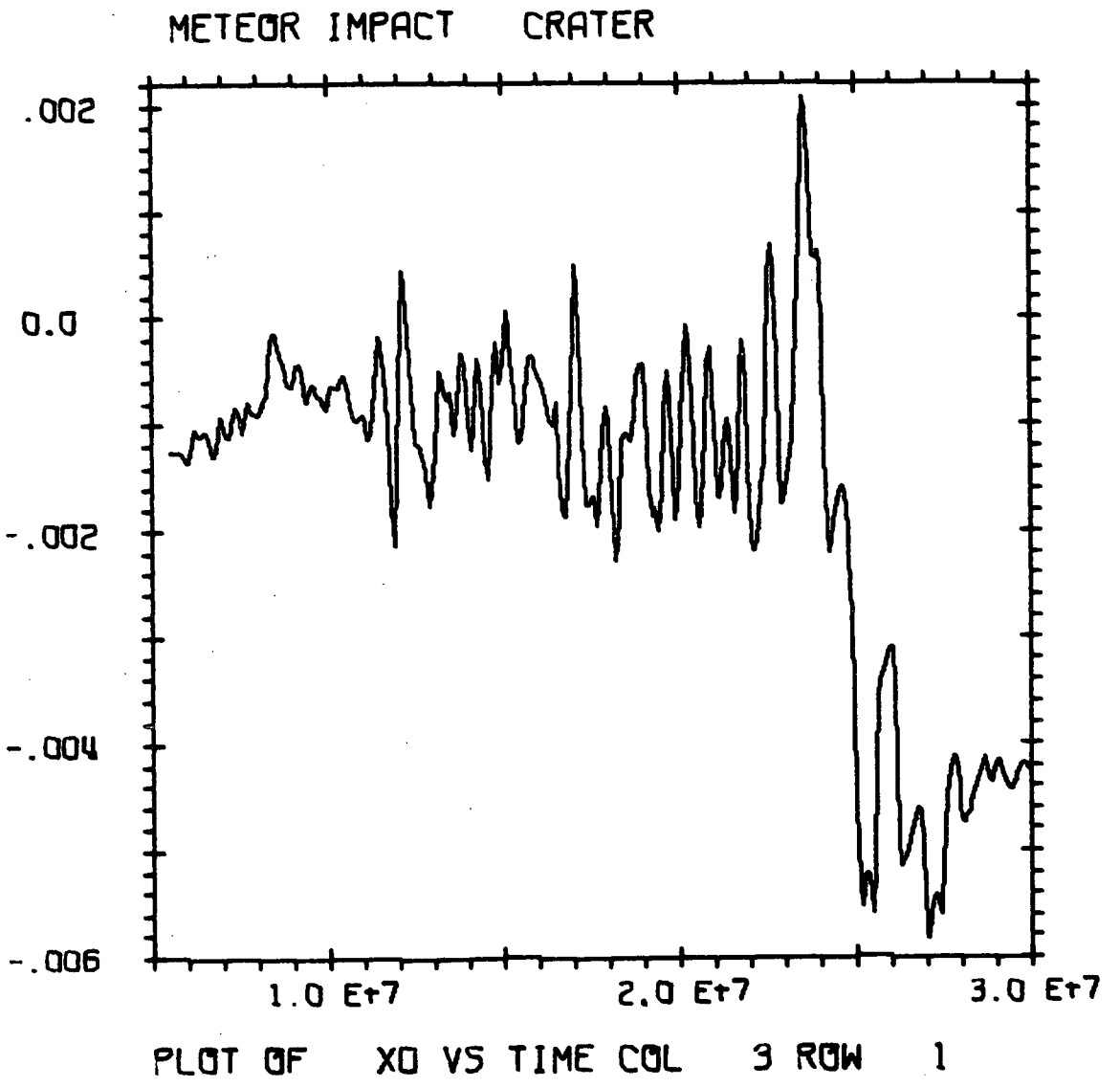
METEOR IMPACT CRATER
.002
0.0
-.002
-.004
-.006
1.0 E+7
2.0 E+7
3.0 E+7
PLOT OF XO VS TIME COL 3 ROW 1

Figure B-68

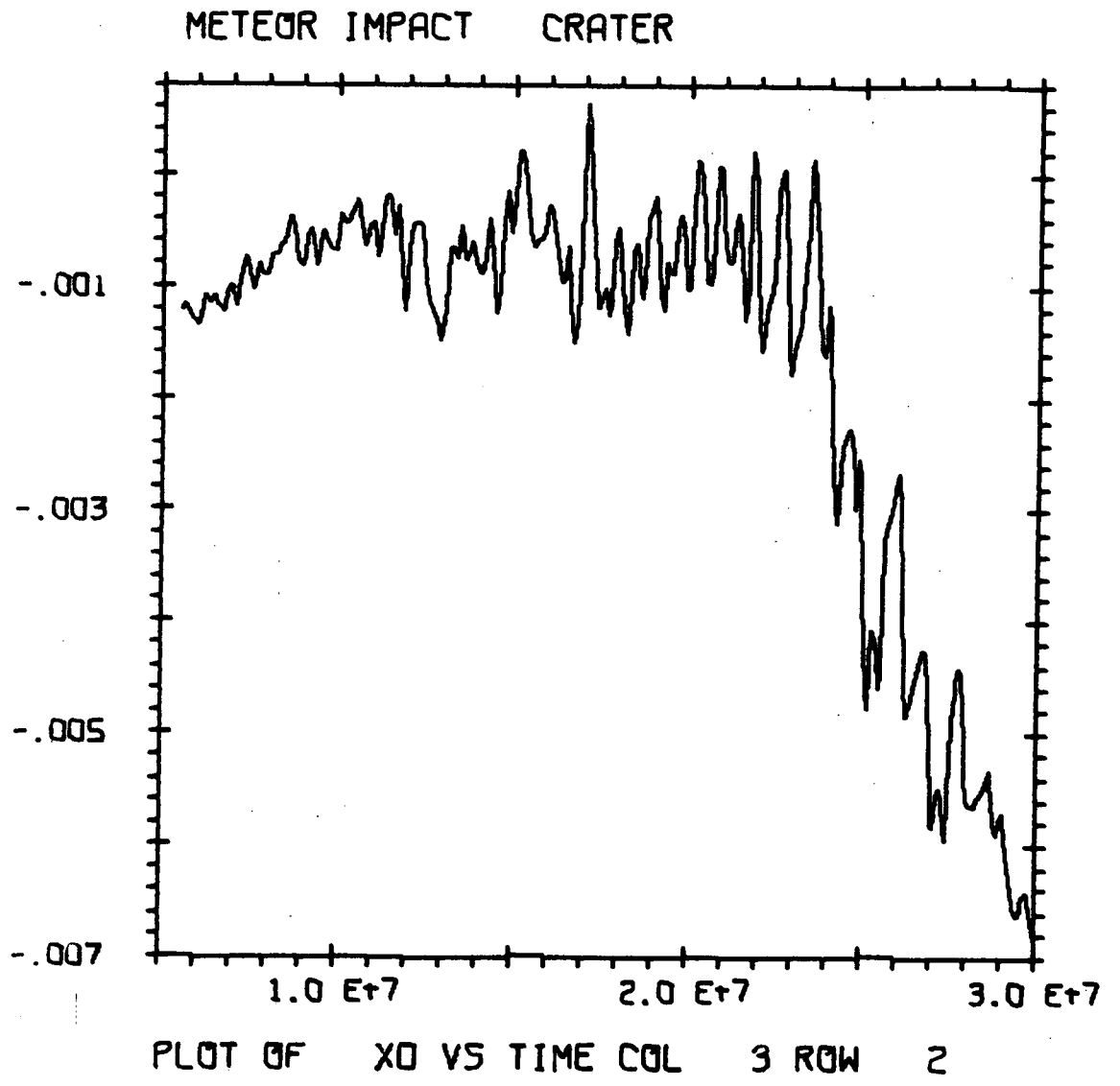
METEOR IMPACT CRATER
-.001
-.003
-.005
-.007
1.0 E+7
2.0 E+7
3.0 E+7
PLOT OF XO VS TIME COL 3 ROW 2

Figure B-69

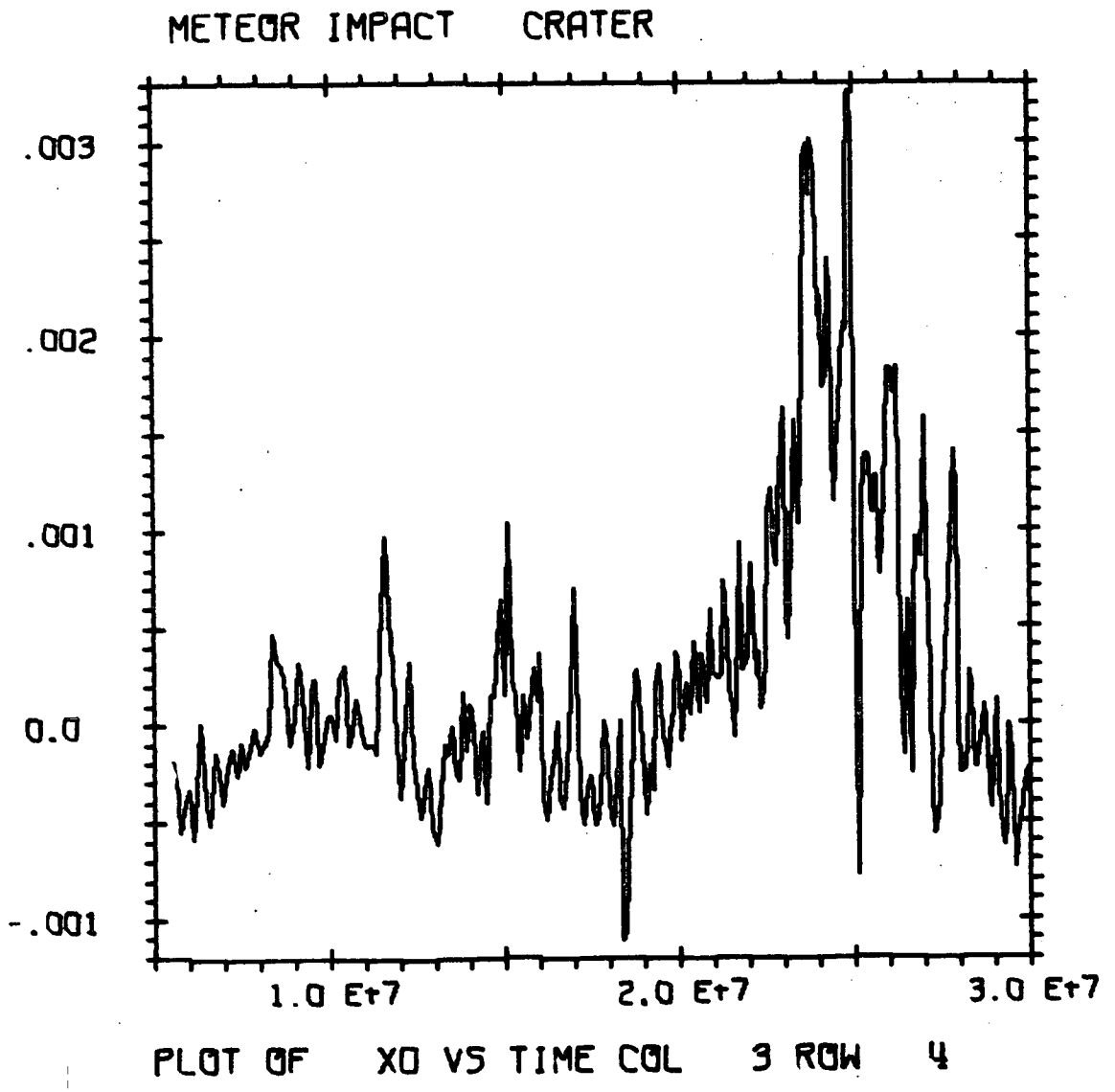
METEOR IMPACT CRATER
.003
.002
.001
0.0
-.001
1.0 E+7
2.0 E+7
3.0 E+7
PLOT OF XO VS TIME COL 3 ROW 4

Figure B-70

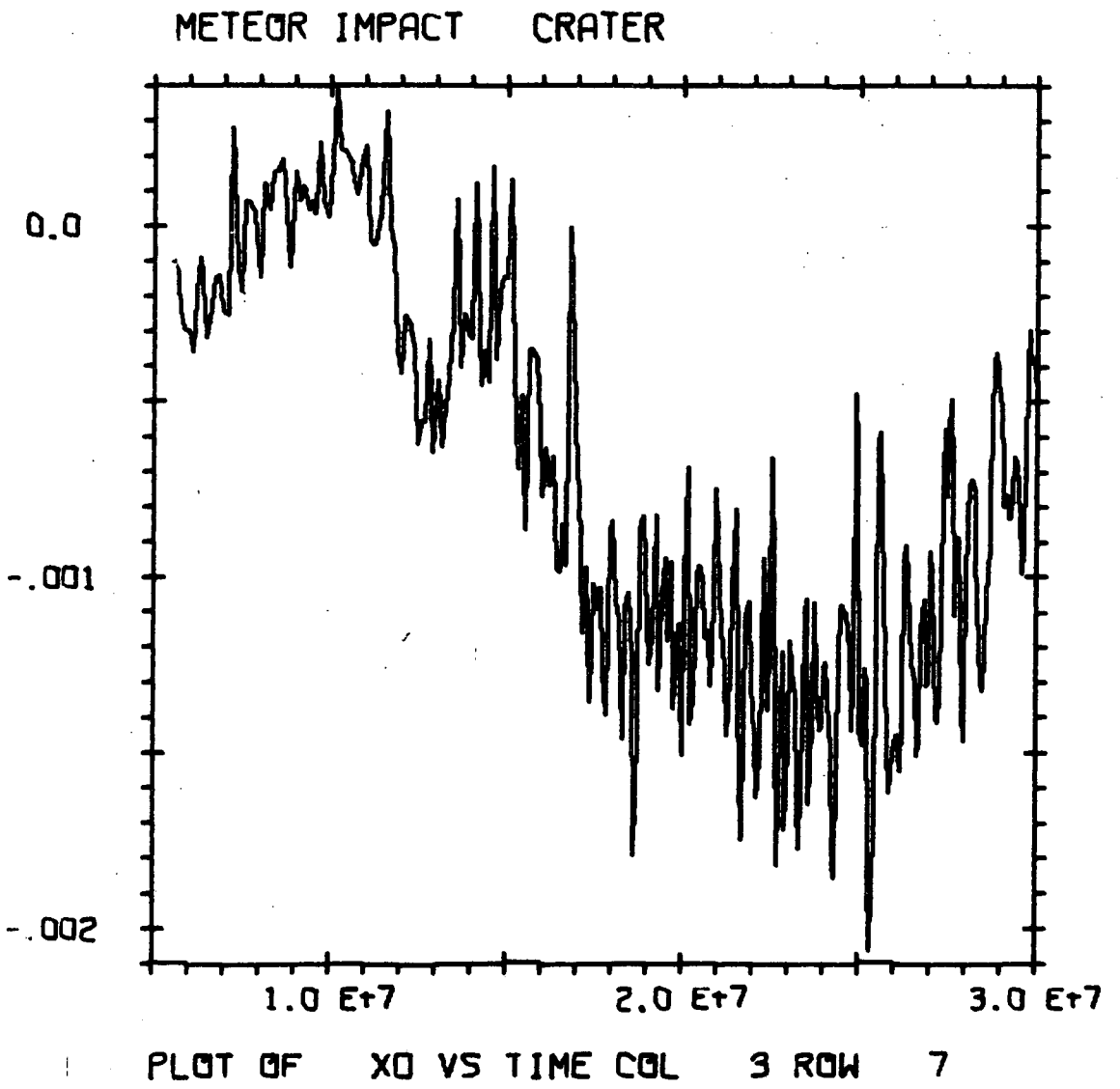
METEOR IMPACT CRATER
0.0
-.001
-.002
1.0 E+7
2.0 E+7
3.0 E+7
PLOT OF XO VS TIME COL 3 ROW 7

Figure B-71

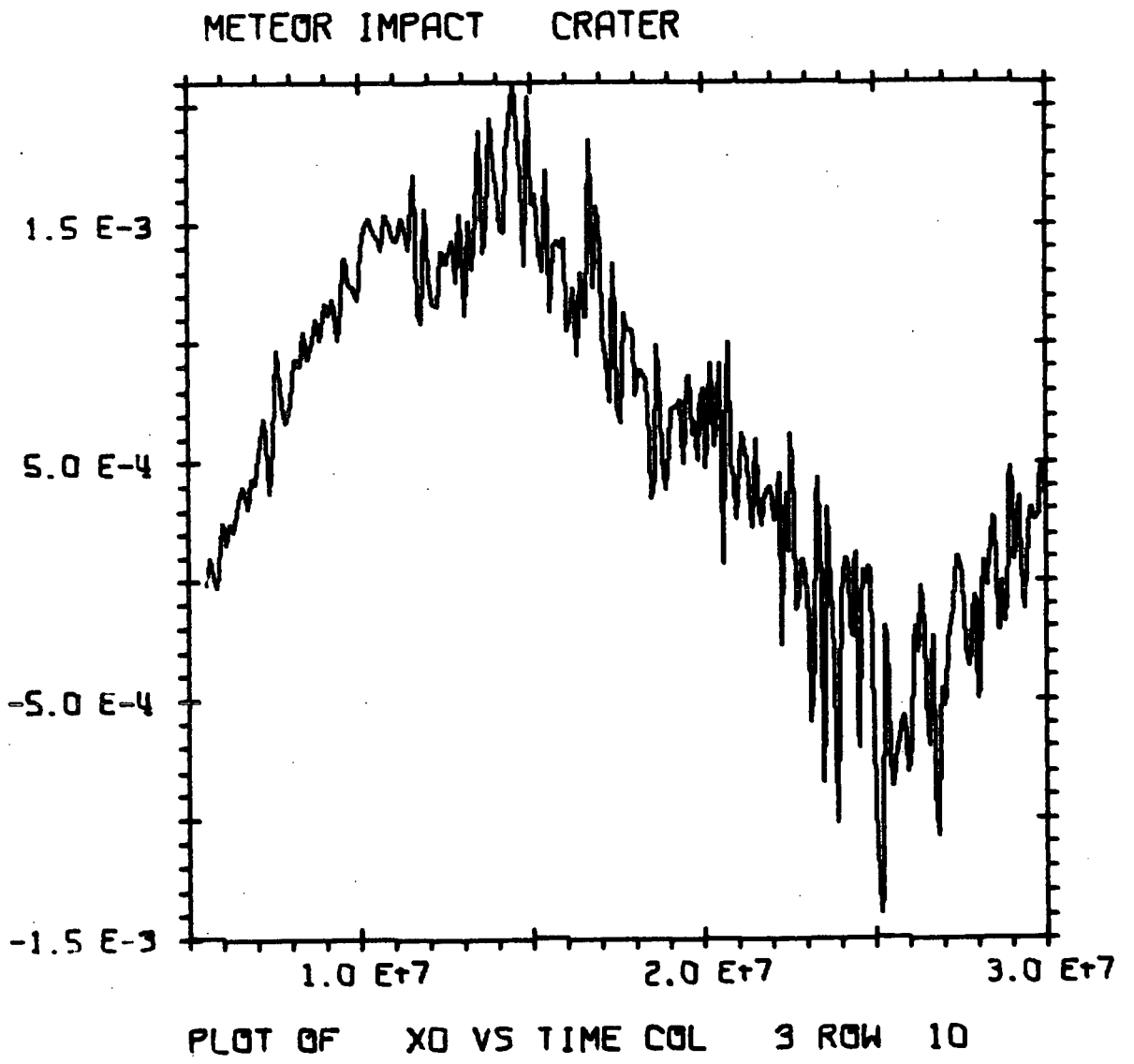
METEOR IMPACT CRATER
1.5 E-3
5.0 E-4
-5.0 E-4
-1.5 E-3
1.0 E+7
2.0 E+7
3.0 E+7
PLOT OF XO VS TIME COL 3 ROW 10

Figure B-72

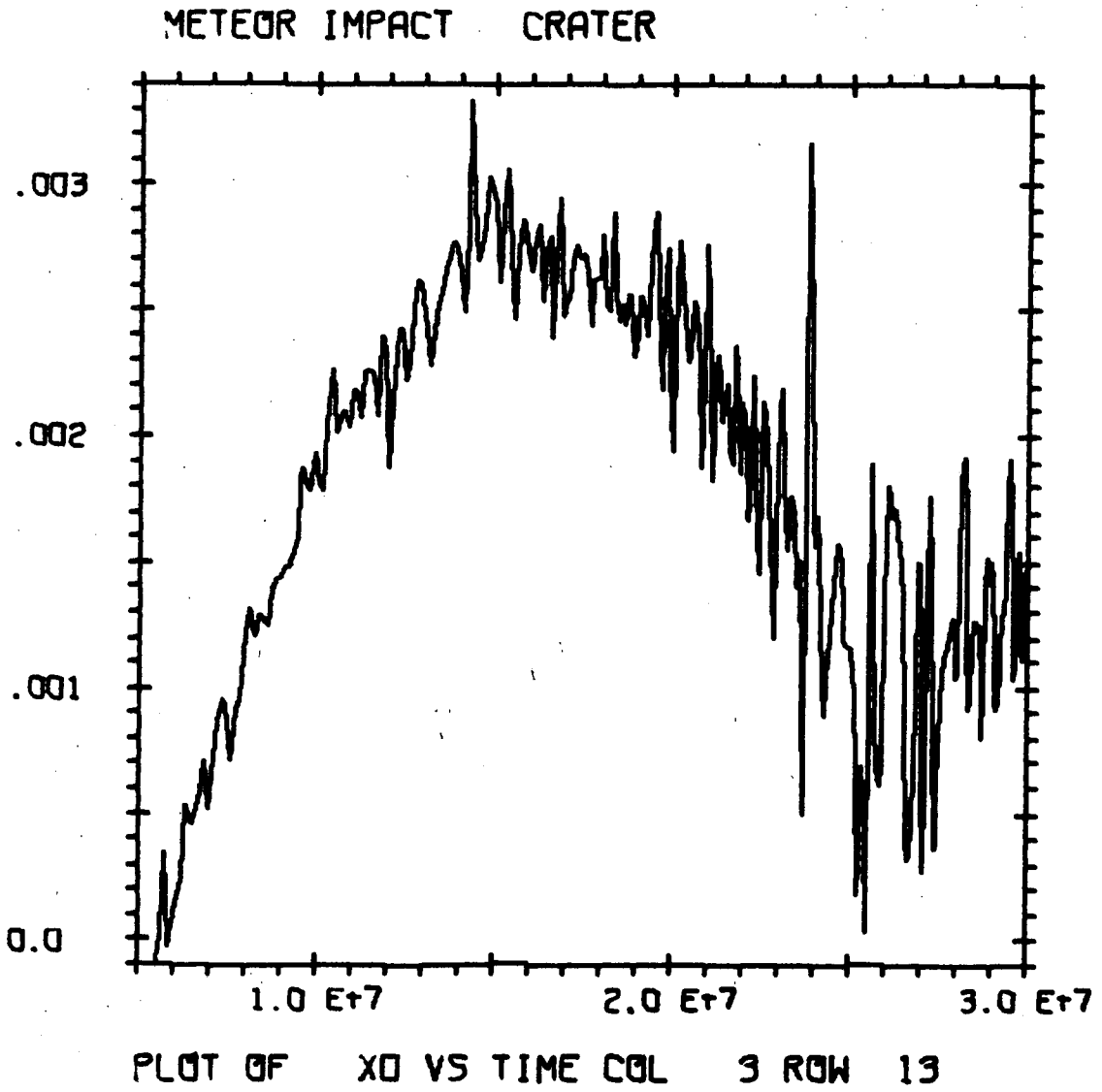
METEOR IMPACT CRATER
.003
.002
.001
0.0
1.0 E+7
2.0 E+7
3.0 E+7
PLOT OF XO VS TIME COL 3 ROW 13

Figure B-73

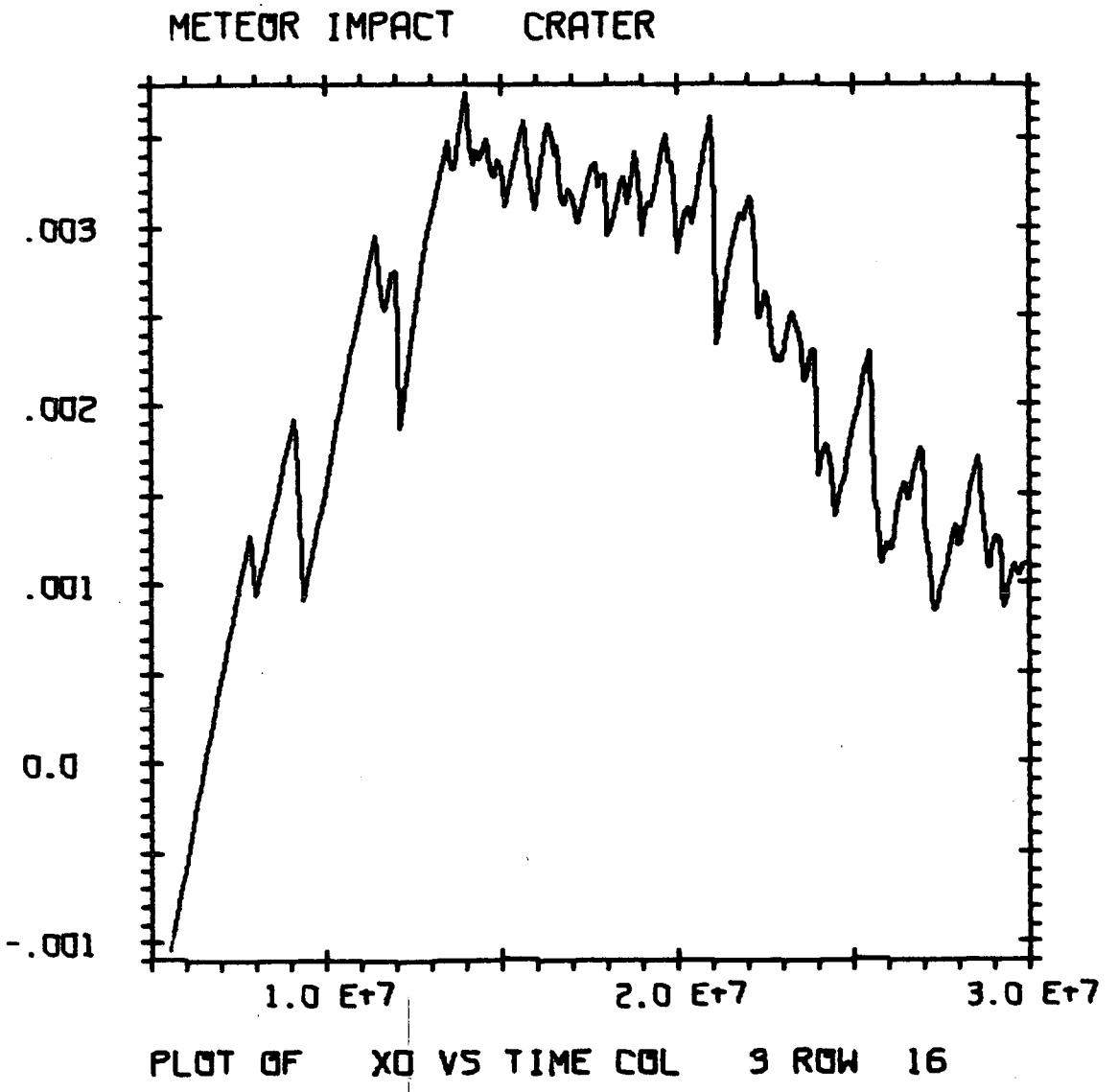
METEOR IMPACT CRATER
.003
.002
.001
0.0
-.001
1.0 E+7
2.0 E+7
3.0 E+7
PLOT OF XO VS TIME COL 3 ROW 16

Figure B-74

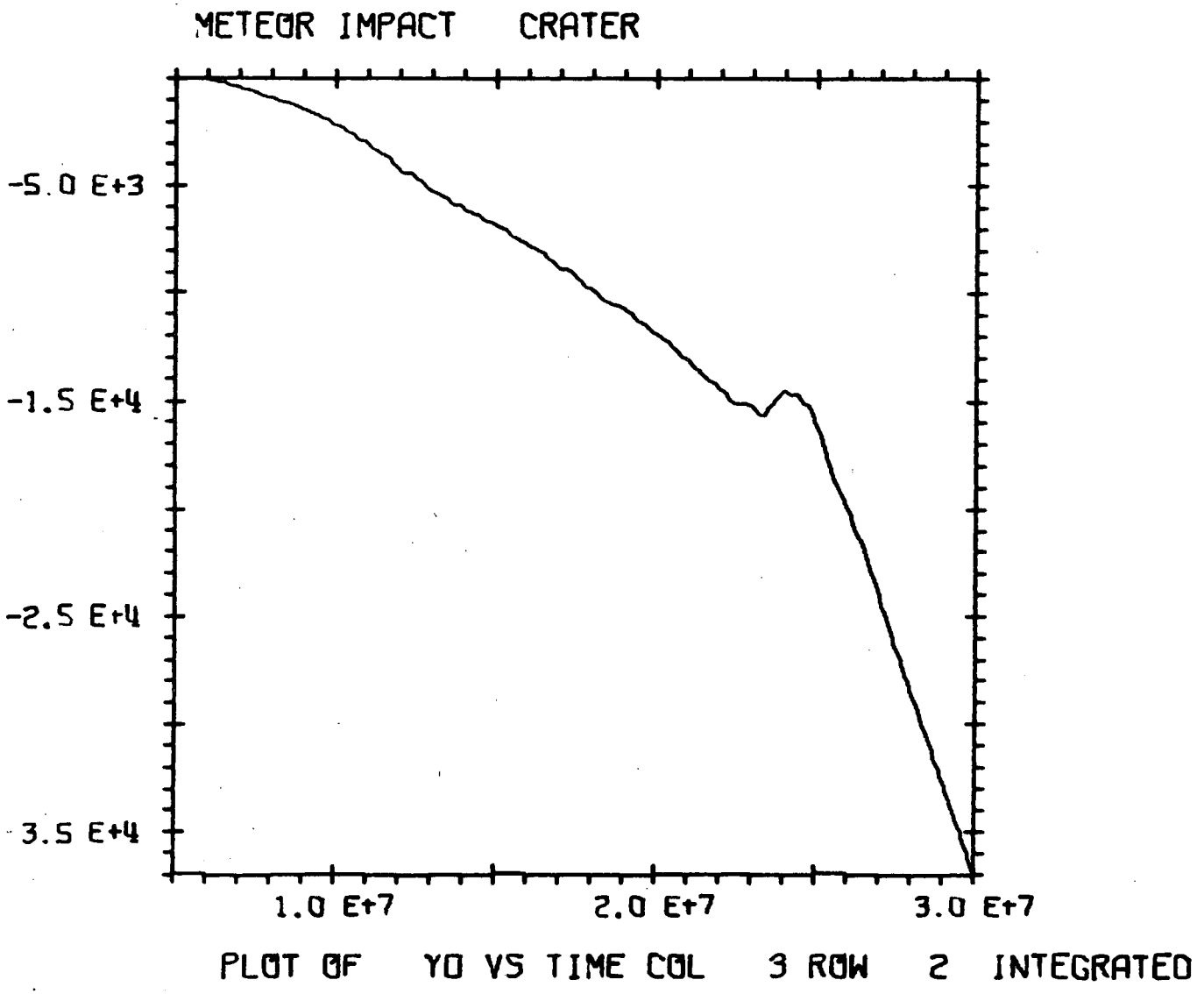
METEOR IMPACT CRATER
-5.0 E+3
-1.5 E+4
-2.5 E+4
-3.5 E+4
1.0 E+7
2.0 E+7
3.0 E+7
PLOT OF YO VS TIME COL 3 ROW 2 INTEGRATED

Figure B-75

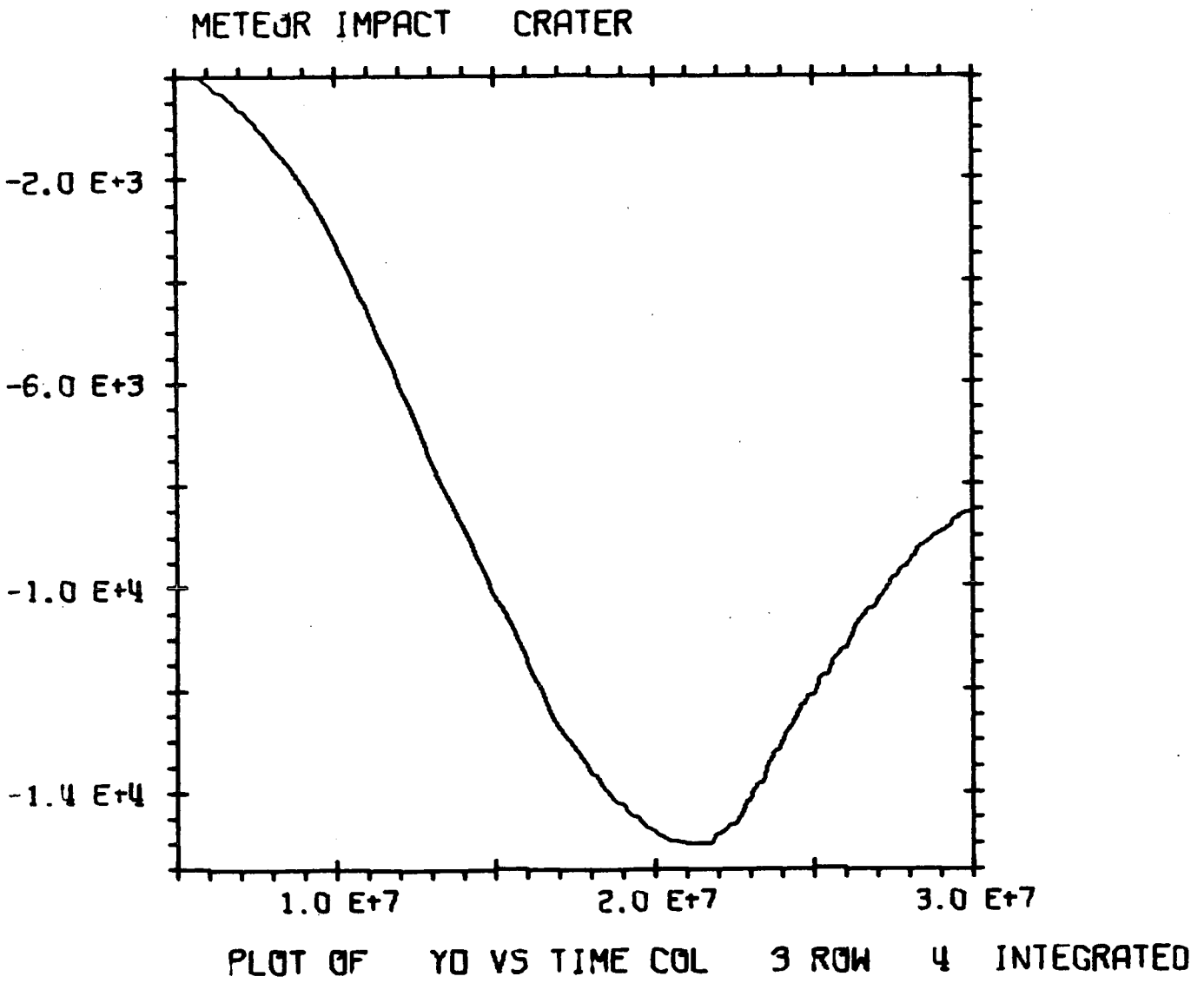
METEOR IMPACT CRATER
-2.0 E+3
-6.0 E+3
-1.0 E+4
-1.4 E+4
1.0 E+7
2.0 E+7
3.0 E+7
PLOT OF YO VS TIME COL 3 ROW 4 INTEGRATED

Figure B-76

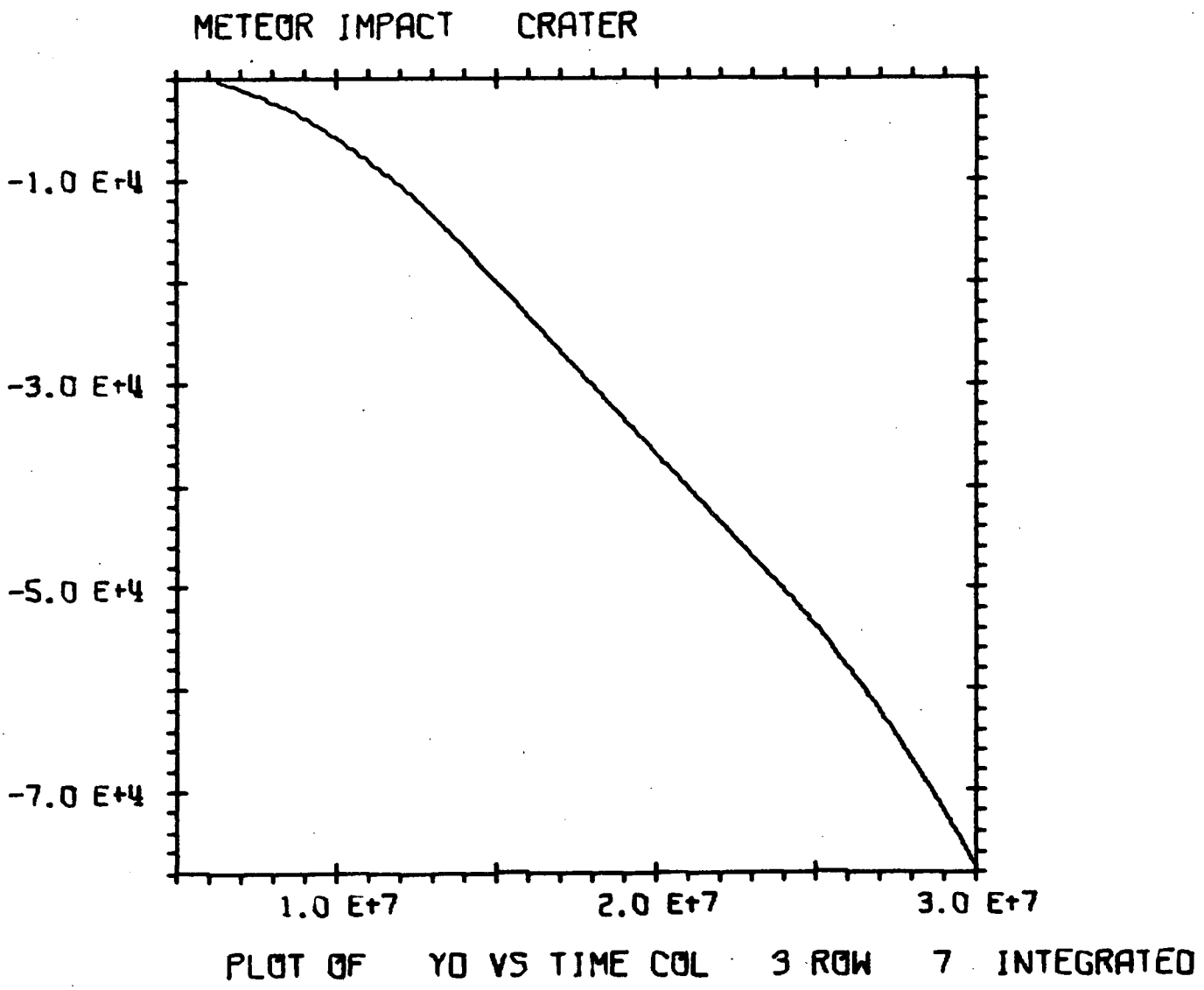
METEOR IMPACT CRATER
-1.0 E+4
-3.0 E+4
-5.0 E+4
-7.0 E+4
1.0 E+7
2.0 E+7
3.0 E+7
PLOT OF YO VS TIME COL 3 ROW 7 INTEGRATED

Figure B-77

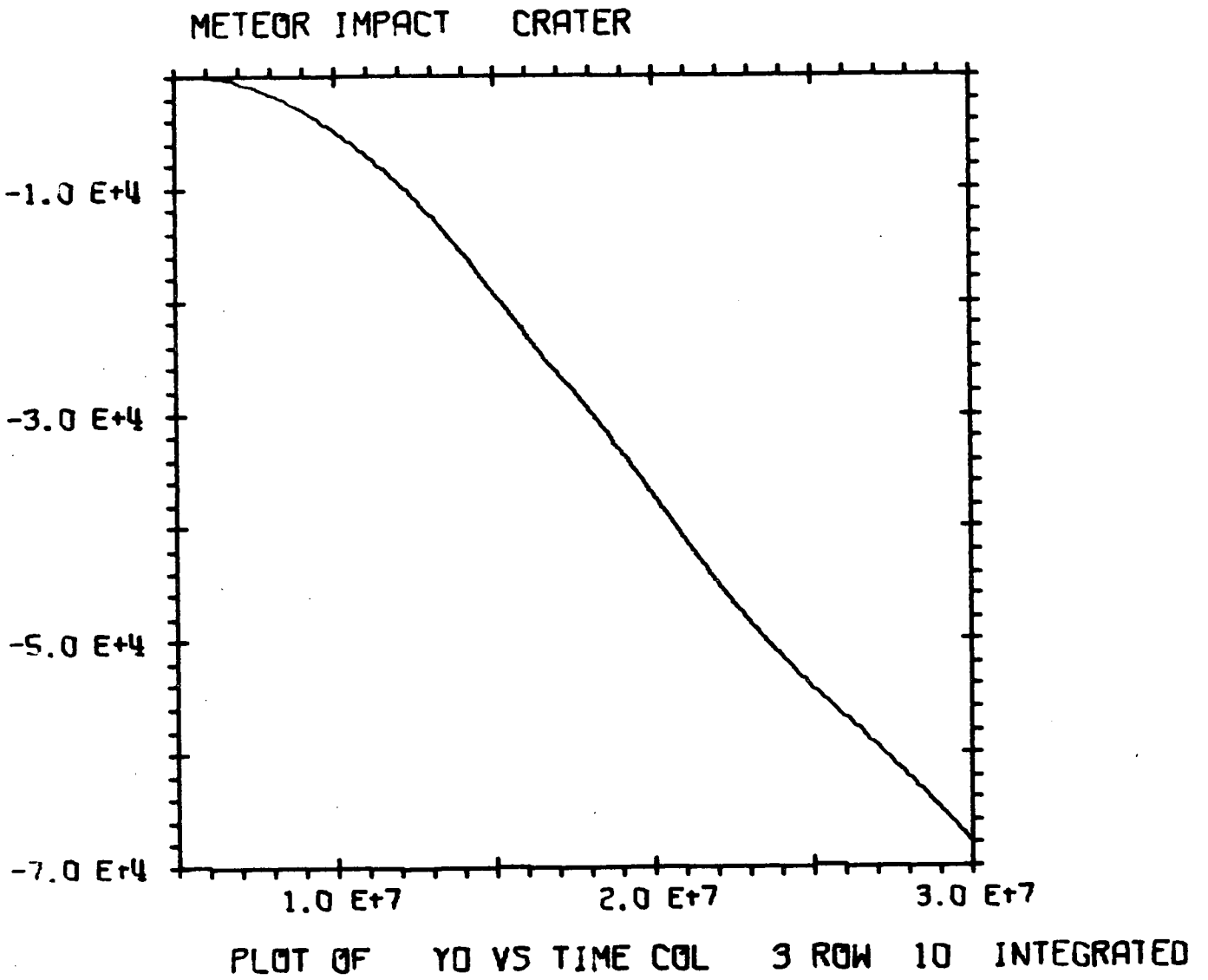
METEOR IMPACT CRATER
-1.0 E+4
-3.0 E+4
-5.0 E+4
-7.0 E+4
1.0 E+7
2.0 E+7
3.0 E+7
PLOT OF YO VS TIME COL 3 ROW 10 INTEGRATED

Figure B-78

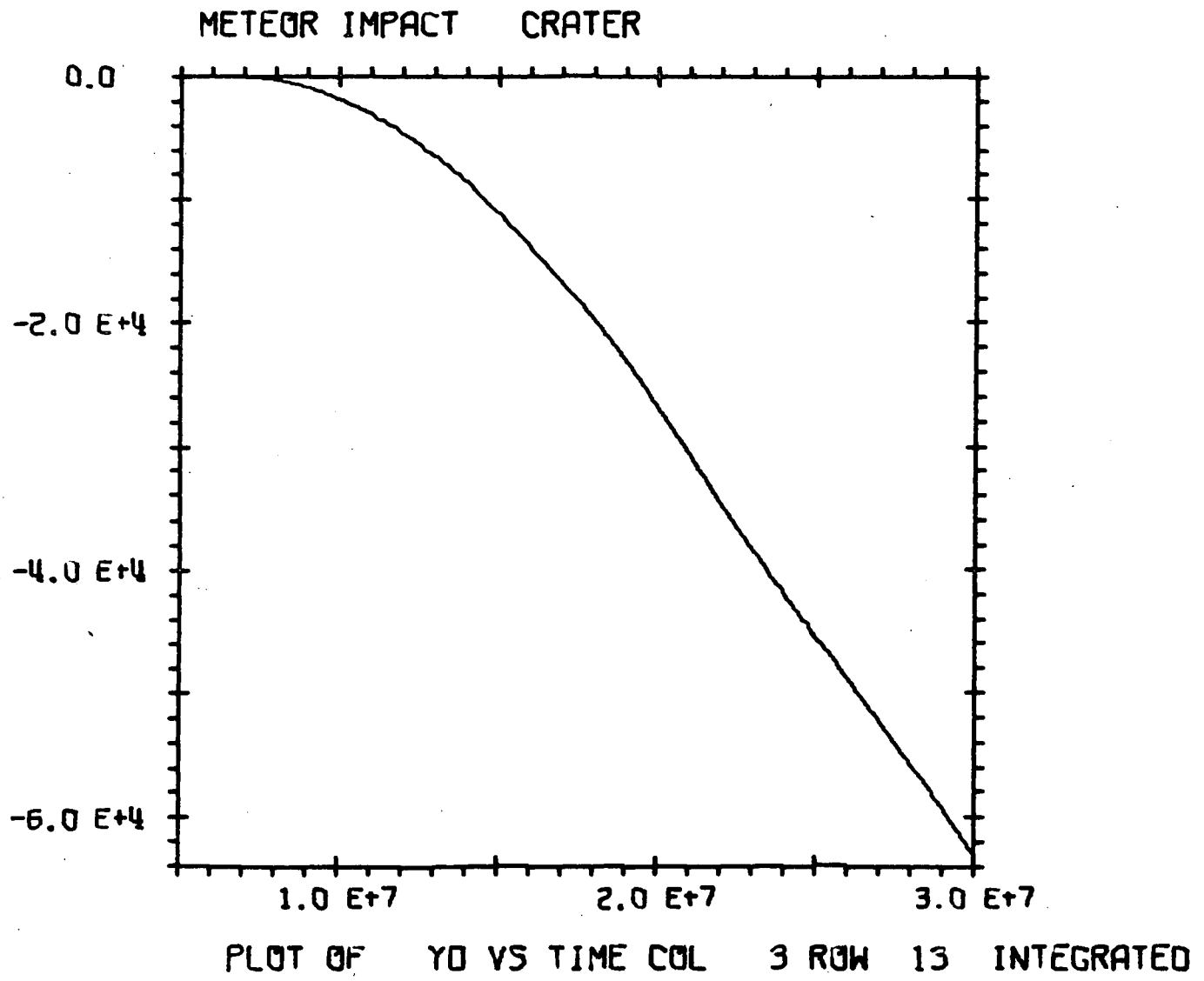
METEOR IMPACT CRATER
0.0
-2.0 E+4
-4.0 E+4
-6.0 E+4
1.0 E+7
2.0 E+7
3.0 E+7
PLOT OF YO VS TIME COL 3 ROW 13 INTEGRATED

Figure B-79

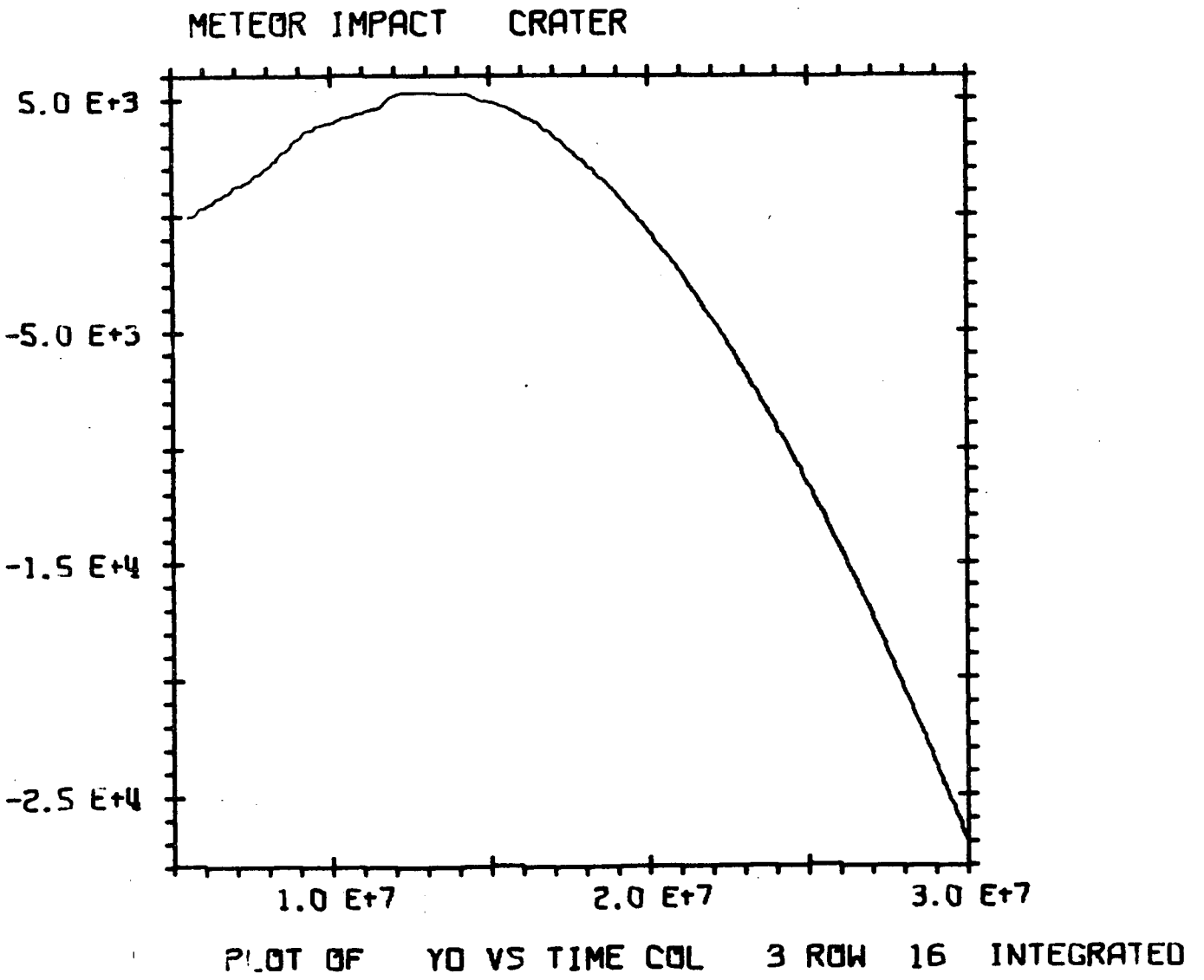
METEOR IMPACT CRATER
5.0 E+3
-5.0 E+3
-1.5 E+4
-2.5 E+4
1.0 E+7
2.0 E+7
3.0 E+7
PLOT OF YO VS TIME COL 3 ROW 16 INTEGRATED

Figure B-80

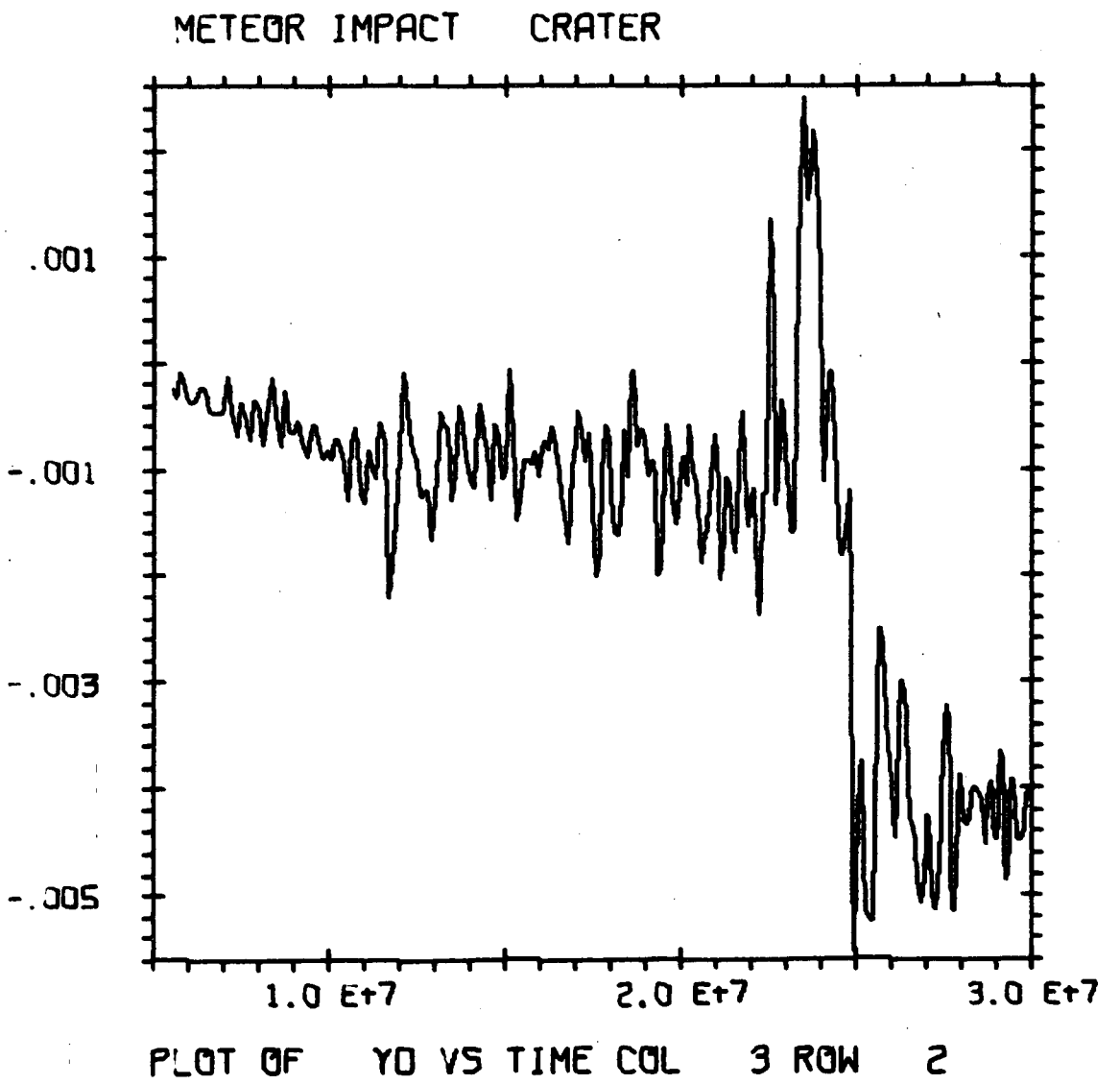
METEOR IMPACT CRATER
.001
-.001
-.003
-.005
1.0 E+7
2.0 E+7
3.0 E+7
PLOT OF YO VS TIME COL 3 ROW 2

Figure B-81

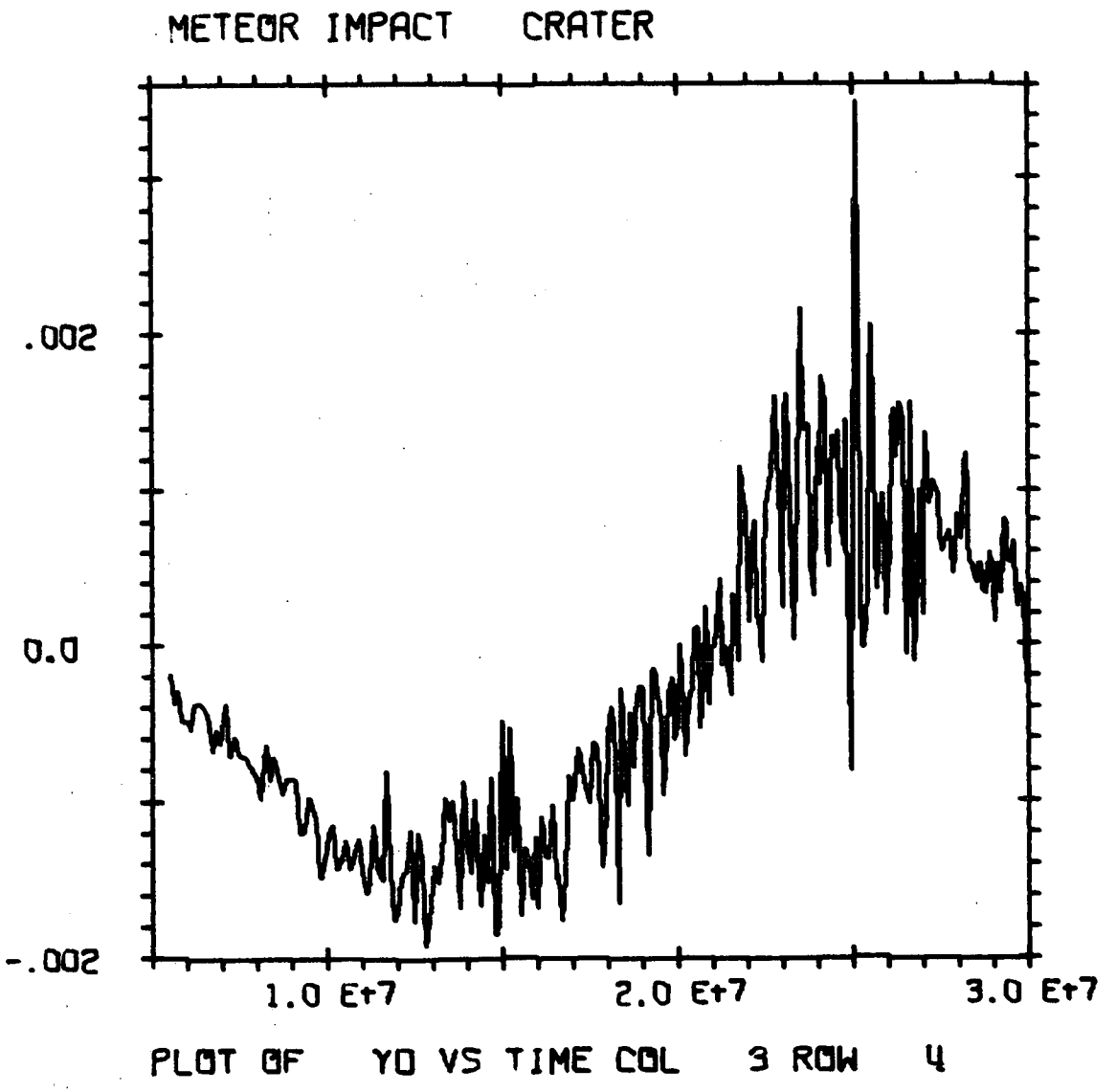
METEOR IMPACT CRATER
.002
0.0
-.002
1.0 E+7
2.0 E+7
3.0 E+7
PLOT OF YO VS TIME COL 3 ROW 4

Figure B-82

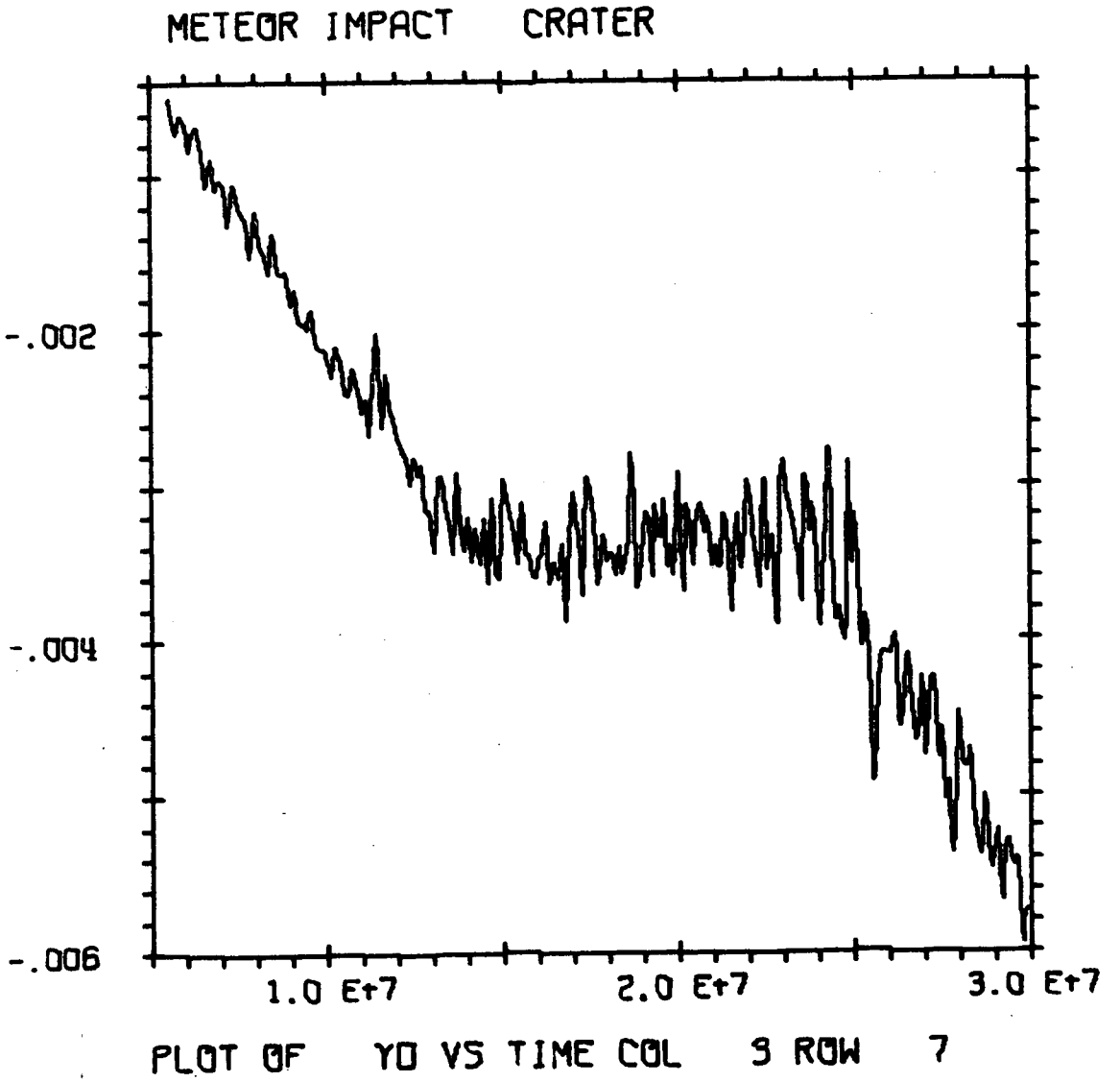
METEOR IMPACT CRATER
-.002
-.004
-.006
1.0 E+7
2.0 E+7
3.0 E+7
PLOT OF YO VS TIME COL 3 ROW 7

Figure B-83

4

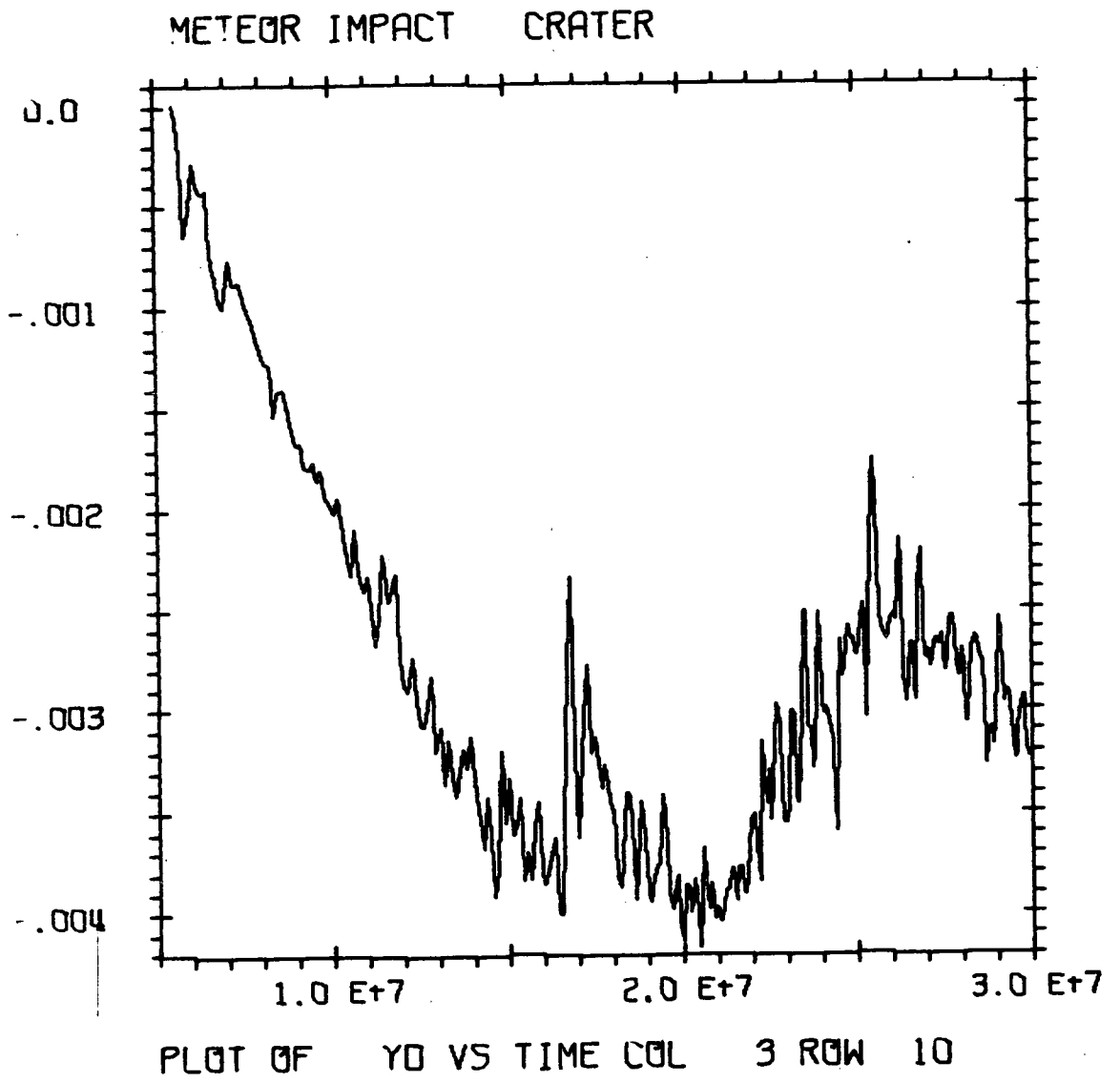
METEOR IMPACT CRATER
0.0
-.001
-.002
-.003
-.004
1.0 E+7
2.0 E+7
3.0 E+7
PLOT OF YO VS TIME COL 3 ROW 10

Figure B-84

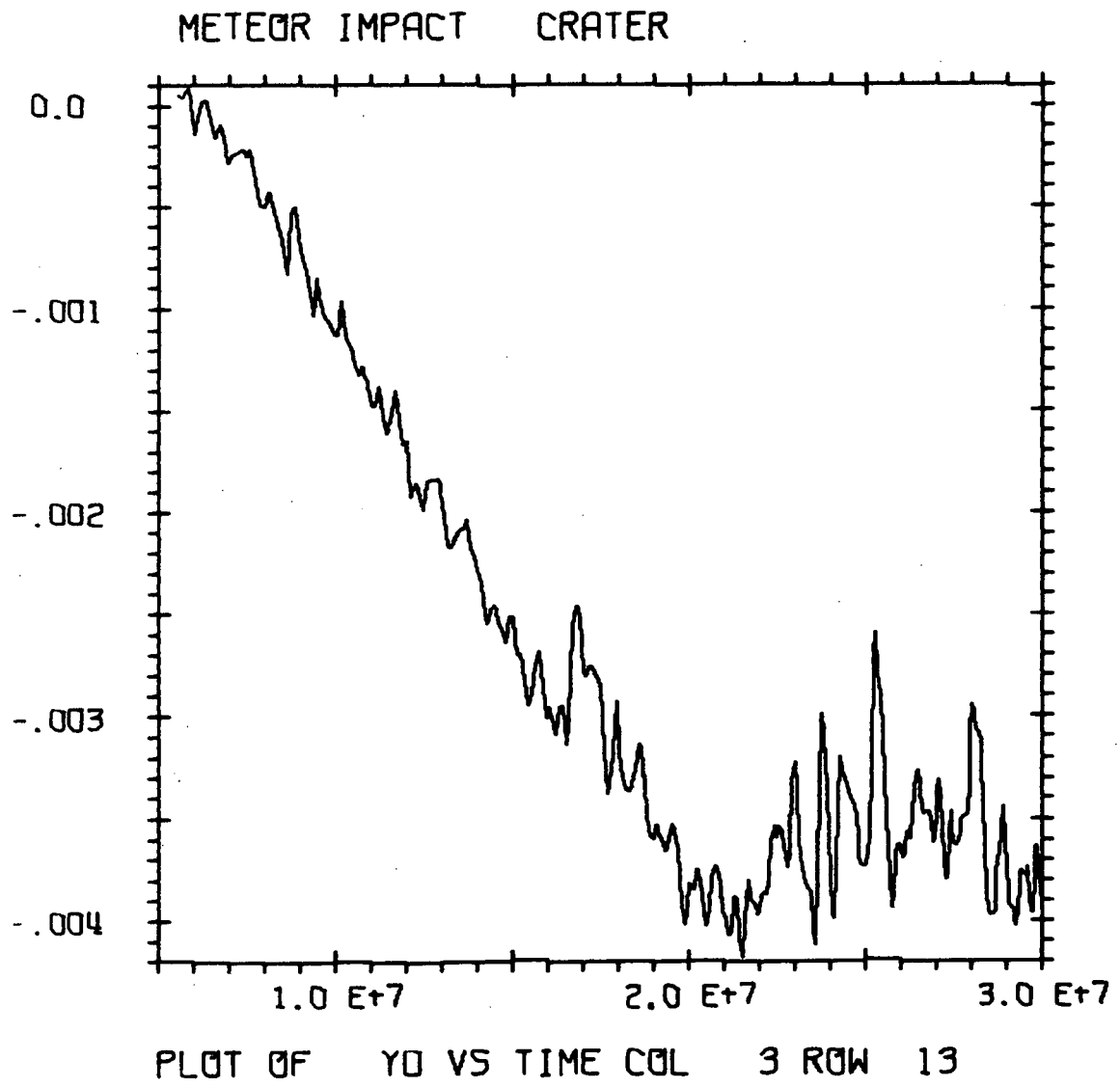
METEOR IMPACT CRATER
0.0
-.001
-.002
-.003
-.004
1.0 E+7
2.0 E+7
3.0 E+7
PLOT OF YO VS TIME COL 3 ROW 13

Figure B-85

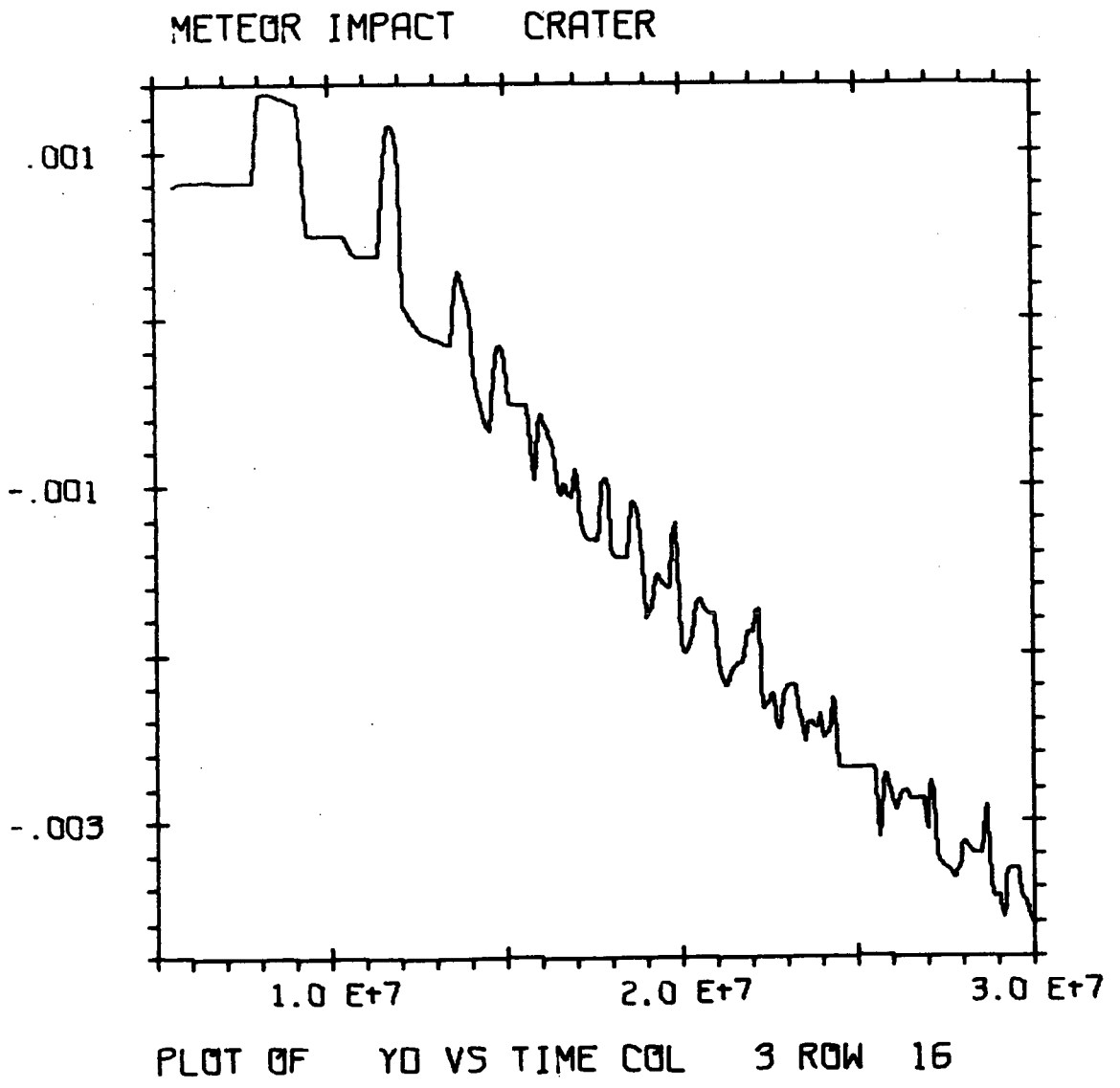
METEOR IMPACT CRATER
.001
-.001
-.003
1.0 E+7
2.0 E+7
3.0 E+7
PLOT OF YO VS TIME COL 3 ROW 16

Figure B-86

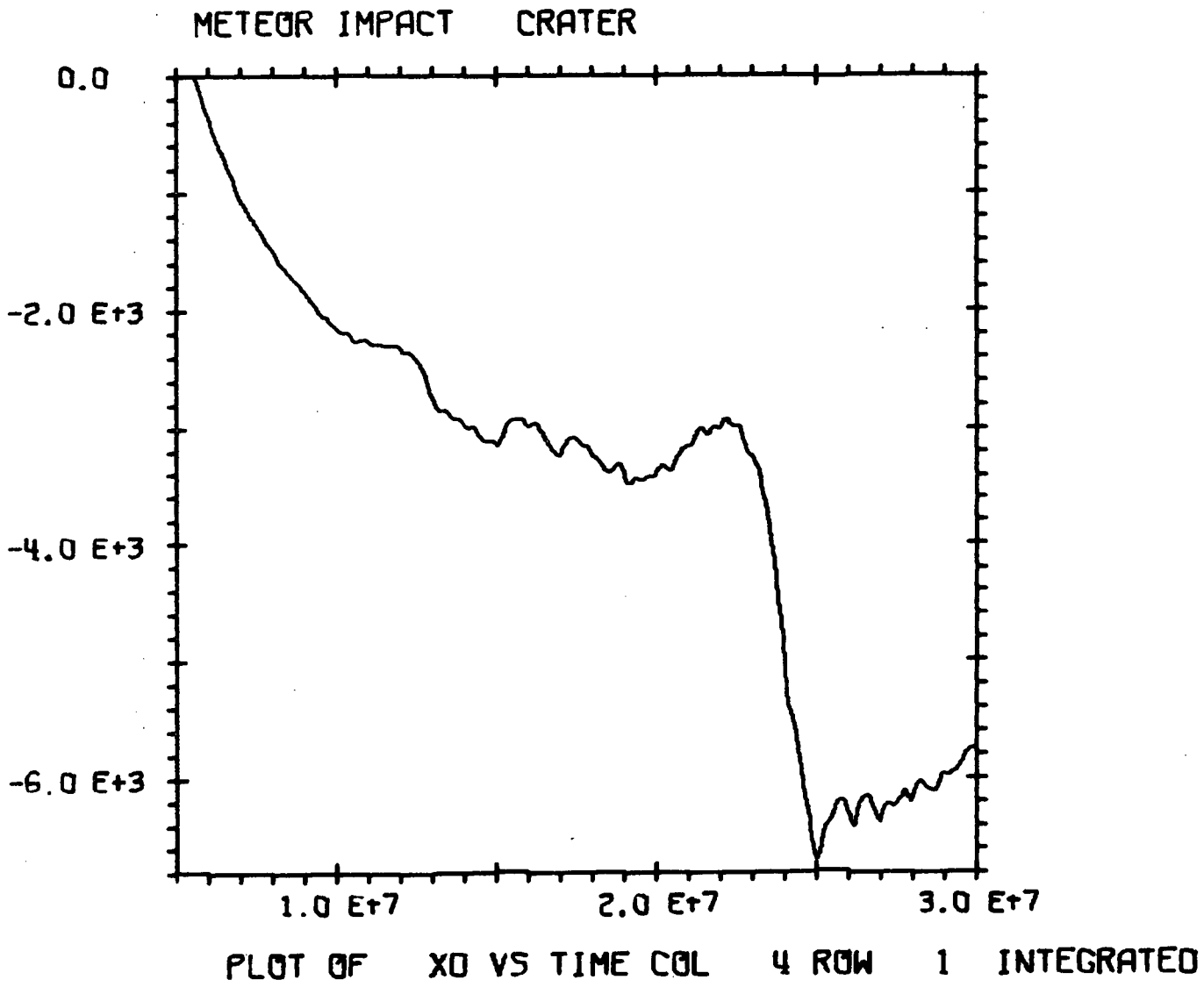
METEOR IMPACT CRATER
0.0
-2.0 E+3
-4.0 E+3
-6.0 E+3
1.0 E+7
2.0 E+7
3.0 E+7
PLOT OF XO VS TIME COL 4 ROW 1 INTEGRATED

Figure B-87

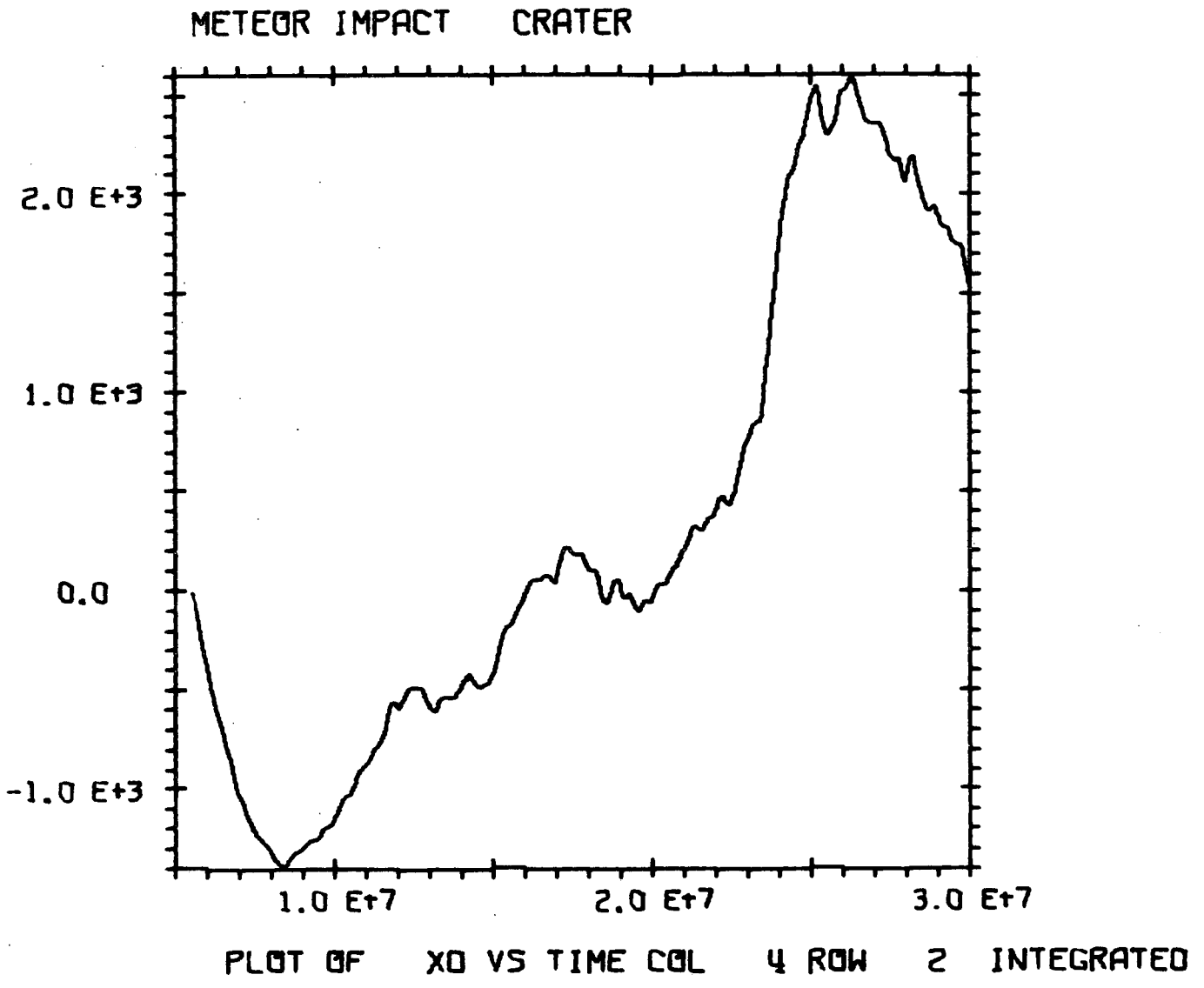
METEOR IMPACT CRATER
2.0 E+3
1.0 E+3
0.0
-1.0 E+3
1.0 E+7
2.0 E+7
3.0 E+7
PLOT OF XO VS TIME COL 4 ROW 2 INTEGRATED

Figure B-88

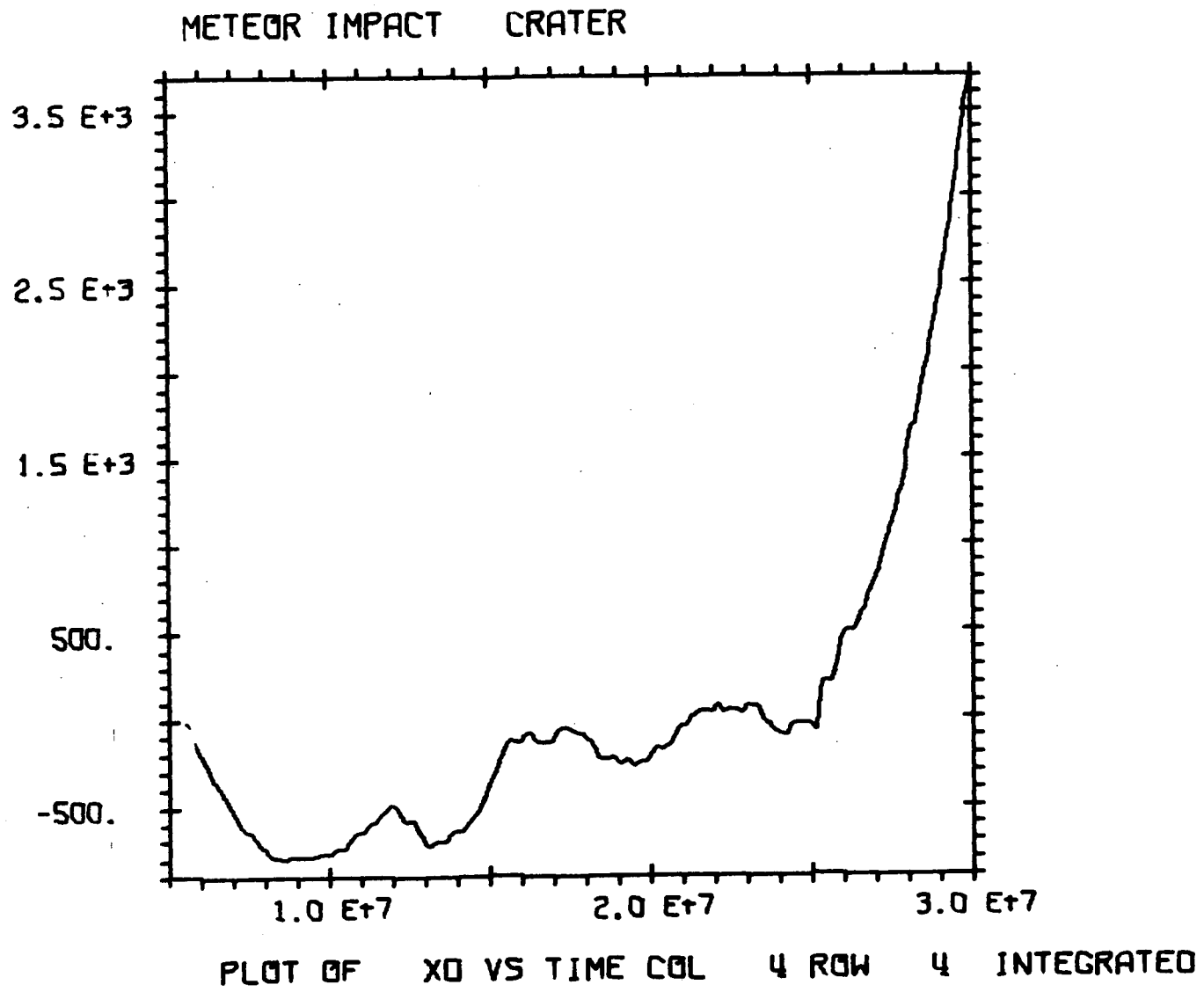
METEOR IMPACT CRATER
3.5 E+3
2.5 E+3
1.5 E+3
500.
-500.
1.0 E+7
2.0 E+7
3.0 E+7
PLOT OF XO VS TIME COL 4 ROW 4 INTEGRATED

Figure B-89

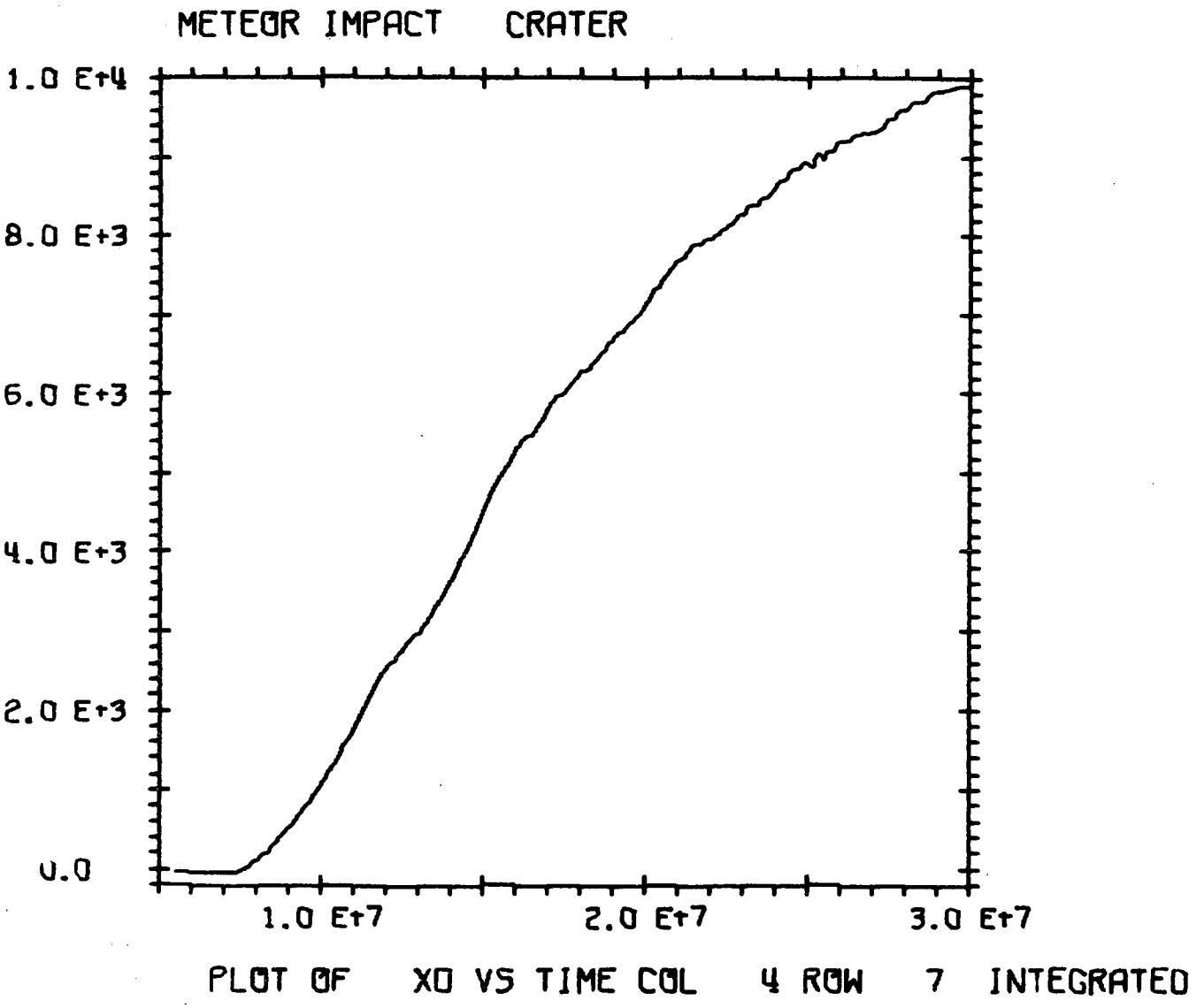
METEOR IMPACT CRATER
1.0 E+4
8.0 E+3
6.0 E+3
4.0 E+3
2.0 E+3
0.0
1.0 E+7
2.0 E+7
3.0 E+7
PLOT OF XO VS TIME COL 4 ROW 7 INTEGRATED

Figure B-90

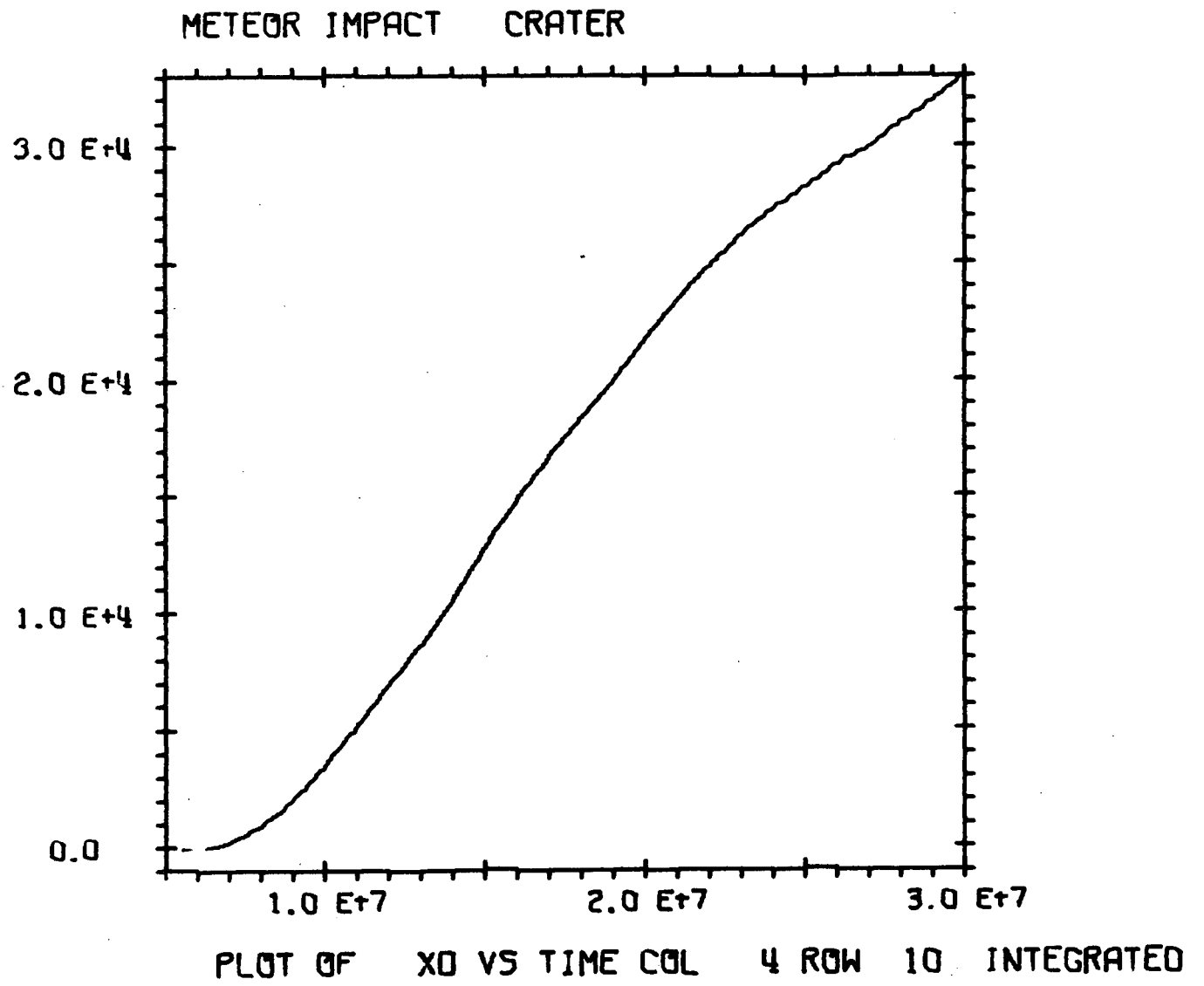
METEOR IMPACT CRATER
3.0 E+4
2.0 E+4
1.0 E+4
0.0
1.0 E+7
2.0 E+7
3.0 E+7
PLOT OF XO VS TIME COL 4 ROW 10 INTEGRATED

Figure B-91

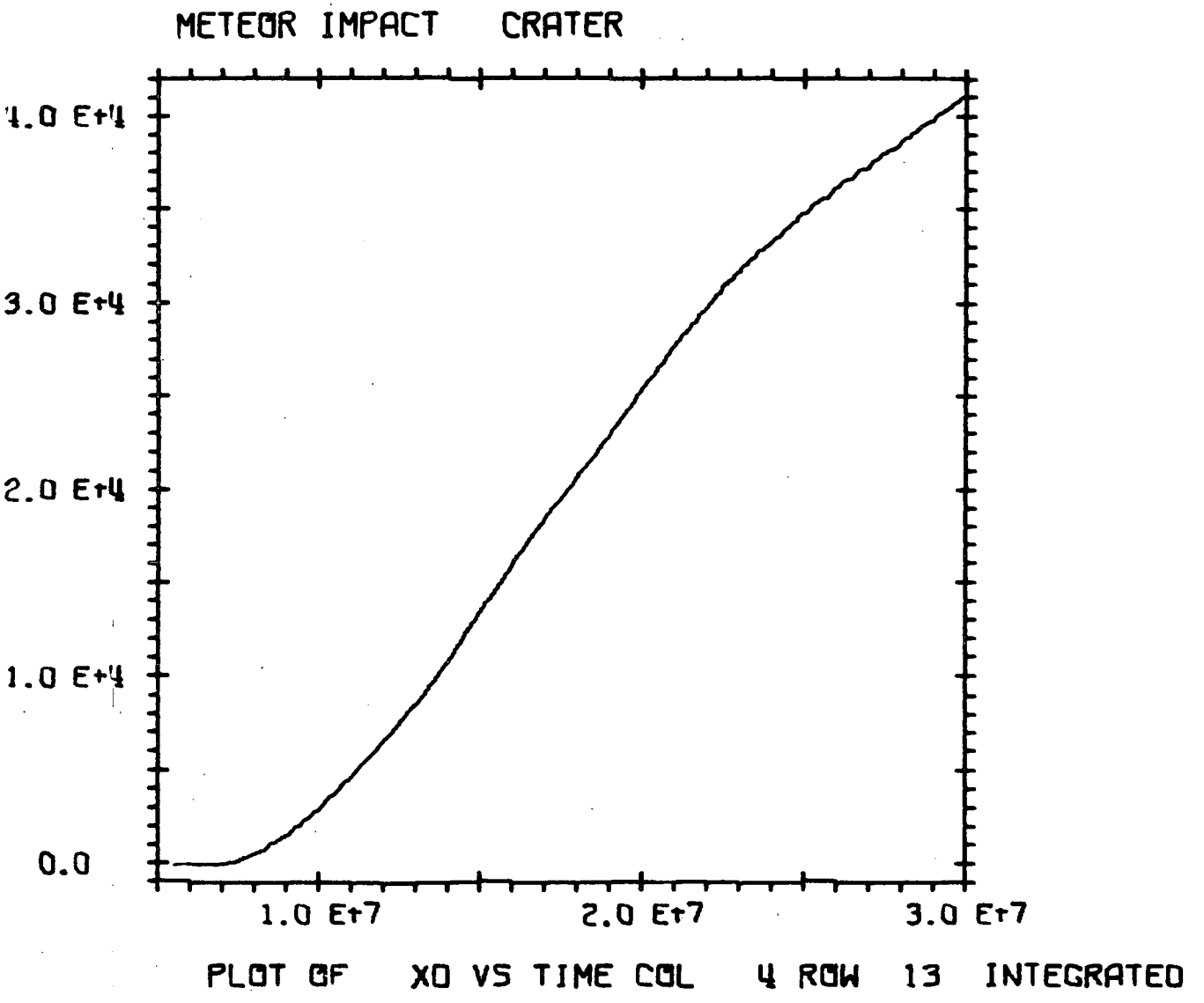
METEOR IMPACT CRATER
4.0 E+4
3.0 E+4
2.0 E+4
1.0 E+4
0.0
1.0 E+7
2.0 E+7
3.0 E+7
PLOT OF XO VS TIME COL 4 ROW 13 INTEGRATED

Figure B-92

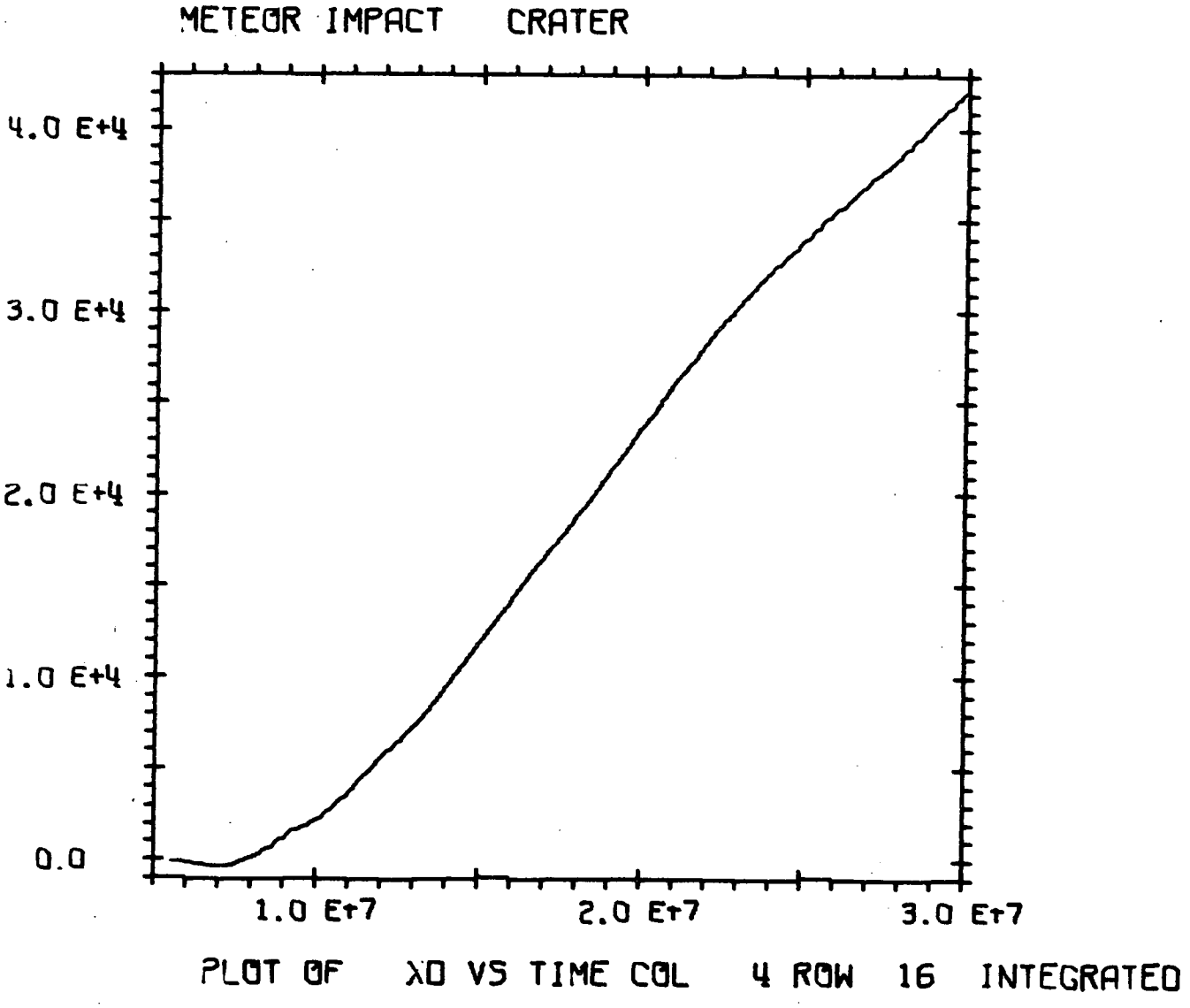
METEOR IMPACT CRATER
4.0 E+4
3.0 E+4
2.0 E+4
1.0 E+4
0.0
1.0 E+7
2.0 E+7
3.0 E+7
PLOT OF XO VS TIME COL 4 ROW 16 INTEGRATED

Figure B-93

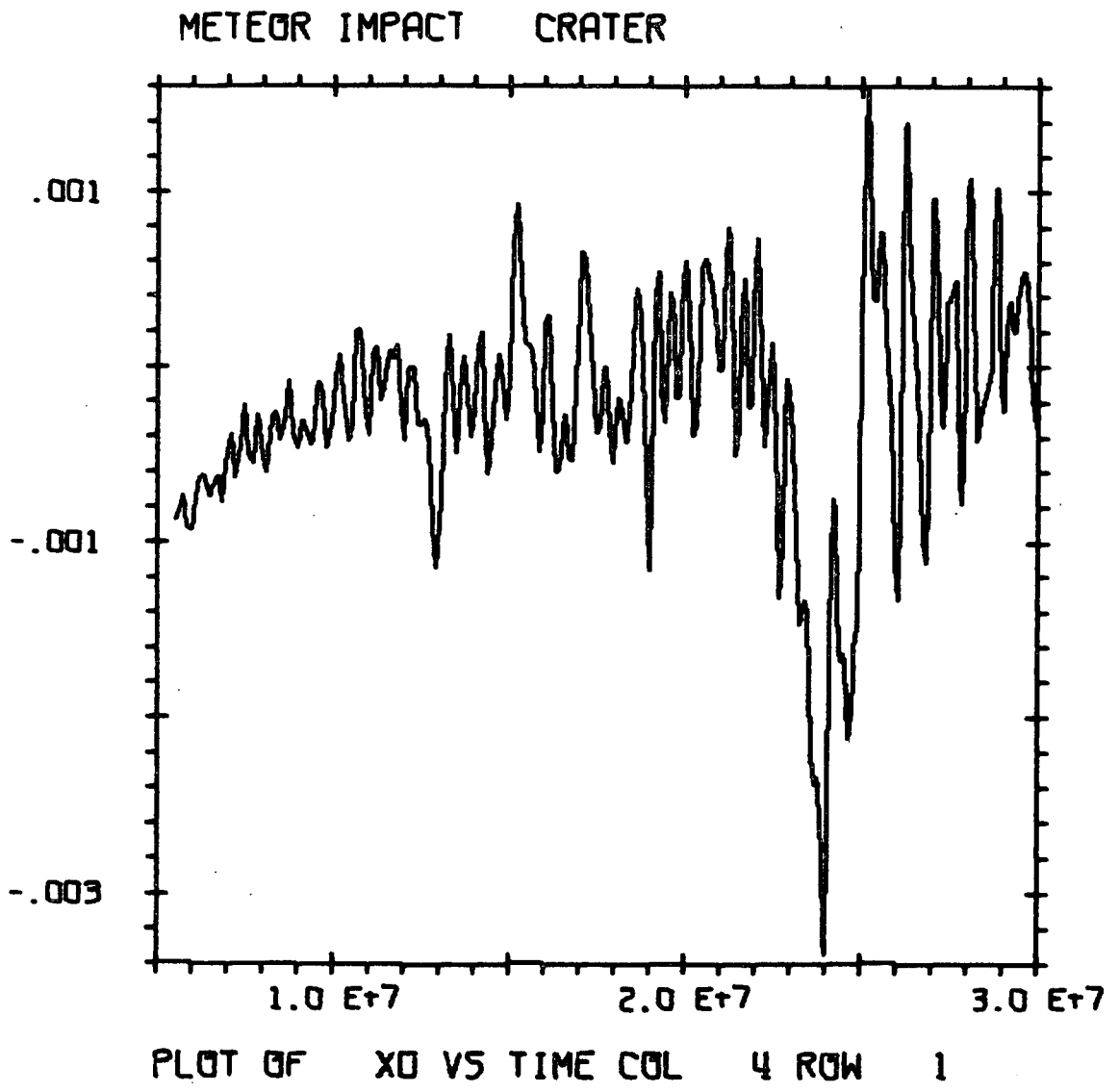
METEOR IMPACT CRATER
.001
-.001
-.003
1.0 E+7
2.0 E+7
3.0 E+7
PLOT OF XO VS TIME COL 4 ROW 1

Figure B-94

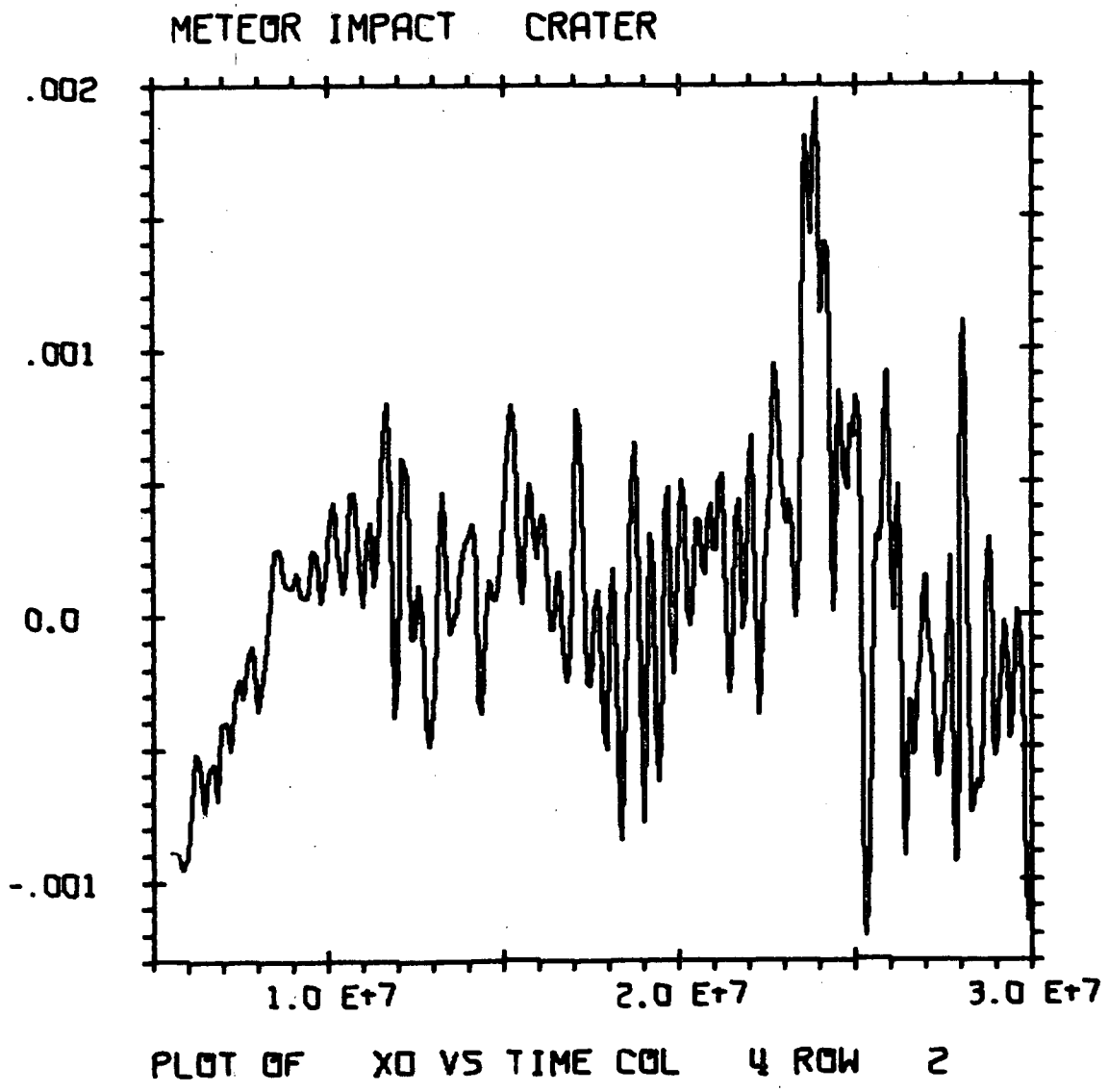
METEOR IMPACT CRATER
.002
.001
0.0
-.001
1.0 E+7
2.0 E+7
3.0 E+7
PLOT OF XO VS TIME COL 4 ROW 2

Figure B-95

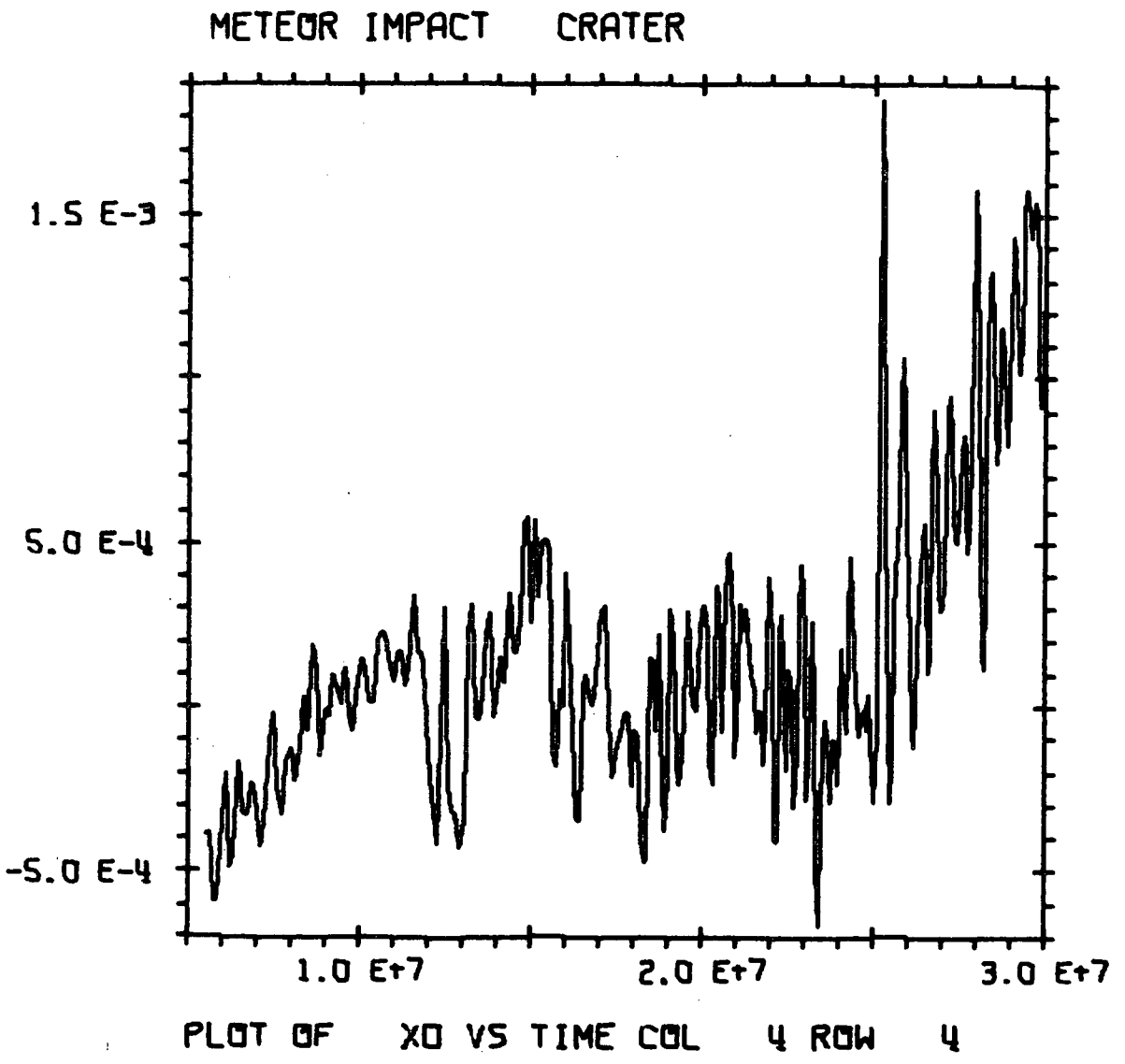
METEOR IMPACT CRATER
1.5 E-3
5.0 E-4
-5.0 E-4
1.0 E+7
2.0 E+7
3.0 E+7
PLOT OF XO VS TIME COL 4 ROW 4

Figure B-96

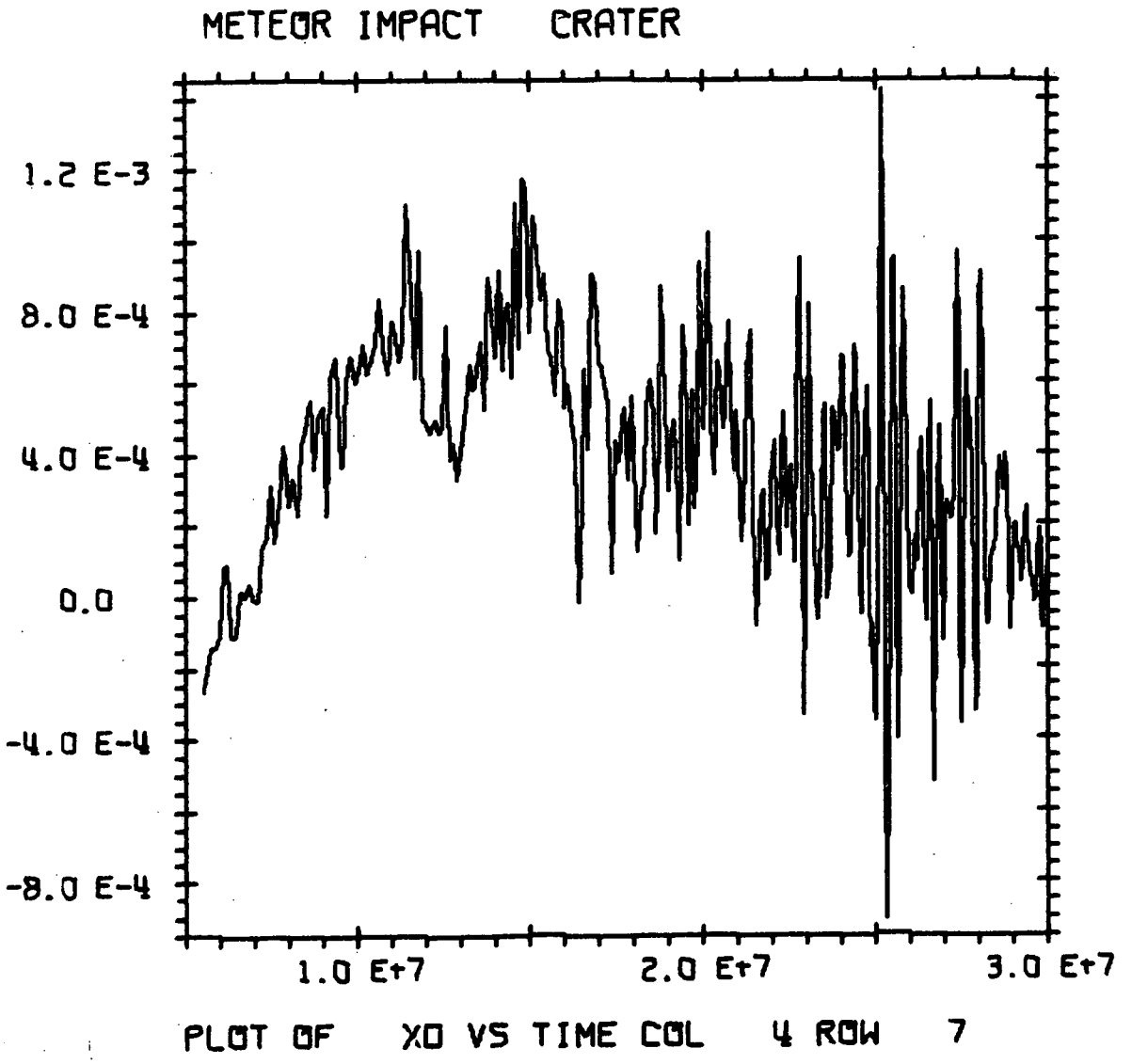
METEOR IMPACT CRATER
1.2 E-3
8.0 E-4
4.0 E-4
0.0
-4.0 E-4
-8.0 E-4
1.0 E+7
2.0 E+7
3.0 E+7
PLOT OF XO VS TIME COL 4 ROW 7

Figure B-97

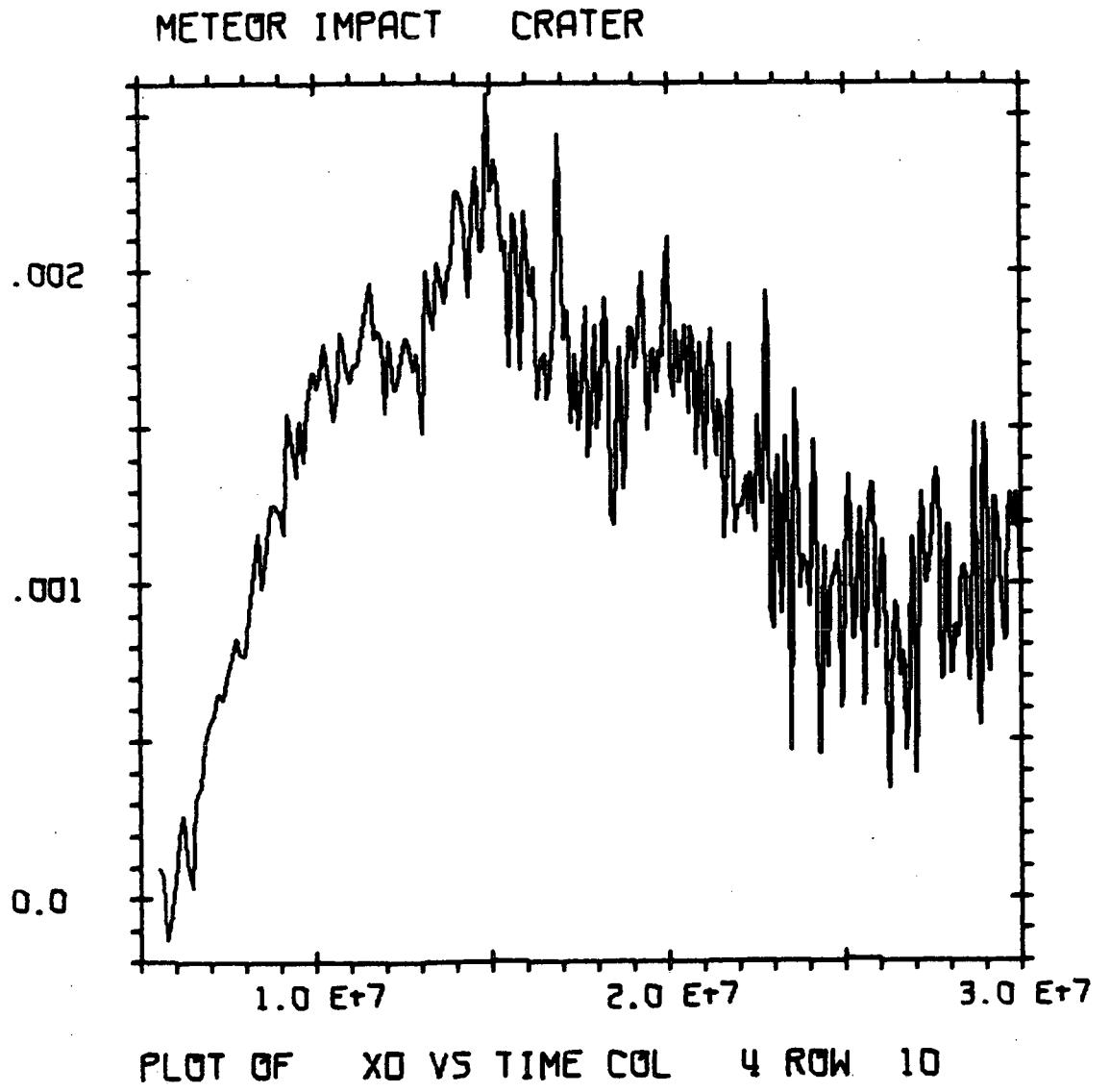
METEOR IMPACT CRATER
.002
.001
0.0
1.0 E+7
2.0 E+7
3.0 E+7
PLOT OF XO VS TIME COL 4 ROW 10

Figure B-98

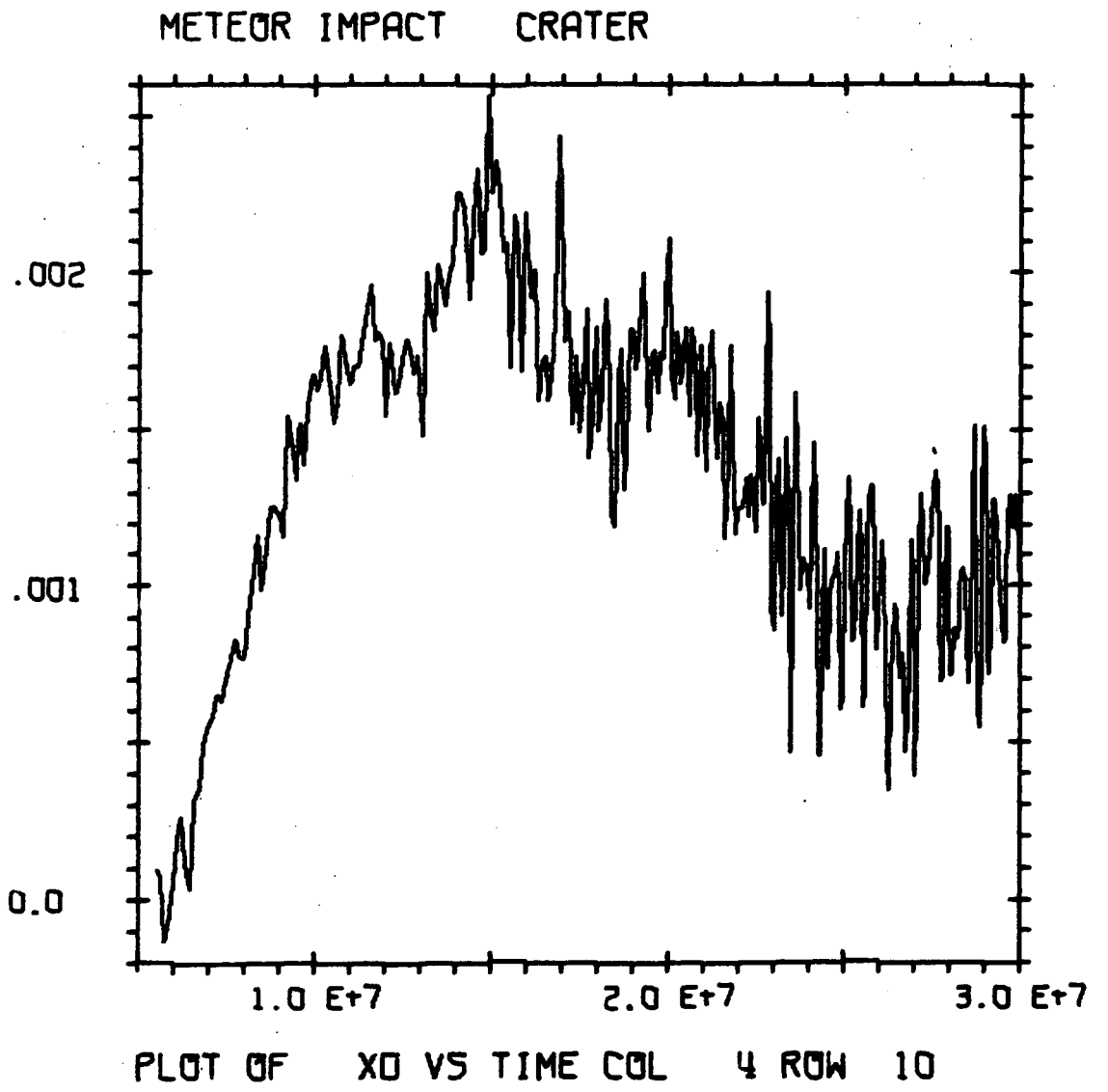
METEOR IMPACT CRATER
.002
.001
0.0
1.0 E+7
2.0 E+7
3.0 E+7
PLOT OF XO VS TIME COL 4 ROW 10

Figure B-99

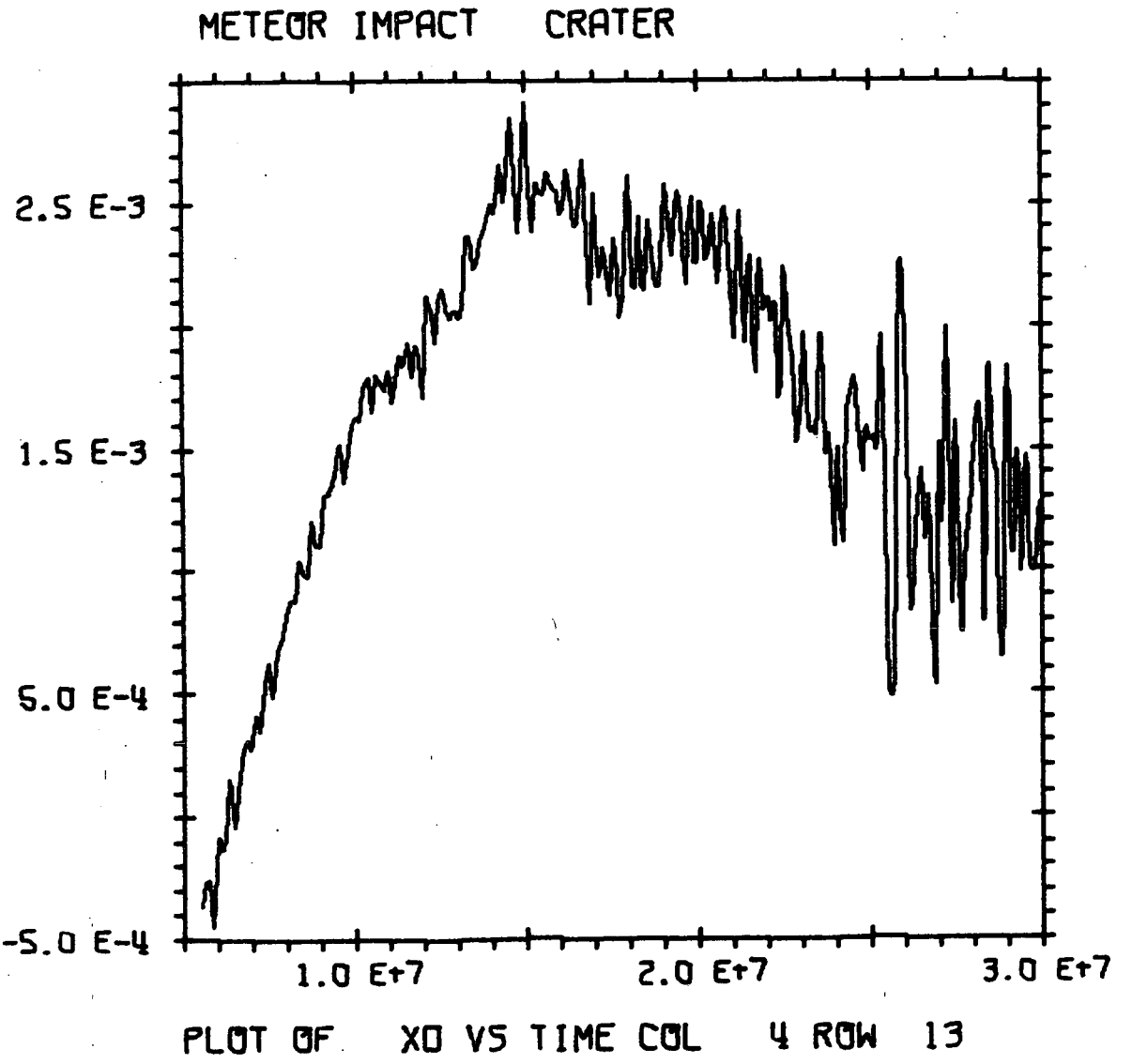
METEOR IMPACT CRATER
2.5 E-3
1.5 E-3
5.0 E-4
-5.0 E-4
1.0 E+7
2.0 E+7
3.0 E+7
PLOT OF XO VS TIME COL 4 ROW 13

Figure B-100

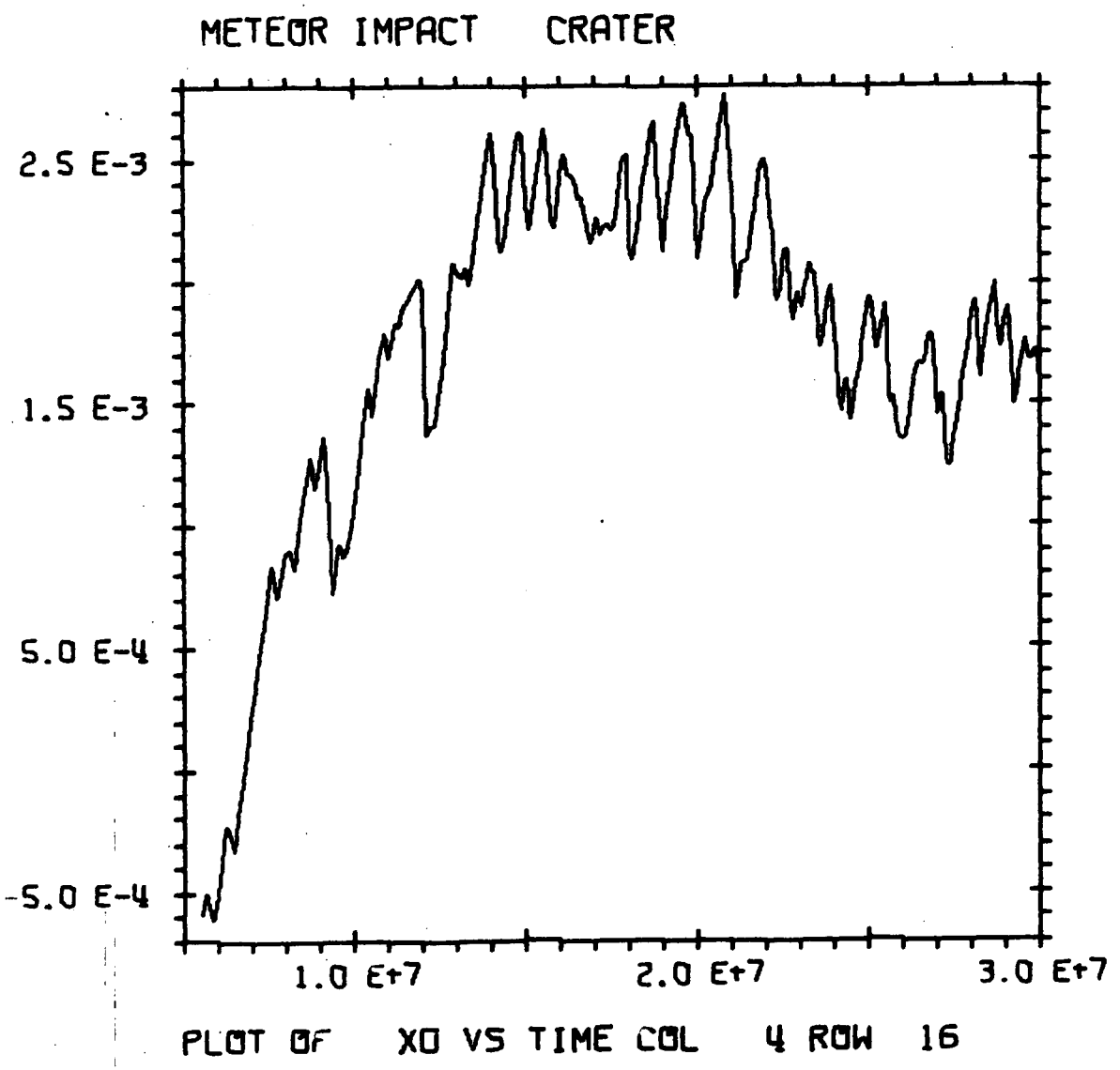
METEOR IMPACT CRATER
2.5 E-3
1.5 E-3
5.0 E-4
-5.0 E-4
1.0 E+7
2.0 E+7
3.0 E+7
PLOT OF XO VS TIME COL 4 ROW 16

Figure B-101

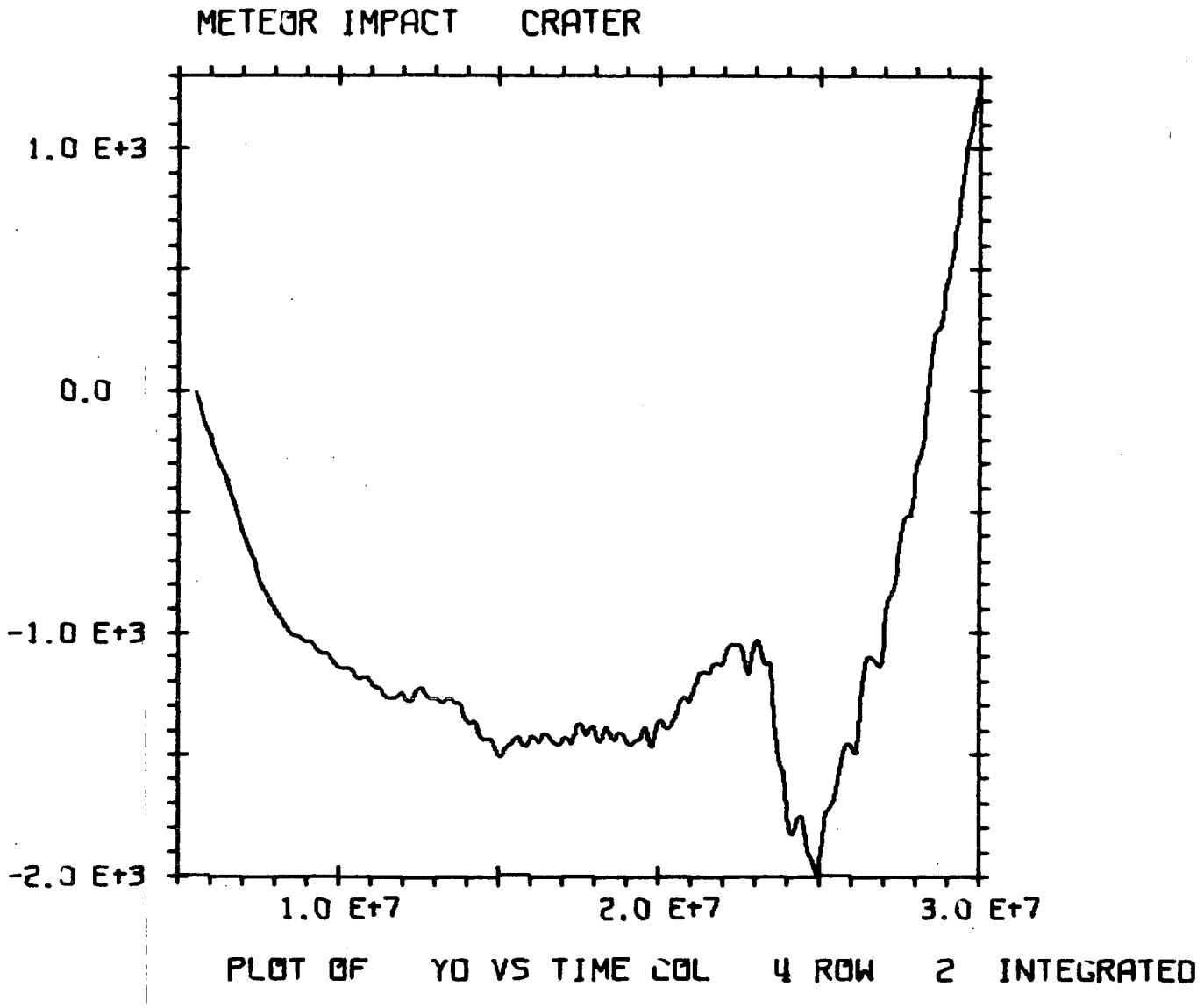
METEOR IMPACT CRATER
1.0 E+3
0.0
-1.0 E+3
-2.0 E+3
1.0 E+7
2.0 E+7
3.0 E+7
PLOT OF YO VS TIME COL 4 ROW 2 INTEGRATED

Figure B-102

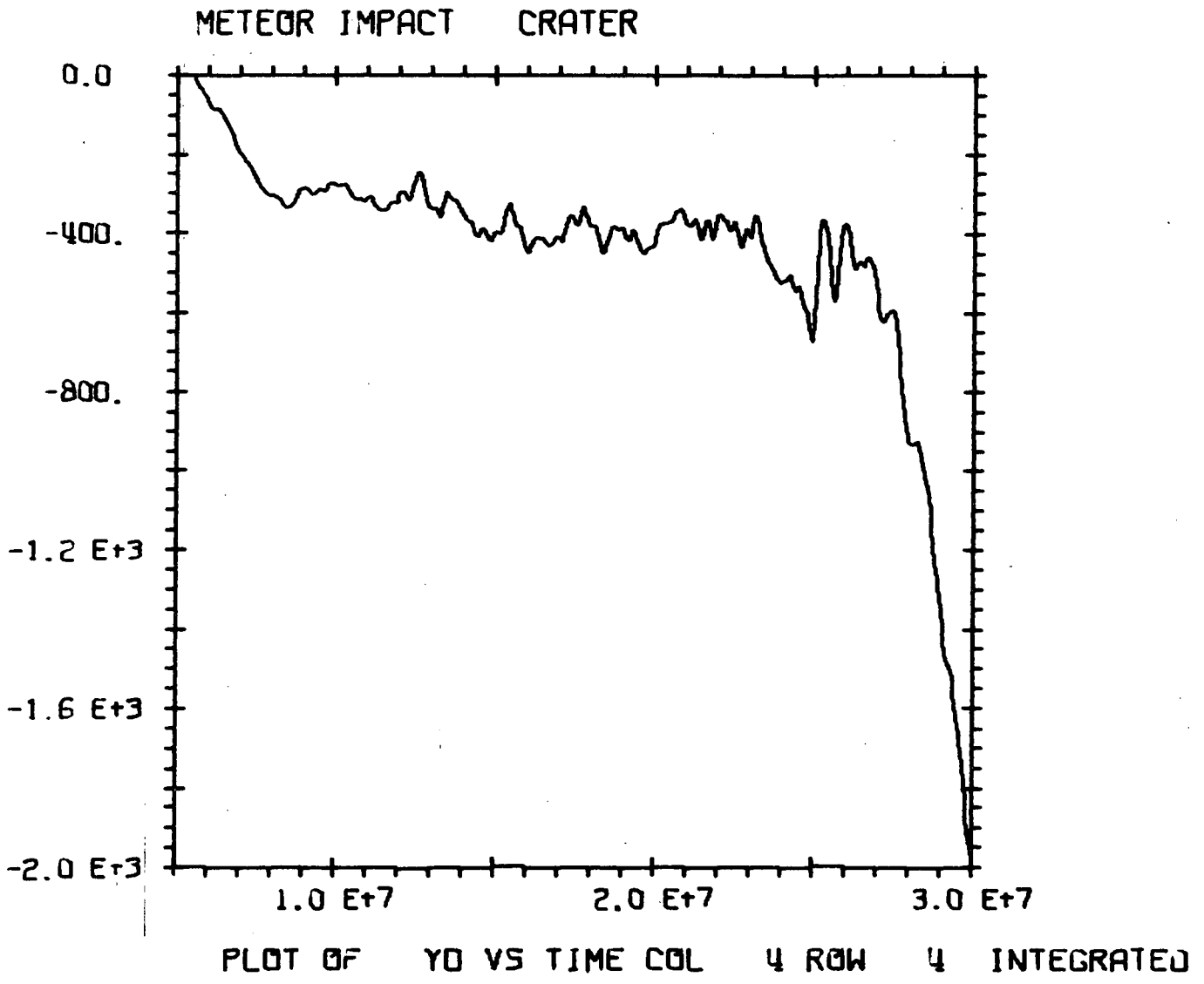
METEOR IMPACT CRATER
0.0
-400.
-800.
-1.2 E+3
-1.6 E+3
-2.0 E+3
1.0 E+7
2.0 E+7
3.0 E+7
PLOT OF YO VS TIME COL 4 ROW 4 INTEGRATED

Figure B-103

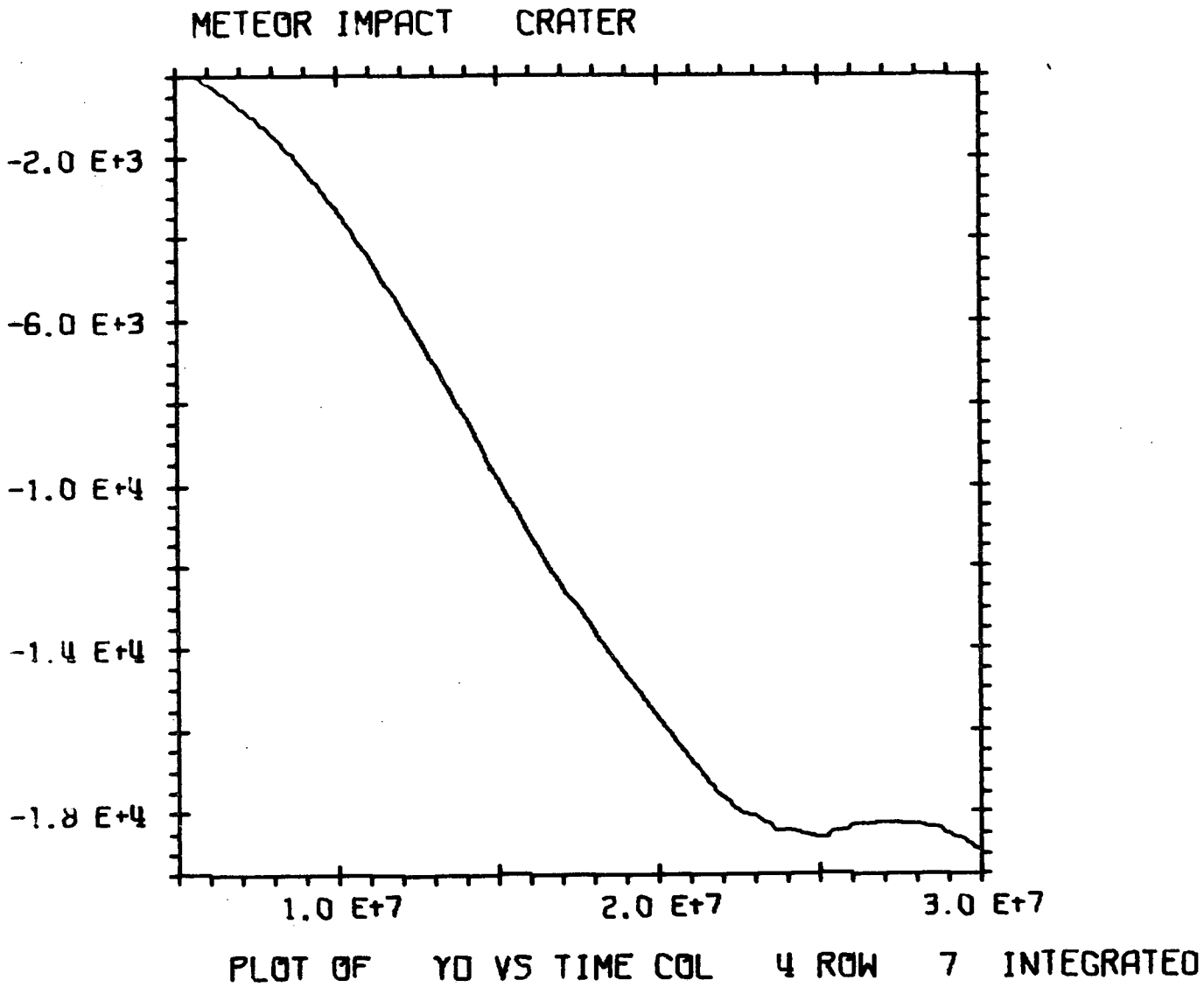
METEOR IMPACT CRATER
-2.0 E+3
-6.0 E+3
-1.0 E+4
-1.4 E+4
-1.8 E+4
1.0 E+7
2.0 E+7
3.0 E+7
PLOT OF YO VS TIME COL 4 ROW 7 INTEGRATED

Figure B-104

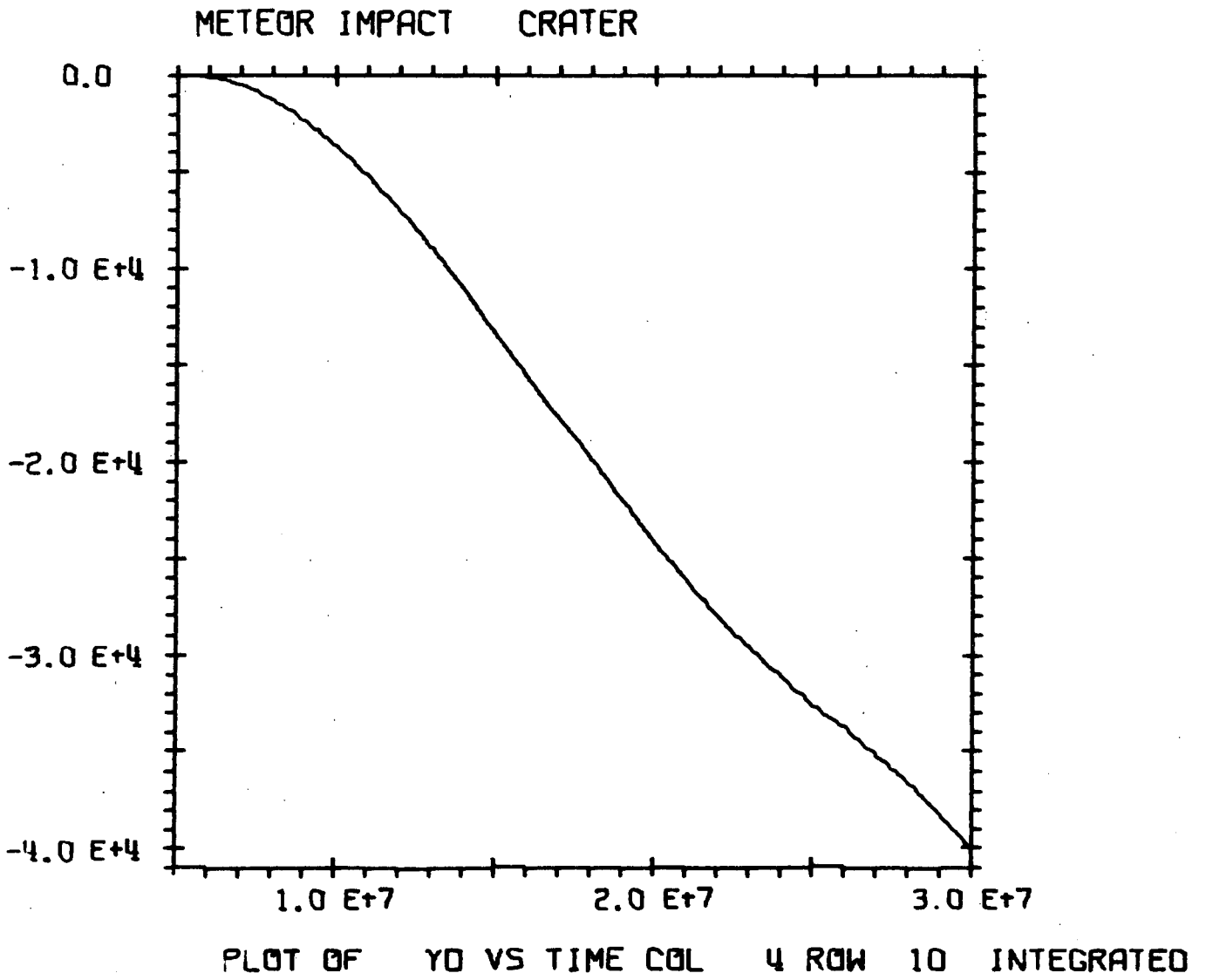
METEOR IMPACT CRATER
0.0
-1.0 E+4
-2.0 E+4
-3.0 E+4
-4.0 E+4
1.0 E+7
2.0 E+7
3.0 E+7
PLOT OF YO VS TIME COL 4 ROW 10 INTEGRATED

Figure B-105

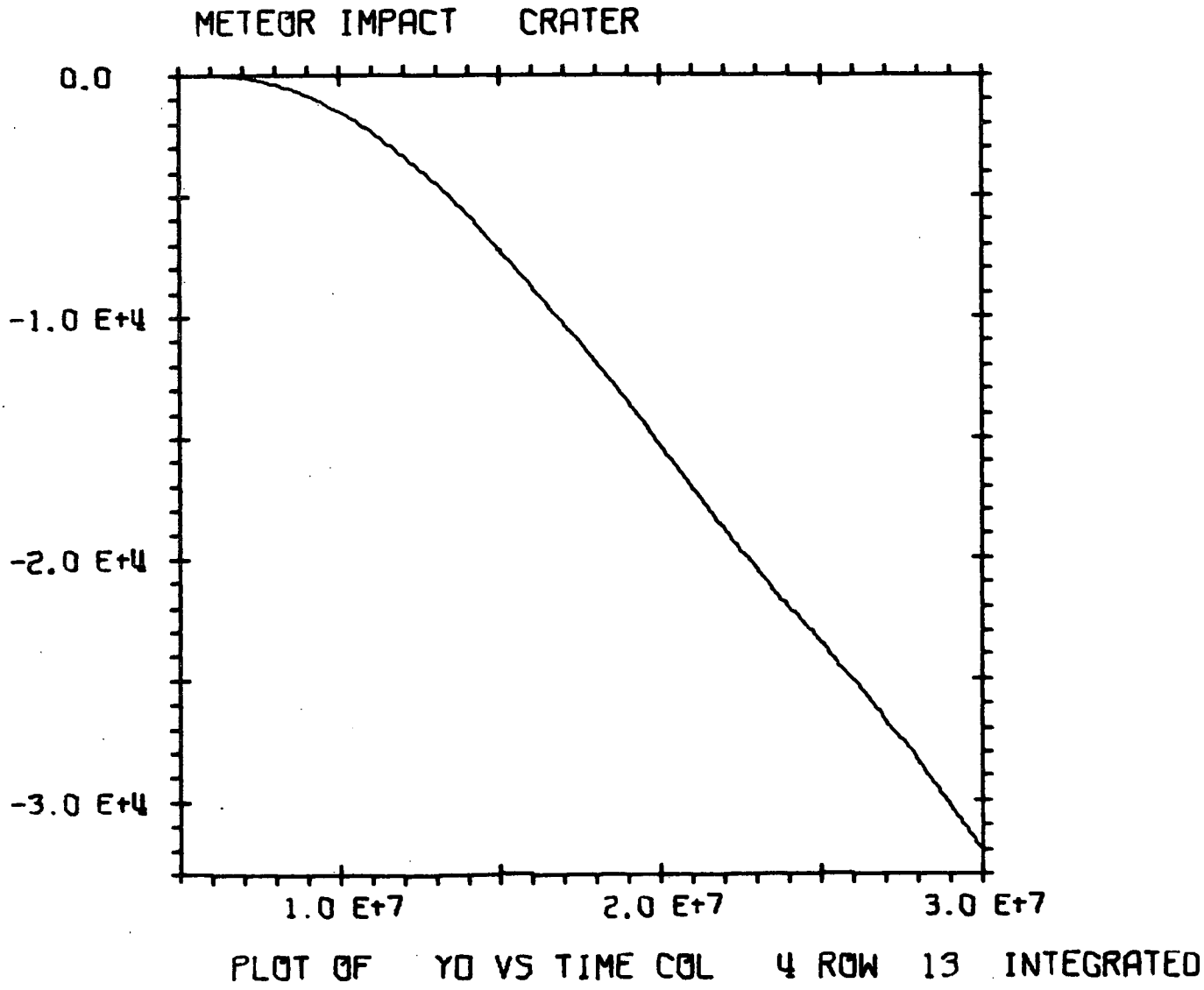
METEOR IMPACT CRATER
0.0
-1.0 E+4
-2.0 E+4
-3.0 E+4
1.0 E+7
2.0 E+7
3.0 E+7
PLOT OF YO VS TIME COL 4 ROW 13 INTEGRATED

Figure B-106

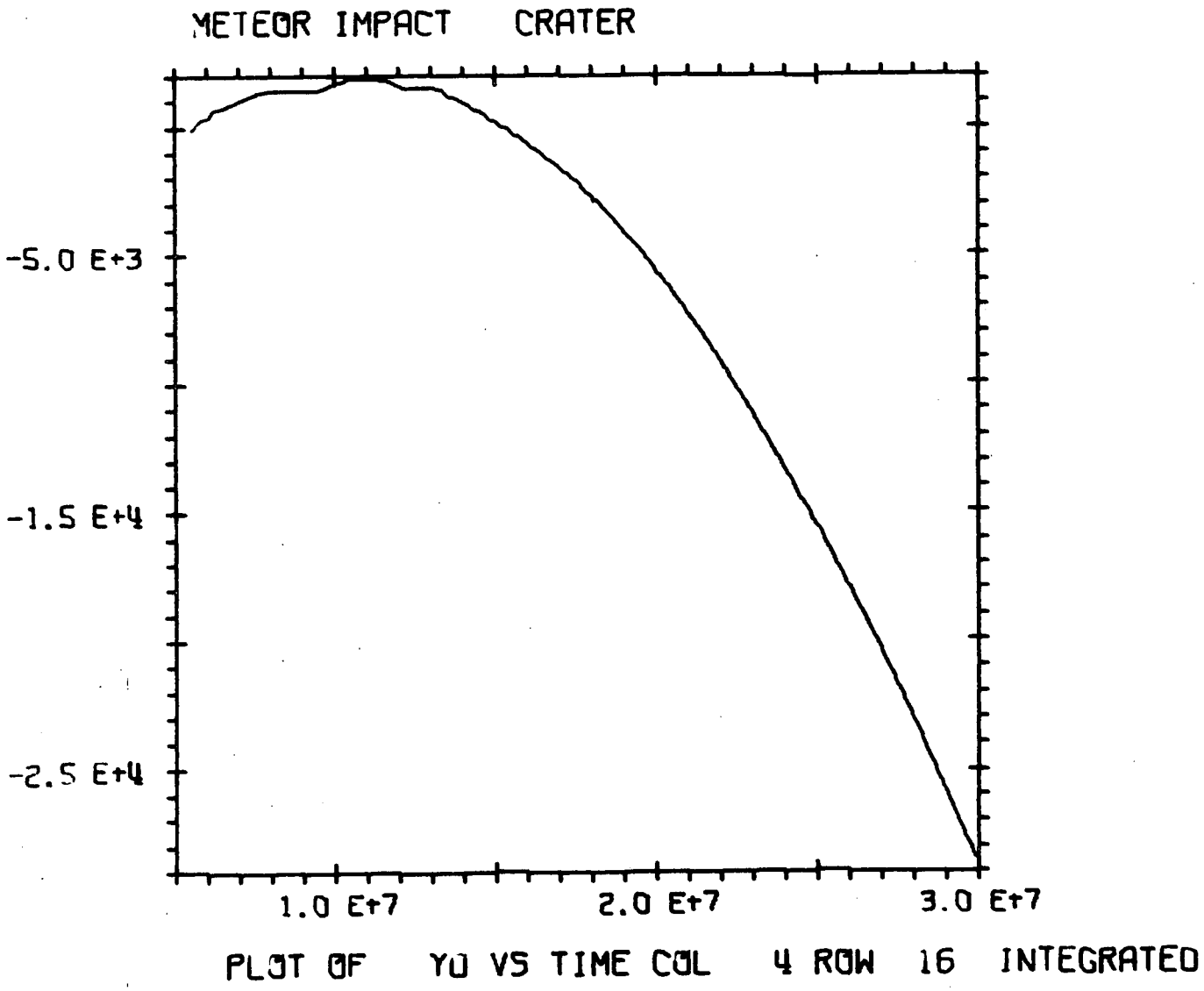
METEOR IMPACT CRATER
-5.0 E+3
-1.5 E+4
-2.5 E+4
1.0 E+7
2.0 E+7
3.0 E+7
PLOT OF YU VS TIME COL 4 ROW 16 INTEGRATED

Figure B-107

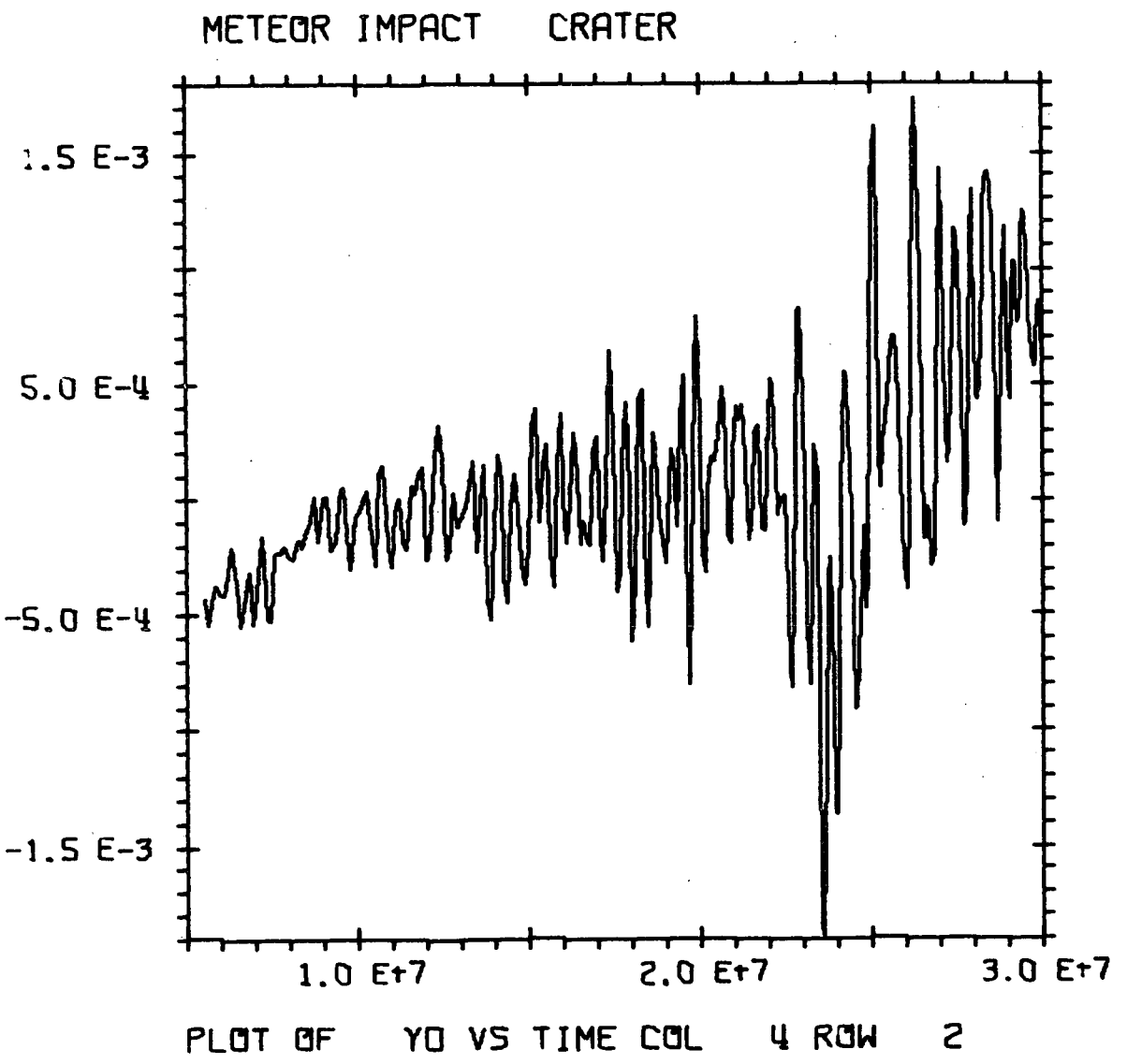
METEOR IMPACT CRATER
1.5 E-3
5.0 E-4
-5.0 E-4
-1.5 E-3
1.0 E+7
2.0 E+7
3.0 E+7
PLOT OF YO VS TIME COL 4 ROW 2

Figure B-108

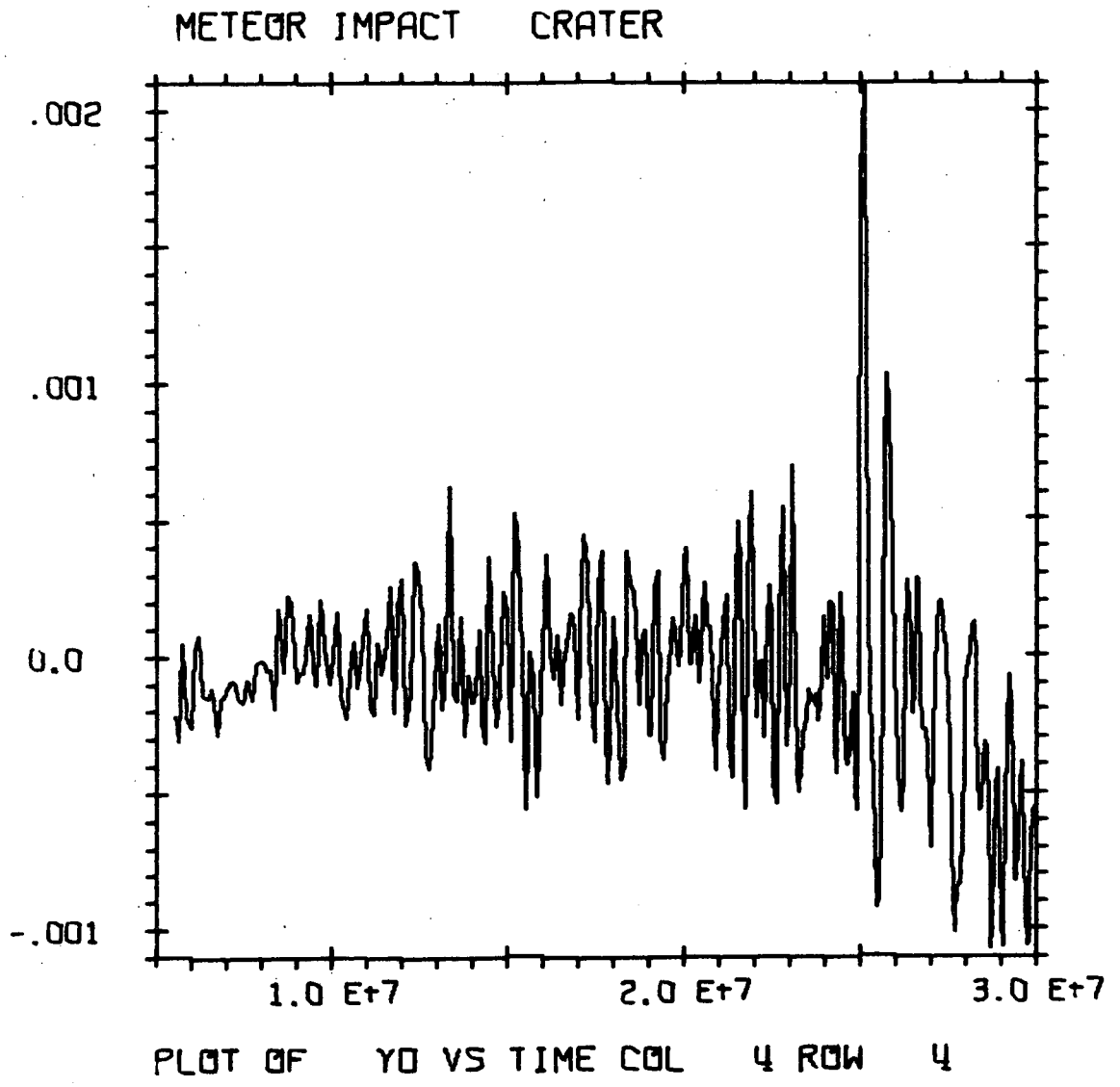
METEOR IMPACT CRATER
.002
.001
0.0
-.001
1.0 E+7
2.0 E+7
3.0 E+7
PLOT OF YO VS TIME COL 4 ROW 4

Figure B-109

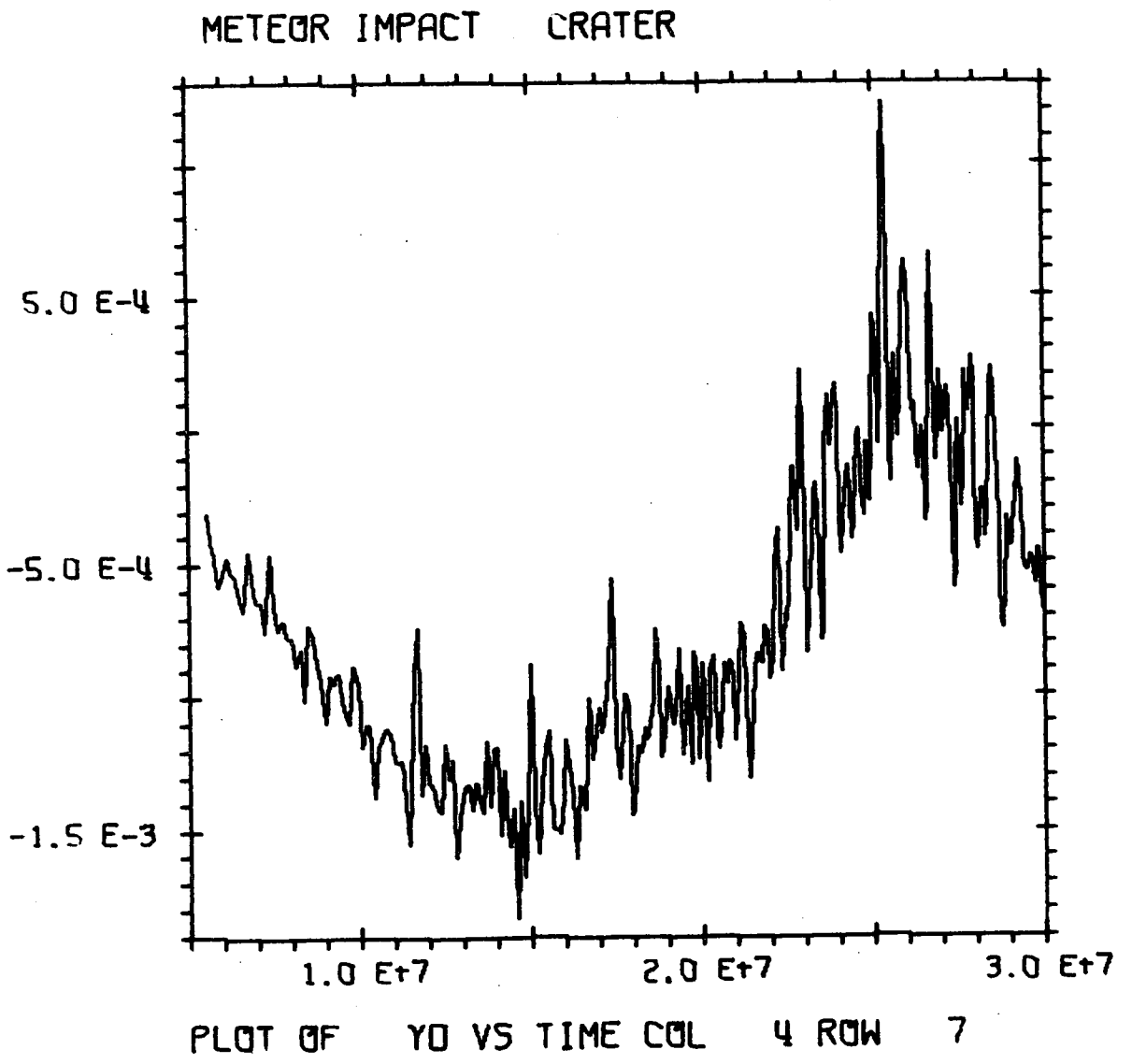
METEOR IMPACT CRATER
5.0 E-4
-5.0 E-4
-1.5 E-3
1.0 E+7
2.0 E+7
3.0 E+7
PLOT OF YO VS TIME COL 4 ROW 7

Figure B-110

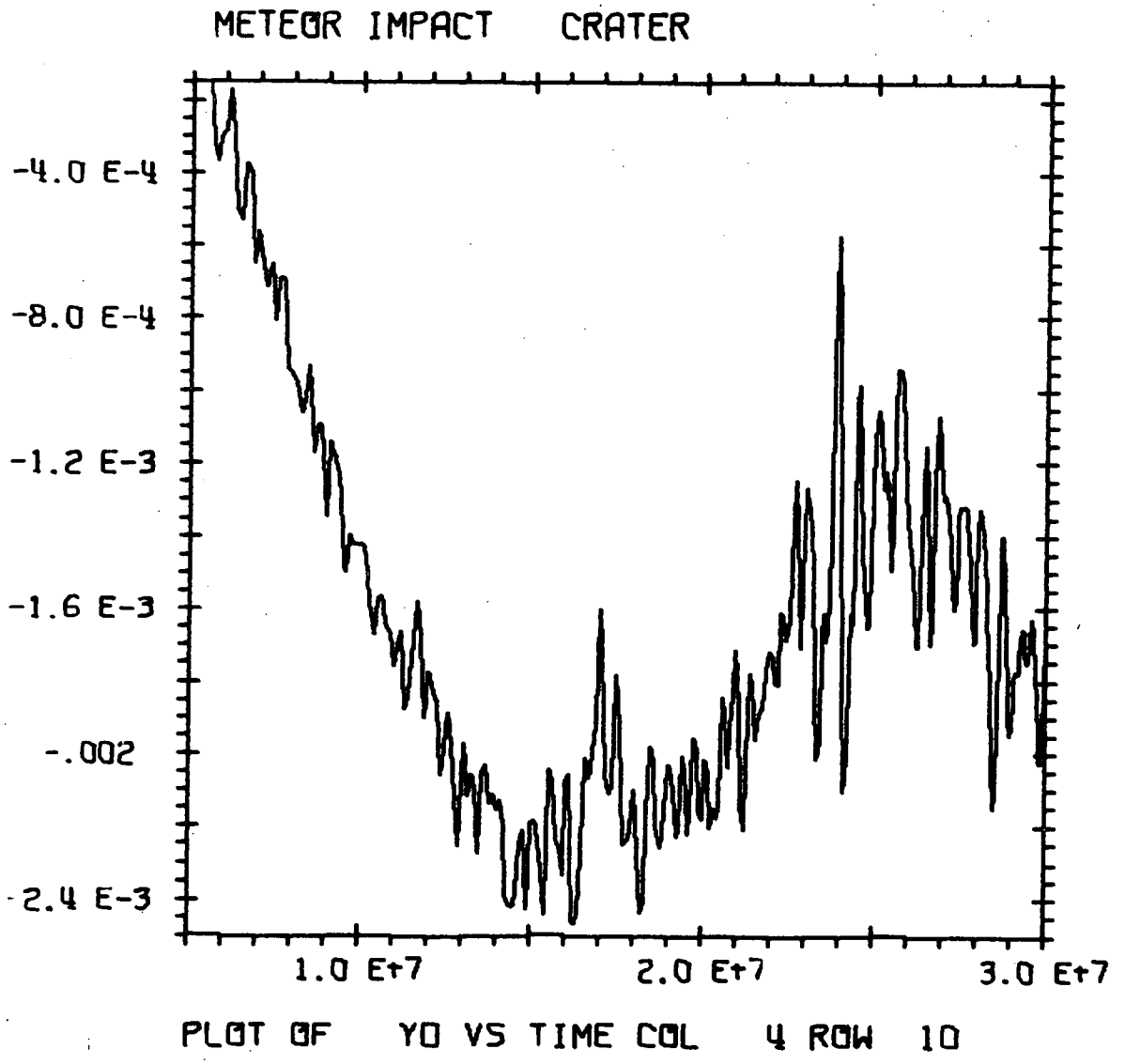
METEOR IMPACT CRATER
-4.0 E-4
-8.0 E-4
-1.2 E-3
-1.6 E-3
-.002
-2.4 E-3
1.0 E+7
2.0 E+7
3.0 E+7
PLOT OF YO VS TIME COL 4 ROW 10

Figure B-111

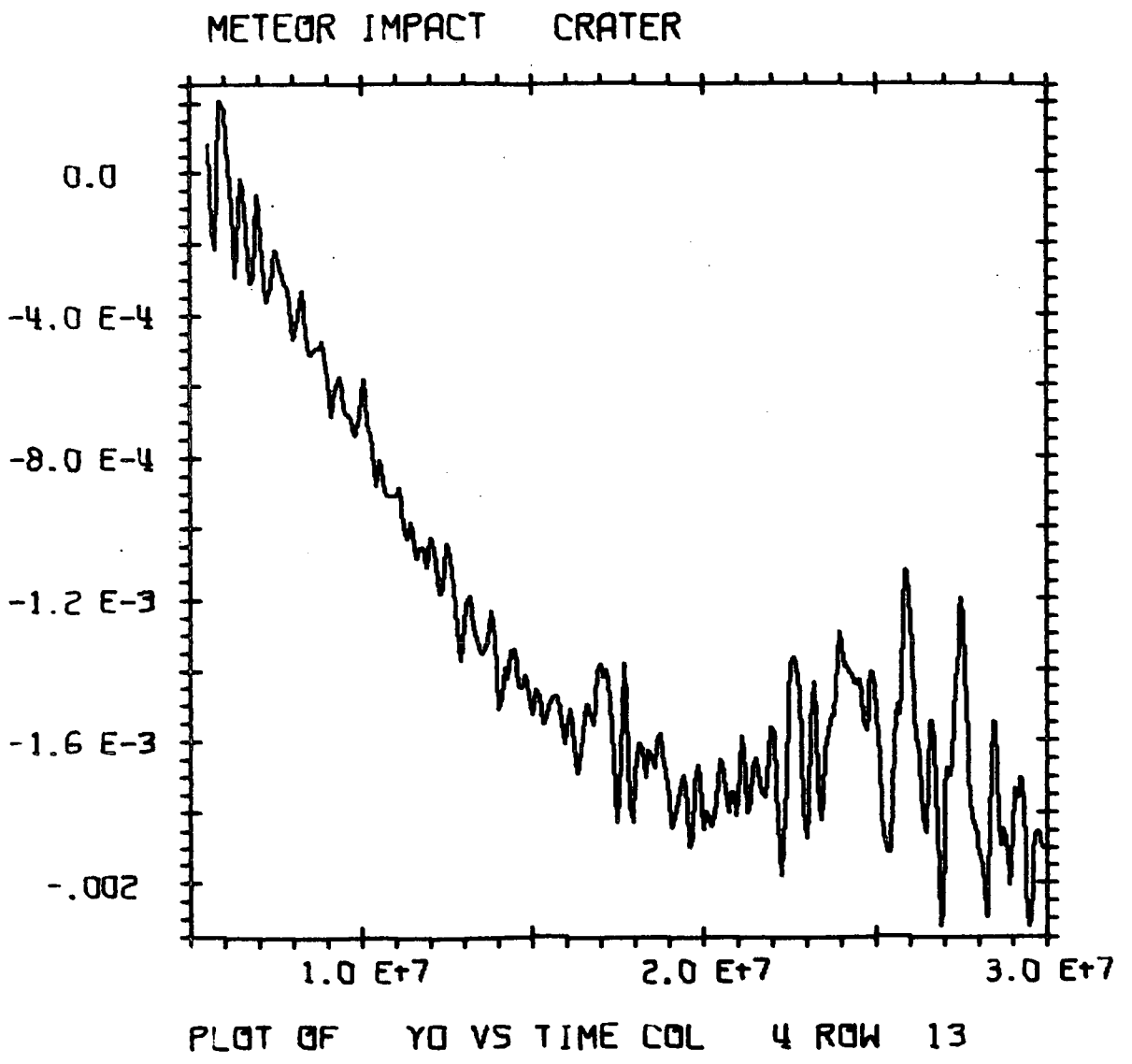
METEOR IMPACT CRATER
0.0
-4.0 E-4
-8.0 E-4
-1.2 E-3
-1.6 E-3
-.002
1.0 E+7
2.0 E+7
3.0 E+7
PLOT OF YO VS TIME COL 4 ROW 13

Figure B-112

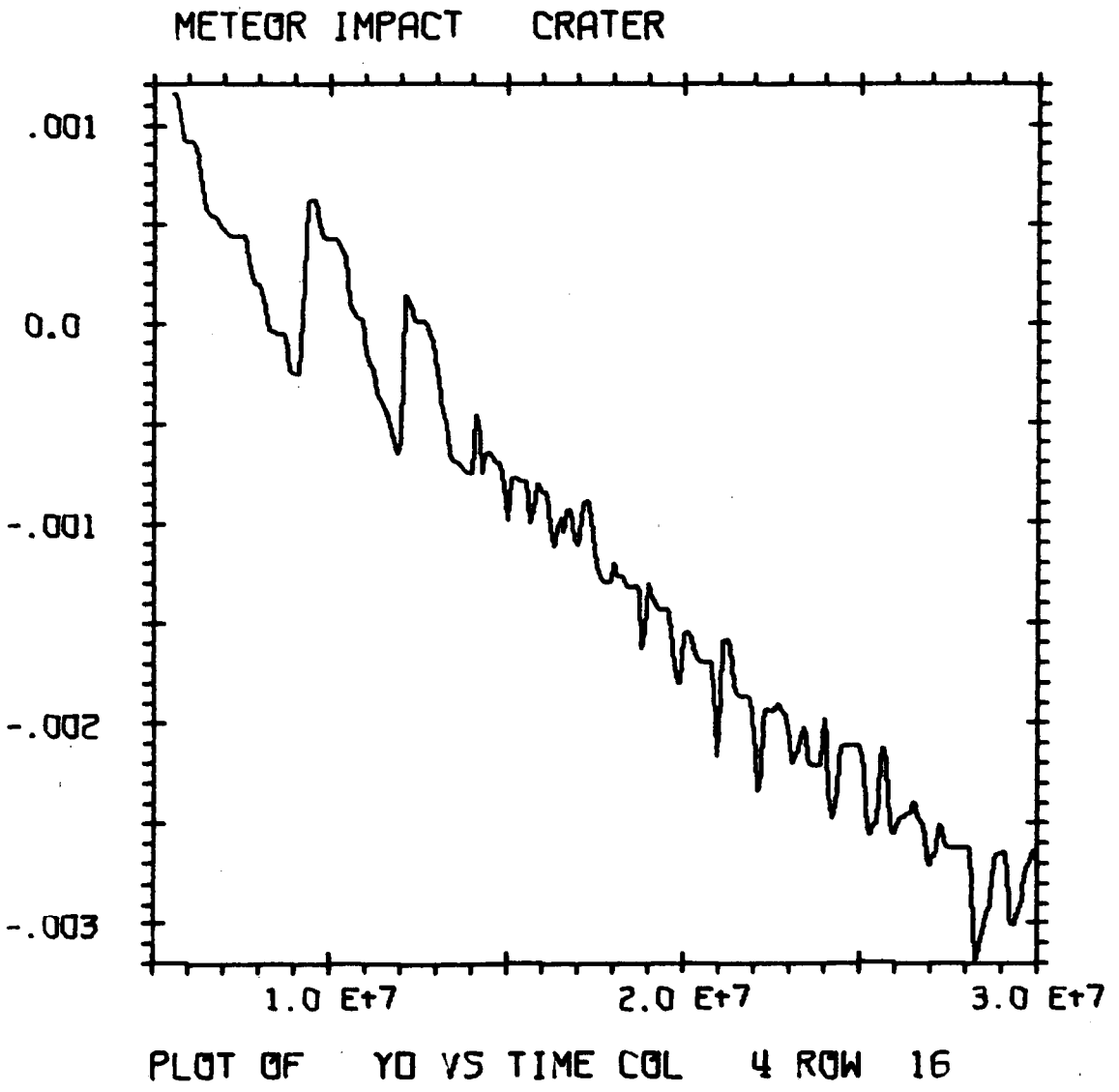
METEOR IMPACT CRATER
.001
0.0
-.001
-.002
-.003
1.0 E+7
2.0 E+7
3.0 E+7
PLOT OF YO VS TIME COL 4 ROW 16

Figure B-113